

ISSN 2312-4334

MINISTRY OF EDUCATION AND SCIENCE OF UKRAINE

East European Journal of Physics

No 1. 2022

2022

East European Journal of Physics

EEJP is an international peer-reviewed journal devoted to experimental and theoretical research on the nuclear physics, cosmic rays and particles, high-energy physics, solid state physics, plasma physics, physics of charged particle beams, plasma electronics, radiation materials science, physics of thin films, condensed matter physics, functional materials and coatings, medical physics and physical technologies in an interdisciplinary context.

Published quarterly in hard copy and online by V.N. Karazin Kharkiv National University Publishing.
ISSN 2312-4334 (Print), ISSN 2312-4539 (Online)

The editorial policy is to maintain the quality of published papers at the highest level by strict peer review.

Approved for publication by the Academic Council of the V. N. Karazin Kharkiv National University (April 11, 2022; Protocol No.7).

EEJP registered by the order of Ministry of Education and Science of Ukraine No. 1643 of 28.12.2019, and included in the list of scientific professional editions of Ukraine (category "A", specialty: 104, 105), in which can be published results of dissertations for obtaining Ph.D. and Dr. Sci. degrees in physical and mathematical sciences.

The Journal is a part of the Web of Science Core Collection (ESCI) scientometric platform and indexed by SCOPUS.

Editor-in-Chief

☉Azarenkov N.A., *Academician of NAS of Ukraine, Professor, V.N. Karazin Kharkiv National University, Kharkiv, Ukraine*

Deputy editor

☉Girka I.O., *Corresponding Member of NAS of Ukraine, Professor, V.N. Karazin Kharkiv National University, Kharkiv, Ukraine*

Editorial Board

- ☉Adamenko I.N., *Professor, V.N. Karazin Kharkiv National University, Ukraine*
- ☉Antonov A.N., *D.Sc., Professor, Institute of Nuclear Research and Nuclear Energy, Sofia, Bulgaria*
- ☉Barannik E.A., *D.Sc., Professor, V.N. Karazin Kharkiv National University, Ukraine*
- ☉Beresnev V.M., *D.Sc., Professor, V.N. Karazin Kharkiv National University, Ukraine*
- ☉Berezhnoy Yu.A., *D.Sc., Professor, V.N. Karazin Kharkiv National University, Ukraine*
- ☉Bizyukov A.A., *D.Sc., Professor, V.N. Karazin Kharkiv National University, Ukraine*
- ☉Bragina L.L. *D.Sc., Professor, STU "Kharkiv Polytechnic Institute", Ukraine*
- ☉Broda B., *D.Sc., University of Lodz, Poland*
- ☉Dragovich B.G., *D.Sc., University of Belgrade, Serbia*
- ☉Duplij S.A., *D.Sc., Center for Information Technology (ZIV), Westfälische Wilhelms-Universität Münster, Münster, Germany*
- ☉Garkusha I.E., *Corresponding Member of NAS of Ukraine, NSC Kharkiv Institute of Physics and Technology, Ukraine*
- ☉Grekov D.L., *D.Sc., NSC Kharkiv Institute of Physics and Technology, Ukraine*
- ☉Karnaukhov I.M., *Academician of NAS of Ukraine, NSC Kharkiv Institute of Physics and Technology, Ukraine*
- ☉Korchin A.Yu., *D.Sc., NSC Kharkiv Institute of Physics and Technology, Ukraine*
- ☉Lazurik V.T., *D.Sc., Professor, V.N. Karazin Kharkiv National University, Ukraine*
- ☉Mel'nik V.N., *D.Sc., Institute of Radio Astronomy, Kharkiv, Ukraine*
- ☉Merenkov N.P., *D.Sc., NSC Kharkiv Institute of Physics and Technology, Ukraine*
- ☉Neklyudov I.M., *Academician of NAS of Ukraine, NSC Kharkiv Institute of Physics and Technology, Ukraine*
- ☉Noterdaeme J.-M., *D.Sc., Max Planck Institute for Plasma Physics, Garching, Germany*
- ☉Nurmagambetov A.Yu., *D.Sc., Professor, NSC Kharkiv Institute of Physics and Technology, Ukraine*
- ☉Ostrikov K.N., *D.Sc., Plasma Nanoscience Centre Australia, Clayton, Australia*
- ☉Peletninsky S.V., *Academician of NAS of Ukraine, NSC Kharkiv Institute of Physics and Technology, Ukraine*
- ☉Pilipenko N.N., *D.Sc. in Technical Sciences, NSC Kharkiv Institute of Physics and Technology, Ukraine*
- ☉Radinschi I., *D.Sc., Gheorghe Asachi Technical University, Iasi, Romania*
- ☉Slyusarenko Yu.V., *Academician of NAS of Ukraine, NSC Kharkiv Institute of Physics and Technology, Ukraine*
- ☉Smolyakov A.I., *University of Saskatchewan, Saskatoon, Canada*
- ☉Shul'ga N.F., *Academician of NAS of Ukraine, NSC Kharkiv Institute of Physics and Technology, Ukraine*
- ☉Tkachenko V.I., *D.Sc., NSC Kharkiv Institute of Physics and Technology, Ukraine*
- ☉Yegorov O.M., *D.Sc., NSC Kharkiv Institute of Physics and Technology, Ukraine*

Executive Secretary

☉Hirnyk S.A., *Ph.D., V.N. Karazin Kharkiv National University, Kharkiv, Ukraine*

Editorial office

Department of Physics and Technologies, V.N. Karazin Kharkiv National University
Kurchatov av., 31, office 402, Kharkiv, 61108, Ukraine

Tel: +38-057-335-18-33,

E-mail: eejp@karazin.ua,

Web-pages: <http://periodicals.karazin.ua/eejp> (Open Journal System)

Certificate of State registration No.20644-10464P, 21.02.2014

ORIGINAL ARTICLES

- Study of $^{14}\text{N}(\gamma, np)3\alpha$ Reaction for E_γ up to 150 MeV** 5
S.N. Afanasiev
Дослідження реакції $^{14}\text{N}(\gamma, np)3\alpha$ при $E_\gamma^{\text{макс}} = 150$ MeB
С.М. Афанасьєв
- Simulation of Heat Transfer in Single-Crystal Lithium Niobate in Interaction with Continuous-Wave Laser Radiation** 10
Denys O. Protektor, Denys O. Lisin
Моделювання теплообміну в монокристалічному ніобаті літію при взаємодії безперервним лазерним випроміненням
Денис О. Протектор, Денис О. Лісін
- An Insight into the Electronic, Optical and Transport Properties of a Half Heusler Alloy: NiVSi** 16
Djelti Radouan, Besbes Anissa, Bestani Benaouda
Огляд електронних оптичних та транспортних властивостей напівгейслерового сплаву: NiVSi
Джелті Радуан, Бесбес Анісса, Бестані Бенауда
- Level Structure of ^{58}Cu Within Modified Surface Delta-Interaction** 26
Dalal N. Hameed, Ali K. Hasan
Структура рівнів ^{58}Cu з модифікованою поверхнею дельта-взаємодії
Далал Н. Хамід, Алі К. Хасан
- Study of Electrostatic Ion-Cyclotron Waves in Magnetosphere of Uranus** 32
Rama S. Pandey, Mukesh Kumar
Вивчення електростатичних іонно-циклотронних хвиль в магнітосфері урану
Рама С. Пандей, Мукеш Кумар
- Effect of the Relativistic Electron Beam on Propagating Whistler-Mode Wave for Ring Distribution in the Saturn Magnetosphere** 40
E.H. Annex, R.S. Pandey, Mukesh Kumar
Вплив релятивістського електронного променя на поширення хвиль з вістлерними модами для кільцевого розподілу в магнітосфері Сатурна
Є.Х. Аннекс, Рама С. Пандей, Мукеш Кумар
- Study of Structural, Elastic, Thermal and Transport Properties of Ternary X(X=Co, Rh and Ir)MnAs Obtained by DFT** 47
Salim Kadri, Tourab Mohamed, Berkani Mahièddine, Amraoui Rabie, Bordjiba Zeyneb
Дослідження структурних, пружних, теплових та транспортних властивостей трійних сполук X(X=Co, Rh та Ir)MnAs, отриманих методом ДПТ
Салім Кадрі, Тураб Мохамед, Беркані Махієддіне, Амрауї Рабіє, Борджиба Зейнеб
- Characteristics and Optical Properties of $\text{Bi}_2\text{Te}_{2.45}\text{Se}_{0.55}$ Thin Film** 58
A.S. Salwa, Azza El-Sayed Ahmed
Характеристики та оптичні властивості тонкої плівки $\text{Bi}_2\text{Te}_{2.45}\text{Se}_{0.55}$
А.С. Салва, Азза Ель-Сайед Ахмед
- Computation of Structure and Electrical Resistivity of Liquid Na-Rb Alloys** 66
R.R. Koireng, P.C. Agarwal, Alpna Gokhroo
Розрахунок структури та електричного опору рідких сплавів Na-Rb
Р.Р. Койренг, П.К. Агарваль, Альпана Гохроо
- Enhanced Third Generation Semiconductor Material-Based Solar Cell Efficiency by Piezo-Phototronic Effect** 70
Michael Gyan, Joseph Parbby, Francis E. Botchey
Підвищення ефективності сонячних елементів третього покоління на основі п'єзо – фототронного ефекту
Майкл Джан, Джозеф Парбі, Френсіс Е. Ботчей
- Interactions of Novel Phosphonium Dye with Lipid Bilayers: A Molecular Dynamics Study** 77
Olga Zhytniakivska
Взаємодія нового фосфонієвого зонду з ліпідними мембранами: Молекулярно-динамічне дослідження
О. Житняківська

- Using a Scanner to Measure Absorbed Doses with Radiochromic Film Dosimeters** 85
Volodymyr Morgunov, Serhii Lytovchenko, Volodymyr Chyshkala, Natalia Didenko, Valentyn Vynnyk
Використання сканера для вимірювання поглинених доз радіохромними плівковими дозиметрами
В.В. Моргунов, С.В. Литовченко, В.О. Чижкалала, Н.В. Діденко, В.О. Лінник
- Fluorescence Study of the Interactions Between Insulin Amyloid Fibrils and Proteins** 96
Uliana Tarabara, Olga Zhytniakivska, Kateryna Vus, Valeriya Trusova, Galyna Gorbenko
Флуоресцентне дослідження взаємодії між амілоїдними фібрилами інсуліну та білками
У. Тарабара, О. Житняківська, К. Вус, В. Трусова, Г. Горбенко
- Investigation of Interaction Mechanisms of High Energy Electrons and Gamma Quantum with Aqueous Solution of Methyl Orange Dye** 105
Vitaliy V. Tsyats'ko, Sergey P. Gokov, Yuri G. Kazarinov, Tetiana V. Malykhina
Дослідження механізмів взаємодії високоенергетичних електронів і гамма-квантів з водним розчином барвника метилового оранжевого
В.В. Цяцько, С.П. Гоков, Ю.Г. Казарінов, Т.В. Малихіна
- Positively Charged Macroparticles in Low-Temperature Plasma** 110
Aleksander A. Bizyukov, Aleksandr D. Chibisov, Dmitry V. Chibisov, Oksana A. Zhernovnykova, Tamara I. Deynichenko, Nikolai N. Yunakov
Позитивно заряджені макрочастки в низькотемпературній плазмі
О.А. Бізюков, О.Д. Чібісов, Д.В. Чібісов, О.А. Жерновникова, Т.І. Дейниченко, М.М. Юнаков
- Resolution of the Ultrasound Doppler System Using Coherent Plane-Wave Compounding Technique** 116
Iryna V. Sheina, Eugen A. Barannik
Роздільна здатність ультразвукової доплерівської системи при використанні технології когерентного компаундінгу плоских хвиль
І.В. Шеїна, Є.О. Баранник

STUDY OF $^{14}\text{N}(\gamma, np)3\alpha$ REACTION FOR E_γ UP TO 150 MeV[†]

 Serhii N. Afanasiev

National Science Center “Kharkov Institute of Physics and Technology”, Kharkiv, Ukraine

E-mail: afanserg@kipt.kharkov.ua

Received November 3, 2021; revised December 24, 2021; accepted March 13, 2022

The reaction $^{14}\text{N}(\gamma, np)3\alpha$ induced by bremsstrahlung photons of endpoint energy $E_\gamma^{\text{max}} = 150$ MeV has been investigated using diffusion chamber, which is placed into the magnetic field. The distribution functions of the reaction yield, the energy and momentum of the final particles from E_γ were measured and it was determined that at $E_\gamma > 45$ MeV, change in the behavior of these functions occurs. The average energy T^{aver} was calculated for the particles with the energy falling within a 1 MeV interval of the total kinetic energy $T_0 = E_\gamma - Q$, where Q is the energy threshold of the reaction ($Q = 19.77$ MeV). At $T_0 \sim 20$ MeV, the dependence of the contributions from T^{aver} to T_0 changes sharply. At $T_0 > 20$ MeV, most of the energy is carried away by nucleons, their relative contribution is equal, and this agrees with the assumption of the quasideuteron interaction mechanism. The momentum distribution distributions for the neutron and proton have a similar form, with a strong shift of the maximum towards higher energies with an increase in the energy of the γ quantum. For a system of 3α -particles, in each distribution, peak is observed centered at 100 MeV/c, the relative contribution of which smoothly decreases with increasing momentum, and a wide high-energy "tail" appears. The energy and angular correlations of the np-pair depends on both of the energy E_γ and the momentum of the system of 3α -particles.

Keywords: diffusion chamber, photoreaction, ^{14}N nucleus, np-pair, energy and angular distributions.

PACS: 25.20.-x.

The mechanism of (γ, np) -reactions has been a subject of research interest for many years. At energy above the giant resonance, the photonuclear reactions represent an effective instrument for studying nucleon correlations, which are an important component of information on nuclear forces, cluster configurations, and meson-exchange currents in nuclei. Studying of the photon absorption mechanism by the correlated np-pair offers a possibility to look into the problem of nucleonic interactions at small and medium distances. The phenomenological quasideuteron model has successfully explained (γ, np) -reactions at intermediate energies [1-3]. This model can express two-nucleon knockout cross-section by two factors: the function, proportional to the probability of finding a nucleon pair in the nucleus and a Fourier transform of the correlation function. At energies below the meson production threshold γ -quanta are absorbing by correlated nucleon or by nucleon pair at the time of the meson exchange. Single-nucleon emission arises when either the proton or the neutron escapes and the other participating nucleon being reabsorbed into the nucleus through final-state interactions. Recently, the model has a further development in new microscopic approaches. An agreement with experimental results was achieved taking into account meson exchange currents [4] and collective nucleus characteristics in the framework of shell model [5]. Experimental results about of a highly excited final nuclear state formation in (γ, np) -reactions are needed to verify the prediction of the model.

In this article, we present results obtained by studying the photodisintegration of nitrogen nuclei via the reaction $^{14}\text{N}(\gamma, np)3\alpha$ at the energies below the meson production threshold. The results given here were obtained by using a diffusion chamber [6-7] placed in a magnetic field and exposed to a beam of bremsstrahlung photons, their endpoint energy being 150 MeV. Low pressure in the chamber and matching of the target and the detector made possible to measure the kinematic parameters of all charged particles from reaction threshold in a wide range of energies and angles and to obtain information on excited intermediate states of nuclei.

The chamber used operated in a mode that made it possible to separate singly and doubly charged particles visually and to compare the ionization density and the width of a track after measuring its radius of curvature. Four-prong events featuring three doubly charged and one singly charged particles were measured simultaneously. The reaction being studied was separated on the basis of the imbalance of the transverse momentum P_\perp , which is equal to the sum of the transverse momenta of the four particles involved. If this imbalance was equal or greater than 30 MeV/c, the respective event was attributed to the reaction being studied. The background-reaction $(\gamma + ^{14}\text{N} \rightarrow d3\alpha)$ contribution was estimated at 3%. From the laws of conservation of energy and momentum, the energy of a γ -quantum equals

$$E_\gamma = \frac{m^2 + P^2 - (M - E)^2}{2 \cdot (M - E + P_x)}, \quad (1)$$

where m and M are the neutron and the ^{14}N nucleus masses; E and P are, respectively, the total energy and the total momentum of the proton and three ^4He nuclei appearing in the final state; and P_x is the projection of this total momentum onto the direction of the photon momentum. In the experiment, the axis OX was directed along the beam of γ -quanta. The

[†] Cite as: S.N. Afanasiev, East. Eur. J. Phys. 1, 5 (2022), <https://doi.org/10.26565/2312-4334-2022-1-01>
© S.N. Afanasiev, 2022

kinematic parameters of a neutron were obtained with the help of conservation laws after having calculated the γ -quantum energy.

Earlier in our experiment, we mainly carried out [8 - 10] studies of (γ, np) -reactions on ${}^4\text{He}$, ${}^{12}\text{C}$, ${}^{14}\text{N}$, and ${}^{16}\text{O}$ nuclei with the formation of a residual nucleus in the ground state. There is also information about the reaction $(\gamma, np)\alpha{}^6\text{Li}$ on the ${}^{12}\text{C}$ nucleus [9]. At energies above the giant dipole resonance, the experimental data agrees with the calculations within the framework of the mechanism of photon absorption by an np -pair.

EXPERIMENTAL RESULTS

We have measured dependence of the number of events for the reaction ${}^{14}\text{N}(\gamma, np)3\alpha$ in the photon energy range from the reaction threshold up to 150 MeV with a step of 2 MeV. The results are shown in Fig. 1a as a histogram.

The measured energy dependence of the number of events exhibits a broad resonance centered at 40 MeV. The rate of decrease in the energy dependence undergoes a change in the region around 45 MeV. Solid curve in Fig. 1a demonstrate the fitting experimental data by using of a linear combination of two Gaussian functions with parameters $E_\gamma^1 = 34.8 \pm 0.41$ MeV and $\Gamma^1 = 10.39 \pm 1.19$ MeV (curve 1), $E_\gamma^2 = 62.99 \pm 2.74$ MeV and $\Gamma^2 = 54.79 \pm 6.65$ MeV (curve 2). The fit qualitatively describes the presented distribution. The area of the function in the region of the first maximum is half that in the region of the second maximum. For $E_\gamma > 45$ MeV, the main contribution is made by the function describing the "high-energy" tail.

A similar irregularity in the region of this energy value was previously observed in the reactions ${}^{14}\text{N}(\gamma, np){}^{12}\text{C}$ [8]. The results are normalized in the region around 40 MeV and are represented by open circles in Fig. 1b. The experimental curves have the same slope and this, apparently, is associated with the same mechanism of interaction of the γ -quantum with the nucleus.

Previously (article [8]), a comparison of the cross sections (γ, np) of reactions on ${}^{12}\text{C}$, ${}^{14}\text{N}$, and ${}^{16}\text{O}$ nuclei with calculations in different theoretical approaches was made. The change in the rate of decrease in the cross section at around 40 MeV may possibly be due to a transition from the mechanism of direct nucleon knockout to the pair-absorption mechanism.

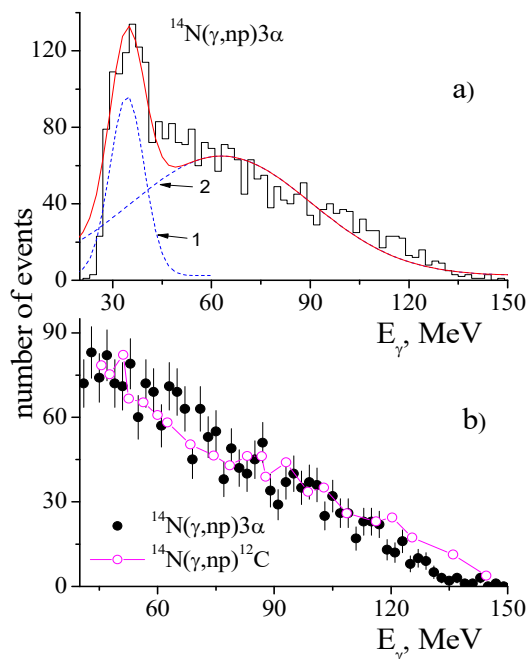


Figure 1. The reaction yield depending on the energy of the γ -quantum: a) – histogram, b) – closed points. Curves - fitting by a linear combination of two Gaussian functions. Open points - reaction ${}^{14}\text{N}(\gamma, np){}^{12}\text{C}$.

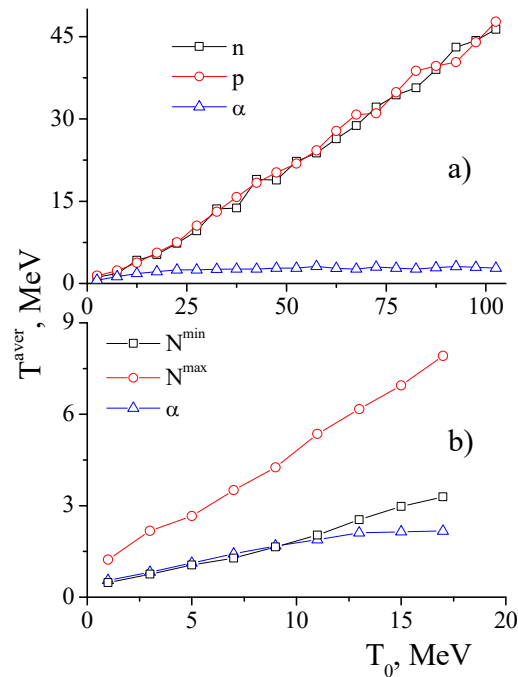


Figure 2. Dependence of the average kinetic energy of the final particles on the total kinetic energy.

Let us consider the relative contribution of the final particles to the total energy dependence of the reaction T_0 , which was defined as $T_0 = E_\gamma - Q$, where Q is the energy threshold of the reaction ($Q = 19.77$ MeV). The average energy T^{aver} was calculated for the particles with the energy falling within a 1 MeV interval of the total kinetic energy. The circles are in the centers of intervals and in Fig. 2a the dependence T^{aver} of the final particles are plotted. The histogram step equals 5 MeV. The squares show the distribution of T^{aver} for the neutron, circles – for the proton, and the triangles – for α -particles (due to the inseparability of α -particles, the figure shows the average value for three α -particles).

At $T_0 \sim 20$ MeV, the dependence of the contributions from T^{aver} to T_0 changes sharply. The value 20 MeV corresponds to the position of the maximum of the reaction's yield at $E_\gamma \sim 40$ MeV (fig. 1) and will be used further as the boundaries of the intervals in the analyze of events. The dependences of the average kinetic energy was approximated by the linear functions and the results of these fits are given in the second and third columns of the Table 1 for all final particles.

At $T_0 > 20$ MeV, most of the energy is carried away by nucleons, their relative contribution is equal, and this agrees with the assumption of the quasi-deuteron interaction mechanism.

At $T_0 < 20$ MeV another mechanism is possible. In the direct mechanism, knocked out nucleon carries most of energy of the final state. The energy of other products of the reaction amounts a smaller portion and weakly increases with the energy of the γ -quantum. Therefore, in each event are compared proton and neutron energy in c.m.s. Nucleon,

which has higher energy, was considered the leading nucleon (N^{max}), and nucleon, which has lower energy, was considered the accompanying nucleon (N^{min}). In the γ -quanta energy interval of 1 MeV the kinetic energies of the leading and accompanying nucleon, which fall into this interval, are separately summed. Total energies are divided on number of events, which fall into interval (Table 1, rows 5-6). Received average values are shown in Fig. 2b with circles for the leading nucleon, the squares are for the accompanying nucleon data and the triangles are for α -particles. An average energy divided by the intervals increases with γ -quanta energy increasing. This fact applies not only to the leading nucleon but also to the rest of nuclear decay products, which is a spectator in the direct mechanism model. The nucleon average energies are proportional to the total energy of the reaction product.

The leading nucleon average energy to the accompanying nucleon average energy ratio was determined and within the limits of errors, it has a value of 2. According to γ -quantum, absorption by the nucleon pair model it should be expected this ratio near 1.

T^{aver} for a α -particle increases at small T_0 , but already at $T_0 > 20$ MeV the relative contribution $T^{\text{aver}}(\alpha)$ is constant and insignificant.

Assuming a statistical distribution of energy between particles, we can calculate the average energy carried away by each particle as a function of T_0 [11]:

$$T = \frac{(A-M)}{(n-1) \cdot A} \cdot T_0, \quad (2)$$

where A and M are the atomic numbers of the target nucleus and the researched particle, respectively; and n is the number of particles in the final state.

In this reaction, the values of calculation by eq. (2) correspond: for the nucleon – 0.23 and for α -particles – 0.18 (should be remembered that there are three

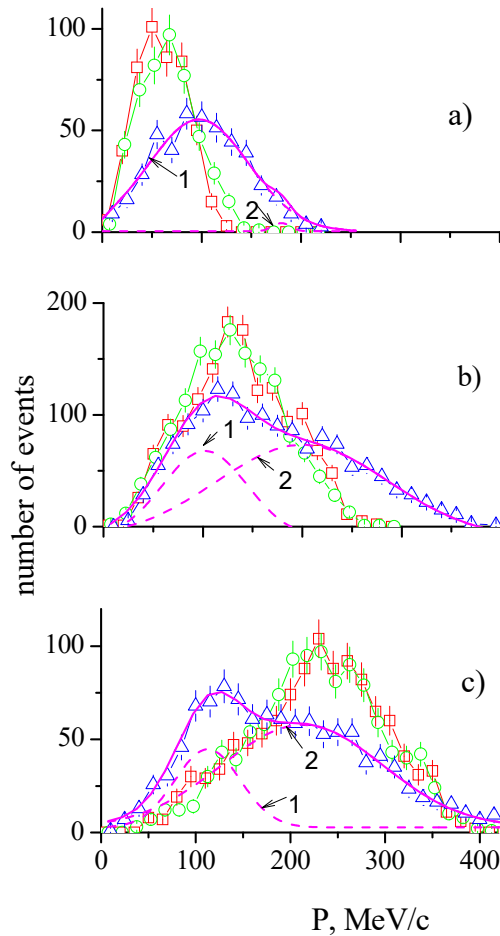


Figure 3. Reaction yield as a function of the particles momentum: a) $E_\gamma < 45$ MeV, b) $E_\gamma = 45 - 70$ MeV, c) $E_\gamma > 70$ MeV. The notation for the curves is explained in the text.

α -particles in the final state).

The experimental values for all final particles at $T_0 < 20$ MeV (Table 1, column 2, lines 2 - 4) agree with the calculation. Note the sharp change in the dependence at $T_0 > 20$ MeV, main part of the energy is carried away by the nucleons. The low rate of change in the dependence of distributions for α -particles may indicate that they are decay products of intermediate excited states.

The momentum distribution of final particles $f(P)$ was measured in a laboratory system in three energy intervals: a) $E_\gamma < 45$ MeV, b) $E_\gamma = 45 - 70$ MeV, c) $E_\gamma > 70$ MeV. The intervals are chosen so that the statistical coverage in each is approximately the same.

The results are given in Fig. 3. The points are placed at the middle of the histogram step, which is equal to 15 MeV/c. The number of events per 1 MeV/c are plotted along the ordinate, and the measurement errors are statistical. The squares show the distribution of for the neutron (P_n), circles – for the proton (P_p), and the triangles – for the system 3α -particles ($P_{3\alpha}$). The distributions for the neutron and proton have a similar form, with a strong shift of the maximum towards higher energies with an increase in the energy of the γ -quantum.

For a system of 3α -particles, in each distribution, a peak is observed centered at $100 \text{ MeV}/c$, the relative contribution of which smoothly decreases with increasing momentum, and a wide high-energy "tail" appears.

In the region of the peak, the distribution for the neutron and proton was approximated by a Gaussian function. The position of the maxima (columns 2-3) are given in Table 2 for various values of the photon energy (column 1) and they coincide for both particles within the error limits.

Solid curve in Fig. 3a demonstrates the fitting of the momentum distribution for the system 3α -particles, by using of a linear combination of two Gaussian functions (curves 1 and 2). The fitting parameters are the momentum positions of the peaks and the results of fitting are quoted in Table 2 (column 4). The positions of the 1st peak for all three energy intervals coincide within the error limits, but the relative contribution decreases with increasing energy E_γ – a) 89.25 %, b) 31.55 %, c) - 23.55 %.

Table 1. Dependence of the relative contributions of the average kinetic energy of particles on T_0 .

	$T_0 < 20 \text{ MeV}$	$T_0 > 20 \text{ MeV}$
n	0.28 ± 0.1	0.48 ± 0.1
p	0.27 ± 0.1	0.49 ± 0.1
α	0.15 ± 0.1	0.01 ± 0.1
N^{min}	0.16 ± 0.1	0.32 ± 0.1
N^{max}	0.39 ± 0.1	0.66 ± 0.1

Table 2. Momentum distributions of reaction products.

	$P_n, \text{ MeV}/c$	$P_p, \text{ MeV}/c$	$P_{3\alpha}, \text{ MeV}/c$
a)	54.5 ± 1.4	56.3 ± 1.3	1. 97.3 ± 2.6 2. 184.4 ± 3.5
b)	129.5 ± 2.8	121.2 ± 1.3	1. 95.6 ± 3.1 2. 192.7 ± 3.3
c)	228.2 ± 2.8	222.4 ± 2.2	1. 101.2 ± 2.3 2. 204.9 ± 5.1

Earlier, in the ${}^4\text{He}(\gamma, np)d$ reaction, a peak in the momentum distribution of deuterons was revealed [10] in the interval between 50 and $100 \text{ MeV}/c$. As the momentum grows above $100 \text{ MeV}/c$, the reaction yield decreases smoothly. The peak in the momentum distribution of deuterons is explained by the contribution of the quasideuteron model without final-state interaction. The position of the maximum is independent on the photon energy. This can be explained based on the law of conservation of energy - deuteron is a spectator and the peak width is associated with the momentum distribution of quasideuterons in the target nucleus.

It is concluded that the momentum distribution of the residual nucleus in (γ, np) -reactions can be very sensitive to changes in the reaction mechanism and can help to find the area of the manifestation of models of interaction of a γ -quantum with a nucleus.

In the studied reaction (${}^{14}\text{N}(\gamma, np)3\alpha$) the peak at $P_{3\alpha} \sim 100 \text{ MeV}/c$ can also appear due to the contribution of the quasideuteron model without taking into account the interaction in the final state.

The dependences of the relative energy (η_{np}) and relative angle (τ_{np}) distributions on the energy of the γ -quantum and the momentum of the system of 3α -particles are obtained.

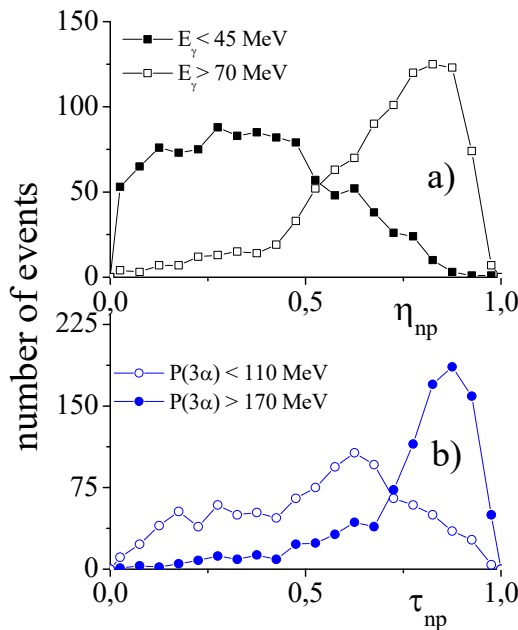


Figure 4. The dependences of the relative energy (a) and relative angle (b) distributions on the energy of the γ -quantum and the momentum of the system of 3α -particles.

The simplest models of the mechanism of photon absorption by ${}^4\text{He}$ nucleus were used in analyzing experimental data for the reaction ${}^4\text{He}(\gamma, np)d$ [10]. The pole diagram represents the quasideuteron model (model 1) - nucleons arising

The kinetic energy of the relative motion of the proton and neutron in their center-of-mass system is $T_{np} = [(E_n + E_p)^2 - (\mathbf{P}_n + \mathbf{P}_p)^2]^{1/2} - (m_n + m_p)$ where E_n, E_p ; $\mathbf{P}_n, \mathbf{P}_p$; m_n, m_p - total energies, momentums and masses of the nucleons respectively. It forms a part of the relative energies $\eta_{np} = T_{np} / (E_\gamma - Q)$, where E_γ - γ -quantum energy, Q - reaction threshold.

The relative angle of the nucleon pair is $\tau_{np} = \Theta_{np}/180$, where Θ_{np} is the nucleon scattering angle in center-of-mass system.

The distribution of events by η_{np} is shown in Fig. 4a in two intervals of the γ -quantum energy: $E_\gamma < 45 \text{ MeV}$ (opened circles) и $E_\gamma > 70 \text{ MeV}$ (closed circles). The distribution of events by τ_{np} is shown in Fig. 4b in two intervals of the momentum distribution the system 3α -particles: $P_{3\alpha} < 110 \text{ MeV}$ (opened circles) and $P_{3\alpha} > 170 \text{ MeV}$ (closed circles). Such intervals on E_γ and $P_{3\alpha}$ are chosen to estimate the influence of the boundary conditions on distributions on η_{np} and τ_{np} . In the first region, the distribution is practically symmetric with respect to 0.3, and in the second the distribution maximum shifts to $\eta \sim 0.85$. The phase distribution for the three-body final state is nearly symmetrical in relation to 0.5.

after quasideuteron disintegration do not interact with the remaining quasideuteron. In the final state, a nucleon may interact, however, with the second quasideuteron - the triangle diagram (model 2) represents this process. The last diagram corresponds to photon absorption by a three-nucleon system without final-state interaction (model 3). The analysis reaction yield in the deuteron momentum has led to the conclusion that at subthreshold meson production energies two models of the quasideuteron mechanism (model 1 and model 2) prevail. Triangular diagram dominates with a gradual increase in the contribution with increasing E_γ .

In our experiment, we also can see that the change in the interval from E_γ and from $P_{3\alpha}$ significantly changes the form of distributions by η_{np} and τ_{np} . Moreover, η_{np} is sensitive to the change of E_γ , and τ_{np} - to $P_{3\alpha}$. It is possible to select the conditions ($E_\gamma > 70$ MeV for η_{np} and $P_{3\alpha} < 110$ MeV for τ_{np}) under which events, corresponding to a pure pole diagram are distinguished.

CONCLUSIONS

Using a spectrometer based on a diffusion chamber, which is placed in the magnetic field, the $^{14}\text{N}(\gamma, np)3\alpha$ reaction was researched in the energy range from the reaction threshold up to 150 MeV. The reaction yield was measured and it was determined that the distribution has a broad resonance centered at 40 MeV. The distribution functions of the energy and momentum of the final particles from the total energy dependence of the reaction T_0 were measured and it was determined that at $T_0 > 20$ MeV occurs the change in the behavior of these functions. The distributions for the neutron and proton have a strong shift of the maximum towards higher energies with an increase in the energy of the γ quantum and for a system of 3α -particles; the peak is observed centered at 100 MeV/c. The energy and angular correlations of the np-pair are dependent on both the energy E_γ and the momentum of the system of 3α -particles.

ORCID IDs

 Serhii Afanasiev, <https://orcid.org/0000-0003-1682-4621>

Acknowledgements

Author is grateful to [A.F. Khodyachikh](#) for stimulating discussions and a number of enlightening comments.

REFERENCES

- [1] K. Gottfried. Nucl. Phys. **5**, 557 (1958). [https://doi.org/10.1016/0029-5582\(58\)90056-7](https://doi.org/10.1016/0029-5582(58)90056-7)
- [2] C.T. Noguchi, and F. Prats. Phys. Rev. C, **14**, 1133 (1974). <https://doi.org/10.1103/PhysRevC.14.1133>
- [3] F. Balestra, E. Bollini, L. Busso, et al. Nuovo Cimento, **38A**, 145 (1977). <https://doi.org/10.1007/BF02724538>
- [4] Y. Lei, S. Pittel, N. Sandulescu, A. Poves, et al. Phys. Rev. C, **84**, 044318 (2011). <https://doi.org/10.1103/PhysRevC.84.044318>
- [5] Y.H. Kim, M. Rejmund, P. Van Isacker, and A. Lemasson. Phys. Rev. C, **97**, 041302(R) (2018). <https://doi.org/10.1103/PhysRevC.97.041302>
- [6] Yu.M. Arkatov, P.I. Vatsset, and V.I. Voloshchuk. Priboiry i Tekhnika Eksperimenta, **3**, 205 (1969) (in Russian).]
- [7] Yu.M. Arkatov, P.I. Vatsset, and V.I. Voloshchuk *et al* Preprint No. 70-73 (Kharkiv Institute of Physics and Technology, 1970) (in Russian).
- [8] A.F. Khodyachikh, and I.V. Dogyust. Ukrainian Journal of Physics, **40**, 775 (1995) (in Russian).
- [9] I.V. Dogyust, A.F. Khodyachikh, and V.P. Yarkov. Yadern. Fiz. **58**, 773 (1995) (in Russian).
- [10] A.F. Khodyachikh, E.S. Gorbenko, and R.T. Murtazin. Yadern. Fiz. **80**, 25 (2017) (in Russian). <https://doi.org/10.1134/S1063778817010100>
- [11] A.M. Baldin, V.I. Gol'danskii, V.M. Maksimenko, and I.L. Rosenthal. *Kinematics of Nuclear Reactions* (Atomizdat, 1968) (in Russian).

ДОСЛІДЖЕННЯ РЕАКЦІЇ $^{14}\text{N}(\gamma, np)3\alpha$ ПРИ $E_\gamma^{\text{макс}} = 150$ МеВ

С.М. Афанасьєв

Національний Науковий Центр «Харківський фізико-технічний інститут», Харків, Україна

Виконано дослідження реакції $^{14}\text{N}(\gamma, np)3\alpha$ за допомогою дифузійної камери, розміщеної в магнітному полі і опроміненій гальмівними фотонами з кінцевою енергією $E_\gamma^{\text{макс}} = 150$ МеВ. Виміряно функції розподілу виходу реакції, енергії та імпульсу кінцевих частинок в залежності від E_γ і встановлено, що при $E_\gamma > 45$ МеВ відбувається зміна поведінки цих функцій. Середню енергію $T^{\text{авер}}$ було розраховано для частинок з енергією, що потрапляє в інтервал 1 МеВ від повної кінетичної енергії $T_0 = E_\gamma - Q$, де Q – енергетичний поріг реакції ($Q = 19.77$ МеВ). При $T_0 > 20$ МеВ, залежність вкладів $T^{\text{авер}}$ частинок до T_0 різко змінюється. При $T_0 > 20$ МеВ більшу частину енергії забирають нуклони, їх відносний внесок однаковий і це узгоджується з припущенням про механізм взаємодії γ -кванта з квазідейтроном. Розподіли імпульсів для нейтрона та протона мають подібний вигляд, із сильним зсувом максимуму в бік високих енергій із збільшенням енергії γ -кванту. Для системи 3α -частинок у кожному розподілі спостерігається пік з центром при 100 МеВ/с, відносний внесок якого плавно спадає із збільшенням імпульсу і з'являється широкий високоенергетичний «хвіст». Енергія та кутові кореляції пр-пари залежать як від енергії E_γ , так і від імпульсу системи 3α -частинок.

Ключові слова: дифузійна камера, фотореакції, ядро ^{14}N , пр-пара, енергетичні та кутові розподіли.

SIMULATION OF HEAT TRANSFER IN SINGLE-CRYSTAL LITHIUM NIOBATE IN INTERACTION WITH CONTINUOUS-WAVE LASER RADIATION[†]

 **Denys O. Protektor***,  **Denys O. Lisin[†]**

*V.N. Karazin Kharkiv National University
4, Svoboda Sq., Kharkiv, 61022, Ukraine*

**Corresponding Author: d.protektor@karazin.ua; [†]E-mail: d.lisin@karazin.ua*

Received December 18, 2021; revised December 18, 2021; accepted December 18, 2021

The paper presents the simulation results of heat transfer in single-crystal lithium niobate (LiNbO_3) in the form of cylinder of diameter $D_{LN} = 40$ mm and height $H = 60$ mm in interaction with continuous-wave laser radiation with the output power of $P = 50$ W and the wavelength of $\lambda = 1064$ nm. The density of the LiNbO_3 crystal is $\rho = 4659$ kg/m³; the thermal conductivity along the [001] direction is $k_{\parallel} = 4.61$ W/(m×K); the thermal conductivity in the (001) plane is $k_{\perp} = 4.19$ W/(m×K); the specific heat at constant pressure is $c_p = 601$ J/(kg×K); the absorption coefficient is $\alpha \sim 0.1$ %/cm @ 1064 nm. The laser beam propagates along the optical axis of the crystal. The laser beam intensity profile is represented as a Gaussian function, and the absorption of laser radiation of the single-crystal lithium niobate is described by Beer-Lambert's law. The numerical solution of the non-stationary heat conduction problem is obtained by meshless scheme using anisotropic radial basis functions. The time interval of the non-stationary boundary-value problem is 2 h 30 min. The results of numerical calculations of the temperature distribution inside and on the surface of the single-crystal lithium niobate at times $t = 10, 100, 1000, 7000$ s are presented. The time required to achieve the steady-state heating mode of the LiNbO_3 crystal, as well as its temperature range over the entire time interval, have been determined. The accuracy of the approximate solution of the boundary-value problem at the n -th iteration is estimated by the value of the norm of relative residual $\|\mathbf{r}\|_{\infty}$. The results of the numerical solution of the non-stationary heat conduction problem obtained by meshless method show its high efficiency even at a small number of interpolation nodes.

Keywords: heat transfer, lithium niobate, anisotropic thermal conductivity, laser radiation, non-stationary heat conduction problem, meshless method.

PACS: 44.10.+i, 77.84.Ek, 02.60.-x

INTRODUCTION

Lithium niobate (LiNbO_3) is a rhombohedral ferroelectric crystal. Lithium niobate is a phase of variable composition, which allows growing single-crystals with different [Li]/[Nb] ratios. Nominally pure LiNbO_3 crystals are usually grown from a congruent melt ([Li]/[Nb] = 48.6/51.4) by Czochralski method [1,2].

As any ferroelectric, LiNbO_3 crystal displays nonlinear optical effects, the piezoelectric effect, the photoelastic effect as well as the Pockels effect. The exclusive feature of lithium niobate is that it has excellent physical properties such as high electro-optic, piezoelectric and nonlinear optical coefficients, which makes it a popular material for various applications.

Due to its high electro-optic coefficients, LiNbO_3 crystal is used to create Pockels cells [3], electro-optic amplitude/phase modulators [4,5] and Q-switched lasers [6]. The nonlinear optical properties of lithium niobate make it possible to use it to create optical parametric oscillators [7,8] and parametric amplifiers for wide wavelength range [9,10], as well as for second harmonic generation of laser radiation with wavelength of > 1 μm [11-13].

It is known that the interaction of laser radiation with crystals in a wide range of luminous-flux densities is well described by the thermal model, according to which the whole process can be conditionally divided into several stages: 1) light absorption and energy transfer to thermal vibrations of the crystal lattice of a solid; 2) heating the crystal without destruction; 3) destruction of the crystal; 4) cooling of the crystal after the end of the interaction.

LiNbO_3 crystals are widely used in lasers, therefore, issues related to the study of the resistance of these crystals to laser radiation are of considerable interest.

Purpose of this work is simulation of heat transfer in single-crystal lithium niobate in interaction with continuous-wave (CW) laser radiation by meshless method.

Unlike grid methods, such as the finite element method (FEM) and the finite difference method (FDM), meshless schemes are devoid of complex and laborious process of constructing an interpolation grid within the considered domain of the boundary-value problem, which makes them computationally efficient and relatively easy to implement.

PROBLEM FORMULATION

Consider LiNbO_3 crystal in the form of cylinder of diameter $D_{LN} = 40$ mm and height $H = 60$ mm with the following physical properties: density is $\rho = 4659$ kg/m³; the thermal conductivity along the [001] direction is

[†] Cite as: D.O. Protektor, and D.O. Lisin, East. Eur. J. Phys. 1, 10-15 (2022), <https://doi.org/10.26565/2312-4334-2022-1-02>
© D.O. Protektor, D.O. Lisin, 2022

$k_{\parallel} = 4.61 \text{ W}/(\text{m} \times \text{K})$; the thermal conductivity in the (001) plane is $k_{\perp} = 4.19 \text{ W}/(\text{m} \times \text{K})$; the specific heat at constant pressure is $c_p = 601 \text{ J}/(\text{kg} \times \text{K})$. The optic axis of the LiNbO_3 crystal is directed along the z-axis.

A laser beam with radiation power $P = 50 \text{ W}$ and radius $r_0 = 5 \text{ mm}$ passes through the crystal as shown in Fig. 1. The wavelength of laser radiation is $\lambda = 1064 \text{ nm}$ and the absorption coefficient of LiNbO_3 is $\alpha \sim 0.1 \text{ \%}/\text{cm}$ @ 1064 nm.

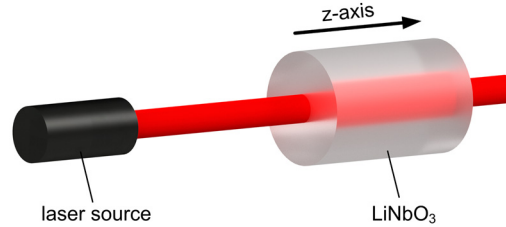


Figure 1. Passage of a laser beam through LiNbO_3 crystal.

When CW laser radiation interacts with a LiNbO_3 crystal, light is absorbed and the absorbed energy transforms into thermal energy.

The non-stationary heat conduction equation for an anisotropic solid in a closed domain can be written as follows:

$$\rho c_p \frac{\partial u}{\partial t} = \text{div}(K \text{ grad } u) + g \quad (1)$$

where u – temperature, K – symmetric positive definite tensor of the second rank, which determines the thermal conductivity of the crystal, g – internal heat source.

At the initial moment of time, the LiNbO_3 crystal is at a temperature $u_0 = 25 \text{ }^\circ\text{C}$. Heat exchange with the environment occurs on the surface of the crystal. The boundary conditions for this case can be written as follows:

$$q = -h(u_e - u) \quad (2)$$

where $q = \frac{\partial u}{\partial \nu}$ – heat flux in anisotropic medium, $h \sim 10 \text{ W}/(\text{m}^2 \times \text{K})$ – heat transfer coefficient, $u_e = 25 \text{ }^\circ\text{C}$ – ambient temperature.

The intensity of the internal heat source at depth z is described by Beer-Lambert's law:

$$g(x, y, z) = \frac{2P\alpha}{\pi r_0^2} \exp\left(-2\left(\frac{x^2 + y^2}{r_0^2}\right)\right) \exp(-\alpha z) \quad (3)$$

where x, y, z – cartesian coordinates, P – radiation power, r_0 – radius of the laser beam, α – absorption coefficient.

Fig. 2 shows a visualization of the intensity of internal heat source at a depth of $z = 0.03 \text{ m}$.

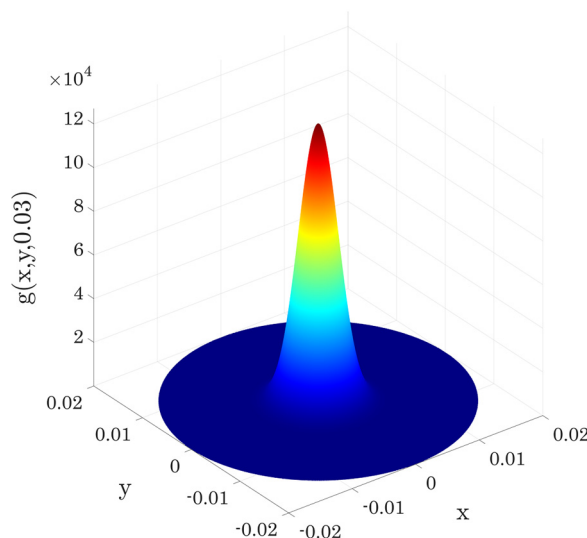


Figure 2. Visualization of the intensity of internal heat source at a depth of $z = 0.03 \text{ m}$.

NUMERICAL RESULTS

The numerical solution of the considered non-stationary heat conduction problem is obtained by meshless method described in [14]. In this scheme, the dual reciprocity method (DRM) [15] with anisotropic radial basis functions (RBFs) [16] and the method of fundamental solutions (MFS) [17] are used to solve the heat conduction problem. The DRM with anisotropic RBFs is used to obtain particular solution, and the MFS is used to obtain a homogeneous solution of boundary-value problem. The time discretization of equation (1) in this method is obtained by θ -scheme [18].

The number of interpolation nodes inside and on the boundary of domain of the heat conduction problem for all calculations is $N_d = 7393$ and $N_b = 7808$, respectively. The time interval of the non-stationary boundary-value problem is 2 h 30 min.

Fig. 3 and Fig. 4 show the simulation results of the temperature field on the surface the LiNbO₃ crystal in interaction with CW laser radiation at different times.

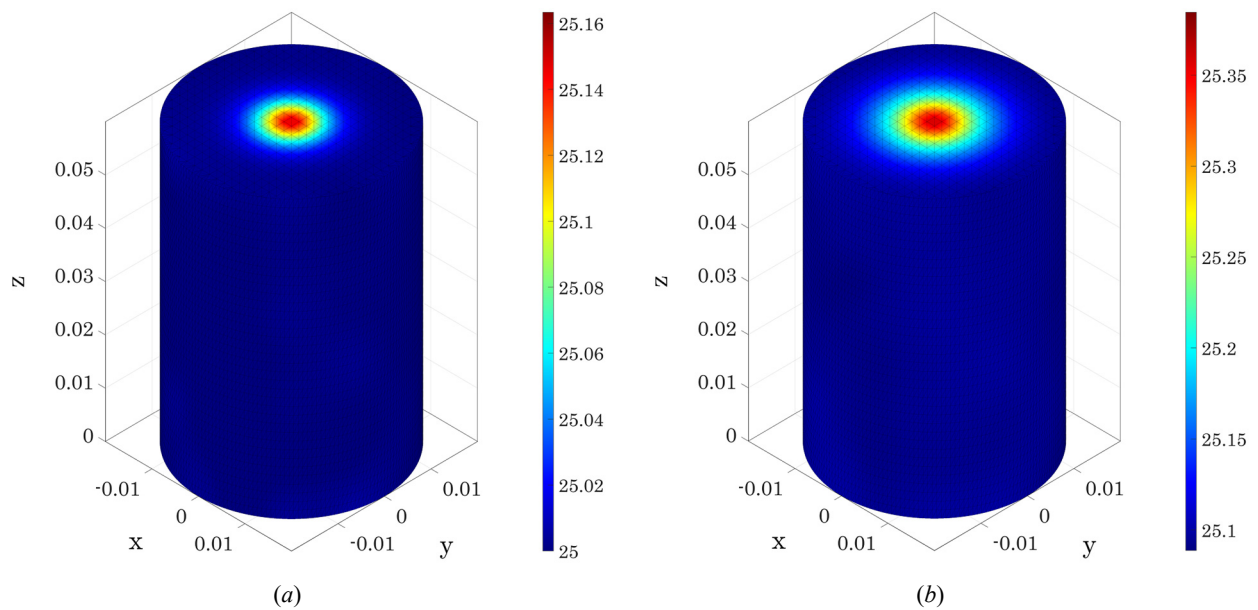


Figure 3. Visualization of the temperature field on the surface the LiNbO₃ crystal at times $t = 10\text{ s}$ (a), $t = 100\text{ s}$ (b).

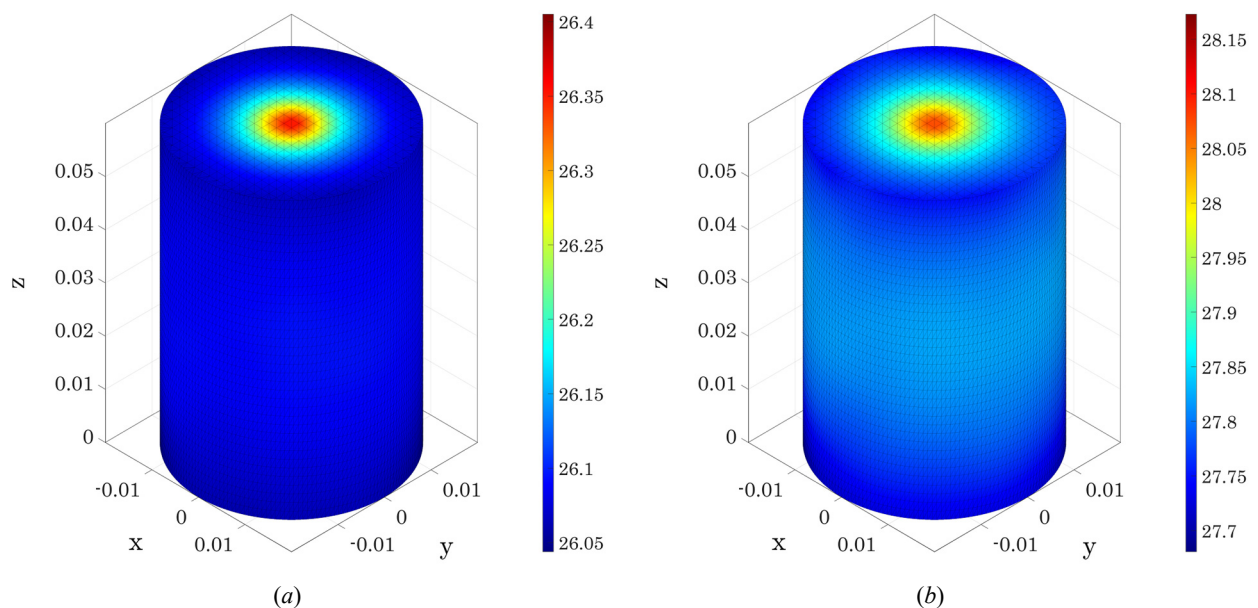


Figure 4. Visualization of the temperature field on the surface the LiNbO₃ crystal at times $t = 1000\text{ s}$ (a), $t = 7000\text{ s}$ (b).

Fig. 5 and Fig. 6 show the simulation results of the temperature field inside the LiNbO₃ crystal in interaction with CW laser radiation at different times.

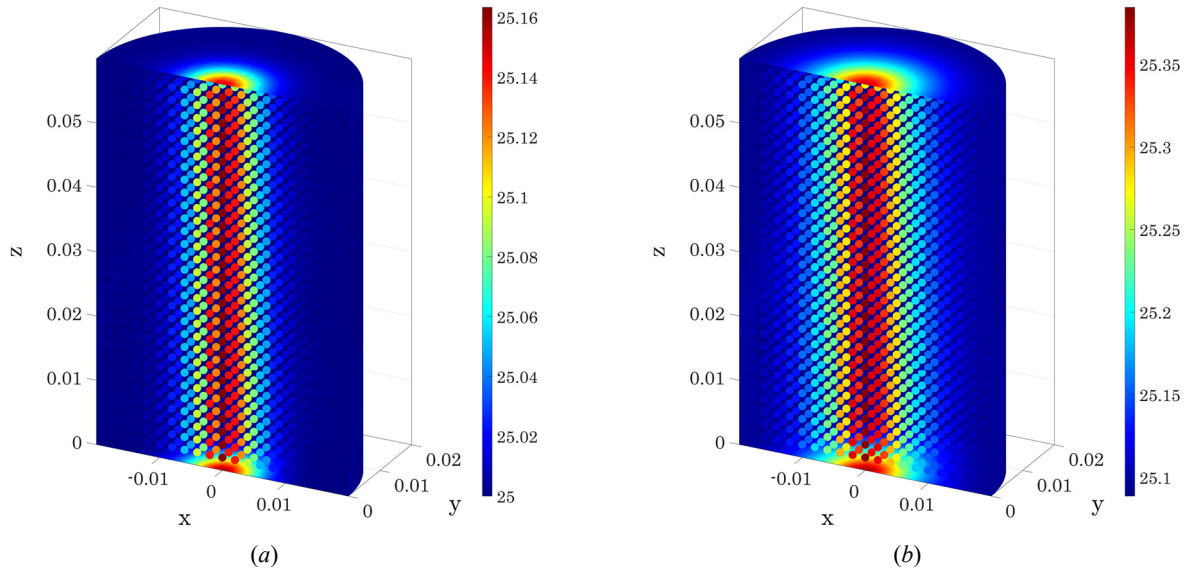


Figure 5. Visualization of the temperature field inside the LiNbO₃ crystal at times $t = 10$ s (a), $t = 100$ s (b).

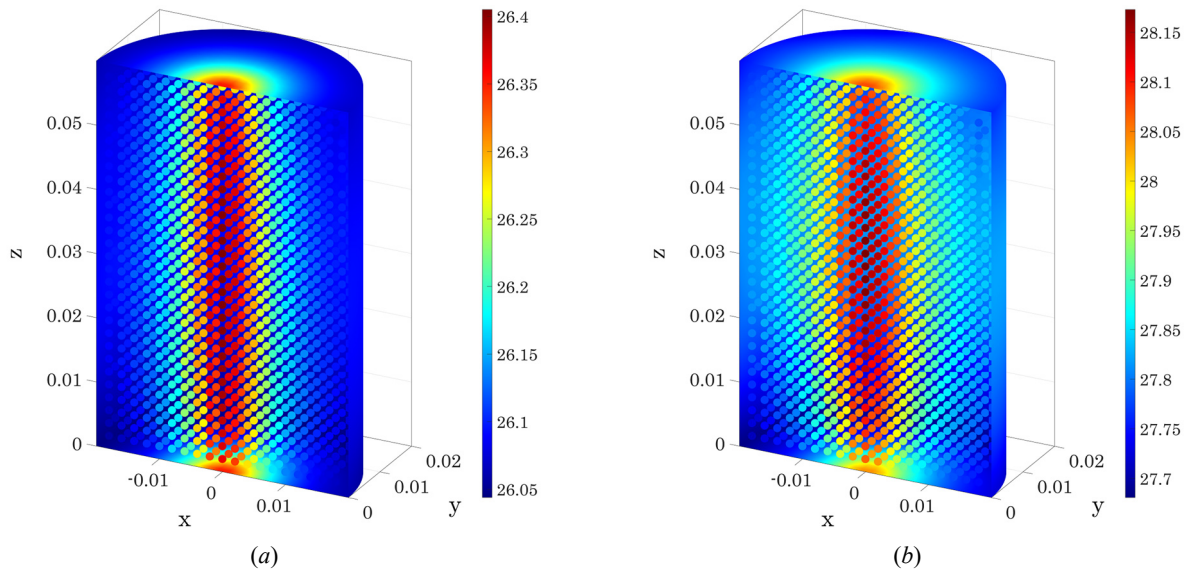


Figure 6. Visualization of the temperature field inside the LiNbO₃ crystal at times $t = 1000$ s (a), $t = 7000$ s (b).

As one can see in Fig. 5 and Fig. 6, with time of irradiation of the crystal, the heated zone inside of the crystal expands and its temperature increases. This process continues until a steady-state thermal regime is reached. Fig. 7 shows the plot of the heating process of the LiNbO₃ crystal in time.

As it was shown Fig. 7, at first the temperature of the crystal increases very fast, and then the rate of increase slows down, and after about 2 h 30 min it goes into a steady-state. The time 35 min, when the crystal temperature reaches 63.2% of the steady-state value is the thermal time constant τ .

The thermal time constant is calculated as follows:

$$\tau = \frac{\rho V c_p}{h A_s} \quad (4)$$

where ρ – crystal density, V – crystal volume, c_p – specific heat at constant pressure, h – heat transfer coefficient, A_s – crystal surface area.

To estimate the accuracy of the approximate solution at the n -th step, we calculate the norm of relative residual:

$$\|\mathbf{r}\|_{\infty} = \max_{i=1, \dots, N} |r_i| \quad (5)$$

where $N = N_d + N_b$ – total number of interpolation nodes, r_i – relative residual of the approximate solution at the i -th node.

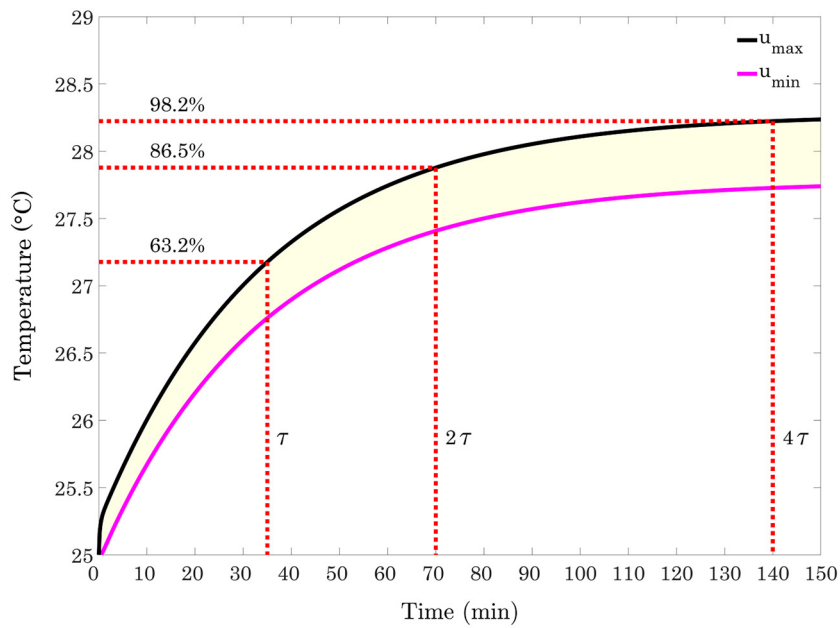


Figure 7. Plot of the heating process of the LiNbO₃ crystal, where u_{max} – maximum temperature of the crystal, u_{min} – minimum temperature of the crystal, τ – thermal time constant.

Fig. 8 shows plot of the change of the norm of relative residual of the approximate solution of the considered boundary-value problem.

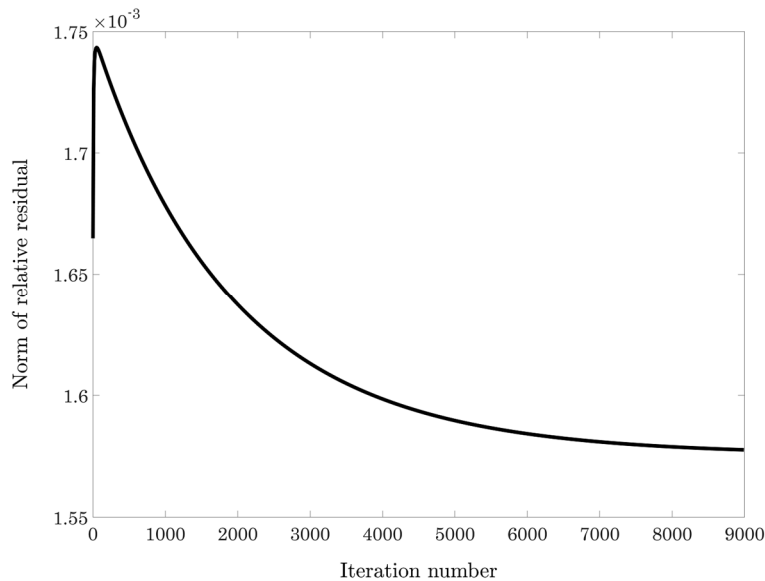


Figure 8. Plot of change of the norm of relative residual

The total estimated simulation time for a non-stationary heat conduction problem is 2303 s, which is comparable to the simulation time when using other numerical methods for solving boundary-value problems.

CONCLUSIONS

This paper presents the simulation results of heat transfer in single-crystal lithium niobate in interaction with CW laser radiation with the output power of 50 W and the wavelength of 1064 nm. The time interval of the non-stationary boundary-value problem was 2 h 30 min. It is defined, that after about 4τ the temperature of the crystal goes into a steady-state, and is in the range of 27.74 to 28.24 °C. The results of numerical calculations of the temperature distribution inside and on the surface of the single-crystal lithium niobate at times $t = 10, 100, 1000, 7000$ s are presented.

The numerical solution of the non-stationary heat conduction problem is obtained by meshless scheme using anisotropic radial basis functions. The accuracy of the approximate solution of the boundary-value problem at a specified time interval is estimated by the value of the norm of relative residual, and in the worst case is 1.74348×10^{-3} . The lower

values of the norm of relative residual are in the range from 2.05119×10^{-14} to 1.25433×10^{-9} . The numerical simulation results obtained using the meshless method are in good agreement with the results obtained using the FEM, which indicates the high efficiency of the meshless scheme even at a small number of interpolation nodes.

ORCID IDs

 Denys O. Protektor, <https://orcid.org/0000-0003-3323-7058>;  Denys O. Lisin, <https://orcid.org/0000-0002-6718-7389>

REFERENCES

- [1] H.H. Kusuma, D.P.N. Made, M.R. Sudin, and M.S. Rohani, AIP Conference Proceedings. **1217**(1), 182-186 (2010), <https://doi.org/10.1063/1.3377808>.
- [2] M. Kosmyna, B. Nazarenko, V. Puzikov, and A. Shekhovtsov, Acta Physica Polonica A. **124**, 305-313 (2013), <http://dx.doi.org/10.12693/APhysPolA.124.305>.
- [3] K.A. Nelson, N. Edwards, M.J. Harrison, A. Kargar, W.J. McNeil, R.A. Rojas, and D.S. McGregor, Nuclear Instruments and Methods in Physics Research Section A: Accelerators, Spectrometers, Detectors and Associated Equipment. **620**, 363-367 (2010), <https://doi.org/10.1016/j.nima.2009.12.042>.
- [4] M. Zhang, C. Wang, P. Kharel, D. Zhu, and M. Lončar, Optica. **8**(5), 652-667 (2021), <https://doi.org/10.1364/OPTICA.415762>.
- [5] T. Sakamoto, T. Kawanishi, and M. Izutsu, Opt. Lett. **31**(6), 811-813 (2006), <https://doi.org/10.1364/OL.31.000811>.
- [6] H. Jelínková, J. Šulc, P. Koranda, M. Němec, M. Čech, M. Jelínek, and V. Škoda, Laser Physics Letters. **1**(2), 59-64 (2004), <http://dx.doi.org/10.1002/lapl.200310020>.
- [7] D.W. Michael, K. Kolenbrander, and J.M. Lisy, Review of Scientific Instruments. **57**(6), 1210-1212 (1986), <https://doi.org/10.1063/1.1138632>.
- [8] C. Yu, and A. Kung, J. Opt. Soc. Am. B. **16**(12), 2233-2238 (1999), <https://doi.org/10.1364/JOSAB.16.002233>.
- [9] T. Kishimoto, K. Inafune, Y. Ogawa, N. Sekine, H. Murai, and H. Sasaki, in: *Integrated Optics: Devices, Materials, and Technologies XXIII*, edited by S.M. García-Blanco (SPIE, San Francisco, 2019), <https://doi.org/10.1117/12.2507784>.
- [10] D. Andreou, Optics Communications. **27**(1), 171-176 (1978), [https://doi.org/10.1016/0030-4018\(78\)90200-6](https://doi.org/10.1016/0030-4018(78)90200-6).
- [11] B.H. Ahn, W.W. Clark III, R.R. Shurtz II, and C.D. Bates, J. Appl. Phys. **54**(3), 1251-1255 (1983), <https://doi.org/10.1063/1.332187>.
- [12] O. Sánchez-Dena, Z. Behel, E. Salmon, E. Benichou, J.-A. Reyes-Esqueda, P.-F. Brevet, and C. Jonin, Opt. Mater. **107**, 110169 (2020), <https://doi.org/10.1016/j.optmat.2020.110169>.
- [13] R. Debnath, P. Kumari, and A. Saha, Optik. **132**, 232-235 (2017), <https://doi.org/10.1016/j.ijleo.2016.12.049>.
- [14] D.O. Protektor, V.M. Kolodyazhny, D.O. Lisin, and O.Yu. Lisina, Cybern. Syst. Anal. **57**, 470-480 (2021), <https://doi.org/10.1007/s10559-021-00372-8>.
- [15] M.S. Ingber, C.S. Chen, and J.A. Tanski, Int. J. Numer. Methods Eng. **60**(13), 2183-2201 (2004), <https://doi.org/10.1002/nme.1043>.
- [16] Wen Chen, Zhuo-Jia Fu, and C.S. Chen, *Recent Advances in Radial Basis Function Collocation Methods*, 1st ed. (Springer, Berlin, 2014), pp. 21-22.
- [17] A. Bogomolny, SIAM J. Numer. Anal. **22**(4), 644-669 (1985), <https://www.jstor.org/stable/2157574>.
- [18] H.P. Langtangen, and S. Linge, *Finite Difference Computing with PDEs*, 1st ed. (Springer, Cham, 2017), pp. 226-227.

МОДЕЛЮВАННЯ ТЕПЛОБМІНУ В МОНОКРИСТАЛІЧНОМУ НІОБАТІ ЛІТІЮ ПРИ ВЗАЄМОДІЇ БЕЗПЕРЕВНИМ ЛАЗЕРНИМ ВИПРОМІНЕННЯМ

Денис О. Протектор, Денис О. Лісін

Харківський національний університет імені В. Н. Каразіна
м. Свободи, 4, Харків, Україна

У статті представлені результати моделювання теплового процесу, який протікає в монокристалі ніобату літію (LiNbO_3) у формі циліндра діаметром $D_{LN} = 40$ мм та висотою $H = 60$ мм при взаємодії з безперервним лазерним випромінюванням потужністю $P = 50$ Вт та довжиною хвилі $\lambda = 1064$ нм. Щільність кристала LiNbO_3 $\rho = 4659$ кг/м³; теплопровідність вздовж напрямку $[001]$ $k_{\parallel} = 4.61$ Вт/(м×К), теплопровідність у площині (001) $k_{\perp} = 4.19$ Вт/(м×К); питома теплоємність при постійному тиску $c_p = 601$ Дж/(кг×К); коефіцієнт поглинання $\alpha \sim 0.1$ %/см @ 1064 нм. Лазерний пучок проходить вздовж оптичної осі кристала. Профіль інтенсивності лазерного пучка представляється у вигляді функції Гауса, а поглинання лазерного випромінювання кристалом ніобату літію описується законом Бугера-Ламберта. Чисельний розв'язок нестационарної задачі теплопровідності здійснюється за безсітковою схемою з використанням анізотропних радіальних базисних функцій. Часовий інтервал, на якому розв'язується нестационарна задача теплопровідності, становить 2 год 30 хв. Наведено результати числових розрахунків розподілу температурного поля всередині та на поверхні кристала ніобату літію в моменти часу $t = 10, 100, 1000, 7000$ с. Визначено час, протягом якого досягається сталий режим нагрівання кристала LiNbO_3 , а також його температурний діапазон на всьому часовому інтервалі. Точність наближеного розв'язку крайової задачі на n -му кроці оцінюється за величиною норми відносної нев'язки $\|r\|_{\infty}$. Результати чисельного розв'язку нестационарної задачі теплопровідності, отримані з використанням безсіткового методу, свідчать про його високу ефективність вже на невеликій кількості інтерполяційних вузлів.

Ключові слова: тепловий процес, ніобат літію, анізотропна теплопровідність, лазерне випромінювання, нестационарна задача теплопровідності, безсітковий метод.

AN INSIGHT INTO THE ELECTRONIC, OPTICAL AND TRANSPORT PROPERTIES OF A HALF HEUSLER ALLOY: NiVSi[†]

 Djelti Radouan^{a,*}, Besbes Anissa^b,  Bestani Benaouda^b

^aTechnology and Solids Properties Laboratory, Mostaganem University (UMAB) – Algeria

^bSEA2M Laboratory, Mostaganem University (UMAB) – Algeria

*Corresponding Author: Radouane.djelti@univ-mosta.dz, djeltired@yahoo.fr

Received November 17, 2021; accepted February 14, 2022

The half-Heusler alloy NiVSi is investigated theoretically by using first-principles calculations based on the density functional theory (DFT). For a better description of the electronic properties, the TB-mBJ potential is used for exchange-correlation potential. The structural, electronic, magnetic, optical and thermoelectric properties was calculated by WIEN2k software. The negative cohesive and formation energies found reveal that the NiVSi is thermodynamically stable. Electronically, the NiVSi is a half-metal with an indirect band gap of 0.73 eV in the spin-down channel whereas the spin up channel is metallic. The total magnetic moment is of 1. Optically, the obtained high absorption coefficient in ultraviolet wavelength range, make the NiVSi useful as effective ultraviolet absorber. Thermoelectrically, a high figure of merit in the p- and n-type region was obtained, what makes this compound very functional for thermoelectric applications. The generation of a fully spin-polarized current make this compound unsuitable for spintronic applications at room temperature, a doping may be a satisfactory solution to improve this property.

Keywords: DFT; mBJ approach; half-metallic; ultraviolet; merit factor.

PACS: 71.20.-b, 72.15.Jf, 72.25.Ba, 73.50.L, 52.70.Kz

The notion of half metallic ferromagnets was established for the first time by de Groot et al. [1]. Since then several researchers paid particular attention to the magnetic half-Heusler (H.H) compounds due to their good physical properties [2-7]. The H.H exhibit fascinating optical and thermoelectric functionalities, those, which present high absorption coefficient and low reflectivity, have become promising candidates for highly efficient solar cells [8-10], while those with high figure of merit (ZT), have gained increasing popularity and are among the new energy resources [11-13]. Numerous studies carried out on H.H compounds have revealed the very good optical, thermoelectric and mechanical performance. The optical investigation conducted by R. Majumder and al., [14] shows that the LuPtBi compound has a good absorption in low energy region and good reflection in vacuum UV region, it exhibit dielectric response even at zero energy. A. Zakutayev [15] synthesized a new half-Heusler compound TaCoSn, which is indicated to possess favorable optical absorption coefficient and high electrical conductivity. According to recent study effected by R. Ahmad and N. Mehmood [16], the NiFeZ, half-Heusler compounds show a half-metallic behaviour with indirect small band gaps and their optical properties are more active at lower energy spectra. Hai-Long Sun et al., [17] have found for the BCaGa, a remarkably high ZT of 7.38 at 700K in the n-type region, while Wendan et al., [18] give a ZT value of 2.43 at 1100 K for the Zr-doped TiPdSn. S.M. Saini [19] shows that the LuNiSb exhibits its best thermoelectric performance at low temperature where the ZT is around 1 at 50K. A. Arunachalam et al [20] give a theoretical analysis of half metallicity and ferromagnetism in NiCrZ (Z = Si, Ge, Ga, Al, In, As), and show that compounds exhibit magnetic interaction and promising figure of merit in magnetic memory element. H.B. Ozisik et al [21] explored the effect of pressure on the electronic properties of half-Heusler NiXS_n (X = Zr, Hf) compounds via the GGA approach, they found that both compound are semiconductor with a narrow-band-gap. Beyond a critical pressure of 161 GPa and 229 GPa for NiZrSn and NiHfSn respectively, the compounds become metallic. P. Hermet et al [22] studied the temperature effect on the mechanical properties of NiTiSn half-Heusler. The authors shows that the compound is very useful when a large temperature fluctuations occurs because it remains ductile and robust at 700K and even conserves its very good mechanical properties up to 1500 K. According to this brief bibliographic review, we can conclude that depending to their composition, the Ni based half-Heusler alloys exhibit a wide variety of magnetic, thermoelectric, optical and mechanical properties, which allows them to be believed as very promising half metallic ferromagnetic materials for several technological application. The main objective to this study is to investigate the structural, electronic, optical and thermoelectric behaviour of the NiVSi half-Heusler compound. This research is arranged as follows. Details of computation are given in Section “Computational method”. Results and discussion are presented in Section “Results and discussion”. A summary of the results is given in Section “Conclusion”

COMPUTATIONAL METHOD

First-principles calculations based on DFT have been conducted to research the structural, electronic, optical and thermoelectric properties of NiVSi half-heusler. Exchange-correlation effects were treated with TB-mBJ potential [23]. The valence electrons for the NiVSi primal cell are 4s² 3d⁸ of Ni, 4s² 3d³ of V and 3s² 3p² of Si. The muffin tin radius

[†] Cite as: D. Radouan, B. Anissa, and B. Benaouda, East. Eur. J. Phys. 1, 16-25 (2022), <https://doi.org/10.26565/2312-4334-2022-1-03>
© D. Radouan, B. Anissa, B. Benaouda, 2022

(R_{MT}) values of 1.85, 2.1 and 2.5 Bohr were used for Ni, V and Si respectively. Other parameters such as $R_{MT} \times \text{wave-vector } k_{max}$ (K_{MAX}), k-point mesh and the maximum value of angular momentum (l_{max}) were selected to 7.0, $16 \times 16 \times 16$ and 10 respectively. The optical constants are derived from the complex dielectric function [24-26]. The semi-classical Boltzmann approach [27] as given in the BoltzTraP code was used to investigate the thermoelectric response of NiVSi compound. A fine grid mesh ($46 \times 46 \times 46$) was used.

RESULTS AND DISCUSSION

Structural properties

The half-Heusler (H.H) is intermetallic compound with general formula XYZ, where X and Y are transition metals and Z a p-block element. The H.H crystallize in the face-centered cubic structure (space group F-43m). The Ni, V and Si atoms are positioned according to one of the three types displayed in Table 1.

Table 1. Wyckoff position of atoms in the unit cell of cubic half-Heusler alloy NiVSi

Type	Ni	V	Si
I	4b (0.5, 0.5, 0.5)	4c (0.25, 0.25, 0.25)	4a (0, 0, 0)
II	4b (0.5, 0.5, 0.5)	4a (0, 0, 0)	4c (0.25, 0.25, 0.25)
III	4c (0.25, 0.25, 0.25)	4b (0.5, 0.5, 0.5)	4a (0, 0, 0)

We have carried out the structural optimization in ferromagnetic (FM) and non-magnetic (NM) configuration for the three possible types of arrangement. From Figure 1 and Table 2, we can see that the ferromagnetic state of the type III arrangement is the most stable among the six possible configurations because it has the lowest energy.

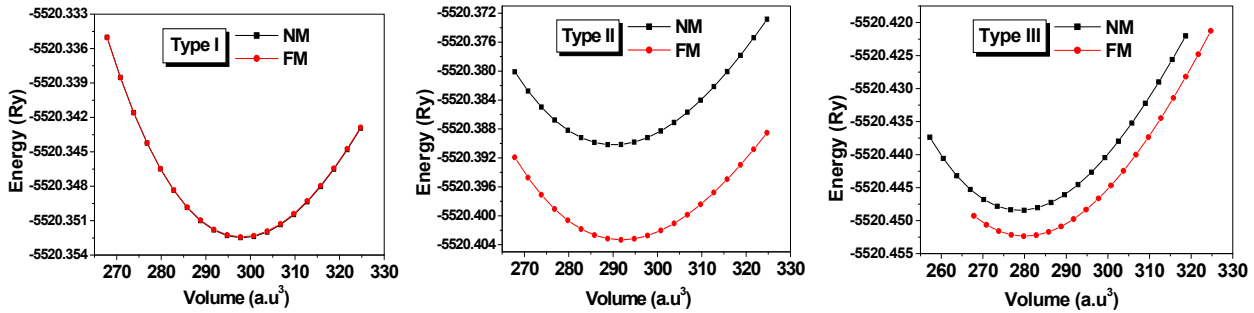


Figure 1. Calculated total energy of NiVSi compound as functions of the unit cell volume for the FM and NM states in each possible atomic arrangement

Table 2. The calculated equilibrium lattice constant a_0 , the ground state energies E_0 , the bulk modulus B , its pressure derivatives B' , the cohesive energy E_c and the formation energy E_f of cubic NiVSi alloy.

Type	State	a_0 (Å)	E_0 (Ry)	B (GPa)	B'	E_c (Ry)	E_f (Ry)
I	FM	5.61	-5520.352411	138.3670	4.15		
	NM	5.61	-5520.352477	138.6531	4.15		
II	FM	5.57	-5520.403317	145.3527	4.97		
	NM	5.56	-5520.390198	152.2824	4.60		
III	FM	5.49 (5.47) ^[32]	-5520.452380	167.3817	4.54	-1.417	-0.304 (-0.316) ^[32]
	NM	5.48	-5520.448458	174.6848	4.85		

To ensure the structural stability in the ground state and also to estimate the chemical stability and see a possible synthesis of NiVSi, we have calculated the formation energy (ΔH_f) and cohesive energy (E_{Coh}). The formation enthalpy is defined as [28]:

$$\Delta H_f = E_{NiVSi}^{Total} - (E_{Ni}^{bulk} + E_V^{bulk} + E_{Si}^{bulk}) \quad (1)$$

Where E_{NiVSi}^{Total} is the total energy of the NiVSi alloy, E_{Ni}^{bulk} , E_V^{bulk} and E_{Si}^{bulk} are the total energy per atom of Ni, V, and Si in their bulk stable states, respectively. The cohesive energy (E_{Coh}) per formula unit have been calculated using the relation [29]:

$$E_{Coh} = E_{NiVSi}^{Total} - (E_{Ni}^{iso} + E_V^{iso} + E_{Si}^{iso}) \quad (2)$$

E_{NiVSi}^{Total} is the total energy of the NiVSi alloy at equilibrium lattice and E_{Ni}^{iso} , E_V^{iso} , E_{Si}^{iso} are the total energies of the isolate atomic components. The negative value of ΔH_f and E_{Coh} (Table 2) confirm the structural and chemical stability of our half-Heusler NiVSi in the type III atomic arrangement with FM state. The crystal structure of NiVSi alloy in the type-III

(FM) given in Figure 2 was plotted by the CrystalMaker 2.7 software [30]. The structure is formed by three interpenetrating fcc sublattices, which are occupied by Ni, V and Si elements.

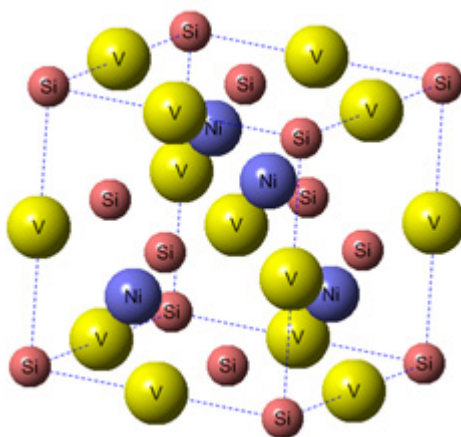


Figure 2. Crystal structure of half-Heusler compound NiVSi

Electronic properties

Fig. 3 shows the spin polarized band structures of the NiVSi half-Heusler alloy. The choice of TB-mBJ approach for this calculation is to obtain an accurate half-metallic gap.

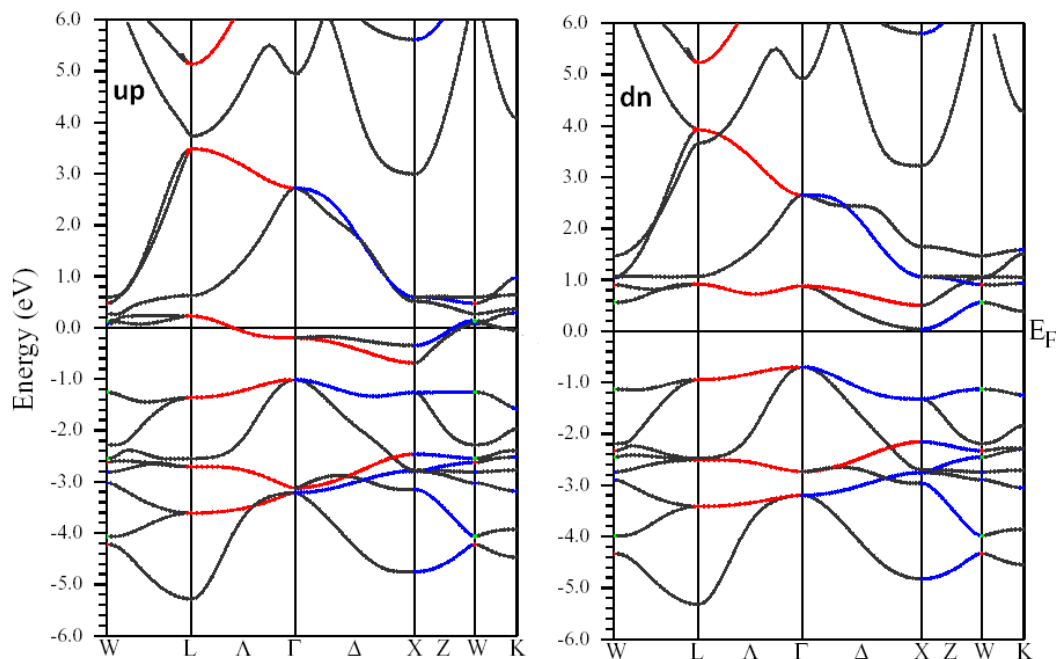


Figure 3. Band structures of NiVSi for both spin channels with mBJ approach

The spin-up (\uparrow) channel, shows a metallic characteristic because the 3d-V band cross the Fermi level. In the spin-down (\downarrow) channel, Fermi level lies inside the forbidden gap, an indirect band gap (between X and Γ points) of about 0.73 eV was observed so confirming the semiconducting nature. This coexistence of metallic nature in spin-up (\uparrow) channel and semiconducting nature in the spin-down (\downarrow) channel leads to the half-metallic nature of NiVSi compound. The origin of the half-metallicity might be due to the strong hybridization between Ni-3d and V-3d states. The calculated band structure presents 100% of spin polarization at the Fermi-level; this can generate a spin-polarized current in the half-metal, only at absolute zero or a temperature very close to zero. According to Fig.3, the Fermi energy is very close to the bottom of conduction band of down spin, that make this compound unsuitable for spintronic applications at room temperature. On the other hand, the 100% of spin polarization at the Fermi-level is very useful to maximizing the efficiency of magneto-electronic devices [31]. In order to study the arrangement of the orbital's in the electronic band structure as well as the electrons involving in the shaping of the band gap, the total and partial density of states (TDOS/PDOSs) of the NiVSi was plotted between -10 and 10 eV Fig. 4(a-b). The dashed line shows the Fermi energy

level (E_F). Fig 4.a, show an asymmetry between spin up (\uparrow) and spin down (\downarrow), this confirms the half-metallic character of NiVSi half-Heusler already predicted by band structure. The energy region around the Fermi level is mainly due to a low contribution of d-Ni states and major contribution of d-V states (Fig 4.b).

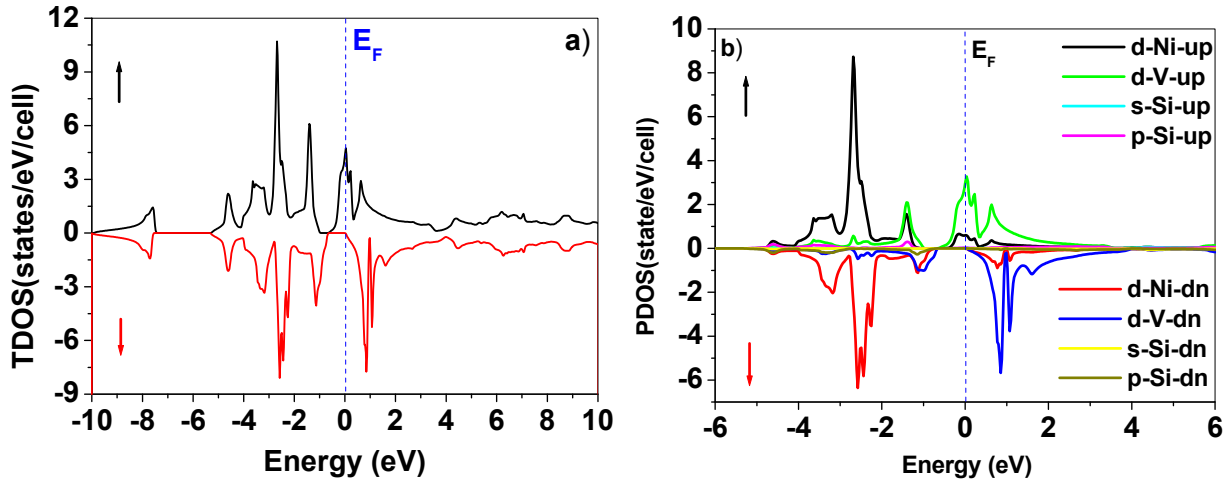


Figure 4. Calculated total and partial density of states with TB-mBJ for NiVSi half-Heusler

We can see that for energies higher than 2eV, the Si-3p state is dominant and for energies lower than -5eV, the principal contribution is due to Si-3s state. In addition, the 3d-V state is most important in the conduction band with a considerable higher DOS values that Ni and Si, whereas in the valence band the 3d-Ni state is the predominant. The combined effect of the crystal field and atoms constituting the alloy induces magnetism. Our study show that the NiVSi half-Heusler possesses FM nature with a total magnetic moment (M_{total}) of $1\mu_B$, (Table. 3). The contribution of the interstitial site and partially filled d-states of vanadium generates this total moment. The positive value of the magnetic spin moment is due to vanadium, whereas the low negative value is attributed to silicon. The M_{total} found is slightly higher than obtained by Ma et al [32], this can be justified by the different exchange correlation functional used in the two works.

Table 3. Individual, interstitial and total magnetic moments of NiVSi half-Heusler calculated by GGA and mBJ approximations.

Method	GGA	mBJ	Other work [32]
M_{Ni}	0.0731	0.1138	0.097
M_V	0.8890	0.8981	0.841
M_{Si}	-0.0349	-0.0406	-0.040
$M_{interstitials}$	0.0738	0.0286	
M_{total}	1.0011	1.0000	0.9582

Optical properties

The optoelectronic applications of a material require in-depth knowledge of their optical properties. In order to describe the interaction of photons with NiVSi alloy, the calculation of optical properties such as polarization, absorption, reflectivity, refractive index and loss energy is necessary. All the optical properties cited above derive from the complex dielectric function $\epsilon(\omega)$ (eq. 3).

$$\epsilon(\omega) = \epsilon_1(\omega) + i\epsilon_2(\omega) \quad (3)$$

Where $\epsilon_2(\omega)$ represents the real transition between the occupied and unoccupied states while $\epsilon_1(\omega)$ depicts the electronic polarizability under incident light [33]. The imaginary part of the dielectric function $\epsilon_2(\omega)$ is derived from the electronic band structure computations with the help of the following relation

$$\epsilon_2(\omega) = \left(\frac{4\pi^2 e^2}{m^2 \omega^2}\right) \sum_{i,j} \int \langle i|M|j \rangle^2 f_i(1-f_j) \delta(E_j - E_i - \omega) d^3k \quad (4)$$

Where e, m, ω and M represent the electron charge, electron mass, photon frequency and dipole matrix, respectively. E_i is the electron energy of the initial state, E_j is the electron energy of the final state, and f_i is the Fermi occupation factor of the single-particle state i . The real part $\epsilon_1(\omega)$ of the dielectric function derives from $\epsilon_2(\omega)$ by using the Kramers Kronig relations [34-36]:

$$\epsilon_1(\omega) = 1 + \frac{2}{\pi} P \int_0^\infty \frac{\omega' \epsilon_2(\omega')}{\omega'^2 - \omega^2} d\omega' \quad (5)$$

Where P is the Cauchy principal value.

Other optical parameters like the absorption coefficient $\alpha(\omega)$, reflectivity $R(\omega)$ and refractive index $n(\omega)$ can be obtained from the calculated values of the real and imaginary parts of the dielectric function [37]:

$$\alpha(\omega) = \frac{\sqrt{2}\omega}{c} \left(\sqrt{\epsilon_1^2(\omega) + \epsilon_2^2(\omega)} - \epsilon_1(\omega) \right)^{1/2} \quad (6)$$

$$R(\omega) = \left| \frac{\sqrt{\epsilon(\omega)} - 1}{\sqrt{\epsilon(\omega)} + 1} \right|^2 \quad (7)$$

$$n(\omega) = \left[\frac{\sqrt{\epsilon_1^2(\omega) + \epsilon_2^2(\omega)} + \epsilon_1(\omega)}{2} \right]^{1/2} \quad (8)$$

As the lattice parameters are constant (cubic structure), the obtained optical properties are isotropic (same dielectric tensor). The variations versus energy of real part $\epsilon_1(\omega)$ and imaginary part $\epsilon_2(\omega)$ of dielectric function (ω) are plotted in Fig. 5a.

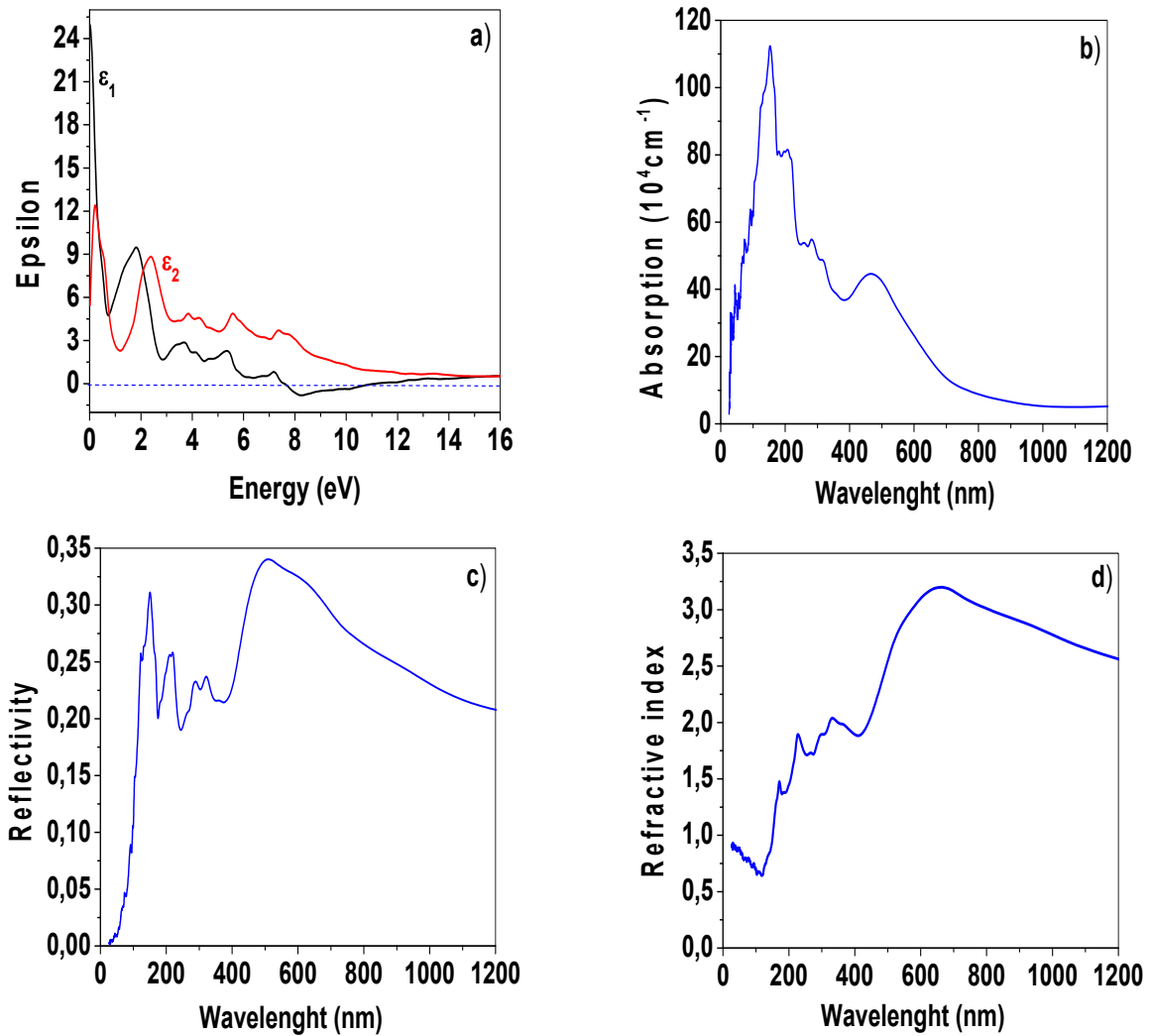


Figure 5. (a) Dielectric function, (b) absorption coefficient, (c) reflectivity and (d) refractive index) for NiVSi compound by using mBJ approximation.

The light absorption by the material is described by the imaginary part of the dielectric function $\epsilon_2(\omega)$, this is associated to the absorption of the incident energy due to the different electronic transitions caused by the impact energies greater than the band-gap. $\epsilon_2(\omega)$ starts at 0eV and attain its maximum value of 12.35 in the infrared domain; domain

characterized by minimal dispersion of light due to the low energy. We can see also that $\epsilon_2(\omega)$ show six absorption peaks located at 0.28 eV, 2.35 eV, 4.03 eV, 4.31 eV, 5.59 eV and 7.39 eV. According to the total and partial density of states (TDOS/PDOS) (Fig 4), these peaks can be related to the inter-band transitions between Si-3p, Ni-3d and V-3d states. The real part of dielectric function $\epsilon_1(\omega)$ depicts the electronic polarizability under an incident light, its static value at zero photon energy $\epsilon_1(0)$ is inversely proportional to the band gap (Eg) (Penn model) [38].

$$\epsilon_1(0) = 1 + \left(\frac{\hbar\omega_p}{E_g}\right)^2 \quad (9)$$

Where ω_p is the plasma frequency.

The obtained value of $\epsilon_1(0)$ is 25.08. In the energy range from zero to 7.72 eV, $\epsilon_1(\omega)$ show positive values, which means the photons, propagate through the material, whereas in the UV range from 7.72 to 10.48 eV, $\epsilon_1(\omega)$ takes negative values, the compound reflects completely the incident radiation and exhibits a metallic character in this region. Beyond 10.48 eV, the values of real part $\epsilon_1(\omega)$ fluctuate around 0. The optical absorption measures the strength of the interaction between light and material, its knowledge is essential for any development of opto-electronic device. The absorption coefficient was calculated versus radiation wavelengths in the UV-Visible-IR range. From Fig.5b we can see that the NiVSi display high level of interband absorption, the presence of the low energy gap in spin-down band structure spectrum, match with the principal peak obtained at wavelength of 154 nm (ultraviolet range). We note that the increase of photons energy leads to a proportional diminution in the wavelength. The absorption is very small at low energy (Infrared range) then increases to reach its maximum of 1171139 cm⁻¹ in the UV region; this means that the photons, which excite electrons of the conduction band, was absorbed. We can remark also that the absorption coefficient is not constant for photon energies greater than the gap, but depends, heavily on wavelength. The reflectivity R(ω) which describes the ratio between the reflected energy to total incident energy is plotted versus wavelength in Fig. 5c. The compound present two major peaks, located below 152 nm (UV range) and above 506 nm (visible region). The utmost values of reflectivity is mostly due to the resonance Plasmon [39]. The minimum value of R(ω), is observed in UV range at 241 nm, whereas in all the UV-visible domain, the value of reflectivity is less than 35%. The decrease in reflectivity noted from 510 nm implies that a substantial amount of photon energy is transmitted through the material. It is to note that the static value of reflectivity R(0) is about 44%. The interaction of electromagnetic radiation with a non-uniform medium such as material causes a change in the path of the radiation by refraction. From Fig 5d, we can see that the index refraction n(ω) reaches its maximum value of 3.22 at 661 nm, and then gradually decreases. This can be explained by the fact that the NiVSi alloy absorbs high-energy photons and can no longer act as a transparent matter [40]. The static refractive index n(0) is 5.01, according to equation n²(0) = $\epsilon_1(0)$, we can deduct the static dielectric constant $\epsilon_1(0)$ is about 25.11, which is fundamentally according with the result of Fig. 5(a). The refractive index remain positive in the considered range of energy, this is due to the linearity of NiVSi to the frequency of light [41]. Finally, as suggestion for future researches, the bandgap of NiVSi half-Heusler can be modulated or improved by selective doping to have a strong optical absorption, which will allow subsequently to involve this material in several optoelectronic devices such as photovoltaic cells.

Thermoelectric properties

The present thermoelectric study is motivated by the narrow band gap of NiVSi, property that allows a good diffusion of the phonons and which reduces in parallel the thermal conductivity of the network. The transport properties are going to be computed with BoltzTraP code (under a constant relaxation time approximation of the charge carriers) [27], where the electrical conductivity (σ/τ), thermal conductivity (κ/τ), Seebeck coefficient (S) and Merit factor (ZT) will be investigated as function of chemical potential (μ) in range between -0.15 to 0.15 eV. Semi-classical Boltzmann transport equations are used to calculate the number of thermoelectric coefficients, which can be represented as follows [42-43]:

$$\sigma_{\alpha\beta}(T, \mu) = \frac{1}{\Omega} \int \sigma_{\alpha\beta}(\epsilon) [-\partial f_{\mu}(T, \epsilon)] d\epsilon \quad (10)$$

$$\kappa_{\alpha\beta}(T, \mu) = \frac{1}{e^2 T \Omega} \int \sigma_{\alpha\beta} \epsilon (\epsilon - \mu)^2 \frac{\partial f_{\mu}(T, \epsilon)}{d\epsilon} \quad (11)$$

$$S = \frac{e}{T\sigma} \int \sigma_{\alpha\beta}(\epsilon) (\epsilon - \mu) \left[\frac{-\partial f_{\mu}(T, \epsilon)}{\partial \epsilon} \right] \quad (12)$$

$$ZT = \frac{S^2 \sigma T}{\kappa} \quad (13)$$

Where Ω , f , μ , σ , κ , S and Z represents the unit-cell volume, Fermi-Dirac distribution function, chemical potential, electrical conductivity, thermal conductivity, Seebeck coefficient and merit factor respectively. The variation of electrical

conductivity (σ/τ) which depicts the fluency at which electrical charge can flow in matter is show in Fig 6.a. The starting points of (σ/τ) for p-type ($\mu < 0$) and n-type ($\mu > 0$) regions are situated at chemical potentials of $-0.05 \mu\text{eV}$ and $0.01 \mu\text{eV}$ respectively. Between these points, (σ/τ) is zero; while a clear, improvement observed beyond these values. A value peak of $2.94 \cdot 10^{20} (\Omega\text{m})^{-1}$ is observed in p-type at $0.122 \mu\text{eV}$, while the n-type show a value peak of $7.5 \cdot 10^{20} (\Omega\text{m})^{-1}$ at $0.15 \mu\text{eV}$. The (σ/τ) values are not influenced by changing the levels of temperature (300, 600 and 900K). The capacity of the half-heusler NiVSi to transfer heat is studied in this section through the calculation of its thermal conductivity (κ/τ). As show in Fig 6b, the profile of thermal conductivity (κ/τ) curves is the same to the electrical conductivity (σ/τ), except that here the temperature change has a significant influence on the (κ/τ) values. At 300 K, the thermal conductivity (κ/τ) is weak then it sudden increases with the increasing in temperature especially in the n-type region, this is due to electron-phonon scattering [44]. Fig 6.c gives the Seebeck coefficient (S) which demonstrates the capacity to generate electric potential from the temperature gradient. The principal peak of Seebeck coefficient occur between -0.052 and 0.007 eV , outside this range, the curve tends rapidly to zero. At 300 K, the magnitude of Seebeck coefficient is about $1235 \mu\text{V/K}$ (-0.026eV), this value is reached in the p-type region. For temperature higher than 300 K, the Seebeck coefficient diminish due to the increase in the holes and in thermal energy [45]. The NiVSi compound is a promising thermoelectric material, exhibiting a high Seebeck coefficient due to its half-metallic character and its narrow band-gap. The scale of the thermoelectric efficiency is measured by the figure of merit (ZT). A high ZT value requires a high electrical conductivity and Seebeck coefficient and low thermal conductivity [46]. The ZT curves obtained at different temperature exhibit a global similarity: the peaks are located at almost similar energies and their magnitudes decrease with increasing in temperature (Fig 6.d).

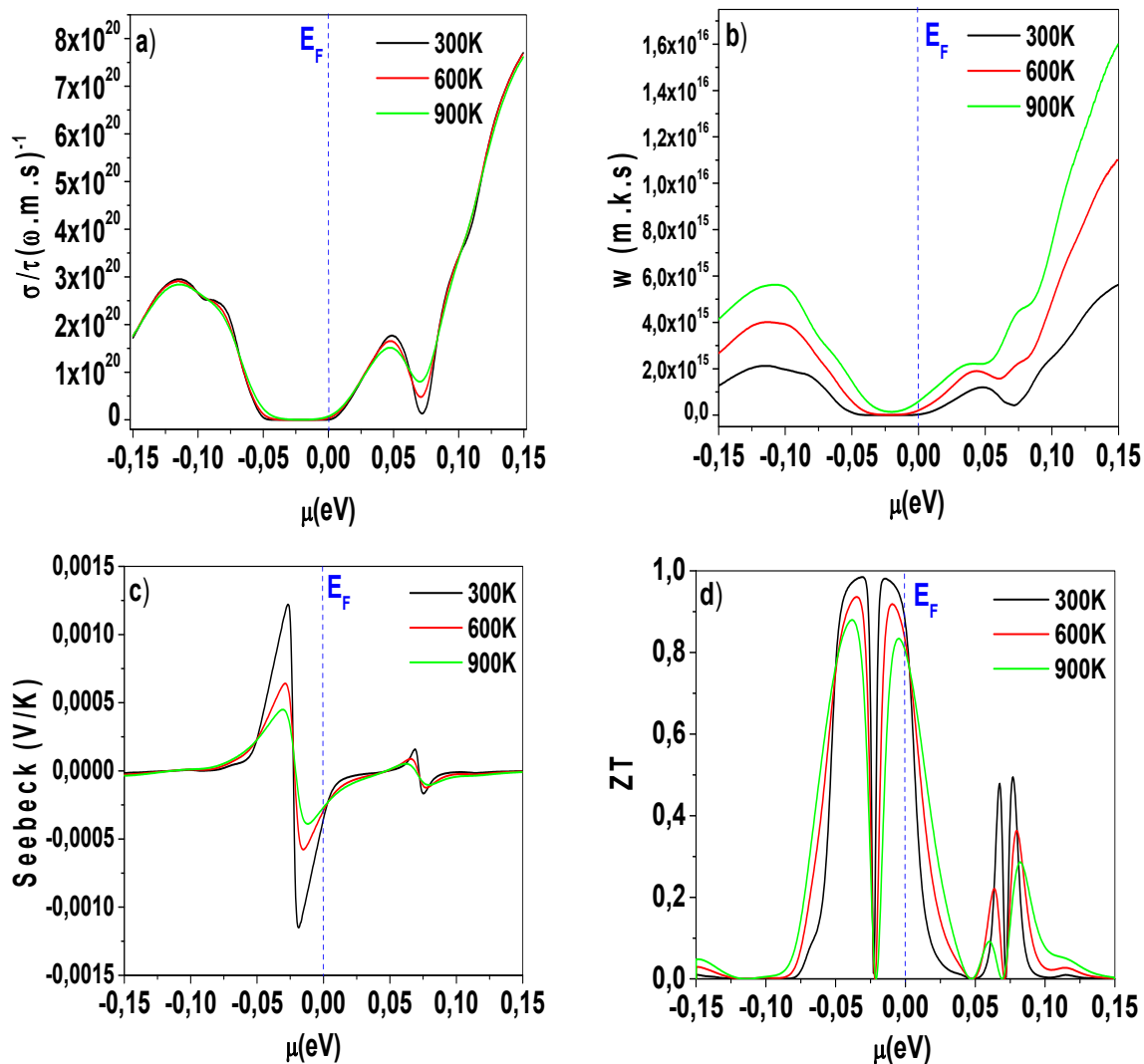


Figure 6. Evolution of (a) electrical conductivity, (b) thermal conductivity, (c) Seebeck coefficient, and (d) Merit factor (ZT) versus chemical potential at different temperatures.

At the chemical potential corresponding to the Fermi level (dashed line) the computations gives a ZT values not less than 0.83 for all considered temperature. Around the zero chemical potential, the conduction charges are small from where a minimum electronic thermal conductivity, which made it possible to have these high merit factors. The maximal ZT

value is 0.98 (300 K), 0.93 (600 K) and 0.87 (900 K) for p-type doping, and it is 0.49 (300 K), 0.36 (600 K) and 0.29 (900 K) for n-type doping. The values of the merit factor is higher for the negative chemical potential compared to the positive one, and the width of the peak in the $\mu < 0$ region is larger than that in the $\mu > 0$ region. The NiVSi tends to be a p-type semiconductor, because the holes rather than the doping of electrons gives the best thermoelectric performance.

The obtained values of ZT are larger to those reported for many half-Heusler compounds such as PdZrGe [47], ZrFeSi [48], RbBaB [49], XLiSn [50], RhTiSb [51].

CONCLUSION

We performed first principles calculations of the structural, electronic, optical and thermoelectrics properties of NiVSi half-Heusler compound using FP-LAPW formalism and semi-classical Boltzmann transport theory. The electronic investigation discloses that the NiVSi is half-metallic with indirect band gap nature, this half-metallicity suggest potential applications in spintronic devices. The magnetic study reveals that NiVSi is a weak ferromagnetic material with 100% spin polarization at Fermi level, this can produces a spin-polarized current useful to maximizing the efficiency of magneto-electronic devices. The optical properties computations attest that the NiVSi has a broad absorption band in the ultraviolet region, its high absorption coefficient of 112.10^4 cm^{-1} suggest that it can be used as ultraviolet absorber. In addition, the compound is transparent in the considered infrared range [780-1200 nm]. Thermoelectric computations disclose that the holes are the main charge carriers. At a room temperature, the obtained merit factor is about 0.98, thus affirming that the NiVSi is a promising material for applications in the thermoelectric domain. Finally, we suggest that to boost the spintronic performance of this alloy, a doping remain necessary to move the bottom of the conduction band away from the Fermi level.

ORCID IDs

 Djelti Radouan, <https://orcid.org/0000-0002-0762-5818>;  Bestani Benaouda, <https://orcid.org/0000-0002-1104-0900>

REFERENCES

- [1] R. De Groot, F. Mueller, P. Van Engen, and K. Buschow, New class of materials: half-metallic ferromagnets, *Phys. Rev. Lett.* **50**(25), 2024 (1983). <https://doi.org/10.1103/PhysRevLett.50.2024>
- [2] M. Zhang, X. Dai, H. Hu, G. Liu, Y. Cui, Z. Liu, J. Chen, J. Wang, and G. Wu, Search for new half-metallic ferromagnets in semi-Heusler alloys NiCrM (M = P, As, Sb, S, Se and Te), *J. Phys.: Condens. Matter.* **15**, 7891 (2003). <https://doi.org/10.1088/0953-8984/15/46/008>
- [3] H. Luo, Z. Zhu, G. Liu, S. Xu, G. Wu, H. Liu, J. Qu, and Y. Li, Ab-initio investigation of electronic properties and magnetism of half-Heusler alloys XCrAl (X = Fe, Co, Ni) and NiCrZ (Z = Al, Ga, In), *Physica B*, **403**, 200 (2008). <https://doi.org/10.1016/j.physb.2007.08.214>
- [4] S.H. Wang, H.M. Cheng, R.J. Wu, and W.H. Chao, Structural and thermoelectric properties of HfNiSn half-Heusler thin films, *Thin Solid Films*, **518**(21), 5901 (2010). <https://doi.org/10.1016/j.tsf.2010.05.080>
- [5] L. Huang, R. He, S. Chen, H. Zhang, K. Dahal, H. Zhou, H. Wang, Q. Zhang, and Z. Ren, A new n-type half-Heusler thermoelectric material NbCoSb, *Materials Research Bulletin*, **70**, 773 (2015). <https://doi.org/10.1016/j.materresbull.2015.06.022>
- [6] S.V. Pedersen, J.R. Croteau, N. Kempf, Y. Zhang, D.P. Butt, and B.J. Jaques, Novel synthesis and processing effects on the figure of merit for NbCoSn, NbFeSb, and ZrNiSn based half-Heusler thermoelectrics, *Journal of Solid State Chemistry*, **285**, 121203 (2020). <https://doi.org/10.1016/j.jssc.2020.121203>
- [7] A. Saini, S. Nag, R. Singh, and R. Kumar, Enhancement in the thermoelectric performance of half-Heusler alloy LiScGe under hydrostatic pressure, *Journal of Alloys and Compounds*, **818**, 152929 (2020). <http://dx.doi.org/10.1016/j.jallcom.2019.152929>
- [8] S. Kacimi, H. Mehnane, and A. Zaoui, I-II-V and I-III-IV half-Heusler compounds for optoelectronic applications: Comparative ab initio study, *Journal of Alloys and Compounds*, **587**, 451 (2014). <https://doi.org/10.1016/j.jallcom.2013.10.046>
- [9] F. Parvin, M.A. Hossain, I. Ahmed, K. Akter, and A.K.M.A. Islam, First-principles calculations to investigate mechanical, optoelectronic and thermoelectric properties of half-Heusler p-type semiconductor BaAgP, *Results in Physics*, **23**, 104068 (2021). <https://doi.org/10.1016/j.rinp.2021.104068>
- [10] D. Kieven, R. Klenk, S. Naghavi, C. Felser, and T. Gruhn, I-II-V half-Heusler compounds for optoelectronics: Ab initio calculations, *Phys. Rev. B*, **81**, 075208 (2010). <https://doi.org/10.1103/PhysRevB.81.075208>
- [11] T. Sekimoto, K. Kurosaki, H. Muta, and S. Yamanaka, Thermoelectric Properties of (Ti, Zr, Hf) CoSb Type Half-Heusler Compounds, *Materials Transactions*, **46**, 1481 (2005). <https://doi.org/10.2320/matertrans.46.1481>
- [12] A. Page, P.F.P. Poudeu, and C. Uher, A first-principles approach to half-Heusler thermoelectrics: Accelerated prediction and understanding of material properties, *Journal of Materiomics*, **2**, 104 (2016). <https://doi.org/10.1016/j.jmat.2016.04.006>
- [13] K. Xia, C. Hu, C. Fu, X. Zhao, and T. Zhu, Half-Heusler thermoelectric materials, *Appl. Phys. Lett.* **118**, 140503 (2021). <https://doi.org/10.1063/5.0043552>
- [14] R. Majumder, and Md.M. Hossain, First-principles study of structural, electronic, elastic, thermodynamic and optical properties of topological superconductor LuPtBi. *Comput. Condens. Matter*, **21**, (2019) e00402. <https://doi.org/10.1016/j.cocom.2019.e00402>
- [15] A. Zakutayev, X. Zhang, Theoretical Prediction and Experimental Realization of New Stable Inorganic Materials Using the Inverse Design Approach, *J. Am. Chem. Soc.* **135**(27), 10048 (2013). <https://doi.org/10.1021/ja311599g>
- [16] R. Ahmad, and N. Mehmood, Theoretical investigations of properties of new half-Heusler compounds NiFeZ (Z = Si, Ge), *J. Supercond. Nov. Magn.* **31**(19), 1751 (2018). <https://doi.org/10.1007/s10948-017-4378-9>

- [17] Hai-Long Sun, Chuan-Lu Yang, Mei-Shan Wang, and Xiao-Guang Ma, Remarkably High Thermoelectric Efficiencies of the Half-Heusler Compounds BXGa (X = Be, Mg, and Ca), *ACS Appl. Mater. Interfaces*, **12**, 5838 (2020). <https://doi.org/10.1021/acsami.9b19198>
- [18] Z. Wendan, L. Yong, L. Yunsheng, W. Jiahua, H. Zhiling, and S. Xiaohong, Structural and thermoelectric properties of Zr-doped TiPdSn half-Heusler compound by first-principles calculations. *Chem. Phys. Lett.* **741**, 137055 (2000). <https://doi.org/10.1016/j.cplett.2019.137055>
- [19] S.M. Saini, Structural, electronic and thermoelectric performance of narrow gap LuNiSb half Heusler compound: Potential thermoelectric material, *Physica B*, **610**, 412823 (2021). <https://doi.org/10.1016/j.physb.2021.412823>
- [20] A.Arunachalam, R. Rajeswarapalanichamy, and K. Iyakutti, Half metallic ferromagnetism in Ni based half Heusler alloys, *Computational Materials Science*, **148**, 87 (2018). <https://doi.org/10.1016/j.commatsci.2018.02.026>
- [21] H B Ozisik et al., Ab-initio calculations on half-Heusler NiXSn (X =Zr, Hf) compounds: electronic and optical properties under pressure, *Indian J. Phys.* **91**(7), 773 (2017). <https://doi.org/10.1007/s12648-017-0971-9>
- [22] P. Hermet et al., Thermal dependence of the mechanical properties of NiTiSn using first-principles calculations and high-pressure X-ray diffraction, *Journal of Alloys and Compounds*, **823**, 153611 (2020). <https://doi.org/10.1016/j.jallcom.2019.153611>
- [23] F. Tran, and P. Blaha, Accurate Band Gaps of Semiconductors and Insulators with a Semi local Exchange-Correlation potential, *Phys. Rev. Lett.* **102**, 226401 (2009). <https://doi.org/10.1103/PhysRevLett.102.226401>
- [24] S. Adachi, *Properties of Semiconductor Alloys: Group-IV, III-V and II-VI Semiconductors* (John Wiley & Sons, 2009). DOI:10.1002/9780470744383
- [25] J.Sun, H.T.Wang and N.B.Ming, Optical properties of heterodiamond B₂CN using first-principles calculations, *Appl. Phys. Lett.* **84**, 4544 (2004). <https://doi.org/10.1063/1.1758781>
- [26] J.M. Hu, S.P. Huang, Z. Xie, H. Hu, and W.D. Cheng, First-principles study of the elastic and optical properties of the pseudocubic Si₃As₄, Ge₃As₄ and Sn₃As₄, *J. Phys.: Condens. Matter*, **19**, 496215 (2007). <https://doi.org/10.1088/0953-8984/19/49/496215>
- [27] G.K.H. Madsen, D.J. Singh, and BoltzTraP. A code for calculating band-structure dependent quantities, *Comput. Phys. Commun.* **175**, 67 (2006). <https://doi.org/10.1016/j.cpc.2006.03.007>
- [28] E. Zhao, and Z. Wu, Electronic and mechanical properties of 5d transition metal mononitrides via first principles, *J. Solid State Chem.* **181**, 2814 (2008). <https://doi.org/10.1016/j.jssc.2008.07.022>
- [29] J.S. Zhao, Q. Gao, L. Li, H.H. Xie, X.R. Hu, C.L. Xu, and J.B. Deng, First-principles study of the structure, electronic, magnetic and elastic properties of half-Heusler compounds LiXGe (X = Ca, Sr and Ba), *Intermetallics*, **89** 65 (2017). <https://doi.org/10.1016/j.intermet.2017.04.011>
- [30] CrystalMaker software, <http://www.crystallmaker.com>
- [31] N. Mehmood, R. Ahmad, and G. Murtaza, Ab initio investigations of structural, elastic, mechanical, electronic, magnetic, and optical properties of half-Heusler compounds RhCrZ (Z = Si, Ge), *J. Supercond. Nov. Magn.* **30**, 2481 (2017). <https://doi.org/10.1007/S10948-017-4051-3>
- [32] J. Ma et al., Computational investigation of half-Heusler compounds for spintronic applications, *Phys. Rev. B*, **95**, 024411 (2017).
- [33] B. Amin, I. Ahmad, M. Maqbool, S. Goumri-Said, and R. Ahmad, Ab initio study of the bandgap engineering of Al_{1-x}Ga_xN for optoelectronic applications, *J. Appl. Phys.* **109**, 023109 (2011). <https://doi.org/10.1063/1.3531996>
- [34] G. Marius, *The Physics of Semiconductors: Kramers-kronig Relations*, (Springer, Berlin Heidelberg, 2010). pp. 775–776. ISBN-13 978-3-540-25370-9
- [35] M. Gajdoš, K. Hummer, G. Kresse, J. Furthmüller, and F. Bechstedt, Linear optical properties in the projector-augmented wave methodology. *Phys. Rev. B*, **73**, 045112 (2006). <https://doi.org/10.1103/PhysRevB.73.045112>
- [36] C. Ambrosch-Draxl, J.O. Sofo, Linear optical properties of solids within the full potential linearized augmented planewave method. *Comput. Phys. Commun* **175**, 1 (2006). <https://doi.org/10.1016/j.cpc.2006.03.005>
- [37] M. Irfan, M.A. Kamran, S. Azam, M.W. Iqbal, T. Alharbi, A. Majid, S.B. Omran, R. Khenata, A. Bouhemadou, and X. Wang, Electronic structure and optical properties of TaNO: an ab initio study, *J. Mol. Graph. Model.* **92**, 296 (2019). <https://doi.org/10.1016/j.jmgm.2019.08.006>
- [38] D.R. Penn, Wave-Number-Dependent Dielectric Function of Semiconductors, *Phys. Rev.* **128**, 2093 (1962). <https://doi.org/10.1103/PhysRev.128.2093>
- [39] A. Benzina, First-principles calculation of structural, optoelectronic properties of the cubic Al_xGa_yIn_{1-x-y}N quaternary alloys matching on AlN substrate, within modified Becke-Johnson (mBJ) exchange potential, *Optik*, **127**, 11577 (2016). <https://doi.org/10.1016/j.ijleo.2016.09.014>
- [40] S. Samanta, and S.M. Saini, First-principle calculations of electronic and optical properties of CdCr₂Te₄ spinel: use of mBJ + U potential in narrow band gap semiconductors, *Indian J. Phys.* **93**(3), 335 (2019). <https://doi.org/10.1007/s12648-018-1298-x>
- [41] N. Yaqoob, et al, Structural, electronic, magnetic, optical and thermoelectric response of half-metallic AMnTe₂ (A = Li, Na, K): An ab-initio calculations, *Physica B: Condensed Matter*, **574**, 311656 (2019). <https://doi.org/10.1016/j.physb.2019.08.033>
- [42] D. Vasileska, H.R. Khan, S.S. Ahmed, C. Ringhofer, and C. Heitzinger, Quantum and Coulomb Effects in Nano Devices, *International Journal of Nanoscience*, **4**, 305 (2005). <https://doi.org/10.1142/S0219581X05003164>
- [43] A. Reshak, Thermoelectric properties of the spin-polarized half-metallic ferromagnetic CsTe and RbSe compounds, *RSC Adv.* **6**, 98197 (2016). <https://doi.org/10.1039/C6RA22758A>
- [44] V.F. Gantmakher, The experimental study of electron-phonon scattering in metals, *Reports on progress in physics*, **37**(3), 317 (1974). <https://doi.org/10.1088/0034-4885/37/3/001>
- [45] C. Lee et al., Density functional theory investigation of the electronic structure and thermoelectric properties of layered MoS₂, MoSe₂ and their mixed-layer compound, *J. Solid State Chem.* **211**, 113 (2014). <https://doi.org/10.1016/j.jssc.2013.12.012>
- [46] T.M. Tritt, Thermoelectric phenomena, materials, and applications, *Annu. Rev. Mater. Res.* **41**, 433 (2011). <https://doi.org/10.1146/annurev-matsci-062910-100453>
- [47] A. Besbes et al. First-principles study of structural, electronic, thermodynamic, and thermoelectric properties of a new ternary half-Heusler alloy PdZrGe, *Chinese Journal of Physics*, **56**, 2926 (2018). <https://doi.org/10.1016/j.cjph.2018.09.027>

- [48] S. Yousuf, D.C. Gupta, Unravelling the magnetism, high spin polarization and thermoelectric efficiency of ZrFeSi half-Heusler, *physica B: condensed matter*, **534**, 5 (2018). <https://doi.org/10.1016/j.physb.2018.01.011>
- [49] S. Parsamehr et al., Half-Metallic, Thermoelectric, Optical, and Thermodynamic Phase Stability of RbBaB (001) Film: A DFT Study, *International Journal of Thermophysics*, **40**, 64 (2019). <https://doi.org/10.1007/s10765-019-2531-3>
- [50] S. Singh, and D.C. Gupta, Investigation of Electronic, Magnetic, Thermodynamic, and Thermoelectric Properties of Half-Metallic XLiSn (X = Ce, Nd) Alloys, *Journal of Superconductivity and Novel Magnetism*, **32**, 2009 (2019). <https://doi.org/10.1007/s10948-018-4907-1>
- [51] A. Besbes et al., Optical and thermoelectric response of RhTiSb half-Heusler, *International Journal of Modern Physics B*, **33**(22) 1950247 (2019). <https://doi.org/10.1142/S0217979219502473>

ОГЛЯД ЕЛЕКТРОННИХ ОПТИЧНИ ТА ТРАНСПОРТНИХ ВЛАСТИВОСТЕЙ НАПІВГЕЙСЛЕРОВОГО СПЛАВУ: NiVSi

Джелті Радун^а, Бесбес Анісса, Бестані Бенауда^б

^аЛабораторія технологій та властивостей твердих речовин, Університет Мостаганем (UMAB) – Алжир

^бЛабораторія EA2M, Університет Мостаганем (UMAB) – Алжир

Теоретично досліджено напівгейслеровий сплав NiVSi за допомогою розрахунків за першопринципами на основі теорії функціоналу щільності (DFT). Для кращого опису електронних властивостей обмінно-кореляційного потенціалу використовується потенціал ТВ-mBJ. Структурні, електронні, магнітні, оптичні та термоелектричні властивості були розраховані за допомогою програмного забезпечення WIEN2k. Знайдені негативні енергії когезії та енергії формування показують, що NiVSi є термодинамічно стабільним. З електронної точки зору NiVSi є напівметалом з непрямою забороненою зоною 0,73 eV у каналі зі спіном вниз, тоді як канал зі спіном вгору є металевим. Загальний магнітний момент дорівнює 1. Оптично, отриманий високий коефіцієнт поглинання в ультрафіолетовому діапазоні довжин хвиль робить NiVSi корисним як ефективний поглинач ультрафіолетового випромінювання. Термоелектрично було отримано високу якість в області p- і n-типу, що робить цю сполуку функціональною для термоелектричних застосувань. Генерація повністю спін-поляризованого струму робить цю сполуку непридатною для застосування спітронів при кімнатній температурі, легування може бути задовільним рішенням для покращення цієї властивості.

Ключові слова: DFT; підхід mBJ; напівметалевий; ультрафіолетовий; фактор якості.

LEVEL STRUCTURE OF ^{58}Cu WITHIN MODIFIED SURFACE DELTA-INTERACTION[†]

Dalal N. Hameed*,  Ali K. Hasan

Department of Physics, College of Education for Girls University of Kufa, Najaf, Iraq

*Corresponding Author: dalal.alkaraawi@uokufa.edu.iq

Received December 16, 2021; revised March 12, 2022; accepted March 13, 2022

The nuclear shell model with modified surface delta interaction MSDI was used to calculate the values of energy levels of the copper nucleus ^{58}Cu . The neutron and proton in the model space $1p_{3/2} 0f_{5/2} 1p_{1/2}$ of the copper nucleus occur outside the closed core ^{56}Ni . This research investigates the excitation energy and angular momentum. As a consequence, theoretical approaches are used to uncover a collection between excitation energies and classical coupling angles $\theta_{a,b}$ at various orbitals. Finally, we demonstrate that our results are supported by experimental evidence: Excitation energies have two major functions, both of which are influenced by classical coupling angles but are unaffected by angular momentum l .

Keywords: energy levels, modified surface delta interaction, ^{58}Cu , classical coupling angle

PACS: 21.60.Cs

Many research have focused on nuclear isotopes, and the element copper will be discussed in this topic [1,2]. According to Ref [3], Martin and Breckon measured ^{58}Cu in 1952. In the last 50 years, many approaches for the effective interaction of nuclei in the "s-d and f-p shells" have been presented. Using the Hamada-Johnston potential, Kuo and Brown estimated the effective two-body interaction in the s-d and f-p shells [4]. Richter et al. "New effective interactions for the $0f_{7/2}$ shell used experimental approaches to derive 195 two-body matrix elements and four single particle energies in the fp-shell, using Wildenthal's nonlinear fit general practice. [3] Talmi employed the surface delta interaction to determine the parameters of nuclear states on a magic core with few' nucleons'. Talmi's theory is based on the following assumptions: First, there is an inert core model of tight shell that works with central forces on valence nucleons; and second, there is 'residual interaction' between the valence nucleons that is induced by two-body forces. Schiffer [5] considered nuclei in which two (hole or particle) are present in addition to a closed shell. Essentially, Schiffer emphasizes that the general behavior of the effective interaction in terms of the angle between the interacting nucleons' angular momenta is a trait that was subsequently linked to the effective interaction's short-range nature [6,7]. In Ref [8] stated the angle between the proton and neutron angular momentum vectors j_a and j_b . In the mass range $A = 50$ to 102, J. Kostensalo and J. Suhonen [9] calculated the characteristics pairing interaction for even-even) reference nuclei. We used modified surface delta interaction and surface delta interaction to investigate the excitation energies for states two-hole and two-particle [10,11,12], one particle – one hole [13,14]. In conclusion, investigations accept the new study's purpose, primarily by the use of MSDI, which predicts low-lying levels structure of ^{58}Cu nuclei.

THEORY

The Schrödinger equation has been essential steps to a particular appropriate Hamiltonian, so that a typical shell-model of effective Hamiltonian may be stated as [11,12].

$$H = \sum_{k=l} H_0 + \sum_{k \leq l} V_{kl} \quad (1)$$

where $\sum_{k < l} V_{kl}$ is the residual 2-body interaction, which exists in addition to the average shell-model potential, and we can express this as:

$$\sum_{k < l} V_{kl} = \sum_{IM} \sum_{j_a \geq j_b} \sum_{j_c \geq j_d} \langle j_a j_b | V | j_c j_d \rangle_I a_{IM}^+ (j_a j_b) a_{IM}^+ (j_c j_d) \quad (2)$$

If ρ_j is single particle energy $\langle j_a j_b | V | j_c j_d \rangle = V_{ab,cd}^{I,T}$ is the matrix element [11,12,14]

If the 2 particles occupy the same level, the energy relative to the closed shell is:

$$\langle H \rangle = 2 \rho_j + \langle j_a j_b | V | j_c j_d \rangle \quad (3)$$

[†] Cite as: D.N. Hameed, and A.K. Hasan, East. Eur. J. Phys. 1, 26-31 (2022), <https://doi.org/10.26565/2312-4334-2022-1-04>
© D.N. Hameed, A.K. Hasan, 2022

Several single-particle levels should be considered the basis for describing low-lying states; if there are two states, they should be indicated by $|j_a j_b IM\rangle$ and $|j_c j_d IM\rangle$ then their energies with respect to the core are given by [11,13,15]

$$\langle H \rangle_{11} = \rho_{j_a} + \rho_{j_b} + V_{abab}^{IT} \quad (4)$$

$$\langle H \rangle_{22} = \rho_{j_c} + \rho_{j_d} + V_{cdcd}^{IT} \quad (5)$$

$$\langle H \rangle_{12} = \langle H \rangle_{21} = V_{abcd}^{IT} \quad (6)$$

To estimate the matrix element for the residual nucleon-nucleon interaction using the MSDI potential [15,16]

$$V_{a,b} = -4\pi A_T \delta \Omega_{a,b} \delta(\hat{r}(a)) - R_0 \delta(\hat{r}(b) - R_0) + B \tau_a \cdot \tau_b \quad (7)$$

where $\hat{r}(a)$, $\hat{r}(b)$ are the position vectors of interacting particles, R_0 is the nuclear radius [14] the strength of interaction A_T . The correction term $B \tau_a \cdot \tau_b$ is introduced to account for the splitting between the groups of levels with different isospin. Such a form of interaction is called MSDI. The antisymmetrized matrix element of V_{acdb}^{IT} is given by [10,15,16]

$$\begin{aligned} V_{ab,cd}^{I,T} = & - \frac{A_T}{2(2I+1)} \times \sqrt{\frac{(2j_a+1)(2j_b+1)(2j_c+1)(2j_d+1)}{(1+\delta_{ab})(1+\delta_{cd})}} \times \\ & [(-1)^{l_a+l_b+j_c+j_d} h_l(j_a j_b) h_l(j_c j_d) \left[1 - (-1)^{l_c+l_d+I+T} \right] - \\ & [k_l(j_a j_b) k_l(j_c j_d)] \left[1 + (-1)^T \right] + \{ [2T(T+1) - 3] B + C \} \delta_{a,c} \delta_{b,d} \end{aligned} \quad (8)$$

where it is $h_l(j_a j_b) = \left\langle j_b \frac{1}{2} j_a \frac{1}{2} \middle| l 0 \right\rangle$, $k_l(j_a j_b) = \left\langle j_a \frac{1}{2} j_b \frac{1}{2} \middle| l \pi \right\rangle$; where $\langle | \rangle$ is the Clebsch-Gordan coefficients

The comportment of the diagonal 2 - body matrix element as a function of the spin I of (particle - particle) state is very distinctive when their value are plotted in a property way. Consider (particle - particle) in orbits j_a and j_b with $I = j_a + j_b$ one can write then [11,10,14]

$$I^2 = (j_a + j_b)^2 = j_a^2 + j_b^2 + 2 \times (j_a j_b) \cos \theta_{a,b} \quad (9)$$

where $\theta_{a,b}$ is the angle between the vectors j_a and j_b . Since the length of vector j is given by $\sqrt{j(j+1)}$ one obtains from eq (10) in a classical picture [6,8,13,16]

$$\cos \theta_{a,b} = \frac{I(I+1) - j_a(j_a+1) - j_b(j_b+1)}{2\sqrt{j_a(j_a+1)j_b(j_b+1)}} \quad (10)$$

The I-dependence of the matrix element V_{abcd}^{IT} can thus be plotted as a function of the angle $\theta_{a,b}$. The radial overlaps of the particle orbits for light nuclei differ from those for heavy nuclei. The proton -neutron configurations correspond to nucleon pair having mixed isospin and one find [13,16]

$$E_{I(p,n)} = 0.5 \left\{ \left(V_{abcd}^{IT} \right)_{I=1} + \left(V_{abcd}^{IT} \right)_{I=0} \right\} \quad (11)$$

Plotting the excitation energy of these states as a function of the corresponding angle $\theta_{a,b}$ determined as specified by Eq.(10). For neutron and proton in various orbits the absolute value of average two body energy is given by [10,15]:

$$\bar{E} = \left| \sum_I (2I + 1) E_I \left\{ \sum_I (2I + 1) \right\}^{0.5} \right| \tag{12}$$

With E_I defined by Eq. (11) .

RESULTS AND DISCUSSION

The main properties of nuclear structure for ground bands of ^{58}Cu nuclei were calculated using MSDI in this paper. The valence nucleons of these nuclei are dispersed in model space $1p_{3/2}, 0f_{5/2}, 1p_{1/2}$. MSDI was used to determine the energy levels and classical coupling angles $\theta_{a,b}$ for (neutron-proton) in these calculations. The nuclear shell model for nucleus ^{58}Cu has one (neutron and proton) outside the inert core ^{56}Ni . The nucleon's that have taken up residence in the model space $1p_{3/2}, 0f_{5/2}, 1p_{1/2}$.

The original MSDI Hamiltonian is also modified to account for the ground state energy. Energy levels were obtained using the equations (4,5,6 and 8). As a result, it's discovered that the experimental value's acceptability is quite high. Configurations mixing between the orbits are used to include the neutron and proton contributions.

To find energy levels, use the single particle energy .For proton particle , $\rho 1p_{3/2} = -0.6901\text{MeV}$, $\rho 0f_{5/2} = 0.3381\text{MeV}$, and $\rho 1p_{1/2} = 0.4161\text{MeV}$ may be used; however, for state neutron particle, $\rho 1p_{3/2} = -10.2543\text{MeV}$, $\rho 0f_{5/2} = -9.4861\text{MeV}$, and $\rho 1p_{1/2} = -9.1422\text{MeV}$ can be used. The use of particle energies inside the space of the aforementioned model, [17,18]. The angular momentum possibilities for this nucleus range from 0 to 5.

Table 1. A comparison between a theoretical result and experimental result excitation energies, MeV, for ^{58}Cu nucleus by using MSDI

I^π	Energy Levels	Energy Levels	I^π	I^π	Energy Levels	Energy Levels	I^π
Theor. Res.		Exp. Res. [19]		Theor. Res.		Exp. Res. [19]	
1^+_1	0.0000	0.0000	1+	2^+_4	3.111	----	----
		0.2029 0.4436 1.051	0+ 3+ 1+	1^+_5	3.26	3.230	----
2^+_1	1.43	1.427	2+	2^+_5	3.28	3.2802	(0+ to 4+)
1^+_2	1.663	1.549	(4+)	1^+_6	3.29	3.310 3.4210 3.4601	---- (7+) (1)+
0^+_1	1.79	----	----	3^+_4	3.5111	3.5126	----
3^+_1	1.8214	1.647	(3+)	5^+_1	3.5743	3.570	----
2^+_2	1.8723	1.652	2+	0^+_2	3.6322	3.6779	(1)+
3^+_2	1.9211	----	----	3^+_5	3.6356		
4^+_1	2.0801	2.0650 2.070 2.170 2.249 2.270	(5+)	2^+_6	3.7645	3.717 3.820	(1)+
1^+_3	2.556	----	----	4^+_3	3.9545	3.890	----
		2.690	4+	3^+_6	4.1403	4.010	----
2^+_3	2.7404	2.7502 2.780 2.8152 2.840 2.9206 2.949	(4+) (5+) (1)+	2^+_7	4.1823	4.0656	(7+)
3^+_3	3.0821	2.9309	(0+ to 4+)	2^+_8	4.5755	4.210 4.4414 4.720 5.065 12.034	(8+) (1)+ (1)+
1^+_4	3.0834	----	----	1^+_7	12.4011	12.45	----
4^+_2	3.0911	----	----	0^+_3	12.543	12.520	(15+)

Theoretically, the energy level (1.8214, 3.0821 and 3.28) MeV was uncertain at the state (3⁺₁, 3⁺₃ and 2⁺₅). The energy of the states (2⁺₁ and 2⁺₂) near the experimental data. The levels 2⁺₃, 1⁺₆, 3⁺₄, 5⁺₁, 2⁺₆, 4⁺₃ and 1⁺₇ with practical energies (2.780, 3.310, 3.5126, 3.570, 3.820, 3.890 and 12.45) MeV, respectively correspond to state for which the angular momentum and/or parity of the corresponding state are not established experimentally.

The new energy levels which are expected for this nucleus in the states 0⁺₁, 3⁺₂, 1⁺₃, 1⁺₄, 4⁺₂ and 2⁺₄ were not well established experimentally.

The particle orbits have a low overlap in the style of the curve in Fig.1 for θ_{a,b}=90, resulting in a weak interaction. The orbits of (neutron- proton) interacting in opposing directions have a high overlap for θ_{a,b}=180. Because the nuclear force has a limited range, the contact will be strong. This interaction explains why the curves in Fig.1 (A, B and C) have an apposite slope for differences ranging from 180 to 90 degrees. For smaller angles, the Pauli principle expresses itself. The two isospin coupling metrics must be recognized for θ_{a,b} = 0.0 and.

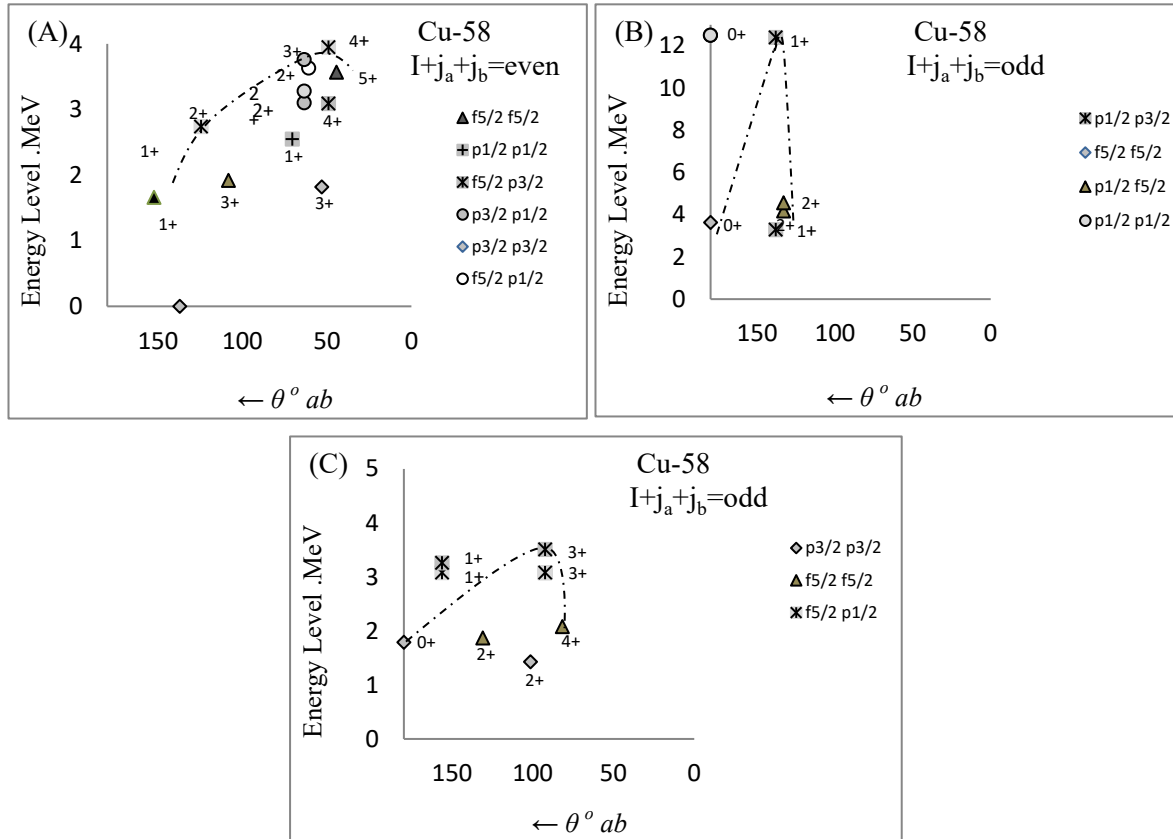


Figure 1. The relationship between classical coupling angles of an even and an odd cases, with the energy levels of all possible states

The particle occupies a spatially symmetric particle state in the θ_{a,b} =180 scenario, which results in a significant negative matrix element due to the high short-range attraction. When T=1, the (neutron- proton) constitute a spatially antisymmetric instance, and their relative space increases when the angle is reduced to 0.0.

The curves displayed in Fig. 1 A. may be created by plotting the excitation energy of these states as a function of the identical angle supplied by Eq. (10) for even states and Fig. 1 (B and C) for odd states of effective interaction determined from the data. Curvature is a measure of short-range attractive force.

Table 2 shows the lowest angle corresponds to the greatest J reading. The angular momentum of the even cases 5⁺₁ which represents the highest angular momentum inside model space 0f_{5/2}0f_{5/2} is 44.4153 degrees as seen in table 3.3. The angle value is 152.3395 with angular momentum 1⁺₂ in model space 0f_{5/2}0f_{5/2} reflects the lowest angular momentum. The angle of 81.7867 degrees is the angular momentum of the odd states 4⁺₁, which represents the maximum angular momentum. The angle value 180.0000 corresponds to the lowest angular momentum 0⁺₁ in the same model space.

Table 2. According to cases of angular momentum I, all possible states of the semi-classical coupling angle value

I^π	Configuration ⁵⁸ Cu	state	$\theta_{a,b}^o$	I^π	Configuration ⁵⁸ Cu	state	$\theta_{a,b}^o$
1 ⁺ ₁	$(\frac{33}{22}, \frac{33}{22})$	Even	137.1665	1 ⁺ ₅	$(\frac{35}{22}, \frac{35}{22})$	Odd	156.4218
2 ⁺ ₁	$(\frac{33}{22}, \frac{33}{22})$	Odd	101.5369	2 ⁺ ₅	$(\frac{31}{22}, \frac{31}{22})$	Even	63.4349

I^π	Configuration ^{58}Cu	state	$\theta_{a,b}^o$	I^π	Configuration ^{58}Cu	state	$\theta_{a,b}^o$
1^+_2	$(\frac{5}{2}, \frac{5}{2}; \frac{5}{2}, \frac{5}{2})$	Even	152.3395	1^+_6	$(\frac{31}{22}, \frac{31}{22})$	Odd	138.1896
0^+_1	$(\frac{33}{22}, \frac{33}{22})$	Odd	180.0000	3^+_4	$(\frac{35}{22}, \frac{35}{22})$	Odd	92.5013
3^+_1	$(\frac{33}{22}, \frac{33}{22})$	Even	53.13010	5^+_1	$(\frac{5}{2}, \frac{5}{2}; \frac{5}{2}, \frac{5}{2})$	Even	44.4153
2^+_2	$(\frac{5}{2}, \frac{5}{2}; \frac{5}{2}, \frac{5}{2})$	Odd	131.0823	0^+_2	$(\frac{5}{2}, \frac{5}{2}; \frac{5}{2}, \frac{5}{2})$	Odd	180.0000
3^+_2	$(\frac{5}{2}, \frac{5}{2}; \frac{5}{2}, \frac{5}{2})$	Even	108.3176	3^+_5	$(\frac{5}{2}, \frac{5}{2}; \frac{5}{2}, \frac{5}{2})$	Even	60.7940
4^+_1	$(\frac{5}{2}, \frac{5}{2}; \frac{5}{2}, \frac{5}{2})$	Odd	81.7867	2^+_6	$(\frac{31}{22}, \frac{31}{22})$	Even	63.4349
1^+_3	$(\frac{1}{2}, \frac{1}{2}; \frac{1}{2}, \frac{1}{2})$	Even	70.5287	4^+_3	$(\frac{35}{22}, \frac{35}{22})$	Even	49.1066
2^+_3	$(\frac{35}{22}, \frac{35}{22})$	Even	124.5667	3^+_6	$(\frac{5}{2}, \frac{5}{2}; \frac{5}{2}, \frac{5}{2})$	Even	60.7940
3^+_3	$(\frac{35}{22}, \frac{35}{22})$	Odd	92.5013	2^+_7	$(\frac{5}{2}, \frac{5}{2}; \frac{5}{2}, \frac{5}{2})$	Odd	133.0881
1^+_4	$(\frac{35}{22}, \frac{35}{22})$	Odd	156.4218	2^+_8	$(\frac{5}{2}, \frac{5}{2}; \frac{5}{2}, \frac{5}{2})$	Odd	133.0887
4^+_2	$(\frac{35}{22}, \frac{35}{22})$	Even	49.1066	1^+_7	$(\frac{31}{22}, \frac{31}{22})$	Odd	138.1896
2^+_4	$(\frac{31}{22}, \frac{31}{22})$	Even	63.4349	0^+_3	$(\frac{1}{2}, \frac{1}{2}; \frac{1}{2}, \frac{1}{2})$	Odd	180.0000

CONCLUSION

For energy levels, theoretical and experimental levels are desirable. As a result, there are much too many experimental excitation energies that are confirmed by calculations and new energy levels is found. As a result, MSDI theoretical calculations are generally consistent with experimental findings. Angler momentum's minimum values agree with the greatest angle. Finally, this highlights an essential fact: The MSDI is enough to show the nuclear structure of ^{58}Cu nuclei.

ORCID IDs

 Ali K. Hasan, <https://orcid.org/0000-0002-9364-3608>

REFERENCES

- [1] D.V. Kutnii, D.D. Burdeynyi, S.A. Vanzha, and N.V. Rud, East Eur. J. Phys. **2**, 104 (2020). <https://doi.org/10.26565/2312-4334-2020-2-09>
- [2] T.A. Younis, NeuroQuantology, **19**(1), 30 (2021). <http://doi.org/10.14704/nq.2021.19.1.NQ21005>
- [3] T. Hamada, and I.D. Johnston, Nucl. Phys. **34**(2), 382 (1962). [https://doi.org/10.1016/0029-5582\(62\)90228-6](https://doi.org/10.1016/0029-5582(62)90228-6)
- [4] W. M. Martin, and S. W. Breckon, Canadian Journal of Physics, **30**(6), 643 (1952). <https://doi.org/10.1139/p52-060>
- [5] A. Molinari, M.B.Johnson, H.A. Bethe, and W.M. Alberico, Nucl. Phys. A, **239**(1), 45 (1975). [https://doi.org/10.1016/0375-9474\(75\)91132-X](https://doi.org/10.1016/0375-9474(75)91132-X)
- [6] P. Van Isacker, EPJ Web Confer. **178**, 05002 (2018). <https://doi.org/10.1051/epjconf/201817805002>
- [7] E. Caurier, G. Martinez-Pinedo, F. Nowacki, A. Poves, and A. P. Zuker, Rev. Mod. Phys. **77**, 427 (2005), <https://doi.org/10.1103/RevModPhys.77.427>
- [8] J.P. Schiffer, Ann. Phys. **66**, 798 (1971). [https://doi.org/10.1016/0003-4916\(71\)90082-0](https://doi.org/10.1016/0003-4916(71)90082-0)
- [9] J. Kostensalo, and J. Suhonen, Phys. Rev. C, **95**, 014322 (2017). <https://doi.org/10.1103/PhysRevC.95.014322>
- [10] D.N. Hameed, and A.K. Hasan, Indian Journal Physics, **95**, 1833 (2021). <https://doi.org/10.1007/s12648-020-01873-6>
- [11] D.N. Hameed, and A.K. Hasan, J. Phys.: Conference Series. **1963**, 012062 (2021). <https://doi.org/10.1088/1742-6596/1963/1/012062>
- [12] A.K. Hasan, and D.N. Hameed, NeuroQuantology, **19**(5), 61 (2021). <http://doi.org/10.14704/nq.2021.19.5.NQ21049>
- [13] D.N. Hameed, and A.K. Hasan, Energy levels of nuclei ^{40}Sc and ^{40}K as a function of semi-classical coupling angle $\theta_{1,2}$ within the modified surface delta-interaction" Nucl. Phys. At. Energy, **20**(2), 146 (2019)
- [14] D.N. Hameed, and A.K. Hasan" Energy Levels Of Isobaric Nuclei (^{16}N , ^{16}F) Within The Modified Surface Delta-Interaction Model" Ukrainian Journal of Physics, **63**, 579 (2018). <http://dx.doi.org/10.15407/ujpe63.7.579>
- [15] R.D. Lawson Theory of the Nuclear Shell Model (Clarendon Press, Oxford, 1980).
- [16] P.J. Brussaard, and P.W.M. Glaudemans, Shell-Model Applications in Nuclear Spectroscopy (North-Holland, Amsterdam, 1977).
- [17] G. Audi, A.H. Wapstr, and C. Thibault, Nuclear Physics A, **729**, 337 (2003). <https://doi.org/10.1016/j.nuclphysa.2003.11.003>
- [18] M.R. Bhat, Nuclear Data Sheets, **85**(3), 415 (1998). <https://inis.iaea.org/search/searchsinglerecord.aspx?recordsFor=SingleRecord&RN=30021608>
- [19] Nesaraja, Caroline D., Scott D. Geraedts, and Balraj Singh. "Nuclear data sheets for A = 58." Nuclear Data Sheets, **111**(4), 897 (2010). <https://doi.org/10.1016/j.nds.2010.03.003>

СТРУКТУРА РІВНІВ ^{58}Cu З МОДИФІКОВАНОЮ ПОВЕРХНЕЮ ДЕЛЬТА-ВЗАЄМОДІЇ

Далал Н. Хамід, Алі К. Хасан

Фізичний факультет, Освітній Коледж для дівчат, Університет Куфи, Наджаф, Ірак

Для розрахунку значень енергетичних рівнів ядра міді ^{58}Cu використано модель ядерної оболонки з модифікованою поверхневою дельта взаємодією MSDI. Нейтрон і протон в модельному просторі $1p_{3/2}$ $0f_{5/2}$ $1p_{1/2}$ ядра міді зустрічаються поза замкнутим ядром ^{56}Ni . У цій роботі досліджується енергія збудження та кутовий момент. Як наслідок, для виявлення сукупності між енергіями збудження та класичними кутами зв'язку $\theta_{a,b}$ на різних орбіталях використовуються теоретичні підходи. Нарешті, ми демонструємо, що наші результати підтверджуються експериментальними доказами: енергії збудження мають дві основні функції, на обидві з яких впливають класичні кути зв'язку, але на них не впливає кутовий момент l .

Ключові слова: енергетичні рівні, модифікована поверхнева дельта взаємодія, ^{58}Cu , класичний кут зв'язку

STUDY OF ELECTROSTATIC ION-CYCLOTRON WAVES IN MAGNETOSPHERE OF URANUS[†]

 Rama S. Pandey^a,  Mukesh Kumar^{b,#}

^aDepartment of Applied Physics, Amity Institute of Applied Science, Amity University Noida UP India

^bDepartment of Physics, Nalanda College Bihar Sharif Nalanda MU Bodh Gaya Bihar, India

*Corresponding Author: rspandey@amity.edu

#E-mail: mukeshkumarpawapuri@gmail.com

Received January 18, 2022; revised February 22, 2022; accepted March 1, 2022

In this manuscript, the method of characteristics particle trajectories details used and the dispersion relation for the ionosphere of Uranus were being used to investigate electrostatic ion-cyclotron waves with parallel flow velocity shear in the presence of perpendicular inhomogeneous DC electric field and density gradient. The growth rate has been calculated using the dispersion relation. Electric fields parallel to the magnetic field transmit energy, mass, and momentum in the auroral regions of the planetary magnetosphere by accelerating charged particles to extremely high energies. The rate of heating of plasma species along and perpendicular to the magnetic field is also said to be influenced by the occurrence of ion cyclotron waves and a parallel electric field in the acceleration area.

Keywords: Electrostatic Ion-cyclotron waves, Velocity shear, density gradient and Inhomogeneous Electric Field, Magnetosphere/Ionosphere of Uranus

PACS: 52.35Fp, 94.30Ch, 96.30Pj

The study of dynamics, which determines the release of free energy, has recently received a lot of attention. Its shear flow is determined by magneto hydrodynamics and plasma physics. The study of dynamics that govern the release of free energy associated with sheared flows has recently garnered a lot of attention in magnetohydrodynamics and plasma physics. In space plasma, sheared flows are ubiquitous, especially around the magnetopause, magnetospheric boundary layer, solar wind stream-stream interactions, comet tails, and the auroral ionosphere. Lemons et al. [1] used a kinetic technique to look at shearing velocity flow perpendicular to a uniform magnetic field for the electrostatic ion-cyclotron (EIC) instability. Simulations of ion-cyclotron waves in a magnetoplasma with transverse inhomogeneous electric field were employed in conjunction with Maxwellian plasma. Using Voyager 2's onboard plasma wave receiver, identical electrostatic ion-cyclotron waves were observed in Uranus' magnetosphere. A minor offset in the occurrence of electrostatic waves from the equator was predicted due to the substantial tilt of Uranian magnetic moment with respect to the planet's rotational axis. The most intense electrostatic waves were discovered around the magnetic equator, at a distance of roughly $11.5R_U$, according to reported measurements [2,3].

Because of the coupling of the zone of positive and negative energy of ion waves, Ganguli et al. [4,5] and Nishikawa et al. [6] argued that electrostatic waves with repetition of the request for ion-cyclotron frequencies can be unpredictable. Some researchers [7] have included the effect of parallel and perpendicular electric fields by modifying velocity terms appearing in the distribution function, actually results in an extension of earlier theory and obscuring the details of particle trajectories and with their effect. Others, using particle aspect investigation, have focused on the impact of an equal electric field on particle cyclotron instability for various distribution capacities. Others have used particle aspect analysis to investigate the effect of a parallel electric field on ion-cyclotron instability for various distribution functions [8,9]. Kandpal, et al.[10] investigated the Kelvin-Helmholtz instability in the magnetosphere of Saturn using an inhomogeneous DC electric field. With an inhomogeneous DC electric field, Kandpal and Pandey [11] explored higher harmonics electrostatic ion cyclotron parallel flow velocity shear instability in the magnetosphere of Saturn. The effect of different parameters on the growth rate of waves has been demonstrated using EIC instability and parallel velocity shear in the presence of an electric field perpendicular to the magnetic field [12].

The dielectric permittivity tensor of a magneto active current-driven plasma has been obtained by employing the kinetic theory based on the Vlasov equation and Lorentz transformation formulas with an emphasize on the q-nonextensive statistics for low frequency wave by Niknam [13]. Niyat et al [14] has solved dispersion relation for magnetized plasmas that has non-extensive electrons drifting with respect to stationary ions, and satisfies the other conditions for the excitation of electrostatic ion cyclotron waves using the standard linear Vlasov theory and q-distributions. The Electrostatic Ion Cyclotron (EIC) instability that includes the effect of wave-particle interaction has been studied owing to the free energy source through the flowing velocity of the inter-penetrating plasmas by Bashir et al [15]. The electrostatic waves in magnetized plasmas have been derived in the context of the nonextensive q-distribution of Tsallis statistics by Sharifi [16].

An ion beam propagating through collisional magnetized plasma containing electrons and two positive ion components has been discussed electrostatic ion cyclotron (EIC) instability via Cerenkov interaction [17]. Liu et al [18]

[†] Cite as: R.S. Pandey, and M. Kumar, East. Eur. J. Phys. 1, 32 (2022), <https://doi.org/10.26565/2312-4334-2022-1-05>
© R.S. Pandey, M. Kumar, 2022

has explained the dispersive Alfvén wave in a low β plasma with anisotropic superthermal particles modeled by a bi-nonextensive distribution is derived from a kinetic theory. The effect of anisotropic temperature on inertial Alfvén wave is so small that it is negligible. The numerical results reveal that the presence of superthermal electrons in the small wavenumber limit will lead the damping rate of the kinetic Alfvén wave (KAW) bigger than the one with Maxwellian distribution.

The experimental studies on electrostatic ion-cyclotron waves (EICWs) and their instability were often performed in a narrow plasma column in Q-machines, in which the wave was conventionally generated via the instability driven by an electron current parallel to a magnetic field. The propagation characteristics of wave patterns have seldom been studied, especially the different characteristics in pulse and continuous wave patterns [19]. Accumulation of carbon dioxide in the Earth's atmosphere leads to an increase in the greenhouse effect and, as a consequence, to significant climate change. Thus, the demand to develop effective technologies of carbon dioxide conversion grows year to year. Additional reason for research in this direction is the intention of Mars exploration, since 96% of the Martian atmosphere is just carbon dioxide, which can be a source of oxygen, rocket fuel, and raw materials for further chemical utilization. The enhancement of negative ion production in a volume Penning based source could be performed by the application of metal hydride cathode. Hydrogen isotopes are stored there in a chemically bound atomic state and desorbed from the metal hydride under the discharge current impact [20,21].

The dispersion equation has been derived on an approximation based for the current from the exact solutions of the characteristic cylindrical geometry form of the Vlasov plasma equation in a uniform magnetized plasma cylinder surrounded by a larger metal boundary outside a vacuum gap, which thus differs from that in unbounded plasmas by Kono et al [22].

Bashir et al [23] has studied the Bernstein mode instability driven by a perpendicular momentum ring distribution function is insensitive to the parallel distribution. However, in the relativistic treatment, owing to the inexorable coupling between the parallel and perpendicular momenta through the Lorentz factor, the parallel momentum distribution may affect the instability. Bashir and Vranjes [24] has studied the unstable kinetic drift wave in an electron-ion plasma can very effectively be suppressed by adding an extra flowing ion (or plasma) population. Theoretical study of the effects of positron density on the electrostatic ion cyclotron instability in an electron-positron-ion plasma using the kinetic theory approach by assuming that positrons and electrons can drift parallel to the magnetic field either in the same or the opposite directions has been studied by Khorashadzadeh et al [25].

The evolution of Filamentation instability in a weakly ionized current-carrying plasma with nonextensive distribution has been studied in the diffusion frequency region, taking into account the effects of electron-neutral collisions Using the kinetic theory, Lorentz transformation formulas by Khorashadzadeh[26]. The dispersion relation for parallel propagating waves in the ion-cyclotron branch has investigated numerically by considering that the velocity distribution of the ion population is a function of type product-bi-kappa. We investigate the effects of the non-thermal features and of the anisotropy associated with this type of distribution on the ion-cyclotron instability, as well as the influence of different forms of the electron distribution, by considering Maxwellian distributions, bi-kappa distributions, and product-bi-kappa distributions [27].

Incorporating the details of particle trajectories in the presence of non-uniform electric field and using them for bi-Maxwellian hot plasma to the magnetic field with velocity shear flow parallel to density gradient perpendicular to magnetic field, a conceptual study of ion-cyclotron instability has been performed for the magnetosphere of Uranus.

DISPERSION RELATION AND GROWTH RATE

Small perturbations in B_1 , f_{s1} and E_1 linearize the Vlasov-Maxwell equations for homogeneous plasma, yielding the dispersion relation. The harmonic dependency of these perturbed quantities is assumed to be as. The following are the linearized first order Vlasov equations:

$$\frac{\partial f_{s1}}{\partial t} + \mathbf{v} \cdot \frac{\partial f_{s1}}{\partial \mathbf{r}} + \left(\frac{\mathbf{F}_s}{m_s} \right) \left(\frac{\partial f_{s1}}{\partial \mathbf{v}} \right) = S_s(\mathbf{r}, \mathbf{v}, t) \quad (1)$$

The term Force can be calculated as

$$\mathbf{F}_s = e_s \left[\mathbf{E}_0(\mathbf{x}) + (\mathbf{v} \times \mathbf{B}_0)/c \right] \quad (2)$$

$$S_s(\mathbf{r}, \mathbf{v}, t) = \left(-\frac{e_s}{m_s} \right) \left[\mathbf{E}_1 + (\mathbf{v} \times \mathbf{B}_1)/c \right] \left(\frac{\partial f_{s0}}{\partial \mathbf{v}} \right) \quad (3)$$

Where 's' stands for species. The perturbed distribution function f_{s1} , which is derived from eq. (1), is calculated using the typical solutions approach.

$$f_{s1}(\mathbf{r}, \mathbf{v}, t) = \int_{-\infty}^0 S_s \left[\mathbf{r}_0(\mathbf{r}, \mathbf{v}, t), \mathbf{v}_0(\mathbf{r}, \mathbf{v}, t), t - t' \right] dt$$

The phase space coordinate system has undergone a transformation. From $(\mathbf{r}, \mathbf{v}, t)$ to $(\mathbf{r}_0, \mathbf{v}_0, t - t')$ where $t - t' = \tau$. The particle trajectories for the inhomogeneous external DC electric field and the homogeneous magnetic field, as specified by [28], are as follows:

$$\begin{aligned} x(\tau) &= x_0 + \frac{v_{\perp}}{\Omega_s} \left(1 + \frac{\bar{E}'(x)}{4\Omega_s^2} \right) \left[\sin(\theta - \Omega_s \tau) - \sin\theta \right] \\ y(\tau) &= y_0 + \Delta' + \frac{v_{\perp}}{\Omega_s} \left(1 + \frac{3\bar{E}'(x)}{4\Omega_s^2} \right) \left[\cos(\theta - \Omega_s \tau) - \cos\theta \right] \\ z(\tau) &= z_0 + v_{\parallel} \tau \end{aligned} \tag{5}$$

Where

$$\begin{aligned} \Delta &= \frac{\bar{E}'(x)\tau}{\Omega_s} \left[1 + \frac{E''(x)}{E(x)} \cdot \frac{1}{4} \left(\frac{v_{\perp}}{\Omega_s} \right)^2 + \dots \right] \\ \bar{E}(x) &= \frac{e_s E(x)}{m_s} \text{ and } E(x) = E_{0x} \left(1 - \frac{x^2}{a^2} \right) \end{aligned}$$

So, $\bar{E}'(x) = \frac{e_s E_{0x} (1-\rho)}{m_s}$

where $\rho = \frac{2X}{a^2}$ and $\Omega_s = \frac{e_s B_0}{m_s}$

After replacing the unperturbed trajectories in equation (4) and followed by simplified algebraic calculations following technique out lined in [11] the perturbed distribution function based on time integration is given as:

$$f_{s1}(\mathbf{r}, \mathbf{v}, t) = \sum_s \frac{ie_s}{m_s \omega} \sum_{m,n,p,g} J_n(\lambda_1) J_m(\lambda_1) J_p(\lambda_2) J_g(\lambda_2) e^{i(m-n)(\pi/2+\theta)} \cdot e^{i(g-p)(\pi/2+\theta)} \frac{[E_{1x} U^* + E_{1y} V^* + E_{1z} W^*]}{k_{\parallel} v_{\parallel} + n\Omega_s + p\Omega_s + k_{\perp} \Delta' - \omega} \tag{6}$$

where

$$\begin{aligned} U^* &= C v_{\perp} \frac{n}{\lambda_1} \left(1 - \frac{\bar{E}'(x)}{4\Omega_s^2} \right) + k_{\perp} v_{\perp} \zeta'' \frac{n}{\lambda_1} \left(1 + \frac{\bar{E}'(x)}{4\Omega_s^2} \right) \\ V^* &= i C v_{\perp} \frac{J_n'}{J_n} + \frac{3}{4} C v_{\perp} \frac{n}{\lambda_1} \frac{\bar{E}'(x)}{4\Omega_s^2} - C \Delta' \\ W^* &= \omega \frac{\delta f_{so}}{\delta v_{\parallel}} + D k_{\perp} v_{\perp} \frac{n}{\lambda_1} + \frac{3}{4} D k_{\perp} v_{\perp} \frac{n}{\lambda_1} \frac{\bar{E}'(x)}{\Omega_s^2} + k_{\perp} v_{\parallel} \Delta' + k_{\perp} v_{\parallel} \zeta'' \\ C &= (\omega - k_{\parallel} v_{\parallel}) \left(\frac{-2f_{so}}{\alpha_{\perp s}^2} \right) + k_{\parallel} \frac{\delta f_{so}}{\delta v_{\parallel}} \\ D &= v_{\parallel} \left(\frac{-2f_{so}}{\alpha_{\perp s}^2} \right) - \frac{\delta f_{so}}{\delta v_{\parallel}} \\ \lambda_1 &= \frac{k_{\perp} v_{\perp}}{\omega_{cs}}, \quad \lambda_2 = \frac{3 k_{\perp} v_{\perp} \bar{E}'(x)}{4 \Omega_s^3}, \quad \Delta' = \frac{\delta \Delta}{\delta t} \end{aligned} \tag{7}$$

Δ is the series variation of inhomogeneous electric field and Δ' is the time derivative of Δ . The unperturbed bi-Maxwellian distribution function can be written by Huba (29):

$$\begin{aligned} f_{so} &= f_{mo} + v_y \zeta'' \\ \zeta'' &= \frac{1}{\Omega_s} \left[\epsilon_n + \frac{2(v_{\parallel} - v_{oz}(x)) \delta v_{oz}(x)}{\alpha_{\parallel s}^2 \delta x} \right] f_{mo} \\ f_{mo} &= \frac{n_o(x)}{\pi^{3/2} \alpha_{\perp s}^2 \alpha_{\parallel s}} \exp \left[-\frac{(v_{ox}^2 + v_{oy}^2)}{\alpha_{\perp s}^2} - \frac{(v_{\parallel} - v_{oz}(x))^2}{\alpha_{\parallel s}^2} \right] \end{aligned}$$

Where ζ'' is being constant of motion:

$$\alpha_{\perp,||s} = \sqrt{\frac{2K_b T_{\perp,||s}}{m_s}} \tag{8}$$

Where ζ'' is being constant of motion and K_b is the Maxwell Boltzmann constant

Now making it easy by replacing $m=n, g=p$ and applying the standard definition of conductivity and current density, the dielectric tensor can be calculated as:

$$\|\epsilon(k,\omega)\| = 1 - \sum_s \frac{4e_s^2 \pi}{m_s \omega^2} \int \sum_{n,p} J_p^2(\lambda_2) \frac{d^3 v \sum_{i,j} \|S_{ij}\|}{k_{||} v_{||} + n\Omega_s + p\Omega_s + k_{\perp} \Delta' - \omega} \tag{9}$$

$$\text{Where, } \|S_{ij}\| = \begin{vmatrix} v_{\perp} J_n^2 \frac{n}{\lambda_1} U^* & J_n^2 v_{\perp} \frac{n}{\lambda_1} V^* & v_{\perp} J_n^2 \frac{n}{\lambda_1} W^* \\ -iv_{\perp} J_n' J_n U^* & -iv_{\perp} J_n^2 V^* & iv_{\perp} J_n^2 W^* \\ v_{||} J_n^2 U^* & v_{||} J_n^2 V^* & v_{||} J_n^2 W^* \end{vmatrix} \tag{10}$$

Now we consider electrostatic ion-cyclotron instability

$$\|\epsilon_{xx}\| = N^2 \tag{11}$$

Here N represents the index of refraction.

The estimating method can be used to obtain the final electrostatic dispersion relation of Huba [29] and combining equation (8), (9), (10) and (11)

$$D(k,\omega) = 1 + \sum_s \frac{2\omega_{ps}^2}{k_{\perp}^2 \alpha_{\perp s}^2} \sum_{n,p} \Gamma_n(\mu_s) \sum_p J_p^2(\lambda_2) \left(1 - \frac{\bar{E}'(x)}{4\Omega_s^2} \right) \cdot \frac{k_{\perp}}{k_{||}} \left[\left(\frac{\bar{\omega}}{k_{||} \alpha_{||s}} - \frac{1}{2} \epsilon_n \rho_s \frac{\alpha_{\perp s}}{\alpha_{||s}} \right) Z(\zeta) + A_T \frac{k_{||}}{k_{\perp}} (1 + \zeta Z(\zeta)) - A_s \left(\frac{\alpha_{\perp s}}{\alpha_{||s}} \right)^2 (1 + \zeta Z(\zeta)) \right] \tag{12}$$

$Z(\zeta) = (\pi)^{-\frac{1}{2}} \int_{-\infty}^{\infty} \frac{e^{-t^2}}{t - \zeta} dt$ is plasma dispersion function with ζ given as:

$$\begin{aligned} \zeta &= \frac{\bar{\omega} - (n+p)\Omega_s - k_{\perp} \Delta'}{k_{||} \alpha_{||s}} \\ A_s &= \frac{1}{\Omega_s} \frac{\delta v_{oz}(x)}{\delta x} \\ A_T &= \frac{\alpha_{\perp s}^2}{\alpha_{||s}^2} - 1 \\ \epsilon_n &= \frac{\delta \ln n(x)}{\delta x}, \quad \bar{\omega} = \omega - k_{||} v_{oz}(x) \\ \mu_s &= \frac{k_{\perp}^2 \rho_i^2}{2}, \quad \lambda_{DS}^2 = \frac{\alpha_{\perp s}^2}{2\omega_{ps}^2} \end{aligned} \tag{13}$$

ω_{ps}^2 = Squared of plasma frequency

Where $Z(\zeta)$ represents plasma dispersion function

Now the above-mentioned dispersion relation comes to a final form to that of Huba [29] by the removal of inhomogeneous DC electric field is removed from the equation, and $\alpha_{\perp s} = \alpha_{||s}$, and based on [29] assumptions for $p=0$ and $s=i, e$. The assumption is used to estimate the dispersion relation for electrons and ion approximations. $k_{\perp} \rho_e \ll 1$ and there is no such approximation for ions. Thus equation (12) is simplified as:

$$D(k,\omega) = 1 + \frac{1}{k_{\perp}^2 \lambda_{De}^2} \eta_e \frac{T_{\perp e}}{T_{||e}} + \frac{1}{k_{\perp}^2 \lambda_{Di}^2} \eta_i \left[\frac{T_{\perp i}}{T_{||i}} \Gamma_n(\mu_i) \frac{k_{\perp}}{k_{||}} \left[\left(\frac{\bar{\omega}}{k \alpha_{||i}} \frac{T_{\perp i}}{T_{||i}} - \frac{1}{2} \epsilon_n \rho_i \frac{\alpha_{\perp i}}{\alpha_{||i}} + \frac{(n\Omega_i + k_{\perp} \Delta')}{k_{||} \alpha_{||i}} \right) \times \left(1 - \frac{T_{\perp i}}{T_{||i}} \right) \right] Z(\zeta_i) - A_i \frac{T_{\perp i}}{T_{||i}} (1 + \zeta Z(\zeta_i)) \right] \tag{14}$$

After substituting $Z(\zeta_i) = -\frac{1}{\zeta_i} - \frac{1}{2\zeta_i^3}$, $n_{oi} = n_{oe}$ and multiplying throughout with $\frac{k_{\perp}^2 \lambda_{Di}^2}{\eta_i}$

$$0 = \frac{\lambda_{Di}^2}{\lambda_{De}^2} \frac{\eta_e}{\eta_i} \frac{T_{\perp e}}{T_{\parallel e}} + \left[\frac{T_{\perp i}}{T_{\parallel i}} - \Gamma_n(\mu_i) \frac{T_{\perp i}}{T_{\parallel i}} + \frac{\Gamma_n(\mu_i) k_{\perp}}{2k_{\parallel}} \varepsilon_n \rho_i \frac{\alpha_{\perp i}}{\alpha_{\parallel i}} \cdot \frac{k_{\parallel} \alpha_{\parallel i}}{\bar{\omega} - n\Omega_i + k_{\perp} \Delta'} - \frac{\Gamma_n(\mu_i) k_{\perp}}{k_{\parallel}} \times \right. \\ \left. \times \frac{n\Omega_i + k_{\parallel} \alpha_{\parallel i}}{\bar{\omega} - n\Omega_i + k_{\perp} \Delta'} - \frac{\Gamma_n(\mu_i)}{2(\bar{\omega} - n\Omega_i + k_{\perp} \Delta')^2} \cdot \frac{T_{\perp i}}{T_{\parallel i}} (k_{\parallel} \alpha_{\parallel i})^2 \left(1 - \frac{k_{\perp}}{k_{\parallel}} A_i \right) \right] \quad (15)$$

$$\eta_e = 1 - \frac{\bar{E}_e(x)}{4\Omega_e^2}$$

$$\eta_i = 1 - \frac{\bar{E}_i(x)}{4\Omega_i^2}$$

Multiplying equation (15) throughout by $\left(\frac{\bar{\omega} - n\Omega_i + k_{\perp} \Delta'}{k_{\parallel} \alpha_{\parallel i}} \right)^2$ we obtain a quadratic dispersion equation as:

$$a_1 \left(\frac{\bar{\omega}'}{\Omega_i} \right)^2 + b_1 \left(\frac{\bar{\omega}'}{\Omega_i} \right) + c_1 = 0 \quad (16)$$

where

$$a_1 = a_2 \left(\frac{\Omega_i}{\alpha_{\parallel i} k_{\parallel}} \right)^2 \\ a_2 = \frac{T_{\perp i}}{T_{\parallel e}} \frac{\eta_e}{\eta_i} + \frac{T_{\perp i}}{T_{\parallel i}} - \Gamma_n(\mu_i) \frac{T_{\perp i}}{T_{\parallel i}} \\ b_1 = b_2 \left(\frac{\Omega_i}{\alpha_{\parallel i} k_{\parallel}} \right) - \frac{2k_{\perp} \Delta'}{\alpha_{\parallel i}^2 k_{\parallel}^2} a_2 \Omega_i \\ b_2 = \frac{k_{\perp}}{2k_{\parallel}} \frac{\Gamma_n(\mu_i) \varepsilon_n \rho_i \alpha_{\perp i}}{\alpha_{\parallel i}} - \Gamma_n(\mu_i) \frac{k_{\perp}}{k_{\parallel}} - \Gamma_n(\mu_i) \frac{k_{\perp} n\Omega_i}{\alpha_{\parallel i} k_{\parallel}^2} \\ c_1 = \frac{\Gamma_n(\mu_i) T_{\perp i}}{2T_{\parallel i}} \left(1 - \frac{k_{\perp}}{k_{\parallel}} A_i \right) - \frac{b_2 k_{\perp} \Delta'}{\alpha_{\parallel i} k_{\parallel}} + \frac{a_2 k_{\perp}^2 (\Delta')^2}{\alpha_{\parallel i}^2 k_{\parallel}^2} \quad (17)$$

$$\bar{\omega}' = \bar{\omega} - n\Omega_i$$

The solution of equation (16) is

$$\bar{\omega}' = -\frac{b_1}{2a_1} \left[1 \mp \left(1 - \frac{4a_1 c_1}{b_1^2} \right)^{1/2} \right] \quad (18)$$

From this expression growth rate has been calculated by computer analysis when $b_1^2 \ll 4a_1 c_1$. This criteria gives a condition for the growth of wave when

$$A_i > \frac{k_{\parallel}}{k_{\perp}} \left[1 - \frac{2T_{\parallel i}}{\Gamma_n(\mu_i) T_{\perp i}} \left(\frac{\left(\frac{b_2 \Omega_i}{\alpha_{\parallel i} k_{\parallel}} - \frac{2a_2 k_{\perp} \Omega_i \Delta'}{\alpha_{\parallel i}^2 k_{\parallel}^2} \right)^2}{4a_2 \left(\frac{\Omega_i}{\alpha_{\parallel i} k_{\parallel}} \right)^2} + \frac{b_2 k_{\perp} \Delta'}{\alpha_{\parallel i} k_{\parallel}} - \frac{a_2 k_{\perp}^2 (\Delta')^2}{\alpha_{\parallel i}^2 k_{\parallel}^2} \right) \right]$$

In long wavelength limit when $k_{\perp}^2 \rho_i^2 \ll 1$ and removal of non-uniform DC electric field for Maxwellian plasma $\alpha_{\perp i} = \alpha_{\parallel i}$

$$A_i > \frac{k_{\parallel}}{k_{\perp}} \left[1 + \frac{T_e}{T_i} \frac{k_{\perp}^2}{k_{\parallel}^2} (\varepsilon_n \rho_i)^2 \right]$$

An expression close to that of Huba [29] is obtained.

PLASMA PARAMETERS

From Kurth et al [2] and Pandey [30] the following values of plasma properties for Uranus' magnetosphere, Growth rate (γ/ω_c) variations with $k_{\perp}\rho_i$ were determined using equation (18): $E_o=1\text{mV/m}$, $B_o=11\text{nT}$, $A_i=0.05$, $T_{\perp}/T_{\parallel}=1.25$, $\rho=0.5$, $T_e/T_i=4$, $\epsilon_n\rho_i=0.02$ and $\theta=89^\circ$ at $11 R_U$.

RESULTS AND DISCUSSION

Figure 1 shows the variation in growth rates in respect to $k_{\perp}\rho_i$ for assumed values of shear scale length (A_i) have been shown.

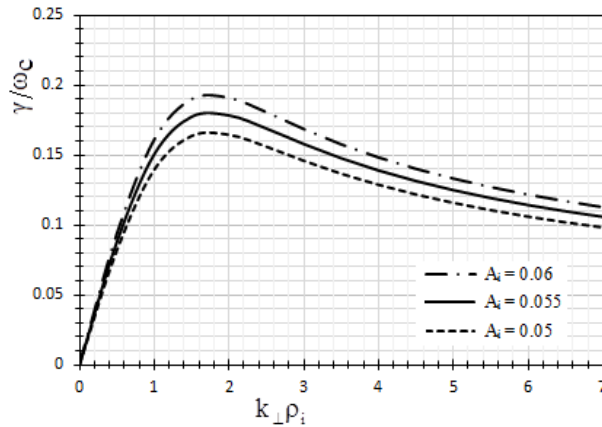


Figure 1. Differences in the rates of growth in relation to $k_{\perp}\rho_i$ for differing values of A_i at $T_{\perp}/T_{\parallel}=1.25$, $T_e/T_i=4$, $\rho=0.5$, $\epsilon_n\rho_i=0.02$, $\theta=89^\circ$ and additional fixed plasma characteristics.

At harmonics $n=1$ and $A_i=0.05$, growth rate is 0.1645. Growth rate increases from 0.1783 to 0.1912 for $A_i=0.055$ and 0.06 respectively. The maxima of growth rate occurs at $k_{\perp}\rho_i=1.8$ in every case. The velocity shear ion-cyclotron like waves are excited for $k_{\perp}\rho_i > 1$ at shorter wavelength regions [5, 31], as shown in this chapter. Our results are similar to numerical simulation using M.H.D. equation valid at large ion larmor radius [32]. When the gyro radius is similar to the velocity shear scale length, the instability appears to have stabilized. Figure 2 represents the growth rate variation with respect to $k_{\perp}\rho_i$ for diverse values of density scale length ($\epsilon_n\rho_i$). The increases in growth rate with increasing value of density scale length, as for $\epsilon_n\rho_i=0.02$ and 0.08, growth rate increases from 0.1645 to 0.1758 with no change in $k_{\perp}\rho_i=1.8$. Fujimoto and Terasawa [33] According to simulation data, the mixing efficiency of non-uniform background plasma is a function of density ratio, plasma, shear layer width, and growth mode wavelength. Their conclusion is supported by our findings. Figure 3 indicates the change in growth rate for the ion-cyclotron instability in Uranus' magnetosphere with harmonic $n=1$.

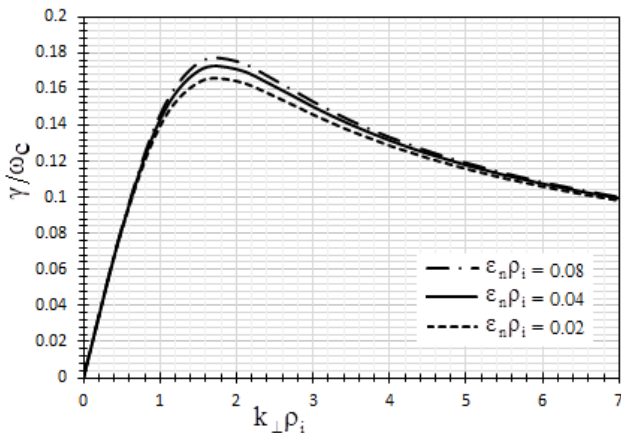


Figure 2. Differences in the rates of growth in relation to $k_{\perp}\rho_i$ for varying values of $\epsilon_n\rho_i$ at $T_{\perp}/T_{\parallel}=1.25$, $T_e/T_i=4$, $\rho=0.5$, $A_i=0.05$, $\theta=89^\circ$ and additional fixed plasma characteristics.

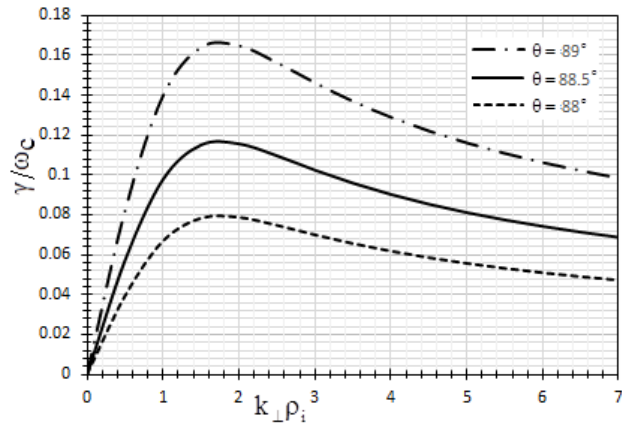


Figure 3. Differences in the rates of growth in relation to $k_{\perp}\rho_i$ for varying values of θ at $T_{\perp}/T_{\parallel}=1.25$, $T_e/T_i=4$, $\rho=0.5$, $A_i=0.05$, $\epsilon_n\rho_i=0.02$ and additional fixed plasma characteristics.

For various values of propagation angle, the growth rate is confirmed with reference to the magnetic field angle (θ). The magnetic dipole axis, which is tilted at sixty degrees like Uranus' spin axis, condenses, resulting in a more bending magnetic field and magnetic field intersection [34,35]. In the graph, for $\theta=88^\circ$, $\gamma/\omega_c=0.0787$, for

$\theta = 88.5^\circ$, $\gamma/\omega_c = 0.1156$ and for $\theta = 89^\circ$, $\gamma/\omega_c = 0.1645$. Therefore, it is concluded that even the slight lowering in angle of propagation decreases the growth rate significantly for Uranian magnetosphere. In Figure 4 variation of growth rate with $k_\perp \rho_i$ for various values of electric field have been showed. For $E_o = 1\text{mV/m}$, maximum growth rate, $\gamma/\omega_c = 0.1645$ appears at $k_\perp \rho_i = 1.8$ and for $E_o = 0.1\text{mV/m}$, maximum growth rate, $\gamma/\omega_c = 0.1753$ appears again at $k_\perp \rho_i = 1.8$. At $n=1$ harmonic of ion cyclotron gyro frequency, growth rate reduces with higher value of electric field. This shows that increasing electric field magnitude has a stabilizing effect on electrostatic ion-cyclotron waves. The behavior is in accordance with Misra and Tiwari [8] this illustrates that the parallel electric field has the effect of stabilizing wave expansion and increasing ion transverse acceleration. Figure 5 shows the effect of varying T_e/T_i on growth rate of ion-cyclotron waves for 11 R_U , other fixed parameters as mentioned in figure caption.

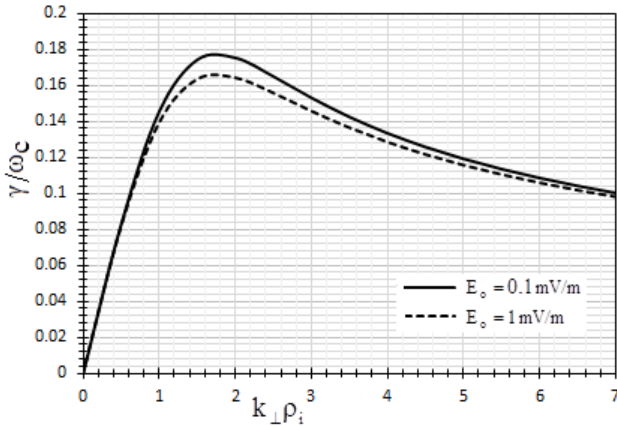


Figure 4. Differences in the rates of growth in relation to $k_\perp \rho_i$ for varying values of E_o at $T_\perp/T_\parallel = 1.25$, $T_e/T_i = 4$, $\rho = 0.5$, $A_i = 0.05$, $\theta = 89^\circ$, $\epsilon_n \rho_i = 0.02$ and additional fixed plasma characteristics.

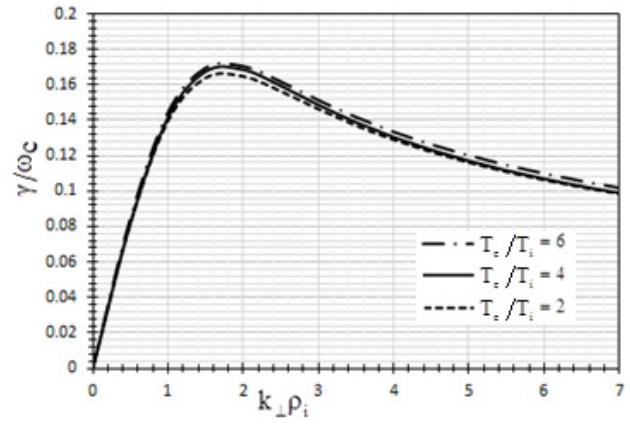


Figure 5. Differences in the rates of growth in relation to $k_\perp \rho_i$ for varying values of η_e/η_i at $T_\perp/T_\parallel = 1.25$, $\epsilon_n \rho_i = 0.02$, $\rho = 0.5$, $A_i = 0.05$, $\theta = 89^\circ$ and additional fixed plasma characteristics.

With $T_e/T_i = 2, 4$ and 6 , $\gamma/\omega_c = 0.1496, 0.1645$ and 0.1705 respectively. It is seen that with increasing the value of T_e/T_i , growth rate also increases. Figure 6 has been made to depict the diversity in growth rates with respect to $k_\perp \rho_i$ for differing value of ρ and other parameters fixed. The effects of inhomogeneity non the electric field with a constant DC field magnitude are depicted in this diagram. The maximum growth rate increases from 0.1645 to 0.1722 as the value of ρ increases from 0.5 to 0.9 . Velocity shear ion-cyclotron like waves are excited in the regions where $E \times B$ drift is localized. The effect of non-uniform electric field in the perpendicular direction makes it to be a function of position as shown in the expression and thus cyclotron frequency is renormalized. In Figure 7 the variation of growth rate with relation to $k_\perp \rho_i$ for varying values of ratio of perpendicular to parallel temperature (T_\perp/T_\parallel) are shown. Since $T_\perp/T_\parallel - 1 = A_T$, the graph actually shows growth rate for different anisotropies (A_T). For $T_\perp/T_\parallel = 1.25$, $\gamma/\omega_c = 0.1645$, for $T_\perp/T_\parallel = 1.5$, $\gamma/\omega_c = 0.1685$ and for $T_\perp/T_\parallel = 1.75$, $\gamma/\omega_c = 0.1708$. Thus, temperature anisotropy becomes an additional source along with velocity shear, density scale length and angle of propagation, for exciting shorter wavelengths. The results can be compared to Misra and Tiwari [8] for terrestrial magnetosphere.

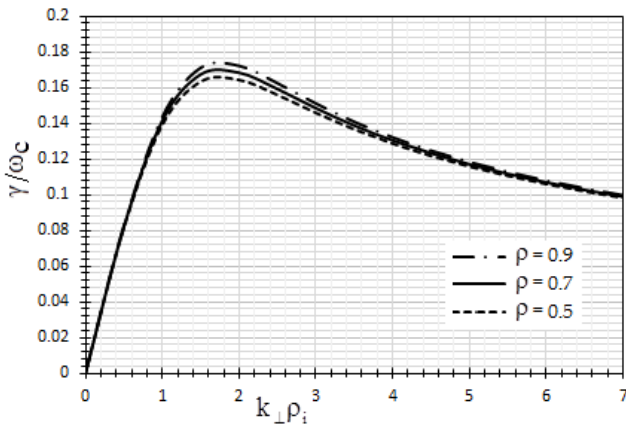


Figure 6. Differences in the rates of growth in relation to $k_\perp \rho_i$ for various values of ρ at $T_\perp/T_\parallel = 1.25$, $T_e/T_i = 4$, $\epsilon_n \rho_i = 0.02$, $A_i = 0.05$, $\theta = 89^\circ$ and additional fixed plasma characteristics.

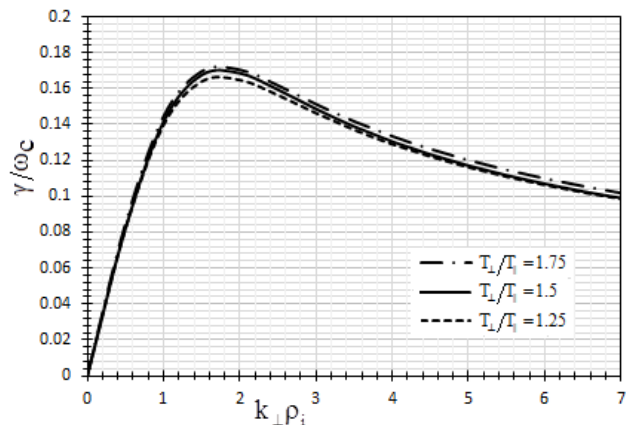


Figure 7. Differences in the rates of growth in relation to $k_\perp \rho_i$ for varying values of T_\perp/T_\parallel at $\epsilon_n \rho_i = 0.05$, $T_e/T_i = 4$, $\rho = 0.5$, $A_i = 0.05$, $\theta = 89^\circ$ and additional fixed plasma characteristics.

CONCLUSION

In the presence of a parallel DC field, this study shows the stimulation of electrostatic ion-cyclotron waves in Uranus' magnetosphere. The inclusion of temperature anisotropy and inhomogeneous electric field through kinetic approach leads to conclusion that in addition to driving sources of instability, such as temperature anisotropy and velocity shear, angle of propagation. In the case of the Uranian magnetosphere, it also has a significant impact on the rate of expansion of ion-cyclotron waves. The increase in electric field magnitude plays stabilizing effect on electrostatic ion-cyclotron instability, thus decreasing the growth rate of the waves as well as enhances transverse acceleration of ions.

ORCID IDs

 Rama S. Pandey, <https://orcid.org/0000-0003-4907-1080>;  Mukesh Kumar, <https://orcid.org/0000-0001-6106-4794>

REFERENCES

- [1] D.S. Lemons D. Winske, and S.P. Gary, J. Geophys. Res. **97**, 19381 (1992). <https://doi.org/10.1029/92JA01735>
- [2] W.S. Kurth, D.D. Barbosa, D.A. Gurnett, and F.L. Scarf, J. Geophys. Res. **92**(A13), 15225 (1987). <https://doi.org/10.1029/ja092ia13p15225>
- [3] P. Zarka, Advances in Sp. Res. **33**, 2045 (2004). <https://doi.org/10.1016/j.asr.2003.07.05>
- [4] G. Ganguli, and Y.C. Lee, Phys. Fluids, **28**, 761 (1985). <https://doi.org/10.1063/1.865096>
- [5] G. Ganguli, Y.C. Lee, and P.J. Palmadesso, Phys. Fluids, **31**, 823 (1988). <https://doi.org/10.1063/1.866818>
- [6] K.I. Nishikawa, G. Ganguli, Y.C. Lee, and P.J. Palmadesso, Phys. Fluids, **31**, 1568 (1988). <https://doi.org/10.1063/1.866696>
- [7] G. Ganguli, Bakshi P. and Palmadesso P., J. Geophys. Res. **89**, 945 (1984). <https://doi.org/10.1029/JA089iA02p00945>
- [8] R. Misra. and Tiwari M.S., Planetary and Space Sci. **54** (2), 188 (2006). <https://doi.org/10.1016/j.pss.2005.11.003>
- [9] G. Ahirwar, P. Varma and M.S.Tiwari, Annales Geophysicae, **24**(7), 1919 (2006). <https://doi.org/10.5194/angeo-24-1919-2006>
- [10] P. Kandpal, R. Kaur, and R.S. Pandey, Advances in Space research, **61**, 581 (2018). <https://doi.org/10.1016/j.asr.2017.09.033>
- [11] P. Kandpal, and R.S. Pandey, Astrophysics and Space Sciences, **363**, 227 (2018). <https://doi.org/10.1007/s10509-018-3442-7>
- [12] R.K. Tyagi, K.K. Srivastava, and R.S. Pandey, Surface Engineering and Applied Electrochemistry, **47**(4), 370 (2011). <https://doi.org/10.3103/S1068375511040144>
- [13] A.R. Niknam, E. Rastbood, and S.M. Khorashadizadeh, Phys. Plasmas, **22**, 122102 (2015). <https://doi.org/10.1063/1.4936825>
- [14] M. Barati Moqadam Niyat, S.M.Khorashadizadeh and A.R. Niknam, Physics of Plasmas, **23**, 122110 (2016). <https://doi.org/10.1063/1.4971810>
- [15] M.F. Bashir, R. Ilie, and G.Murtaza, Physics of Plasmas, **25**, 052114 (2018). <https://doi.org/10.1063/1.5025843>
- [16] M. Sharif, and A. Parvazian, Physica A, **393**, 489 (2014). <https://doi.org/10.1016/j.physa.2013.09.024>
- [17] J. Sharma, S.C. Sharma, and D. Kaur Progress In Electromagnetics Research Letters, **54**, 123 (2015). <https://doi.org/10.2528/PIERL15042703>
- [18] Y. Liu, Y.F. Wang, and T.P. Hu, Phys. Plasmas, **23**, 042103 (2016). <https://doi.org/10.1063/1.4945635>
- [19] K.-Y. Yi, Z.A. Wei, J.X. Ma, Q. Liu, and Z.Y. Li, Physics of Plasmas, **27**, 082103 (2020). <https://doi.org/10.1063/1.5144453>
- [20] I. Sereda, Ya. Hrechko, Ie. Babenko, East Eur. J. Phys. **3**, 81 (2021). <https://doi.org/10.26565/2312-4334-2021-3-12>
- [21] V.A. Lisovskiy, S.V. Dudin, P.P. Platonov, and V.D. Yegorenkov, East Eur. J. Phys. **4**, 152 (2021). <https://doi.org/10.26565/2312-4334-2021-4-20>
- [22] M. Kono, J. Vranjes, and N. Batool, Phys. Rev. Lett. **112**, 105001 (2014). <https://doi.org/10.1103/PhysRevLett.112.105001>
- [23] M.F. Bashir, N. Noreen, G. Murtaza, and P.H. Yoon, Plasma Phys. Controlled Fusion, **56**, 055009 (2014). <https://doi.org/10.1088/0741-3335/56/5/055009>
- [24] M.F. Bashir, and J. Vranjes, Phys. Rev. E, **91**, 033113 (2015). <https://doi.org/10.1103/PhysRevE.91.033113>
- [25] S.M. Khorashadizadeh, M. Barati M. Niyat, and A.R. Niknam, Phys. Plasmas, **23**, 062102 (2016). <https://doi.org/10.1063/1.4953094>
- [26] S.M. Khorashadizadeh, E. Rastbood, and A.R. Niknam, Phys. Plasmas, **22**, 072103 (2015). <https://doi.org/10.1063/1.4926521>
- [27] M.S. dos Santos, L.F. Ziebell, and R. Gaelzer, Phys. Plasmas, **22**, 122107 (2015). <https://doi.org/10.1063/1.4936972>
- [28] P. Verma, and M.S. Tiwari, Physica Scripta, **44**, 296 (1991). <https://doi.org/10.1088/0031-8949/44/3/010>
- [29] J.D. Huba, J. Geophys. Res. **86**, 3653 (1981). <https://doi.org/10.1029/JA086iA05p03653>
- [30] R.S. Pandey, Progress in Electromagnetics Research B, **11**, 39 (2009). <https://www.jpier.org/PIERB/pierb11/04.08073101>
- [31] Eliasson, P.K. Shukla, and J.O. Hall, **13**, 024502 (2006). <https://doi.org/10.1063/1.2173934>
- [32] E.N. Opp, and A.B. Hassam, Phys. of Fluids B, **3**, 885 (1991). <https://doi.org/10.1063/1.859845>
- [33] M. Fujimoto, and T. Terasawa, J. Geophys. Res. **100**, 12025 (1995). <https://doi.org/10.1029/94JA02219>
- [34] N.F. Ness, et al. Science, **233**, 4759 (1986). <https://doi.org/10.1126/science.233.4759.85>
- [35] S. Stanley, and J. Bloxham, Nature, **428**, 151 (2004). <https://doi.org/10.1038/nature02376>

ВИВЧЕННЯ ЕЛЕКТРОСТАТИЧНИХ ІОННО-ЦИКЛОТРОННИХ ХВИЛЬ У МАГНІТОСФЕРІ УРАНУ

Рама С. Пандей, Мукеш Кумар

^aФакультет прикладної фізики Інституту прикладних наук Аміті, Університет Аміті Нойда, Індія.

^bФакультет фізики, Коледж Наланда Біхаріаріф Наланда МУ Бодх Гая Біхар, Індія

У цьому рукописі використано метод характеристик деталей траєкторій частинок та дисперсійне співвідношення для іоносфери Урана для дослідження електростатичних іонно-циклотронних хвиль із паралельним зсувом швидкості потоку за наявності перпендикулярного неоднорідного постійного електричного поля та градієнта щільності. Швидкість зростання розрахована за допомогою дисперсійного співвідношення. Електричні поля, паралельні магнітному полю, передають енергію, масу та імпульс в авроральних областях магнітосфери планети, прискорюючи заряджені частинки до надзвичайно високих енергій. Вважається, що на швидкість нагрівання частинок плазми вздовж і перпендикулярно магнітному полю також впливає виникнення іонних циклотронних хвиль і паралельного електричного поля в області прискорення.

Ключові слова: електростатичні іонно-циклотронні хвилі, швидкість зсуву, градієнт щільності та неоднорідне електричне поле, магнітосфера/іоносфера Урана

EFFECT OF THE RELATIVISTIC ELECTRON BEAM ON PROPAGATING WHISTLER-MODE WAVE FOR RING DISTRIBUTION IN THE SATURN MAGNETOSPHERE[†]

 E.H. Annex^{a,#},  Rama S. Pandey^{a,*},  Mukesh Kumar^{b,§}

^aDepartment of Applied Physics, Amity Institute of Applied Science, Amity University Noida UP India

^bDepartment of Physics, Nalanda College Biharsharif Nalanda MU Bodh Gaya Bihar, India

*Corresponding Author: rspandey@amity.edu

[#]E-mail: annex.h@student.amity.edu; [§]E-mail: mukeshkumarpawapuri@gmail.com

Received February 10, 2022; accepted March 15, 2022

Cassini and many investigators reported whistler chorus near Saturn equatorial plane moving outwards. Whistler can propagate when going to high latitude and can alter its characteristics while interacting resonantly with available energetic electrons. Here investigating wave for a relativistic beam of the electron. It is observed and reported by Cassini Magnetospheric Imaging Instrument (MIMI) that inward radial injection of highly energetic particles is most dominant in Saturn intrinsic magnetosphere. Within this paradigm, an empirical energy dispersion relation for propagated whistler-mode oscillations in quasi Saturn magnetospheric plasma from such a non-monotonous ringed distribution function has been established. The kinetic approach and method of characteristics methodologies were used in the computations, which have been shown to be the best for building perturbed plasma states. The perturbed distribution function was estimated using the unperturbed particle routes. The ring distribution function was used to construct an unexpected growth rate expression for relativistic plasma in the inner magnetosphere. The results from the Saturn magnetosphere have been calculated and interpreted using a range of parameters. Temperature heterogeneity was shown to be a significant source of free energy that aided the propagation of a whistler-mode wave. By raising the peak value, the bulk injection of energetic hot electron injection impacts the growth rate. Growth was also demonstrated to be accelerated when the propagation angle increased. The research contributes to a better understanding of the relationship between wave and particle emissions and VLF emissions on a large scale.

Keywords: Magnetospheric environment of Saturn, rate of growth, wave-particle interactions, Whistler Mode Waves

PACS: 41.75Hf, 94.30Tz, 96.30Wr, 96.30Mh

Gurnett et al [1] were the first to report on the plasma spectrum detected by Voyager 1 on Saturn. Voyager found Whistler mode hissing and choral noises when it reached the equator at an inner radius of around 5 Rs (Rs is Saturn's radius). Voyager 2's plasma wave instruments detected Whistler mode pulses from Saturn's magnetosphere [2]. Gurnett et al [1] supplied the earliest Cassini and Plasma Waves Scientific Instrument information, along with Saturn's first orbit, during the 2005 approach. Some diffuse emissions (electron cyclotron frequency) were detected at frequencies lower than FC. Whistler mode wave emissions have been identified. The radial distance between these radiations ranges between 2 and 6 Rs. Whistler waves are electromagnetic waves that arise in magnetised plasma and have a lower frequency than the electron cyclotron frequency. The magnetosphere causes plasma instabilities, causing waves to move in the Whistler mode wave forks. Non-uniform electron distributions, such as beams, rings, and thermal anisotropy, produce the majority of these instabilities. Whistler's launch mode is also activated when it is created by lightning. The addition of relativistic energetic hot electrons in bulk alters the growth rate by raising its maximum value [3]. A crucial mechanism that might result in wave amplification and the precipitation of high-energy electrons as from magnetic region into the lower atmosphere is the interaction of Whistler mode wave particles. Cassini was the first spacecraft to arrive at Saturn in 2004. It has a wide radial cover of Saturn's ionosphere.

Understanding non-relativistic astrophysical shocks is a significant aspect toward Treumann's [4] general account of collisionless astrophysical shocks with high Mach numbers and their effects on dispersing flow-energy, heating matter, ramping up particles to high supposedly cosmic-ray energies, and generating distinguishable radiation varying from radio to X-rays. The waves, according to Sundkvist et al [5], are an important part of the shock structure, with the dispersive shock serving as the source of the waves by pushing the Poynting flux of the oblique whistler waves upstream in the shock normal frame commencing at the shock ramp.

Went et al. [6] presented a new analytical and numerical model of Saturn's dayside bow shock based on empirical evidence from the Pioneer 11, Voyager 1, and Voyager 2 flybys, as well as data from the first six years of the Cassini mission (2004–2010), in order to derive the average structure of the shock surface and the variance of shock sub solar distance with solar wind dynamic pressure. Wilson et al [7] started to investigate electromagnetic precursor waves, distinguished as whistler-mode waves at supercritical interplanetary shocks, which continue to spread obliquely about the local magnetic field, shock normal vector, and solar wind speed and are not phase standing structures, using the Wind search coil magnetometer.

Recently Sokolovsky [8] has been discussed the relaxation of the electron energy and momentum densities in spatially uniform states of completely ionized plasma in the presence of small constant and spatially homogeneous external electric field on based on linear kinetic equation obtained by us early from the Landau kinetic equation. Whistler-

[†] Cite as: E.H. Annex, R.S. Pandey, and M. Kumar, East. Eur. J. Phys. 1, 40 (2022), <https://doi.org/10.26565/2312-4334-2022-1-06>

© E.H. Annex, R.S. Pandey, M. Kumar, 2022

mode waves are acknowledged to have a role in electron thermodynamics/acceleration and are identified as wave trains before the shock ramp under specified conditions by Sulaiman et al [9]. Sulaiman et al.[10] provided the parameter space of MA bow shock crossings detected by the Cassini probe from 2004 to 2014. We discover that Saturn's bow shock has properties similar to both terrestrial and astrophysical regimes (MA of order 100), which are primarily determined by the intensity of the upstream magnetic field. Sulaiman et al [11] researched the process thoroughly, both theoretically and through simulations, but their conclusions are few and few between. We examine extremely high Mach number events in previously unknown parameter space, and we use in situ magnetosphere data from the Cassini mission at 10 AU to investigate reformation.

GOVERNING DISPERSION RELATION

To get the dispersion relation, uniform anisotropy in space is used, as well as collision-free plasma hit by an external magnetic field with $B_0 = B_0 \hat{z}$. Inhomogeneities in the contact region are minor. Kaur and Pandey's [12] technical and geometric principles are being pursued. As a consequence of a long derivation, Kumari and Pandey[13] wrote the Vlasov equation – the Dielectric tensor from equation (14)

$$\varepsilon_{ij}(\mathbf{k}, \omega) = 1 + \left\{ \frac{4e_s^2 \pi}{(\beta m_e)^2 \omega^2} \right\} \int \frac{d^3 \mathbf{P} \sum_{i,j}^{x,y,z} S_{ij}^*}{\left(\omega - k_{\parallel} \frac{P_{\parallel}}{\beta m_e} - n \frac{\omega_{cs}}{\beta} \right)}. \quad (1)$$

For the parallel propagation and instability of whistler mode waves with $\mathbf{k}_{\perp} = 0$, the branch of general dispersion relation (1) reduces to:

$$\varepsilon_{xx} \pm i\varepsilon_{xy} = N^2, \quad (2)$$

where $N^2 = (k^2 c^2) / \omega^2$ is refractive index. As a result, the dispersion relation for $n=1$ may be stated as follows:

$$N^2 = 1 + \frac{4e_s^2 \pi}{(\beta m_e)^2 \omega^2} \int \frac{d^3 \mathbf{P}}{2} \mathbf{P}_{\perp} [N_1 + N_2] \times \left[\frac{1}{\omega - \frac{k_{\parallel} \mathbf{P}_{\parallel}}{\beta m_e} \pm n \frac{\omega_{cs}}{\beta}} \right], \quad (3)$$

where

$$N_1 = \frac{(\beta m_e)^2}{\mathbf{P}_{\perp}} \frac{\partial f_o}{\partial \mathbf{P}_{\perp}} \left(\omega - \frac{k_{\parallel} \mathbf{P}_{\parallel}}{\beta m_e} \right) \left(\frac{\mathbf{P}_{\perp}}{\beta m_e} \right), \quad (4)$$

$$N_2 = \beta m_e k_{\parallel} \frac{\partial f_o}{\partial \mathbf{P}_{\parallel}} \left(\frac{\mathbf{P}_{\perp}}{\beta m_e} \right). \quad (5)$$

The trapped electron distribution function is considered to be a Maxwellian ring momentum distribution function.

$$f(\mathbf{P}_{\perp}, \mathbf{P}_{\parallel}) = \frac{n_e/n}{\pi^{3/2} P_{o\parallel}^2 P_{o\perp}^2 B} \exp \left[-\frac{(\mathbf{P}_{\perp} - \mathbf{P}_o)^2}{P_{o\perp}^2} - \frac{(\mathbf{P}_{\parallel})^2}{P_{o\parallel}^2} \right], \quad (6)$$

$$B = \exp(-P_o^2/P_{o\perp}^2) + \sqrt{\pi} \left(\frac{P_o}{P_{o\perp}} \right) \operatorname{erfc}(-P_o/P_{o\parallel}), \quad (7)$$

where,

$$P_{o\parallel} = \left(\frac{2k_b T_{\parallel}}{\beta m_e} \right)^{1/2} \quad \text{and} \quad P_{o\perp} = \left(\frac{2k_b T_{\perp}}{\beta m_e} \right)^{1/2},$$

are the associated parallel and perpendicular electron thermal velocities.

Substituting $d^3 \mathbf{P} = 2\pi \int_0^{\infty} \mathbf{P}_{\perp} d\mathbf{P}_{\perp} \int_{-\infty}^{\infty} d\mathbf{P}_{\parallel}$ Then by plugging expression (6) into equation (3) and solving the integrations, we get the dispersion relation as follows:

$$\frac{k^2 c^2}{\omega^2} = 1 + \frac{4\pi e_s^2}{(\beta m_e)^2 \omega^2} \frac{(n_e/n)}{B} \left[X_1 \frac{\beta m_e \omega}{k_{\parallel} P_{o\parallel}} Z(\xi) + X_2 (1 + \xi Z(\xi)) \right], \quad (8)$$

where $X_1 = 1 + \frac{P_o^2}{P_{o\perp}^2} - \frac{P_o}{P_{o\perp}} \sqrt{\pi}$

$$X_2 = \left[X_1 + \frac{P_{o\perp}^2}{P_{o\parallel}^2} \left(1 - \sqrt{\pi} \frac{P_o^3}{P_{o\perp}^3} \operatorname{erf} \left(\frac{P'_\perp}{P_{o\perp}} \right) + 3 \frac{P_o^2}{P_{o\perp}^2} - \frac{3}{2} \sqrt{\pi} \frac{P_o}{P_{o\perp}} \right) \right],$$

where

$$Z(\xi) = \frac{1}{\sqrt{\pi}} \int_{-\infty}^{\infty} \frac{e^{-t^2}}{t - \xi} dt, \text{ is the plasma dispersion function with } \xi = \frac{\beta m_e}{k_{\parallel} P_{o\parallel}} \left(\omega \mp \frac{\omega_c}{\beta} \right).$$

Applying condition $\frac{k^2 c^2}{\omega^2} \gg 1$ for whistler waves

$$\omega_{ps}^2 = \frac{4e^2 \pi n_e / n}{B_o m_e}.$$

The equation (8) reduces to

$$D(k, \omega) = \frac{-k^2 c^2}{\omega_{ps}^2} + \frac{1}{\beta} \left[\frac{X_1 \omega}{k_{\parallel} P_{o\parallel}} (\beta m_e) \left\{ -\frac{1}{\xi} - \frac{1}{2\xi^3} \right\} - \left\{ X_2 \frac{1}{2\xi^2} \right\} + \left[\frac{(\beta m_e) \omega}{k_{\parallel} P_{o\parallel}} X_1 + X_2 \xi \right] \left\{ i\sqrt{\pi} \exp(-\xi^2) \right\} \right]. \quad (9)$$

Introducing the dimensionless parameters as $\tilde{k} = \frac{k_{\parallel} P_{o\parallel}}{\omega_{cs}}$,

$$\text{where } K_2 = \frac{1}{2X_1} \text{ and } \beta_1 = \frac{4\pi\mu_o \epsilon_o k_b T_{\parallel} (n_e/n)}{m_e^2 B_o^2}.$$

Growth rate expression for oblique propagation

When Whistler mode wave propagate oblique to magnetic field direction, the expression of dimensionless growth rate and dimensionless real frequency becomes:

$$\frac{\gamma}{\omega_c} = \frac{\frac{\sqrt{\pi}}{\beta \tilde{k} \cos \theta} \left(\frac{X_2}{X_1} - \frac{\beta X_3}{1 - \beta X_3} \right) (1 - \beta X_3)^3 \exp \left[-\left(\frac{1 - \beta X_3}{\tilde{k} \cos \theta} \right)^2 \right]}{1 + \beta X_4 + \frac{(\tilde{k} \cos \theta)^2}{2(1 - \beta X_3)^2} - \frac{(\tilde{k} \cos \theta)^2}{(1 - \beta X_3)} \left(\frac{X_2}{X_1} - \frac{\beta X_3}{1 - \beta X_3} \right)}, \quad (10)$$

$$X_3 = -\frac{\omega_r}{\omega_c} = \frac{(\tilde{k} \cos \theta)^2}{\beta_1} \left[K_2 + \frac{X_2}{X_1} \frac{\beta_1}{2\beta} \right]. \quad (11)$$

Expression for growth rate for parallel propagation

When Whistler mode wave propagate parallel to magnetic field direction, the expression of dimensionless growth rate and dimensionless real frequency becomes:

$$\frac{\gamma}{\omega_c} = \frac{\frac{\sqrt{\pi}}{\beta \tilde{k}} \left(\frac{X_2}{X_1} - \frac{\beta X_3}{1 - \beta X_3} \right) (1 - \beta X_3)^3 \exp \left[-\left(\frac{1 - \beta X_3}{\tilde{k}} \right)^2 \right]}{1 + \beta X_4 + \frac{(\tilde{k})^2}{2(1 - \beta X_3)^2} - \frac{(\tilde{k})^2}{(1 - \beta X_3)} \left(\frac{X_2}{X_1} - \frac{\beta X_3}{1 - \beta X_3} \right)}, \quad (12)$$

$$X_3 = -\frac{\omega_r}{\omega_c} = \frac{(\tilde{k})^2}{\beta_1} \left[K_2 + \frac{X_2}{X_1} \frac{\beta_1}{2\beta} \right]. \quad (13)$$

Plasma Parameters

The estimation of the growth rate of Whistler mode waves at radial distances was validated using characteristics from Voyager 1 and Cassini data [12,13] at $R \sim 5R_s$ within the Saturn plasma sheet. For a radial distance of $5R_s$, the magnetic field strength is 184 nT and the number density is $5 \times 10^7 \text{ m}^{-3}$. Energy density $K_B T_{\parallel}$ According to observation, the energy density at $R \sim 5R_s$ is 300 eV.

RESULT AND DISCUSSION

In Fig. 1 the maximum growth rate shows for $A_T = 0.75$, and reaches up to 4, other profiles of $A_T = 0.5$ and $A_T = 0.25$ shows same pattern of growth rate but significantly low maxima 3.6 and 3.25 for $A_T = 0.5$ and $A_T = 0.25$ respectively.

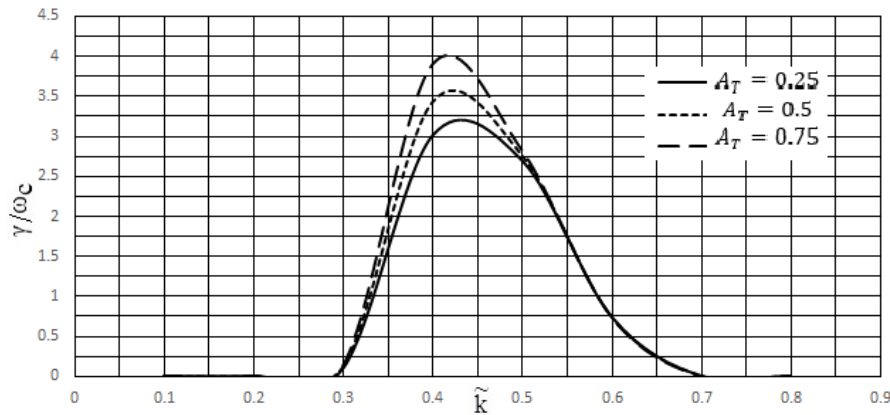


Figure 1. Variation in the pace of growth and actual frequencies in relationship to \tilde{k} for various values of A_T for $\theta = 10^\circ$ at, $n_o = 5 \times 10^5 \text{ m}^{-3}$, $n_c/n_w = 1/10$, $P_0 = 0.2$, and as well as other fixed plasma characteristics

The increasing growth rate is of same pattern with substantial increment in the growth rate. But the decreasing pattern it follows same path below 2.75 and ends in \tilde{k} value of 0.7. The variation in growth rate with regard to wave number for various values of temperature anisotropy has recently been shown. According to the dispersion relation, when temperature anisotropy grows, the growth rate increases in both sense, frequency, and magnitude due to the presence of a hot ring's electron and a cool electron around it. Maniitti et al.[14] found an increase in whistler owing to an increase in temperature ratio. In Fig. 2 the maximum growth rate for $\theta = 30$, reaches up to 4.25 for a \tilde{k} value of 0.4, other profiles of $\theta = 20$ and $\theta = 10$ shows same pattern of growth rate but significantly low maxima 4 and 3.25 respectively.

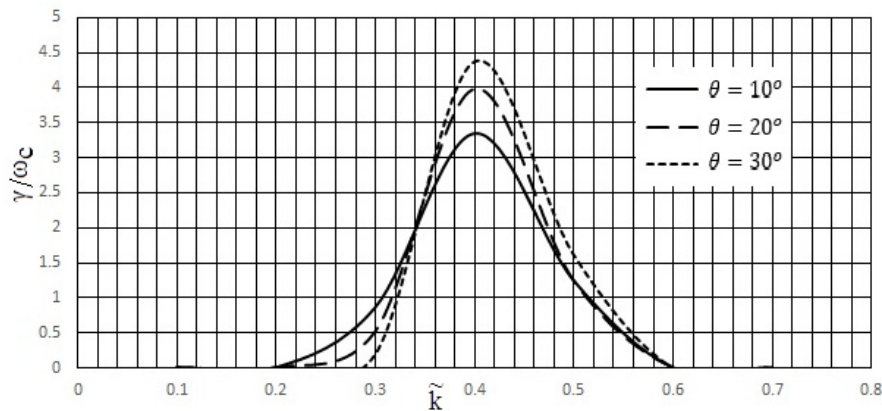


Figure 2. Variation in the pace of growth and actual frequencies in relationship to \tilde{k} for various values of θ for at $K_B T_{||} = 2 \text{ KeV}$, $T_{||}/T_{\perp} = 1.5$, $n_o = 5 \times 10^5 \text{ m}^{-3}$, $n_c/n_w = 1/10$, $P_0 = 0.2$, as well as other fixed plasma characteristics.

The growing growth rate follows the same trend, with a significant increase in the growth rate. The variation in growth rate with regard to wavenumber has been demonstrated for various propagation angle values. It has been revealed that increasing the propagation angle value increases the growth rate. Fig. 3: With a \tilde{k} value of 0.8, the maximum growth rate for $\beta = 0.5$ is achieved.

And the maximum growth rate for $\beta = 0.6$, reaches maximum at a \tilde{k} value of 0.84 Similarly, the maximum growth rate for $\beta = 0.7$, reaches maximum at a \tilde{k} value of 0.72. $\beta = 0.5$ curve shows a phenomenal growth rate than the $\beta = 0.6$ and $\beta = 0.7$. as compared to the $\beta = 0.5$ other curves are shallow. In terms of wavenumber, raising the value of relativistic factor leads in a decreasing growth rate, i.e., the greatest peak occurs for the lowest value. Similarly, at higher velocity of highly energetic particles, smaller is measured, signifying more expansion of whistlers. Thus, while this cannot be referred to as the key component responsible for whistler expansion in particle ring distributions, it can be substantial in other types of distributions such as Maxwellian [15]. In Fig. 4 the maximum growth rate for $n_c/n_w = 1/10$, reaches maximum at a \tilde{k} value of 0.5 And the maximum growth rate for $n_c/n_w = 1/20$, reaches maximum at a \tilde{k} value of 0.4 Similarly, the maximum growth rate $n_c/n_w = 1/30$, reaches maximum at a \tilde{k} value of 0.4. The growing growth rate follows the same trend, with a significant increase in the growth rate. the variation in growth rate caused by relativistic warm electrons, i.e., n_c/n_w . The graphic clearly shows that the growing ratio of number density causes an increase in growth rate.

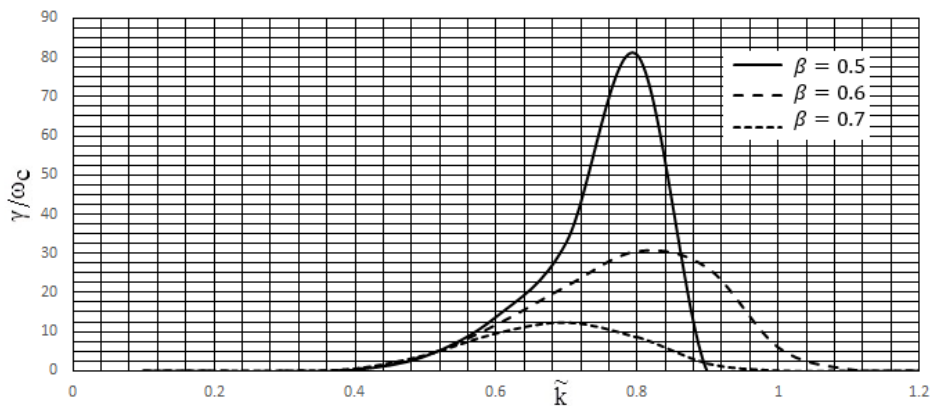


Figure 3. Variation in the pace of growth and actual frequencies in relationship to \tilde{k} for various values of β for $\theta = 10^\circ$ at $K_B T_{\parallel} = 2\text{KeV}$, $T_{\parallel}/T_{\perp} = 1.5$, $n_o = 5 \times 10^5 \text{m}^{-3}$, $n_c/n_w = 1/10$, $P_0 = 0.2$, as well as other fixed plasma characteristics.

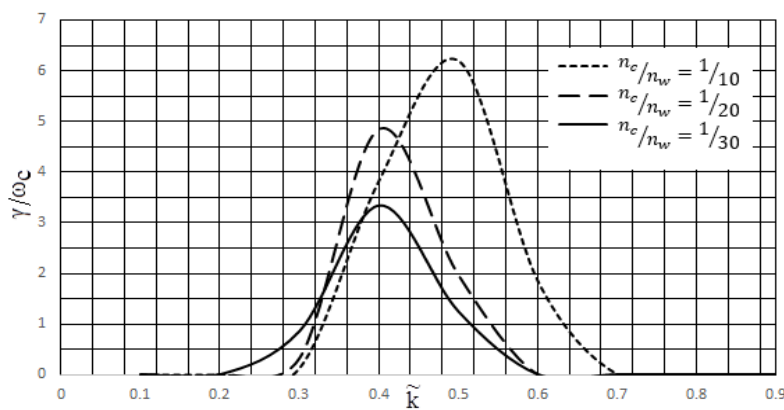


Figure 4. Variation in the pace of growth and actual frequencies in relationship to \tilde{k} for various values of n_c/n_w for $\theta = 10^\circ$ at, $n_o = 5 \times 10^5 \text{m}^{-3}$, $n_c/n_w = 1/10$, $P_0 = 0.2$, as well as other fixed plasma characteristics.

Fig. 5: The maximum growth rate for $n_c/n_w = 1/10$, reaches maximum at a \tilde{k} value of 0.4. And the maximum growth rate for $n_c/n_w = 1/20$, reaches maximum at a \tilde{k} value of 0.4. Similarly, the maximum growth rate $n_c/n_w = 1/30$, reaches maximum at a \tilde{k} value of 0.4.

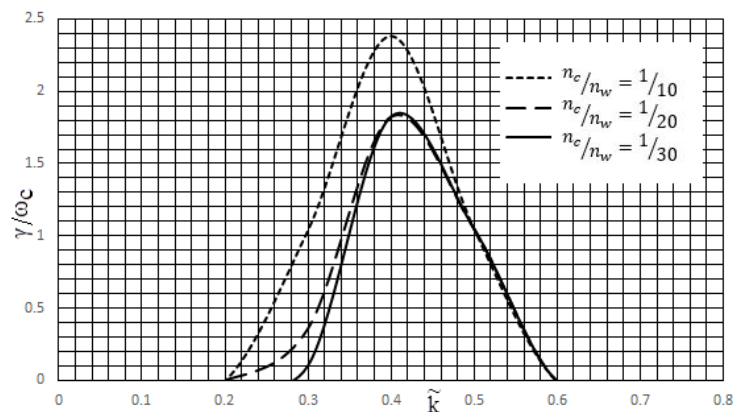


Figure 5. Variation in the pace of growth and actual frequencies in relationship to \tilde{k} for various values of n_c/n_w for parallel beam at, $P_0 = 0.2$, $K_B T_{\parallel} = 2\text{keV}$, $A_T = 0.75$, $\beta = 0.7$ as well as other fixed plasma characteristics.

Growth rate builds up for a \tilde{k} value of 0.2 and 0.3 where $n_c/n_w = 1/20$ and $1/30$ respectively. Both the curves reach a maximum at a \tilde{k} value of 0.4 and decay to a \tilde{k} value of 0.6. Fig. 6: The maximum growth rate shows for $A_T = 0.75$, reaches a maximum at a \tilde{k} value of 0.4, other profiles of $A_T = 0.5$ and $A_T = 0.25$ show the same pattern of growth rate. At $A_T = 0.5$ and $A_T = 0.25$ the \tilde{k} value reaches a maximum of 0.4. All the three curves decay to the same point at a \tilde{k} value of 0.6. The growth curves are of similar nature but the $A_T = 0.75$ growth is higher than all other two values. In the incremental phase the growth pattern is different but the decremental phase falls in the same pattern. Fig. 7: The highest growth rate for $\beta = 0.5$ occurs with \tilde{k} value of 0.72. And the greatest growth rate for $\beta = 0.6$ occurs with \tilde{k} value of 0.62.

Similarly, the maximum growth rate for $\beta = 0.7$ is reached at $\tilde{k} = 0.58$. The three curves begin at the same place with \tilde{k} value of 0.32 and decline at various \tilde{k} values.

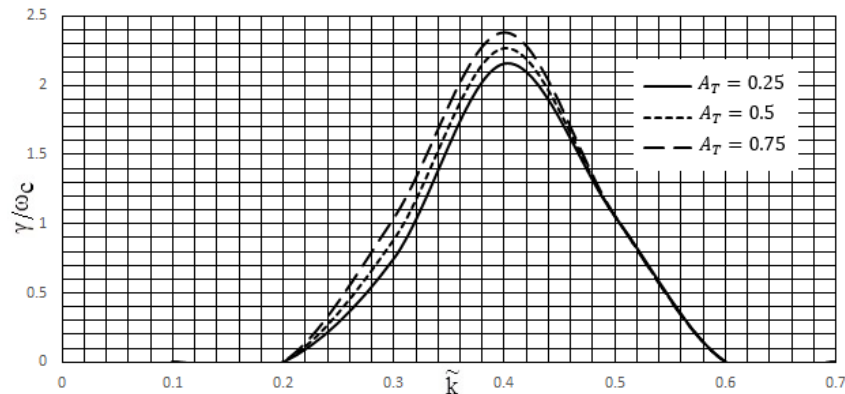


Figure 6. Variation in the pace of growth and actual frequencies in relationship to \tilde{k} for various values of A_T for *parallel beam* at, $P_{\perp 0} = 0.2$, $K_B T_{\parallel} = 2\text{keV}$, $\beta = 0.7$ as well as other fixed plasma characteristics.

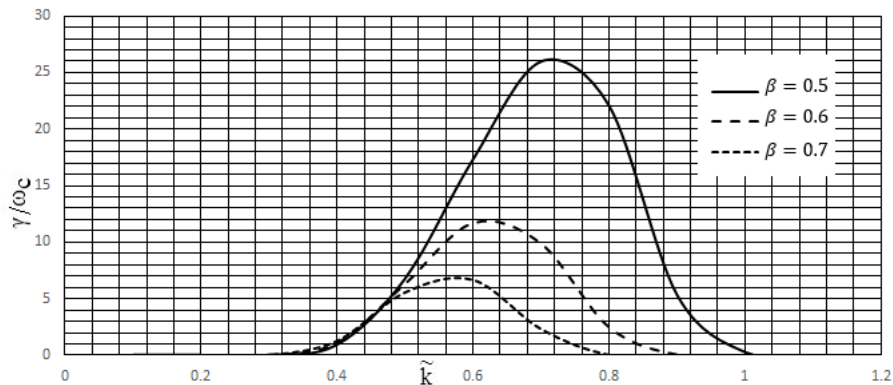


Figure 7. Variation in the pace of growth and actual frequencies in relationship to \tilde{k} for various values of β for *parallel beam* at, $P_{\perp 0} = 0.2$, $K_B T_{\parallel} = 2\text{keV}$, $A_T = 0.75$ as well as other fixed plasma characteristics.

CONCLUSION

The influence of temperature anisotropy and relativistic beam characteristics on the evolution of whistler-mode waveforms in the Saturnian magnetosphere is explored, and these qualities are shown to be favourable. The rate of growth slows as the value of temperature anisotropy rises, but it accelerates when the AC frequency rises. As the propagation angle rises, so does the bandwidth of oblique propagation. By assuming that electrons are the major high energy particles influenced by electromagnetic activity in the magnetospheres of other planets, the preceding results help us comprehend the character of this unpredictable whistler-mode wave scenarios [16].

ORCID IDs

 **E.H. Annex**, <https://orcid.org/0000-0002-5193-6795>;  **Rama S. Pandey**, <https://orcid.org/0000-0003-4907-1080>;
 **Mukesh Kumar**, <https://orcid.org/0000-0001-6106-4794>

REFERENCES

- [1] D.A. Gurnett, W.S. Kurth, and F.L. Scarf, *Science*, **212**, 235 (1981), <https://doi.org/10.1126/science.212.4491.235>
- [2] F.L. Scarf, D.A. Gurnett, W.S. Kurth, and R.L. Poynter, **215**, 587 (1982), <https://doi.org/10.1126/science.215.4532.587>
- [3] S. Kumar, S.K. Singh, and A.K. Gwal, *Pramana J. Phys.* **68**(4), 611 (2007), <https://doi.org/10.1007/s12043-007-0063-z>
- [4] R.A. Treumann, *Astron. Astrophys. Rev.* **17**, 409 (2009), <https://doi.org/10.1007/s00159-009-0024-2>
- [5] D. Sundkvist, V. Krasnoselskikh, S.D. Bale, S.J. Schwartz, J. Soucek, and F. Mozer, *Phys. Rev. Lett.* **108**, 2 (2012), <https://doi.org/10.1103/PhysRevLett.108.025002>
- [6] D.R. Went, G.B. Hospodarsky, A. Masters, K.C. Hansen, and M.K. Dougherty, *J. Geophys. Res.* **116**, A07202, (2011), <https://doi.org/10.1029/2010JA016349>
- [7] L.B. Wilson, A. Koval, A. Szabo, A. Breneman, C.A. Cattell, K. Goetz, P.J. Kellogg, K. Kersten, J.C. Kasper, B.A. Maruca, and M. Pulupa, *Geophys. Res. Lett.* **39**, L08109 (2012), <https://doi.org/10.1029/2012GL051581>
- [8] A.I. Sokolovsky, S.A. Sokolovsky, and O.A. Hrinishyn, *East European Journal of Physics*, **3**, 19, (2020), <https://doi.org/10.26565/2312-4334-2020-3-03>
- [9] A.H. Sulaiman, D.A. Gurnett, J.S. Halekas, J.N. Yates, W.S. Kurth, and M.K. Dougherty, **122**(1), 227 (2017) <https://doi.org/10.1002/2016JA023501>

- [10] A.H. Sulaiman, et al. J. Geophys. Res. **121**, 4425 (2016), <https://doi.org/10.1002/2016JA022449>
- [11] A.H. Sulaiman, et al. Phys. Rev. Lett. **115**, 12 (2015), <https://doi.org/10.1103/PhysRevLett.115.125001>
- [12] R. Kaur, and R. S. Pandey, Adv. Space Res. **59**, 2434 (2017), <https://doi.org/10.1016/j.asr.2017.02.015>
- [13] J. Kumari, and R.S. Pandey, J. Astrophys. Astr. **40**, 14 (2019), <https://doi.org/10.1007/s12036-019-9576-3>
- [14] J.D. Menietti, O. Santolík, and M.K. Dougherty, J. Geophys. Res. **113**, A12206 (2008), <https://doi.org/10.1029/2008JA013237>
- [15] Y. Omura, and D.J. Summers, Geophys. Res. **111**, A09222 (2006), <https://doi.org/10.1029/2006JA011600>
- [16] C.S. Wu, P.H. Yoon, and H.P. Freund, Geophys. Res. Lett. **16**(12), 1461 (1989), <https://doi.org/10.1029/GL016i012p01461>

ВПЛИВ РЕЛЯТИВІСТСЬКОГО ЕЛЕКТРОННОГО ПРОМЕНЯ НА ПОШИРЕННЯ ХВИЛЬ З ВІСТЛЕРНИМИ МОДАМИ ДЛЯ КІЛЬЦЕВОГО РОЗПОДІЛУ В МАГНІТОСФЕРІ САТУРНА

Є.Х. Аннекс, Рама С. Пандей, Мукеш Кумар

^aФакультет прикладної фізики, Інститут прикладних наук Аміті, Університет Аміті, Нойда UP, Індія

^bФакультет фізики, Наланда Коледж, Біхариаріф Наланда, Бодх Гайя Біхар, Індія

Кассіні та багато дослідників повідомили, що whistler хор поблизу екваторіальної площини Сатурна рухається за його межі. Він може поширюватися, коли піднімається у високі широти, і може змінювати свої характеристики, резонансно взаємодіючи з доступними енергійними електронами. У статті досліджується хвиля для релятивістського електронного променя. За допомогою Cassini Magnetosphere Imaging Instrument (MIMI) спостерігається та повідомляється, що радіальна інжекція високоенергетичних частинок всередину є найбільш домінуючим у внутрішній магнітосфері Сатурна. В рамках цієї парадигми було встановлено емпіричне співвідношення дисперсії енергії для поширюваних коливань вістлерної моди в квазісатурновій магнітосферній плазмі від такої немонотонної кільцевої функції розподілу. У розрахунках використано кінетичний підхід та методику характеристик, які виявилися найкращими для побудови збурених станів плазми. Збурену функцію розподілу оцінили з використанням маршрутів незбурених частинок. Кільцева функція розподілу була використана для побудови виразу неочікуваної швидкості зростання релятивістської плазми у внутрішній магнітосфері. Результати для магнітосфери Сатурна були розраховані та інтерпретовані з використанням ряду параметрів. Було показано, що температурна неоднорідність є значним джерелом вільної енергії, яка сприяє поширенню хвилі вістлерної моди. Підвищуючи пікове значення, об'ємна інжекція енергетичних гарячих електронів впливає на швидкість росту. Було також продемонстровано, що зростання прискорюється при збільшенні кута поширення. Дослідження сприяє кращому розумінню зв'язку між випромінюваннями хвиль і частинок і VLF-випромінюванням у великому масштабі.

Ключові слова: магнітосферне середовище Сатурна, швидкість росту, взаємодія хвиля-частинка, хвилі моди Вістлера

STUDY OF STRUCTURAL, ELASTIC, THERMAL AND TRANSPORT PROPERTIES OF TERNARY X(X=Co, Rh and Ir)MnAs OBTAINED BY DFT[†]

Salim Kadri^a, Tourab Mohamed^b, Berkani Mahièddine^c,  Amraoui Rabie^d, Bordjiba Zeyneb^d

^aDynamic Motors and Vibroacoustic Laboratory, M'Hamed Bougara University of Boumerdes

^bFaculty of Technology, M'Hamed Bougara University, Cité Frantz Fanon, Boumerdes 35000-Algeria

^cLSELM Laboratory, Badji Mokhtar Annaba University, Annaba 23000, Algeria

^dMaterial Physics Laboratory - L2PM, 8 May 1945 University of Guelma, Algeria

*Corresponding Author: amraoui.rabie@yahoo.com

Received January 14, 2022; revised February 23, 2022; accepted March 16, 2022

The Density Functional Theory (DFT) with an approximation of generalised gradient is used for the study of elastic, thermodynamic and transport properties and for that of structural stability of ternary Half-Heuslers compounds X(X=Co, Rh and Ir)MnAs. This first predictive study of this compounds determines the mechanical properties such that the compression, shearing, Young modulla and Poisson coefficient without omitting the checking parameters of the nature of these compounds such that hardness, Zener anisotropic facto rand Cauchy pressure. The Pugh ratio and Poisson coefficient have allowed the identification of ductile nature of these compounds. The speed of sound and Debye temperature of these compounds has also been estimated from the elastic constants. The thermodynamic properties have been calculated as well for a pressure interval from zero to 25 GPa. The effect of chemical potential variation on Seebeck coefficient, electric, thermal and electronic conductivities, the power and merit factors have also been studied for different temperatures (300, 600, 900°K), so that these alloys can be better potential candidates for thermoelectric applications.

Keywords: Half-Heusler, DFT, elastic, thermoelectric, transport properties

PACS: 71.15.Mb; 71.20.-b; 71.55.Ak; 72.20.Pa

The big challenge of material science specialists is to be able to produce new semi conductor materials with the best properties allowing them to be used in diverse applications. The ternary material of half-Heusler type is compound family showing several qualities such that elastic stability, high melting temperature high thermoelectric power factor and other stable thermal properties.

These material qualities make of these materials the best candidates to be used in several system manufacturing such as the Micro Electro Mechanical Systems (MEMS), dedectors and sensors of high accuracy. These compounds known through their best thermoelectric properties are chemically presented by XYZ where X, Y corresponding to transition elements and Z to group elements III, IV or V [1].

Since their discovery by R.A Groot et al [2] the thermoelectrical HH compounds are known through their merit factor which indicates their ability to convert the lost heat to electricity. The ZT indicator is also a performance characteristic of this type of materials. The present challenge for the scientists is to look for the best Peltier and Seebeck effect efficiency. We seek to minimize the important volumes of exploitable natural resources in energy conversion to get a cost-effective utilization corresponding to the best power factors.

Many theoretical [3,4,5] and experimental [6,7] studies on the transport properties of HH compounds have been recently published. Among these works Ma et al [8] who by using DFT calculation they were be able to predict the structural, magnetic and electronic properties of of CoVX (X = Ge et Si) compounds. In their remarkable work, Ahmed et al [9], an artificial neural network model has been developed to predict the network constants of 137 HH compounds.

This work is considered as the most reliable reference for the network constants of several HH compounds. Moreover the work of Chibani et al [10], whose process has been as guide for the present work have used a DFT calculation to determine the structural, electronic and transport properties of HH CoVX (X=Ge and Si) compounds whose elastic stability has been verified.

The aim of the present work is by using ab initio calculation, to study the structural, elastic and thermoelectric properties of X(X=Co, Rh and Ir) MnAs materials. First, a verification of both structural state and elastic stabilities of the compounds is done. Then, using the power of Gibbs and Boltztrap calculation codes the Debye and Boltzman quasi harmonic equations are solved. The solutions of these equations determine and illustrate some thermodynamic transport parameters such as Seebeck coefficient, electric, thermal and electronic conductivities, the power and merit factor.

Some results of the study such as elastic, thermal and transport properties of X(X=Co, Rh and Ir)MnAs half-Heusler compounds will be used for the analysis by finite elements of the MEMS driver behavior.

COMPUTATIONAL METHOD

In this work the WIEN2K [11] package has been used for the calculation in theoretical DFT domain [12]. This package has been used to calculate the electronic structure of (X=Co, Rh and Ir)MnAs compounds, in cubic phase using Augmented Planes Waves method (FP-LAPW) exploiting generalized gradient approximation (GGA-WC) for exchange

[†] Cite as: S. Kadri, T. Mohamed, B. Mahièddine, A. Rabie, and B. Zeyneb, East. Eur. J. Phys. 1, 47 (2022), <https://doi.org/10.26565/2312-4334-2022-1-07>
© S. Kadri, T. Mohamed, B. Mahièddine, A. Rabie, B. Zeyneb, 2022

energy and correlation. The number of particular k points used the irreducible Integration in Brillouin zone is 3000. The value of density plane cut-off is RKmax equal to 8 for energy eigen values and eigen vectors of these points.

Generally the half-Heusler X(X=Co, Rh and Ir)MnAs crystallize in $C1_b$ structure in cubic phase Fig.1 in a way that the atoms X(X=Co, Rh and Ir) occupy 4a (0.25, 0.25, 0.25) sites. The Mn atom occupies 4b (0.5, 0.5, 0.5) site and, As atom occupies the site 4c (0, 0, 0) in Wyckoff coordinates [13].

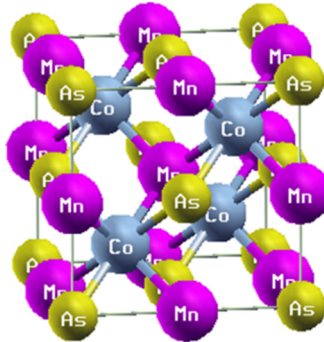


Figure 1. Half Heusler compound Structure.

RESULTS AND DISCUSSION

Structural stability

The study of materials structural properties of X(X=Co, Rh and Ir)MnAs is to determine at static equilibrium, the material structure parameters such as the mesh parameters a_0 , the compression modulus B and its derivative B' . By using the total quantities of energies as function of volume at the equilibrium. The present study is for predicting the more stable phase of the compounds using the state equation of Murnaghan [13].

$$E(V) = E_0 + \frac{B}{B'(B' - 1)} \left[v \left(\frac{V_0}{V} \right)^{B'} - V_0 \right] + \frac{B}{B'} (V - V_0)$$

Where E_0 , B and V_0 are respectively: total energy, compression modulus and the volume at the equilibrium.

An auto coherent calculation has been carried out to determine the total energy of X(X=Co, Rh and Ir)MnAs ternary compounds in two phases: non magnetic named MN, and ferromagnetic named FM of space group (216_F43m). The total energy evolution as function of volume mesh in phase MN and FM is depicted on the same curve (Figure 2) in order to provide evidence of the lowest energy.

The Figure 2 shows that the most stable structure among the three studied materials are that of ferromagnetic of cubic structure of X(X=Co, Rh and Ir)MnAs materials and that of 216_F43m space group. The Table 1 shows the parameter values of a_0 mesh, compression modulus B and its derivative B' of the same X(X=Co, Rh and Ir)MnAs compounds in the most stable ferromagnetic phase.

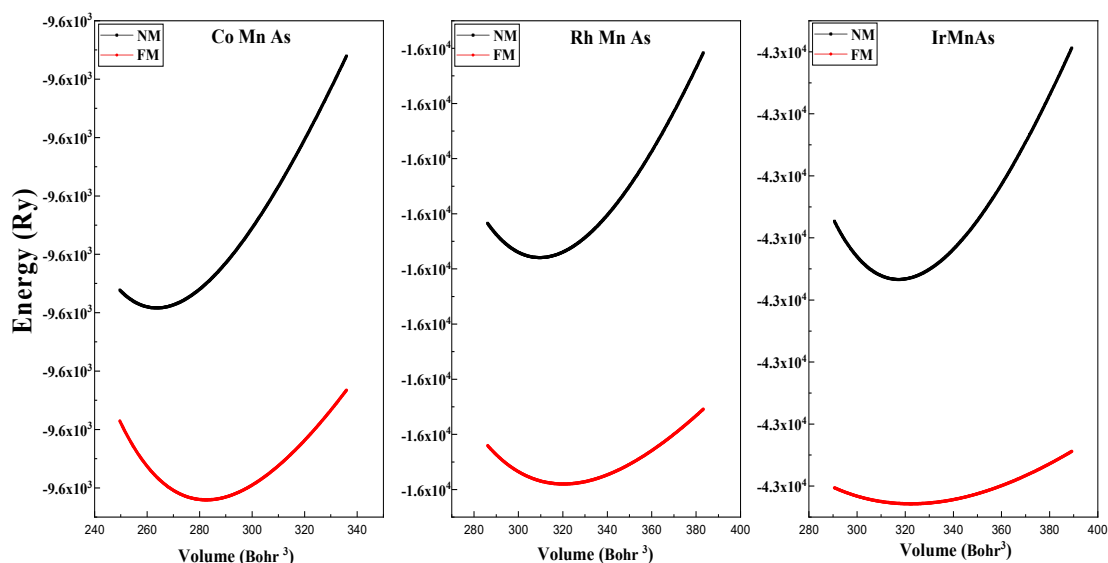


Figure 2. Optimisation of total energy of X(X=Co, Rh et Ir)MnAs compounds for all structure types

Table 1. Fundamental state properties of X(X=Co, Rh et Ir)MnAs half-Heuslers

	Constante de réseau $a_0(\text{Å})$			Module de compression B (GPa)		La dérivée de B' (GPa)	
	Notre travail	Exp	Autre calcul	Notre travail	Autre calcul	Notre travail	Autre calcul
CoMnAs	5.468	-	5.53 ^[9]	164.279	-	5.470	-
RhMnAs	5.768	-	5.83 ^[9]	162.842	-	6.456	-
IrMnAs	5.810	-	-	179.849	-	5.239	-

Elastic Properties

The study aim of the mechanical behaviour of materials is to determine their response to a given Stress. In physics, elasticity is the capacity of a material to regain its initial geometry after suppression of applied forces. The elastic constraints C_{ij} have been calculated by Thomas Charpin method [14] incorporated in Wien2k code.

Because of the lack of data in the literature, all X(X=Co, Rh and Ir)MnAs alloys C_{ij} are calculated and put in Table 2. The calculated elastic constants $C_{44} > 0$, $C_{11} - C_{12} > 0$ and $C_{11} + 2 C_{12} > 0$, with C_{12} less than C_{11} , respect the criteria of Born-Huang relative to mechanical stability [15]. These constants respect the cubic stability condition too i.e. $C_{12} < B < C_{11}$. This is confirming that the alloys are elastically stable.

Table 2. Calculated values of elastic constants for X(X=Co, Rh and Ir)MnAs compounds.

Elasticity coefficients	CoMnAs	RhMnAs	IrMnAs
$C_{11}(\text{GPa})$	164.4	262.2	195.6
$C_{12}(\text{GPa})$	126.4	76.2	122.2
$C_{44}(\text{GPa})$	72.3	71.6	74.5

To describe the mechanical behaviour of these materials on the basis of C_{ij} constants the elastic amounts such as shearing modulus G , the Young modulus E and the Poisson ν ratio are evaluated using Voigt-Reuss-Hill approximation [16] at the equilibrium for a pressure $P = 0$.

In the following the indices R and V of the shearing modula are relative respectively to Voigt and Reuss approximation. For the cubic systems these elastic quantities are calculated using the following expressions:

$$B = \frac{C_{11} + 2C_{12}}{3}$$

$$G = \frac{G_V + G_R}{2}$$

$$G_V = \frac{(C_{11} - C_{12} + 3C_{44})}{5}$$

$$G_R = \frac{5C_{44}(C_{11} - C_{12})}{4C_{44} + 3(C_{11} - C_{12})}$$

$$E = \frac{9BG}{(3B + G)}$$

$$\nu = \frac{3B - E}{6B}$$

The obtained results of this work compounds are given in Table 3. It should be noticed that the theoretical values are not available in the literature. The compressibility modulus B gives information on the hardness of the material; the more B is large the more the material is hard.

Table 3. Compression Modulus (B) GPa, Shearing modulus (G) GPa, Young modulus(E) GPa, Poisson Coefficient (ν), the ratio B/G , The micro hardness (H), the l'anisotropy A , Cauchy CP coefficients The volumetric mass ρ in Kg/m^3 , Fusion Temperatures (T_m) in $^\circ\text{K}$.

Materials	B	G	E	ν	B/G	H	A	CP	ρ	$T_m \pm 300$
CoMnAs	139.06	42.52	115.76	0.36	3.27	3.33	3.8	54.1	5561.31	1300.15
RhMnAs	138.2	63.08	164.25	0.30	2.19	6.94	0.77	4.6	6041.4	1003.41
IrMnAs	146.67	56.07	149.19	0.33	2.61	5.14	2.03	2.03	8179.7	1275.32

The compressibility modulus values determined for these half- Heusler are large ($B > 30$ GPa); This implies these alloys have weak compressibility [17], consequently, these alloys can be classified as relatively hard and able to resist to volume and shape changes in ambient conditions.

It should be noticed that the shearing modulus of considered alloys is much weaker than that of compressibility one. This points out that these alloys are susceptible rather to resist to volume compression than to shape variation.

Knowing that Pugh (B/G) ratio [17] permits the distinction of the ductility when ($B/G \geq 1.75$) and fragility in the opposite case. The values of (B/G) on Table 3 shows well the ductility of the studied materials. The Poisson coefficient can also be used as indicator of the ductility, fragility of an alloy.

In general, it is equal or greater than 1/3 for ductile materials and smaller than this value for fragile materials. In this study the Poisson coefficient of half-Heusler compounds is greater than 1/3. This confirms these compounds ductility as it was determined previously.

The Young modulus E characterises a given material rigidity. When its Young modulus increases, this material becomes rigid. The calculated values of E for considered materials are less elevated. This points out that their rigidity is more or less elevated.

In this work the hardness of these alloys is calculated as well. This mechanical property gives information on the elasticity, the plasticity and the rupture of these alloys. In the literature many methods are used for hardness calculations. In the present work the Vickers micro- hardness model has been adopted. The Vickers hardness is determined by the following Tian et al equation [18]:

$$H_v = 0.92 \cdot \left(\frac{G}{B}\right)^{1.137} \cdot G^{0.703}$$

From Table 3 it can be shown that the alloys present a weak hardness. So they cannot withstand large loads. These materials cannot be recommended for electronic and mechanical small spares manufacturing.

On the other hand, the elastic constant knowledge has permitted the deduction of other mechanical characteristics such as the anisotropy A , the coefficient of Cauchy CP and the fusion temperature.

To know if a material is isotropic or anisotropic the value of Zener anisotropy factor should first be known. This factor measures the solid anisotropy degree. The material is perfectly isotropic if $A = 1$ and anisotropic if $A \neq 1$ This Zener factor is determined by the following equation [19]:

$$A = \frac{2C_{44}}{(C_{11} - C_{12})}$$

The three studied compounds have anisotropic factors (A different of 1), therefore, they are anisotropic. If the Zener coefficient, $A > 1$ then it is maximal rigidity case along the diagonal of the cube $\langle 111 \rangle$. It's the case of CoMnAs and IrMnAs compounds.

In opposite way if $A < 1$ the isotropy is maximal along the axis of the cube $\langle 100 \rangle$ it is the case of RhMnAs compounds. To see whether the character of the atomic bound is fragile or ductile among the metals and the compounds, the pressure of Cauchy CP [20] should determined as:

$$CP = C_{12} - C_{44}$$

For the present work alloys the pressure value of Cauchy is positive. This means that the metallic characters of these compounds are of ductile nature. Moreover, the alloy fusion temperature can be determined from the elastic constants using the following equation [21]:

$$T_m(^{\circ}K) = [553 + (5.911)C_{12}] \pm 300$$

Debye temperature (θ_D) offers many information on the solid material undergoing temperature effect during its exploitation. (θ_D) is also related to the upper limit of photon frequencies. It is calculated as function of elastic constants according to the following equation:

$$\theta_D = \frac{h}{k_B} \left[\frac{3}{4\pi} \left(\frac{N_A \rho}{M} \right) \right]^{\frac{1}{3}} V_m$$

With N_A Avogadro number; the molar mass, the volumetric mass; h the Planck constant; the Boltzmann constant; the mean sound speed. This latter can be expressed as:

$$V_m = \left[\frac{1}{3} \left(\frac{2}{V_l^3} + \frac{1}{V_t^3} \right) \right]^{-\frac{1}{3}}$$

where: $V_l = \left(\frac{3B+4G}{3\rho}\right)^{\frac{1}{2}}$, $V_t = \left(\frac{G}{\rho}\right)^{\frac{1}{2}}$, V_l Represent the longitudinal propagation of sound velocity, and V_t its transversal velocity.

The velocities of sound propagation and the Debye temperature are put in Table 4:

Table 4. Longitudinal propagation sound velocity (m/s), Transversal propagation sound velocity (m/s), mean sound velocity (m/s), Debye Temperature (°K).

	V_l	V_t	V_m	θ_D
CoMnAs	5833.8	2718.9	3061.6	244.81
RhMnAs	6066	3231.3	3610.2	314.66
IrMnAs	5202.9	2618.2	2936	315.46

Thermal properties

Thermal properties of X(X=Co, Rh and Ir)MnAs compounds have been determined using quasi harmonic model of Debye [22]. This approximation put in action in Gibbs code is compatible with the Wien2k code.

This code has the merit to display several thermodynamic parameters at different temperatures and pressures such as heat capacity, Debye temperature thermal expansion, entropy, enthalpy....etc.

Thermal quantities calculation as function of pressure and temperature, of X(X=Co, Rh and Ir)MnAs compounds, using quasi harmonic Debye model. This latter uses as input data in Gibbs program the $E-V$ data of the primitive cell. $E-V$ stands for total energy E and volume V .

The heat capacity at constant pressure C_p , the heat capacity at constant volume C_v , and the thermal expansion coefficient α are determined and presented in the temperature range of temperature (0 to 900 °K) and of pressure (0 to 25 GPa).

Debye model parameters targeted here are respectively θ_D , the heat capacity at constant volume C_v , and the thermal expansion coefficient α [23,24]:

$$\theta_D = \frac{\hbar}{k} \left[6\pi^2 V^{\frac{1}{3}} n \right]^{\frac{1}{3}} f(\nu) \sqrt{\frac{B_s}{M}}$$

$$C_v = 3nk_B \left[4D\left(\frac{\theta}{T}\right) - \frac{\frac{3\theta_D}{T}}{e^{\frac{\theta}{T}} - 1} \right]$$

$$\alpha = \frac{\gamma C_v}{B_T V}$$

Where M is the molar mass; B_s is the adiabatic compression modulus, which is by the static compressibility.

$$B_s \cong B(V) = V \frac{d^2 E(V)}{dV^2}$$

$f(\nu)$ est donnée par :

$$f(\nu) = \left\{ 3 \left[2 \left(\frac{2(1+\nu)}{3(1-2\nu)} \right)^{3/2} + \left(\frac{1(1+\nu)}{3(1-\nu)} \right)^{3/2} \right]^{-1} \right\}^{1/3}$$

ν is Poisson coefficient and γ is Grüneisen parameter.

The Figure 3 curve giving the thermal expansion coefficient α shows the three materials have sensibly identical behaviour for the same variations of temperature and pressure. α increases with the increase of the temperature, but decreases considerably with the increase of pressure.

It should be noted that the increase of the pressure weakens α growth with the temperature as it is shown clearly on Figure 3. It should be emphasized as well that α of CoMnAs compound presents the largest value compared to other compounds for a given temperature and pressure.

Let at $T = 300$ °K and $P = 0$ GPa, the thermal expansion coefficient be equal to 3.2805 (10^{-5} °K⁻¹), 2.5559 (10^{-5} °K⁻¹), 2.858 (10^{-5} °K⁻¹) for CoMnAs, RhMnAs, IrMnAs compounds respectively.

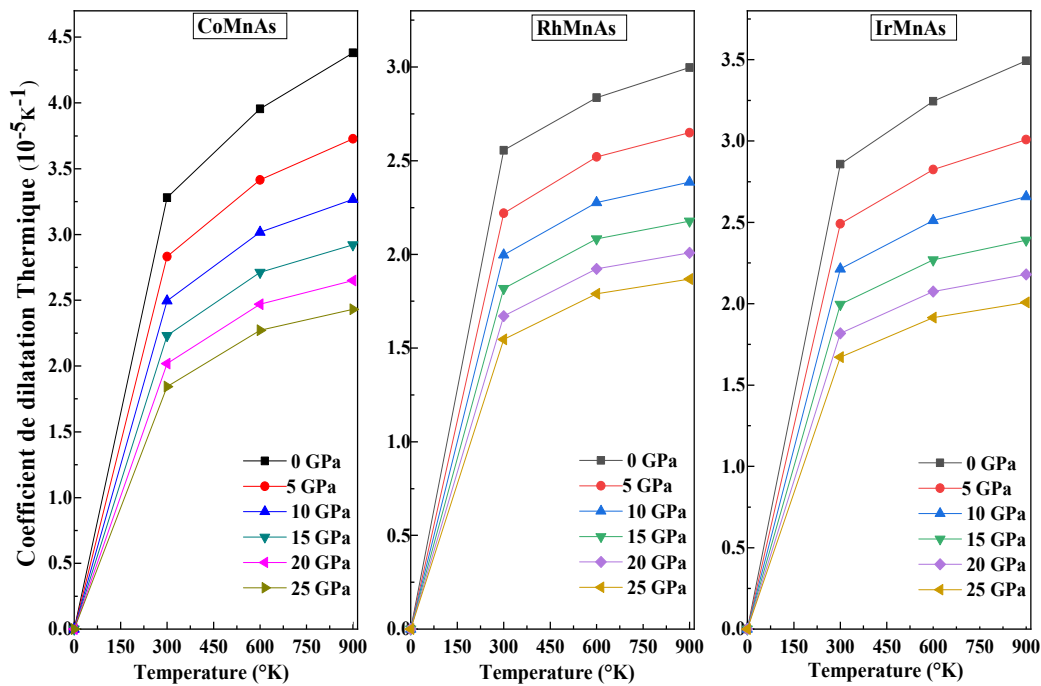


Figure 3. Thermal dilatation coefficient variation as function of temperature and pressure for XMnAs (X=Co, Rh et Ir) compounds.

The specific heat C_p expresses the energy or the photon number needed to increase the temperature of the material by one degree K [12]. C_p represents the change in temperature of thermal excitement energy U , associated to lattice vibrations. The Figure 4 represents the evolution of thermal capacity C_p at constant pressure as function of temperature at different pressure.

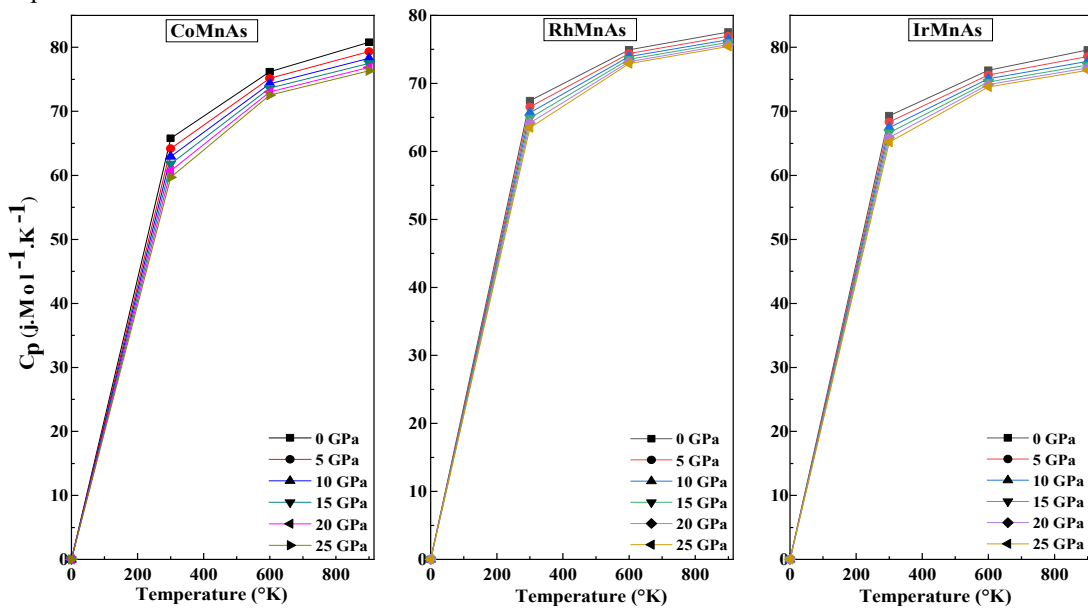


Figure 4. Calorific capacity (C_p variation as function of temperature at different pressures for) XMnAs (X=Co, Rh and Ir) compounds.

The results show, for the three half Huslers that the curves are nearly superimposed. This confirms that the pressure increase has no effect on C_p value. The heat capacity at constant pressure increases with an obvious monotony when temperature increases and converge towards a constant value. Thus, at high temperature this heat capacity could be thought as constant. This hypothesis will be used in the following thermoelectric properties calculation.

The heat capacity C_v characterizes the material aptitude to store heat. C_v evolution as function of temperature in a pressure going from 0 to 25 GPa is shown on Fig. 5. For temperature less than 450 °K, C_v depends on temperature and pressure because of lack of harmony, beyond a certain temperature, C_v shows a horizontal profile and the differences between the thermal capacities at different pressures become more and more discrete with the temperature increase.

The heat capacity C_v decreases with pressure increase and increases with temperature increase. This implies that the temperature and the pressure have opposite effect with more impact of temperature compared to that of the pressure.

C_p and C_v values of the three compounds are nearly of the same order of magnitude. They are purely theoretical because none of the experimental data is available.

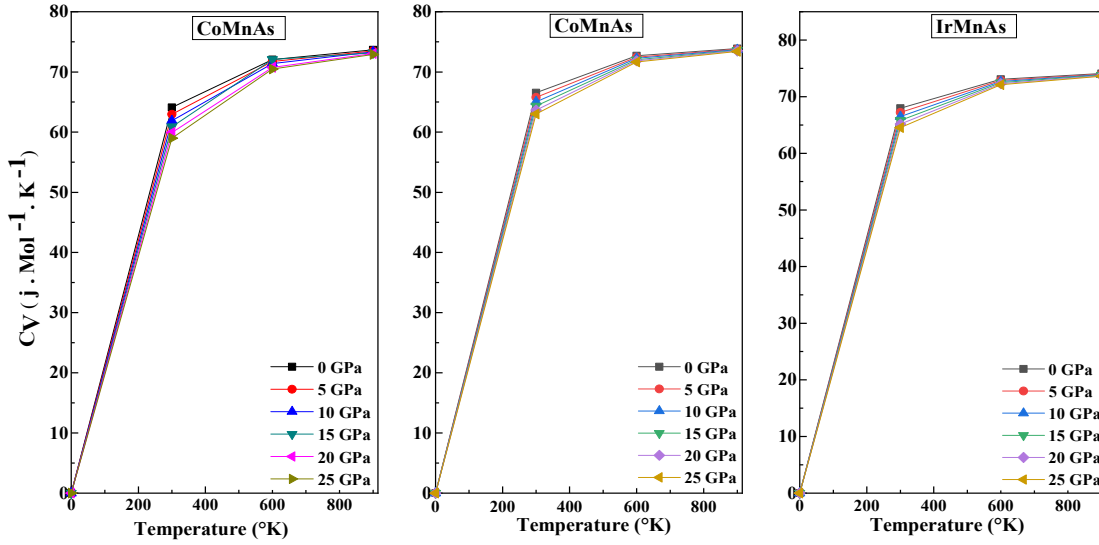


Figure 5. Calorific capacity (C_v variation as function of temperature at different pressures for (X)MnAs (X=Co, Rh and Ir) compounds;

Transport properties

By keeping the diffusion time constant, the thermoelectric properties have been determined by using the semi classic theory of Boltzmann [25], as it was used in BoltzTraP code [26]. To get electronic and transport properties, including electric conductivity, Seebeck coefficient and electronic and thermal conductivities, the calculated band structure are given as input data in BoltzTraP package. To calculate the X(X=Co, Rh and Ir)MnAs compounds thermoelectric properties the calculated band structure has been used by WC-GGA approximation.

The Seebeck coefficient $S_{\alpha\beta}$, electrical conductivity σ and the tensors of electronic transport and thermal conductivity are expressed as follows k [27,28]:

$$S_{\alpha\beta}(T, \mu) = \frac{1}{eT\sigma_{\alpha\beta}(T, \mu)} \int \sigma_{\alpha\beta}(\epsilon) \cdot (\epsilon - \mu)^2 \left[-\frac{\partial f_0(T, \epsilon, \mu)}{\partial \epsilon} \right]$$

$$\sigma_{\alpha\beta} = \frac{1}{\Omega} \int \sigma_{\alpha\beta}(\epsilon) \left[-\frac{\partial f_0(T, \epsilon, \mu)}{\partial \epsilon} \right] \cdot d\epsilon$$

$$k_{\alpha\beta}^0(T, \mu) = \frac{1}{e^2 T \Omega} \int \sigma_{\alpha\beta}(\epsilon) \cdot (\epsilon - \mu)^2 \left[-\frac{\partial f_0(T, \epsilon, \mu)}{\partial \epsilon} \right] \cdot d\epsilon$$

Where: e is the electro charge, Ω is the reciprocal space volume, ϵ is the bearing energy, f_0 is the Fermi distribution function, μ is the chemical potential and T is the absolute temperature.

The conductivity tensor $\sigma_{\alpha\beta}(\epsilon)$ as function of energy and electronic and thermal energy k , is expressed as follows

$$\sigma_{\alpha\beta}(\epsilon) = \frac{1}{N} \sum_{i,k} \sigma_{\alpha\beta}(i, k) \frac{\delta(\epsilon - \epsilon_{i,k})}{d\epsilon}$$

Where N is the number of k-points.

It is well known in semi-conductors materials domain that in a p-type semi-conductor the majority charge carriers are holes and minority charge carriers are electrons.

In n type semi-conductor, the electrons are the majority charge carriers and the holes are the minority charge carriers [29]. On Figure 6 it is shown the Seebeck coefficient variation as function of the chemical potential varying between $\mu - E_f = \pm 2eV$ (considered as charge carrier concentration for the alloys) at different constant temperatures (300, 600 et 900 °K), in case of X(X=Co, Rh and Ir)MnAs [30] half-Husler compounds.

The negative characteristic of S indicates the n-type conduction, with the electrons as main charge carriers. Whereas the positive sign of S implies the p-type conduction with holes as majority carriers.

For the three compounds, the optimal values of S are obtained around E_f because S is inversely proportional to electrical conductivity and since in this region the conduction is intrinsic, therefore the conductivity is weak. These optimal values decrease when the temperature increases (Figure 6).

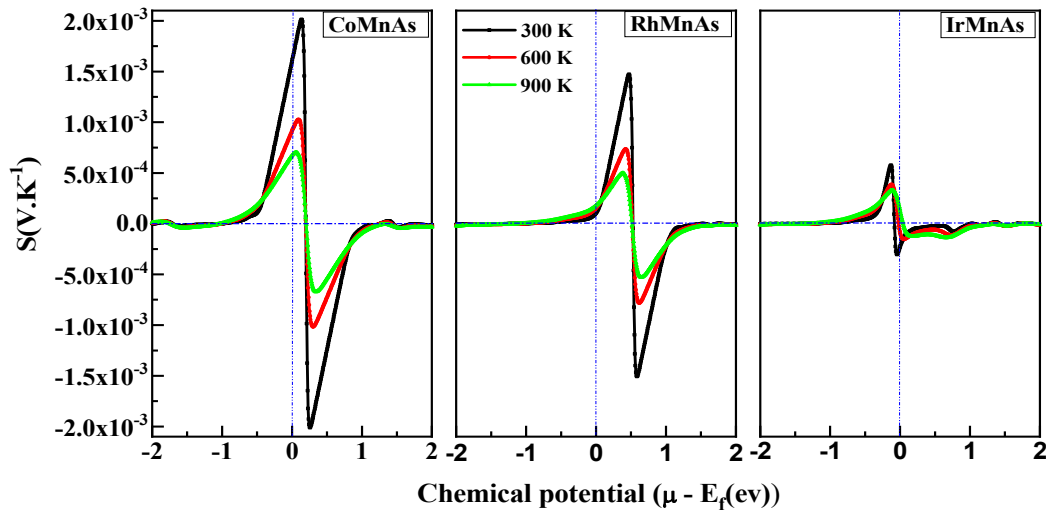


Figure 6. Seebeck coefficient S as function of chemical potential μ .

In case of CoMnAs and RhMnAs compounds, when $\mu = E_f$, the value of S is positive and the conduction is of p-type. So, these half-Heusler compounds are semi-conductors of p-type. On the contrary, for IrMnAs compounds, the value of S is negative in the level $\mu = E_f$, this entails that the conduction is of n-type and in this case, the compound is a semi-conductor of n-type.

On Figure 6, the peaks of CoMnAs compound are very important compared to the other peaks among them the IrMnAs compound is representing the weakest peaks.

The Figure 7 shows the electric conductivity variation as function of chemical potential $\mu - E_f = \pm 2eV$ at different temperatures (300°K, 600°K et 900°K). This curve shows the temperature effect on the electric conductivity is weak for the three considered compounds.

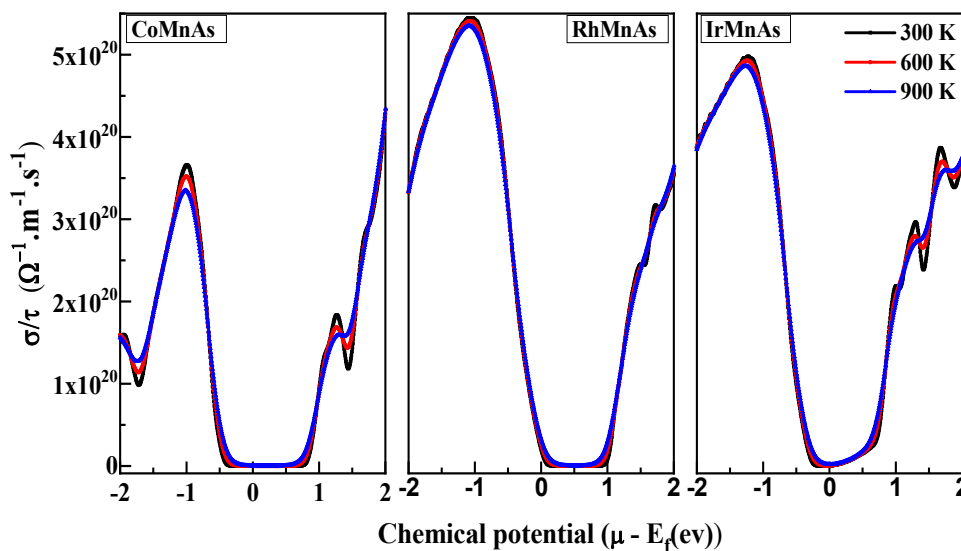


Figure 7. Electrical conductivity σ / τ as function of chemical potential μ .

For CoMnAs compound the n-type conductivity ($\mu > E_f$) is greater than that of p-type ($\mu < E_f$). This is due to the difference between the electrons and holes mobility. On the contrary, for RhMnAs et IrMnAs compounds, the n-type conductivity is less than that of p-type.

The three main zones are well illustrated on Figure 7, the first zone when $\mu < E_f$ where the electric conductivity diminishes for the three compounds becoming intrinsic under the effect of the charge carriers (holes) concentration decrease at the vicinity of the chemical potential.

The electric conductivity diminishes for the three compounds. These latter become intrinsic under the decrease of charge carriers (holes) concentrations at the vicinity of the chemical potential.

In second zone corresponding to $\mu = E_F$ the electric conductivity becomes weaker with feeble charge carriers concentration, the last zone where $\mu > E_F$ the charge carriers which are electrons will increase with chemical potential increase. And this leads to an electric conductivity.

Concerning the electronic thermal conductivity, Figure 8, it is clearly observed that the temperature rise increases significantly the electronic thermal conductivity of the three compounds. It is also noticed that the rise in temperature and the tendency of the electronic thermal conductivity are similar to that of the electric conductivity, having in mind that the charge carriers are also heat carriers [31].

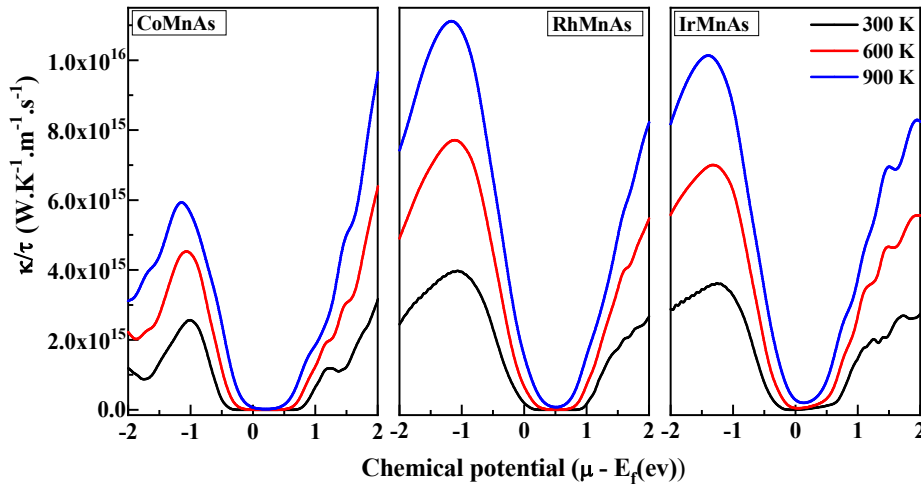


Figure 8. Electronic thermal conductivity k/τ as function of chemical potential μ

The qualities of a thermoelectric material is measured by a dimensionless number called merit factor i.e. the improvement in the material thermoelectric performance could be obtained through its merit factor ZT [32,33] expressed by:

$$ZT = \frac{S^2 \sigma}{k_e + k_l} T$$

Where T is absolute temperature absolute, S the Seebeck coefficient, σ the electric conductivity, k_e the electronic thermal conductivity and k_l the lattice thermal conductivity.

To ensure whether the system could withstand higher temperatures the merit factor variations has been calculated as function of the chemical potential and this for an extended temperature range.

On Figure 9, ZT is maximal at only 300°K at the peaks, but as far as ZT takes the allure of fall starts its fall the highest temperature (900°K) becomes dominant with regard to the temperature of 300°K for the three compounds.

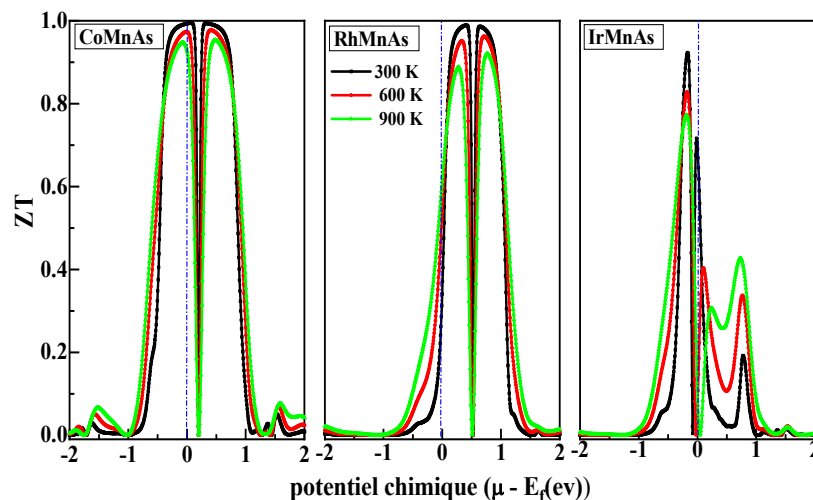


Figure 9. Merit factor (ZT) as function of chemical potential μ .

The merit factor of CoMnAs and RhMnAs compounds is close to the unit at ambient temperature. This makes of these alloys good candidates for thermoelectric apparatuses.

The small values of merit factor associated to IrMnAs half-Heusler are due to small values of Seebeck coefficient, to the electric conductivity, and to the increased values of the thermal conductivity too.

The Figure 10 represents the power factor PF, as function of the chemical potential where it can be noticed that PF increases with the temperature rise. It reaches a maximal value at $T=900^{\circ}\text{K}$ for the three compounds.

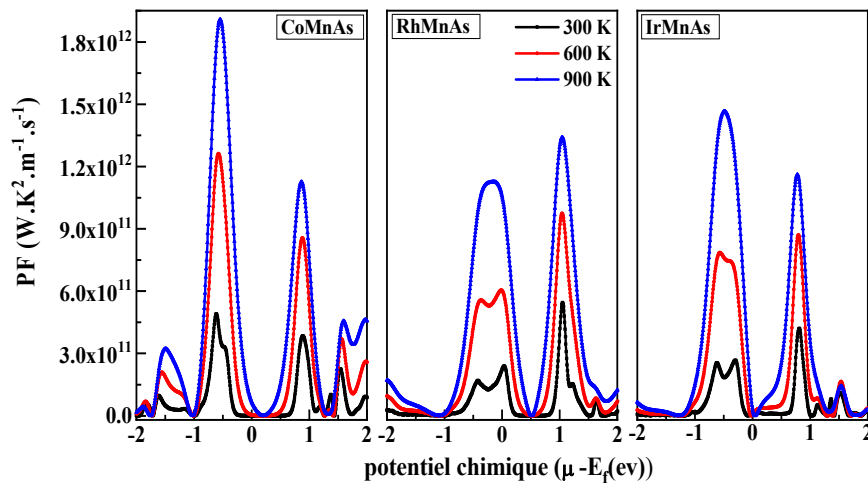


Figure 10. Power factor (PF) as function of chemical potential μ .

Two peaks of high intensity are also observed. One of them is a main peak near the Fermi level limit $\mu - E_f = -0.55$, et -0.48 respectively for the X(X=Co, Ir)MnAs compounds for respectively, the values of $1.899.10^{12}$, and $1.46.10^{12}$ W/Mk²s. contrarily, the principal peak of the RhMnAs compound comes after Fermi level, precisely at $\mu - E_f = 1.048$ with a value of PF= $1.335.10^{12}$ W/Mk²s.

CONCLUSION

In the present study, the electronic, elastic, thermodynamic and transport properties of half- Heusler X(X=Co, Rh and Ir)MnAs have been treated using the DFT associated to general gradient approximation.

The elastic constants confirm the material ductile nature with stability in cubic phase C_{1b}. The studied materials have a high Debey temperature (600 °K) at a pressure of 0 GPa.

The thermal properties including the heat capacities C_v and C_p and the thermal expansion coefficient have been studied using the quasi harmonic Debey model in the range of pressure 0 to 25 GPa and of temperature 0 à 900 °K, show that the CoMnAs compound has high values of expansion coefficient with regard to the other compounds. The transport properties have been determined by means of BoltzTraP code.

The CoMnAs materiel presents a high thermoelectric parameter such that Seebeck coefficient, the power and the merit factors. Contrarily, The IrMnAs compounds show weak values for these parameters.

These results could offer a useful reference for the development of thermoelectric material based on XMnAs.

ORCID IDs

Amraoui Rabie, <https://orcid.org/0000-0001-9256-488X>

REFERENCES

- [1] Enamullah, S.K. Sharma, Sameh, and S. Ahmed, J. Phys. Condens. Matter. **32**, 405501 (2020). <https://doi.org/10.1088/1361-648X/ab96f0>
- [2] R. De Groot, F. Mueller, P. Van Engen, and K. Buschow, New class of materials: halfmetallic ferromagnets, Phys. Rev. Lett. **50**, (25) (1983) 2024. <https://doi.org/10.1103/PhysRevLett.50.2024>
- [3] S. Chibani, O. Arbouche, M. Zemouli, Y. Benallou, K. Amara, N. Chami, M. Ameri, and M. El Keurti, First-principles investigation of structural, mechanical, electronic, and thermoelectric properties of Half-Heusler compounds RuVX (X= As,P, and Sb), Comput. Condens. Matter, **16**, e00312 (2018). <https://doi.org/10.1016/j.cocom.2018.e00312>
- [4] F. Benzoudji, O. Miloud Abid, T. Seddik, A. Yakoubi, R. Khenata, H. Meradji, G. Uğur, S. Uğur, and H.Y. Ocak, Insight into the structural, elastic, electronic, thermo- electric, thermodynamic and optical properties of MRhSb (MDTi, Zr, Hf) half Heuslers from ab initio calculations, Chinese Journal of Physics, **59**, 434 (2019), <https://doi.org/10.1016/j.cjph.2019.04.009>
- [5] A. Amudhavalli, R. Rajeswarapalanichamy, K. Iyakutti, and A.K. Kushwaha, First principles study of structural and optoelectronic properties of Li based half Heusler alloys, Computational Condensed Matter, **14**, 55 (2018), <https://doi.org/10.1016/j.cocom.2018.01.002>
- [6] F. Aversano, A. Ferrario, S. Boldrini, C. Fanciulli, M. Baricco, and A. Castellero, Thermoelectric Properties of TiNiSn Half Heusler Alloy Obtained by Rapid Solidification and Sintering, J. Mater. Eng. Perform. **27**, 6306 (2018). <https://doi.org/10.1007/s11665-018-3735-6>
- [7] W. Xie, A. Weidenkaff, X. Tang, Q. Zhang, J. Poon, and T.M. Tritt, Recent advances in nanostructured thermoelectric half-Heusler compounds, Nanomaterials, **2**, 379 (2012). <https://doi.org/10.3390/nano2040379>

- [8] J. Ma, V.I. Hegde, K. Munira, Y. Xie, S. Keshavarz, D.T. Mildebrath, C. Wolverton, A.W. Ghosh, and W. Butler, Computational investigation of half-Heusler compounds for spintronics applications, *Phys. Rev. B*, **95**, 024411 (2017). <https://doi.org/10.1103/PhysRevB.95.024411>
- [9] R. Ahmad, A. Gul, N. Mehmood, Artificial neural networks and vector regression models for prediction of lattice constants of half-Heusler compounds, *Mater. Res. Express*, **6**, 046517 (2018). <https://doi.org/10.1088/2053-1591/aafa9f>
- [10] S. Chibani, N. Chami, O. Arbouche, K. Amara, A. Kafi, Structural, elastic, electronic and transport properties of CoVX (X=Ge and Si) compounds: A DFT prediction, *Computational Condensed Matter*, **24**, e00475 (2020). <https://doi.org/10.1016/j.cocom.2020.e00475>
- [11] P. Blaha, K. Schwarz, G.K.H. Madsen, D. Knasnicka, J. Lunitz, R. Laskowski, F. Tran, and L.D. Marks, *WIEN2k, An Augmented Plane Wave Plus Local Orbital Programme for calculating crystal properties*, (Vienna University of Technology, Vienna, Austria, 2001). http://www.wien2k.at/reg_user/textbooks/usersguide.pdf
- [12] W. Kohn, L.J. Sham, Self-consistent equations including exchange and correlation effects, *Phys. Rev.* **140**, A1133 (1965). <https://doi.org/10.1103/PhysRev.140.A1133>
- [13] F.D. Murnaghan, *Proc. Natl. Acad. Sci. USA*, **30**, 244 (1944). <https://doi.org/10.1073/pnas.30.9.244>
- [14] P. Blaha, K. Schwarz, F. Tran, R. Laskowski, G.K.H. Madsen, and D.L. Marks, *J. Chem. Phys.* **152**, 074101 (2020), <https://doi.org/10.1063/1.5143061>.
- [15] M. Born, K. Huang, *Dynamical theory of crystal lattices (international series of monographs on physics)*, (Oxford University Press, Oxford, U.K., 1954).
- [16] Hill, R. The Elastic Behaviour of a Crystalline Aggregate. *Proc. Phys. Soc. Sect. A*, **65**, 349 (1952). <https://doi.org/10.1088/0370-1298/65/5/307>
- [17] S.F. Pugh, *Philos. Mag.* **45**, 823 (1954). <https://doi.org/10.1080/14786440808520496>
- [18] Y. Tian, B. Xu, and Z. Zhao, *Int. J. Refract. Metals Hard Mater.* **33**, 93 (2012). <https://doi.org/10.1016/j.ijrmhm.2012.02.021>
- [19] V.I. Razumovskiy, E.I. Isaev, A.V. Ruban, and P.A. Korzhavyi, *Intermetallics*, **16**, 982 (2008). <https://doi.org/10.1016/j.intermet.2008.04.016>
- [20] N. Arıkan, A. İyigör, A. Candan, Ş. Uğur, Z. Charifi, H. Baaziz, and G. Uğur, Electronic and phonon properties of the full-Heusler alloys X₂YAl (X=Co, Fe and Y=Cr, Sc): a density functional theory study, *J. Mater. Sci.* **49**, 4180 (2014). <https://doi.org/10.1007/s10853-014-8113-7>
- [21] D.-y. Jung, K. Kurosaki, C.-e. Kim, H. Muta, and S. Yamanaka, Thermal expansion and melting temperature of the half-Heusler compounds: MNiSn (M = Ti, Zr, Hf), *J. Alloys. Compd.* **489**, 328 (2010). <https://doi.org/10.1016/j.jallcom.2009.09.139>
- [22] P. Debye, *Ann. Phys.* **39**, 789 (1912).
- [23] A. Otero-de-la-Roza, D. Abbasi-Pérez, and V. Luaña, Gibbs2: A new version of the quasiharmonic model code. II. Models for solid-state thermodynamics, features and implementation, *Comput. Phys. Commun.* **182**, 2232 (2011). <https://doi.org/10.1016/j.cpc.2011.05.009>
- [24] A.T. Petit, and P.L. Dulong, *Ann. Chim. Phys.* **10**, 395 (1819).
- [25] E. Bringuier, L'équation de transport électronique de Boltzmann dans les solides et l'approximation du temps de relaxation, *European Journal of Physics*, **40**, 025103 (2019). <https://doi.org/10.1088/1361-6404/aaf5f0>
- [26] G.K.H. Madsen, and D.J. Singh, BoltzTraP. A code for calculating band-structure dependent quantities, *Computer Physics Communications*, **175**, 67 (2006). <https://doi.org/10.1016/j.cpc.2006.03.007>
- [27] G. Snyder, in *CRC Handbook of Thermoelectrics*, ed. D.M. Rowe (Boca Raton: CRC Press, 2006), p. 144.
- [28] B. Lenoir, *Thermoélectricité: des principes aux applications*, (Transport, 1990), pp. 1–19.
- [29] C.H.L. Goodman, The prediction of semiconducting properties in inorganic compounds, *Journal of Physics and Chemistry of Solids*, **6**, 305 (1958). [https://doi.org/10.1016/0022-3697\(58\)90050-7](https://doi.org/10.1016/0022-3697(58)90050-7)
- [30] T. J. Seebeck, *Abhand. Deut. Akad. Wiss, Berlin*, (1822).
- [31] F.Z. Fouddad, S. Hiadsi, L. Bouzid, Y.F. Ghrici, and K. Bekhadda, Low temperature study of the structural stability, electronic and optical properties of the acanthite α -Ag₂S: Spin-orbit coupling effects and new important ultra-refraction property, *Materials Science in Semiconductor Processing*, **107**, 104801 (2020). <https://doi.org/10.1016/j.mssp.2019.104801>
- [32] P.F. Taylor, and C. Wood, *Advan. Energy Conversion*, **1**, 141 (1961). [https://doi.org/10.1016/0365-1789\(61\)90023-6](https://doi.org/10.1016/0365-1789(61)90023-6)
- [33] A.I. Ioffe, *Энергетические основы термоэлектрических батарей полупроводников [Energeticheskie osnovi termoelctricheskikh battery poluprovodnikov]*, (Academy of Science of the USSR, Moscow, 1949).

ДОСЛІДЖЕННЯ СТРУКТУРНИХ, ПРУЖНИХ, ТЕПЛОВИХ ТА ТРАНСПОРТНИХ ВЛАСТИВОСТЕЙ ПОТРІЙНИХ СПОЛУК X(X=Co, Rh та Ir)MnAs, ОТРИМАНИХ МЕТОДОМ DFT

Салім Кадрі^a, Тураб Мохамед^b, Беркани Махмедіне^c, Амрауї Рабіє^d, Борджиба Зейнеб^d

^aЛабораторія динамічних двигунів та віброакустичної лабораторії, Університет М'Хамеда Бугари в Бумердесі

^bФакультет технологій, Університет М'Хамеда Бугари, Сіте Франц Фанон, Бумердес 35000-Алжир

^cЛабораторія LSELM, Університет Баджі Мохтар Аннаба, Аннаба 23000, Алжир

^dЛабораторія фізики матеріалу - L2PM, 8 травня 1945 р. Університет Гельми, Алжир

Теорія функціональної щільності (DFT) з апроксимацією узагальненого градієнта використовується для дослідження пружних, термодинамічних і транспортних властивостей, а також для структурної стабільності потрійних напівгейслерівських сполук X(X=Co, Rh та Ir)MnAs. Це перше прогностичне дослідження цих сполук визначає такі механічні властивості, як стиснення, зсув, модуль Юнга та коефіцієнт Пуассона, не пропускаючи параметрів перевірки природи цих сполук, таких як твердість, анізотропний факт Зенера та тиск Коші. Коефіцієнт П'ю та коефіцієнт Пуассона дозволили визначити пластичну природу цих сполук. Швидкість звуку та температура Дебая цих сполук також була оцінена за пружними константами. Термодинамічні властивості також розраховані для інтервалу тиску від нуля до 25 ГПа. Вплив зміни хімічного потенціалу на коефіцієнт Зеебека, електричну, теплову та електронну провідність, коефіцієнти потужності та переваги також досліджували для різних температур (300, 600, 900°K), так що ці сплави можуть бути кращими потенційними кандидатами для термоелектричних додатків.

Ключові слова: Напів-Гейслер, DFT, пружність, термоелектричні, транспортні властивості

CHARACTERISTICS AND OPTICAL PROPERTIES OF $\text{Bi}_2\text{Te}_{2.45}\text{Se}_{0.55}$ THIN FILM[†]

 A.S. Salwa*,  Azza El-Sayed Ahmed

Physics Department, Faculty of Science and Arts, Jouf University, Gurayat 77431, Kingdom of Saudi Arabia

*Corresponding author: ssaali@ju.edu.sa

Received January 17, 2022; revised February 20, 2022; accepted March 5, 2022

Thermally evaporated $\text{Bi}_2\text{Te}_{2.45}\text{Se}_{0.55}$ thin films were examined for structural alterations and electrical conductivity. Crystallite size, micro-strain, and dislocations were all calculated using the XRD data. By using transmission electron microscopy, the morphology of thin films was investigated (TEM). The study was performed within a temperature range of (300 – 500) K. The electrical energy gap and the conductivity of the as-deposited and annealed (373, 473K) $\text{Bi}_2\text{Te}_{2.45}\text{Se}_{0.55}$ films were measured. The obtained values are (0.27, 0.26, 0.24 eV) and 3.6×10^3 , 3.7×10^3 and $4.1 \times 10^3 \text{ ohm}^{-1} \cdot \text{cm}^{-1}$ respectively. Hall coefficient, the mean free time, the diffusion coefficient of holes, and the diffusion length, charge carrier's concentration, charge carriers' scattering mechanism, and Hall mobility were also examined. The obtained values of the charge carrier's concentration are 2.12×10^{17} - $2.73 \times 10^{17} \text{ cm}^{-3}$. The direct and indirect allowed energy gap decreased with increasing annealing temperature. The obtained values of indirect band gap and direct band gap ranges from 0.27- 0.24 eV and 0.375- 0.379 eV, respectively.

Keywords: Thin film; electrical properties; transmission electron microscopy; Hall Effect; optical energy gap

PACS: 32.30.Rj, 07.50.-e, 07.05.Kf, 03.65.Nk, 42.25.Bs

Recently, compounds of semiconducting chalcogenides type $\text{A}_2\text{VB}_3\text{VI}$ (where A = Bi, Sb, and B = Te, Se) and their solid solutions are considered to be promising materials for their unique optical, electrical and magnetic properties [1-4] and concomitantly to their potential applications in solid-state thermoelectric cooling and thermoelectric generators [5-8]. The electrical, thermal conductivities and the Seebeck coefficient properties of $\text{Bi}_2(\text{Te}_{1-x}\text{Se}_x)_3$ single crystal solid solutions with $x = 0.025$ ($\text{S}_{2.5}$) and $x = 0.05$ (S_5) were studied [9]. The results showed the scattering mechanism is mainly due to acoustical phonons. Transport properties of $\text{Bi}_2\text{Te}_{2.55}\text{Se}_{0.45}$ solid solutions as a function of carrier concentration and temperature were studied [10].

J. Dheepa et al [11] studied the structural and the optical properties of thermally evaporated Bi_2Te_3 thin films. The XRD shows the hexagonal and polycrystalline structure of the focused films. The calculated lattice parameters are $a = 4.4 \text{ \AA}$ and $C = 3.4 \text{ \AA}$. A. Saji et al.[12] studied the effects of fast electron bombardment and annealing on Bi_2Te_3 and $\text{Bi}_2\text{Te}_{2.9}\text{Se}_{0.1}$ single crystals. Conductivity variations from p to n-type are possible by irradiation with high-energy electrons. Koksai Yildiz et al [13] used scanning electron microscopy, SEM to examine the surface morphology and the elemental composition of the deposited film as well as a high-resolution TEM to examine the lattice image for sample $\text{Bi}_2(\text{Te}_{0.9}\text{Se}_{0.1})_3$.

In this work, the annealing temperature effect on structural properties, D.C electrical conductivity, Hall Effect and optical band gap were investigated.

EXPERIMENTAL PROCEDURE

The modified Bridgeman method [2] was used to fabricate n-type almost stoichiometric single-phase polycrystalline bulk ingot materials of $\text{Bi}_2\text{Te}_{2.45}\text{Se}_{0.55}$ using the pure (99.999%) Te, Se, Bi elements enclosed in vacuum-sealed silica tubes ($=10^{-4} \text{ Pa}$). The silica tube was placed in the hot zone of the furnace for 24 hours to melt the contents.

The tube was shaken several times during heating to ensure homogeneity. The crystallization front moved at a rate of 1.7 mm/h. The temperature of the middle zone ranges from (870 – 995) K corresponding to the crystallization temperature of the produced samples of different compositions. The consumed time to make a crystal is twelve days. The final crystal had a diameter of 1.5 cm and a length of 1.5 cm using a high vacuum coating unit, thin films were deposited on glass substrates at room temperature by conventional evaporation of synthetic solid solutions at a vacuum of 10^{-4} Pa (Edwards 306 A). During the evaporation process, the deposition rate was kept constant at 3nm/s. The film thickness was determined interferometrically as well as utilizing a quartz crystal thickness monitor (Edwards FTM4) [2]. Thin films were annealed by progressively heating them to various annealing temperatures of 373K and 473 K at a pressure of 10^{-3} Pa for two hours at each annealing temperature. After annealing, films were allowed to cool slowly to ambient temperature in a vacuum. X-ray diffractometer, XRD technique is used to verify the crystal structure of the studied material in thin films form. The morphology of the samples was examined by (TEM). Electrical conductivity, σ was measured by the conventional four-probe method using a direct current in a temperature range (300 - 500) K and Hall coefficient as well. The optical transmittance spectrum was measured using a single beam Fourier transform infrared spectrophotometer (FTIR-300E) in wavelength range (2500 – 5000) nm.

[†] Cite as: A.S. Salwa, and A. El-Sayed Ahmed, East. Eur. J. Phys. 1, 58 (2022), <https://doi.org/10.26565/2312-4334-2022-1-08>
© A.S. Salwa, A. El-Sayed Ahmed, 2022

RESULTS AND DISCUSSION

Structure analysis

Figure 1 shows the XRD patterns of the as-deposited and annealed Bi₂Te_{2.45}Se_{0.55} films, it was found that the peak intensity increases appreciably with the increasing of annealing temperature. Analysis of XRD data reveals good crystallinity of films by annealing, with preferred orientation (015) at 2θ = 32.5°C. The crystallite size is calculated by Debye - Scherer equation [14]:

$$D = 0.9 \lambda / \beta \cos \theta \tag{1}$$

Where λ is the wavelength of CuKα radiation of XRD, β is the full width at half maximum at reflection plane (015) and θ is diffraction angle.

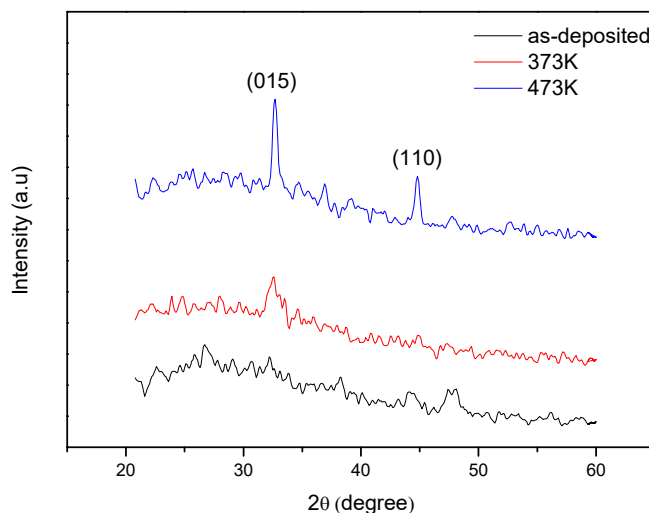


Figure 1. XRD pattern of Bi₂Te_{2.45}Se_{0.55} thin films

The obtained results confirm the increasing of crystallite size with the increase of annealing temperature because of re-crystallization which leads to the reduction of deformation or defects present in the film. The annealing at (473 K) enhances the quality of the crystalline structure of Bi₂Te_{2.45}Se_{0.55} films [15]. Micro-strain, S (non-uniform strain) was determined using XRD according to [16]:

$$s = \beta \cos \theta / 4 \tag{2}$$

As the annealing temperature increases, the micro-strain decreases. This may be attributed to the imperfections in the crystal structure. As a result of crystallinity improvement because of annealing, the micro-strain is reduced. The dislocation density δ is defined as the length of dislocation lines per volume unity of a crystal. δ is a significant characteristic of the structure, so it is estimated by [16]:

$$\delta = n / D^2 \tag{3}$$

where (n) is an integer number, D is the crystallite size.

As the annealing temperature increases, the dislocation density decreases as a result of the reduction of lattice defects, and consequently, the crystalline quality increases due to the modification of the periodic arrangements of atoms in their crystal lattice. This confirms the crystalline enhancement of material at 373K and 473K annealing temperature, as documented by authors [17].

The calculated values of crystallite size, micro-strain, dislocation density, and the numbers of crystallites are listed in Table 1.

Table 1. The calculated values of crystalline size from (XRD, TEM), micro-strain, and dislocations for the annealing temperature (373, 473) K for Bi₂Te_{2.45}Se_{0.55} thin film.

Ta (K)	Crystalline Size XRD D (nm)	Crystalline Size TEM D (nm)	Micro-strain S×10 ⁻³	Dislocation density (Line/m ²) δ×10 ¹⁴
373	43	45	7.95	5.27
473	75	80	4.61	1.76

Morphology analysis of $\text{Bi}_2\text{Te}_{2.45}\text{Se}_{0.55}$ thin film

Figure 2(a,b,c) shows a TEM image of the as-deposited and annealed $\text{Bi}_2\text{Te}_{2.45}\text{Se}_{0.55}$ thin films. As seen in Figure 2a, the as-deposited film has a rough surface with irregular crystallite size. The morphology of the annealed films at 373 K does not change much but the crystallite size uniformity improved as shown in Figure 2b. Additionally, the annealed films at 473K have a continuous and homogeneous surface as observed in Figure 2c.

From TEM analysis, the crystallite size was around 45 nm and 80 nm for different annealed temperatures (373 K and 473 K) respectively. This result is matched with the data obtained from the XRD diffraction method.

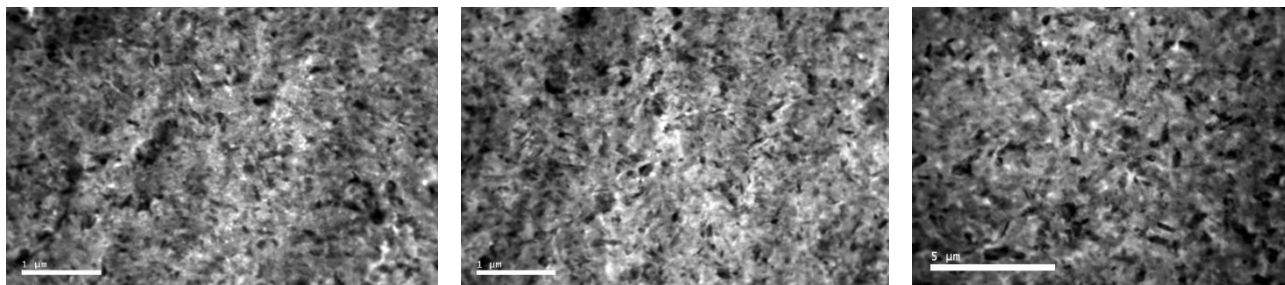


Figure 2a. Transmission electron microscopy images of the as-deposited $\text{Bi}_2\text{Te}_{2.45}\text{Se}_{0.55}$ thin film.

Figure 2b. Transmission electron microscopy images of $\text{Bi}_2\text{Te}_{2.45}\text{Se}_{0.55}$ thin films at $T_a = 373\text{K}$.

Figure 2c. Transmission electron microscopy images of $\text{Bi}_2\text{Te}_{2.45}\text{Se}_{0.55}$ thin film at $T_a = 473\text{K}$.

Annealing effect of electrical conductivity

Figure 3 shows the results of the temperature dependence of the electrical conductivity of the as-deposited and that annealed $\text{Bi}_2\text{Te}_{2.45}\text{Se}_{0.55}$, thin films at 373, 473K for two hours

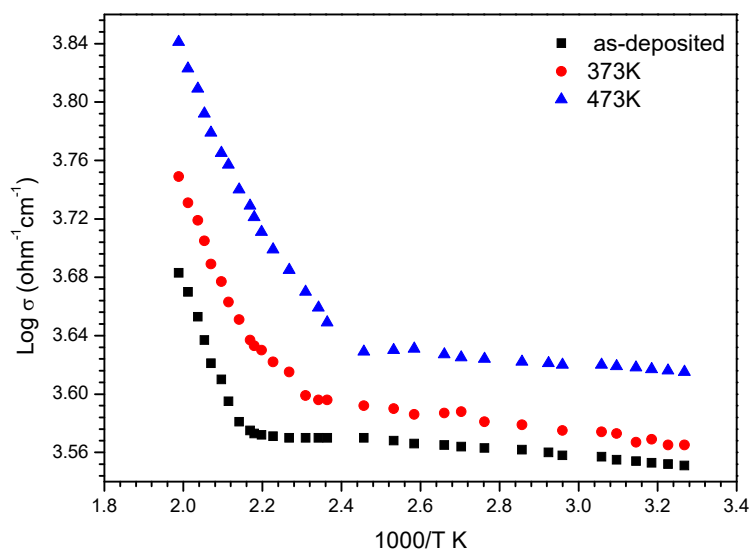


Figure 3. The temperature dependence of electrical conductivity $\text{Log } \sigma$ for the deposited thin films and annealed $\text{Bi}_2\text{Te}_{2.45}\text{Se}_{0.55}$ films.

One can confirm that the as-deposited and annealed films at 373,473 have a semiconductor behavior. The curve consists of three regions; the first region in the temperature range (300-385) K and σ finishes in the extrinsic region. The conductivity shows a slightly increase in the low- temperature range due to the release of ionized acceptors and their transition from the impurity level. The second region refers to the transition region, where the behavior of σ is influenced by the charge carrier's concentration as well as its mobility. A rapid linear rise in conductivity is observed within the third region at high temperatures of over 400 K. This result demonstrates that, at the high temperature region, both electrons and holes contribute to conductance. By annealing temperature, the conductivity (σ) increases. The conductivity at room temperature for the as-deposited sample and annealed temperature 373, 473K are 3.6×10^3 , 3.7×10^3 , and $4.1 \times 10^3 \text{ ohm}^{-1} \text{ cm}^{-1}$ respectively.

This increase in conductivity by annealing may be attributed to the improvement of crystallite size and a decrease of defects' number which allows more carriers to flow through the system to take part in conduction [18]. These results confirm the structural investigations by X-ray, which indicates the increase of crystallinity of the films by annealing. This agrees well with the results of other works for chalcogenide materials [18].

The temperature dependence of electrical conductivity was investigated using Arrhenius equation [19]:

$$\sigma = \sigma_0 \exp(-\Delta E_g / 2KT) \tag{4}$$

The measured d.c electrical conductivity indicates two straight lines with different slopes, both could fit the relation. The conduction mechanism due to carriers excited into localized states at the edge of the band by hopping at low temperatures (300 - 400) K, and the conduction mechanism due to carriers excited into extended states beyond the mobility edge by thermal excitation at higher temperatures (400-500) K. The activation energy calculated from the first line is in the temperature range 300 - 400K, while the energy gap calculated from the other line within temperature range 400-500K. The values of energy gap and activation energy are tabulated in a table (2). This agrees well with the results of other works for chalcogenide materials [19].

Table (2) Values of energy gap and activation energy.

Ta (K)	E _g (σ) e.v 400-500K	ΔE(σ) e.v 300-400K
473	0.24	7.74 x 10 ⁻³
373	0.26	7.94 x 10 ⁻³
As-deposited	0.27	9.02 x 10 ⁻³

Hall Effect analysis

Hall measurements are an important tool for the characterization of materials, particularly semiconductors so Hall coefficient, R_H of the as-prepared and annealed Bi₂Te_{2.45}Se_{0.55} films is measured and depicted in Fig. 4. It is clear that curves have the same trend at different annealing temperatures. Besides, the results indicate that the samples have p-type conduction because of the positive sign of R_H values so that the majority of carriers are holes.

At room temperature, R_H has a positive value range from (29.5 - 23.9) cm³/C for as-deposited and annealed films.

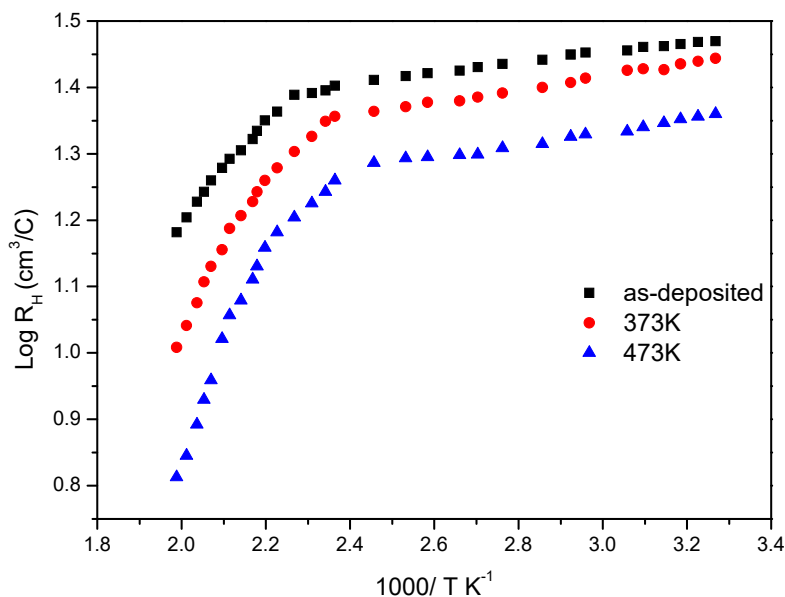


Figure 4. The temperature dependence of Log R_H Vs 1000/T(k) for the as-deposited and annealed Bi₂Te_{2.45}Se_{0.55} films.

The charge carrier's concentration is estimated by equation:

$$P = 1/e R_H \tag{5}$$

And the concentration of charge carriers at a room temperature range from 2.12×10¹⁷ to 2.73×10¹⁷ cm⁻³ for as-deposited and annealed films. The increase of charge carriers with annealing temperature is due to the crystalline enhancement of the material. Figure 5 shows the temperature dependence of carrier concentration calculated by:

$$P = C \exp(-\Delta E_g / 2K_{\beta}T) \tag{6}$$

Within the temperature range of (300 – 400) K, the number of free carrier P increases slightly with increasing temperature, suggesting ionization of the impurity centers whereas the number of free carriers increased sharply as the temperature rises to 400 K refers to intrinsic conduction. The energy gap can be computed from the slope of the curve within the temperature range (400- 500) K through the intrinsic region. It was (0.24 - 0.264) eV for as-deposited and annealed films. The acceptor levels energy above the top of the valence band in the extrinsic region (300-400) K

ranging from $(7.69 \times 10^{-3} - 8.9 \times 10^{-3})$ for as-deposited and annealed films. The values of energy gap and energy of acceptor level are closed to that obtained from electrical conductivity measurements.

Fig. 5 shows the temperature dependence of charge carrier concentration Log P of as-deposited thin films and annealed $\text{Bi}_2\text{Te}_{2.45}\text{Se}_{0.55}$ films.

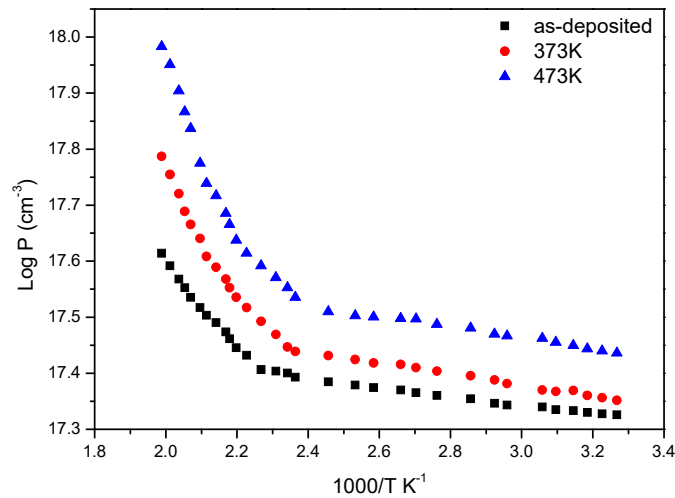


Figure 5. The temperature dependence of charge carrier concentration Log P Vs $1000/T(k)$ for the as- deposited and annealed $\text{Bi}_2\text{Te}_{2.45}\text{Se}_{0.55}$ films.

By using the data of R_H and conductivity, the charge carrier's mobility can be evaluated by the relation:

$$\mu_H = \sigma R_H \quad (7)$$

The temperature dependence of Hall mobility is shown in figure 6. The curve is divided into two regions at the transition temperature of 440K.

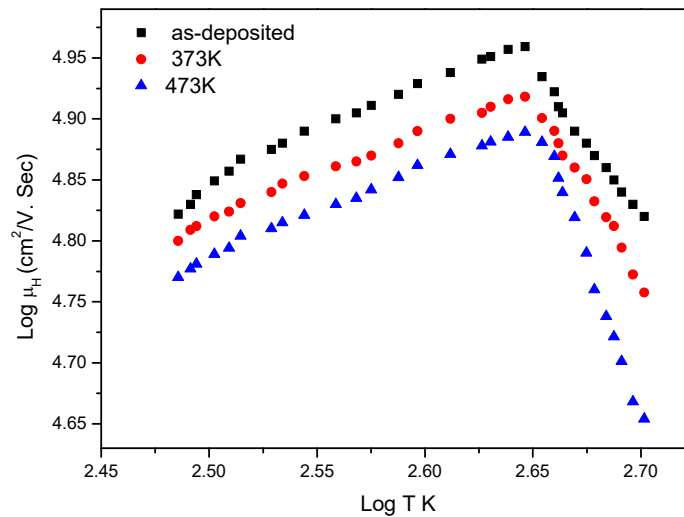


Figure 6. The temperature dependence of Hall mobility Log μ_H Vs $\log/T(k)$ for the as-deposited and annealed $\text{Bi}_2\text{Te}_{2.45}\text{Se}_{0.55}$ films.

The presence of two different types of modes on mobility variation around the transition temperature, 440K, can be seen in figure 6. At low-temperature $T < 440$ K, the mobility increases by the increase of temperature obeying $T^{2.4}$. The ionized impurities scattering mechanism [20, 21] is dominant for $T < 440$ K. At the region $T \geq 440$ K, the carrier's mobility decreases by the increasing of temperature obeying $T^{-1.4}$. The lattice scattering mechanism [22] is dominant in this region. The mobility of $\text{Bi}_2\text{Te}_{2.45}\text{Se}_{0.55}$ increases by increasing the annealing temperature is due to the enhancement of the crystallinity. The diffusion coefficient of holes can be determined using the assumption that the effective mass of holes is equal to the rest mass:

$$D_p = (KT/e) \mu_p \quad (8)$$

The computed values of the diffusion coefficient at room temperature are $(1962.8 - 1523.6) \text{ cm}^2.\text{sec}^{-1}$ for as-deposited and annealed films. In addition, the mean free time of hole estimated according to:

$$\tau_p = \mu_p m / e \tag{9}$$

The obtained values are $(1.11 \times 10^{-12} - 0.86 \times 10^{-12})$ sec for as-deposited and annealed films. The diffusion length of holes L_p was calculated at room temperature for as-deposited and annealed films and its values are $(7 \times 10^{-11} - 8 \times 10^{-11})$ cm.

Optical analysis

The knowledge of the optical characteristics of materials is important in the design and analysis of the optoelectronic devices.

The optical transmittance spectrum T of the as-deposited and annealed films were measured at room temperature within wavelength range (2500-5000) nm using Fourier transform infrared (FTIR) as shown in Figure 7.

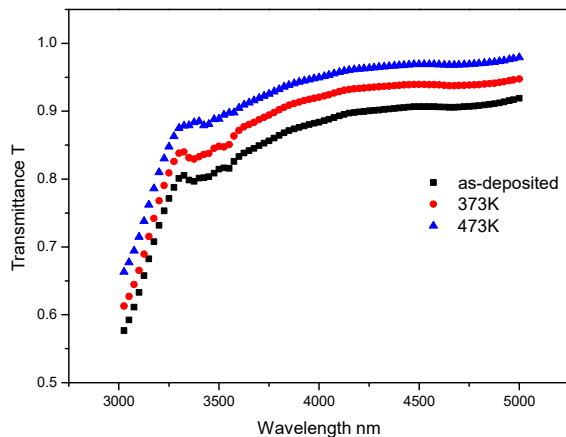


Figure 7. Transmittance spectrum versus wavelength for the as-deposited and annealed Bi₂Te_{2.45}Se_{0.55} films.

It is clear that the transmittance increase by increasing temperature. The average value of transmittance increases from 90% to 99% with annealing temperature. The absorption edges shift toward higher values of wavelength with increasing the annealing temperatures. The increase of transmittance spectra with increasing annealing temperature attributed to the enhancement of the crystallinity of films [17].

The absorption coefficient calculated using:

$$\alpha = 1/d \ln (1/T) \tag{10}$$

Where α is absorption coefficient, d is a film thickness and T optical transmittance.

In the high absorption region, the optical band gap can be determined by Tauc model [17].

$$\alpha h\nu = B(h\nu - E_g)^n \tag{11}$$

Where B is a constant, $h\nu$ the photon energy, E_g the optical band gap and n is a number refer to the optical transition type (1/2, 2/3, 2, 3) for direct allowed transition, direct forbidden transition, indirect allowed transition and indirect forbidden transition, respectively. Figure 8 represent the variation of $(\alpha h\nu)^{0.5}$ as a function of photon energy ($h\nu$). The indirect energy gap can be computed from the extrapolating straight line with photon energy axis. The energy gap decreases with increase of annealed films from 0.27 - 0.24 eV as a result of enhancement of film's crystallinity. These results match with data obtained by electrical and Hall measurements.

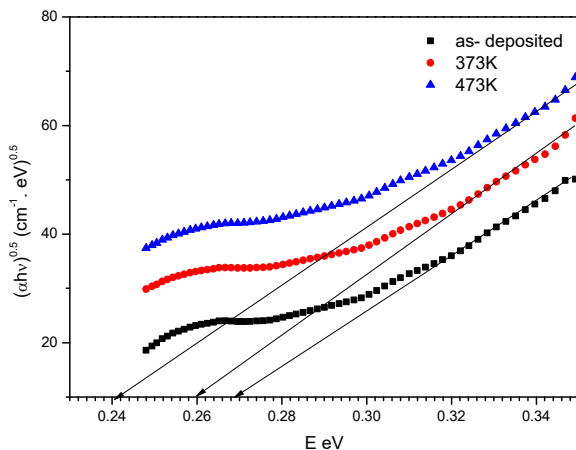


Figure 8. Plot $(\alpha h\nu)^{0.5}$ versus of photon energy(E) for the as-deposited and annealed Bi₂Te_{2.45}Se_{0.55} films.

Figure 9 describes $(\alpha h\nu)^2$ as a function of photon energy. The direct allowed band gap can be determined by extrapolating straight line with photon energy axis. The values of direct allowed and indirect allowed energy gap record in table 3.

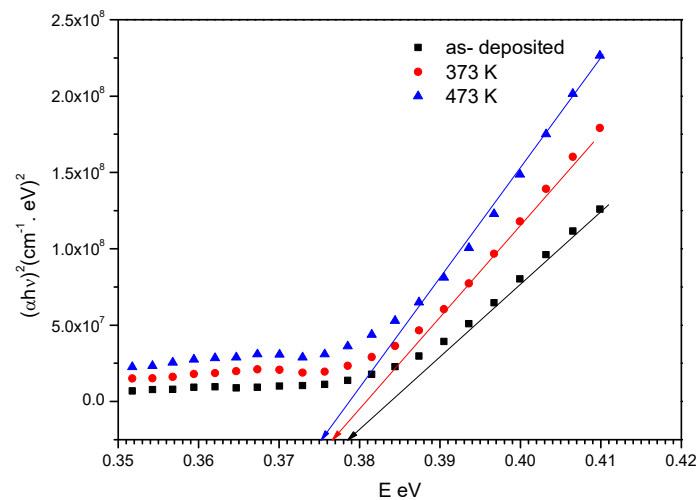


Figure 9. Plot $(\alpha h\nu)^2$ versus of photon energy(E) for the as-deposited and annealed $\text{Bi}_2\text{Te}_{2.45}\text{Se}_{0.55}$ films.

Table 3. Optical energy gap values for the as-deposited and annealed $\text{Bi}_2\text{Te}_{2.45}\text{Se}_{0.55}$ films.

Ta(K)	E_g^{ind} e.v	E_g^d e.v
473	0.24	0.375
373	0.259	0.377
As-deposited	0.272	0.379

CONCLUSION

The effect of thermal annealing at (373, 473K) on the physical properties of $\text{Bi}_2\text{Te}_{2.45}\text{Se}_{0.55}$ films has been studied. The as-deposited and the annealed thin films have a rhombohedral structure. Crystalline size, micro-strain, and dislocation density were calculated at 373, 473K annealing temperature.

The electrical conductivity has been measured in the temperature range 300- 500K.

The measurements have been done for the as-deposited and annealed films (373, 473K). The conductivity of the as-deposited and annealed films varies with temperature it shows conductivity enhancement as a function of annealing.

The Hall coefficient has been measured in the temperature range 300-500K for the as-deposited and annealed films (373, 473K) where the charge carrier's concentration was calculated. The scattering mechanism is classified into two kinds, at low temperature the scattering mechanism dominant acoustical phonon while, at high temperature the scattering mechanism dominant ionized impurities. In addition, the mean free time, the diffusion coefficient of holes, and the diffusion length were computed. The optical energy gap calculated for as-deposited and annealed films. The values of direct allowed and indirect allowed energy gaps were decreased by increasing of annealing temperature. This behavior is attributed to the enhancement of the films crystallinity.

Funding. The authors did not receive any support from any organization for the submitted work.

Conflict of interest. The authors declare that they have no conflict of interest.

ORCID IDs

A.S. Salwa, <https://orcid.org/0000-0003-4000-4754>; Azza El-Sayed Ahmed, <https://orcid.org/0000-0002-5389-4111>

REFERENCE

- [1] D. Arivuoli, F.D. Gnanam, P. Ramasamy, Growth and microhardness studies of chalcogenides of arsenic, antimony and bismuth, *J. Mater. Sci. Lett.* **7**, 711 (1988). <https://doi.org/10.1007/BF00722076>
- [2] L.I. Soliman, M.M. Nassary, H.T. Shaban, A.S. Salwa. Influence of Se on the electron mobility in thermal evaporated $\text{Bi}_2(\text{Te}_{1-x}\text{Se}_x)_3$ thin films, *Vacuum*, **85**, 358 (2010). <https://doi.org/10.1016/j.vacuum.2010.06.003>
- [3] D. Qian, Z. Ye, L. Pan, Z. Zuo, D. Yang, and Y. Yan, The Mechanical and Thermoelectric Properties of Bi_2Te_3 -Based Alloy Prepared by Constrained Hot Compression Technique, *Metals*, **11**, 1060, (2021). <https://doi.org/10.3390/met11071060>
- [4] D.D. Awschalom, D.P. Divincenzo, J.F. Smyth, Macroscopic quantum effects in nanometer-scale magnets, *Science*, **258**, 414 (1992). <https://doi.org/10.1126/science.258.5081.414>
- [5] N. Jaziri, A. Boughamoura, J. Müller, B. Mezghani, F. Tounsi, and M. Ismail, A comprehensive review of Thermoelectric Generators: Technologies and common applications, *Energy Reports*, **6**, 264 (2020). <https://doi.org/10.1016/j.egy.2019.12.011>

- [6] G.J. Snyder, J.R. Lim, C-K. Huang, and J.P. Fleurial, Thermoelectric microdevice fabricated by a MEMS-like electrochemical process, *Nat. Mater.* **2**, 528 (2003). <https://doi.org/10.1038/nmat943>
- [7] C.B. Vining, Thermopower to the people, *Nature* **423**, 391 (2003). <https://doi.org/10.1038/423391a>
- [8] T.C. Harman, P.J. Taylor, M.P. Walsh, and B.E. La Forge. Quantum Dot Superlattice Thermoelectric Materials and Device. *Science*, **297**, 2229 (2002). <https://doi.org/10.1126/science.1072886>
- [9] M. Carle, P. Pierrat, C. Lahalle-Gravier, S. Scherrer, and H. Scherrer, Transport properties of n -type $\text{Bi}_2(\text{Te}_{1-x}\text{Se}_x)_3$ single crystal solid solutions ($x \leq 0.05$); *J. Phys. Chem. Solids*, **56**, 201 (1995). [https://doi.org/10.1016/0022-3697\(94\)00166-9](https://doi.org/10.1016/0022-3697(94)00166-9)
- [10] C. Lahalle-Gravier, B. Lenoir, H. Scherrer, and S. Scherrer, Thermoelectric characterization of $\text{Bi}_2\text{Te}_{2.55}\text{Se}_{0.45}$ solid solution crystal. *J. Phys. Chem. Solids*, **59**, 13 (1998). [https://doi.org/10.1016/S0022-3697\(97\)00119-4](https://doi.org/10.1016/S0022-3697(97)00119-4)
- [11] J. Dheepa, R. Sathyamoorthy, and A. Subbarayan, Optical properties of thermally evaporated Bi_2Te_3 thin films, *Journal of Crystal Growth*, **274**, 100 (2005). <https://doi.org/10.1016/j.jcrysgro.2004.09.070>
- [12] K. Yildiz, U. Akgul, H.S. Leipner, and Y. Atici, Electron microscopy study of thermoelectric n -type $\text{Bi}_2(\text{Te}_{0.9}\text{Se}_{0.1})_3$ film deposited by dc sputtering Superlattices and Microstructures **58**, 60 (2013). <https://doi.org/10.1016/j.spmi.2013.02.013>
- [13] A. Saji, and M. Elizabeth; Effects of fast electron bombardment and annealing on Bi_2Te_3 and $\text{Bi}_2\text{Te}_{2.9}\text{Se}_{0.1}$ single crystals, *Semicond. Sci. Technol.* **18**, 745 (2003). <https://doi.org/10.1088/0268-1242/18/8/305>
- [14] A.S. Salwa, A. Salem, and H.T. Shaban, Linear and nonlinear optical studies of indium selenide thin films prepared by thermal evaporation technique, *Optik*, **241**, 166874 (2021). <https://doi.org/10.1016/j.ijleo.2021.166874>
- [15] M.H. Kabir, M.M. Ali, M.A. Kaiyum, and M.S. Rahman, Effect of annealing temperature on structural morphological and optical properties of spray pyrolyzed Al-doped ZnO thin films, *J. Phys. Commun.* **3**, 105007 (2019). <https://doi.org/10.1088/2399-6528/ab496f>
- [16] A.S. Salwa, and A. Salema, "Linear and nonlinear optical properties of SnS thermally evaporated thin films" *Optik*. **196**, 163140 (2019). <https://doi.org/10.1016/j.ijleo.2019.163140>
- [17] A.S. Salwa, and M.S. Abd El-Sadek, Annealing temperature effect to optimize the optical properties of SnS thin films, *Eur. Phys. J. Plus*, **136**, 696 (2021). <https://doi.org/10.1140/epjp/s13360-021-01676-6>
- [18] T. Daniel, U. Uno, K. Isah, and U. Ahmadu, Tuning of SNS thin film conductivity on annealing in an open air environment for transistor application, *East Eur. J. Phys.* **2**, 94 (2020). <https://doi.org/10.26565/2312-4334-2020-2-08>
- [19] A. Salem, and M.H. Alhossainy, Electrical conductivity and Hall effect measurements of crystalline copper indium gallium diselenide, *Materials Chemistry and Physics*, **263**, 124436 (2021). <https://doi.org/10.1016/j.matchemphys.2021.124436>
- [20] C. Riha, B. Düzel, K. Graser, O. Chiatti, E. Goliass, J. Sánchez-Barriga, O. Rader, O.E. Tereshchenko, and S.F. Fischer, Electrical Transport Properties of Vanadium-Doped $\text{Bi}_2\text{Te}_{2.4}\text{Se}_{0.6}$, *Phys. Status Solidi B*, **258**, 2000088 (2021). <https://doi.org/10.1002/pssb.202000088>
- [21] A. Salem, A.S. Salwa, S.A. Hussein, and M. Ezzeldien, Synthesis and Electrical Transport Properties of CuInGaTe_2 . *J Laser Opt Photonics*, **5**, 2 (2018). <https://doi.org/10.4172/2469-410X.1000183>
- [22] S. Majdi, V. Djurberg, N. Suntornwipat, M. Gabrysch, and J. Isberg, Carrier Scattering Mechanisms: Identification via the Scaling Properties of the Boltzmann Transport Equation, *Adv. Theory Simul.* **4**, 2000103, (2021). <https://doi.org/10.1002/adts.202000103>

ХАРАКТЕРИСТИКИ ТА ОПТИЧНІ ВЛАСТИВОСТІ ТОНКОЇ ПЛІВКИ $\text{Bi}_2\text{Te}_{2.45}\text{Se}_{0.55}$

А.С. Салва, Азза Ель-Сайед Ахмед

Фізичний факультет, факультет науки і мистецтв, Університет Джуфа

Гураят 77431, Королівство Саудівська Аравія

Термічно випарені тонкі плівки $\text{Bi}_2\text{Te}_{2.45}\text{Se}_{0.55}$ були досліджені на предмет структурних змін та електропровідності. Розмір кристалітів, мікродеформація та дислокації були розраховані з використанням даних XRD. За допомогою просвічуючої електронної мікроскопії досліджено морфологію тонких плівок (ТЕМ). Дослідження проводили в інтервалі температур (300–500) К. Виміряно електричний енергетичний зазор та провідність наплавлених і відпалених (373, 473 К) плівок $\text{Bi}_2\text{Te}_{2.45}\text{Se}_{0.55}$. Отримані значення (0,27, 0,26, 0,24 еВ) і $3,6 \times 10^3$, $3,7 \times 10^3$ та $4,1 \times 10^3 \text{ Ом}^{-1}\text{см}^{-1}$ відповідно. Також досліджено коефіцієнт Холла, середній вільний час, коефіцієнт дифузії дірок, довжину дифузії, концентрацію носіїв заряду, механізм розсіювання носіїв заряду та рухливість Холла. Отримані значення концентрації носіїв заряду становлять $2,12 \times 10^{17}$ – $2,73 \times 10^{17} \text{ см}^{-3}$. Прямий і непрямої дозволений енергетичний зазор зменшувався з підвищенням температури віддалу. Отримані значення непрямої забороненої зони і прямої забороненої зони коливаються в межах 0,27–0,24 еВ і 0,375–0,379 еВ відповідно.

Ключові слова: тонка плівка, електричні властивості, просвічувальна електронна мікроскопія, ефект Холла, оптичний енергетичний зазор

COMPUTATION OF STRUCTURE AND ELECTRICAL RESISTIVITY OF LIQUID Na-Rb ALLOYS[†]

 **R.R. Koireng^{a,b,*}**,  **P.C. Agarwal^c**,  **Alpana Gokhroo^a**

^aSamrat Prithviraj Chauhan Government College, Ajmer-305001, Rajasthan, India

^bNational Institute of Education (NCERT), New Delhi-110016, India

^cRegional Institute of Education (NCERT), Bhubaneswar-751022, Odisha, India

^{*}Corresponding author: karenkrr@gmail.com

Received December 15, 2021; revised March 15, 2022; accepted March 16, 2022

The structure and electrical resistivity of Na_{1-x}Rb_x binary alloys (where x = 0, 0.1, 0.2, ..., 1) are computed using Percus-Yevick (PY) equation, hard-sphere model and Faber-Ziman formula respectively. The partial structure factors and total structure factor are computed using hard-sphere model for Na_{1-x}Rb_x. In the calculation of resistivity using Faber-Ziman formula, we have employed Ashcroft empty-core pseudo-potential and Hartree dielectric screening. Calculated values of resistivity are compared with the experimental results and other theoretical values reported in literature. It is found that the electrical resistivity calculated using Faber-Ziman formula for binary alloy Na_{1-x}Rb_x is in good agreement with the values reported experimentally.

Keywords: Structure factor, electrical resistivity, pseudo-potential, dielectric screening, liquid metal

PACS: 61.20.Ne; 61.25.Mv; 72.15.Cz

The study of structural and electron transport properties of liquid metals have attracted many researchers [1-2]. The studies related to liquid structure have been a concern for condensed matter physics and material science. The knowledge of the structural information and electron transport properties of liquid alloys are essential for understanding the alloys. Recently, the applicability of alkali-liquid metal alloys (such as Na-Rb, Na-K) in developing futuristic electrochemical devices makes it inevitable to study the electronic and chemical properties of such alloys [3-7]. The electrical resistivity of liquid binary alkali alloys has been computed theoretically by pairing Faber-Ziman formula [8] with a suitable pseudo-potential [9-10]. Islam et.al [9] has computed the electrical resistivity of Na_{1-x}Rb_x binary alloys using Faber-Ziman formula employing Bretonnet and Silbert (BS) pseudo-potential [10] with two different local field corrections viz. Ichimaru-Utsumi (IU) and Vashishta-Singhwi (VS). It is important that a suitable potential associated with electron-ion interaction is chosen for the computation of the electrical resistivity as the choice of electron-ion pair potential plays a crucial role in the study of electrical resistivity.

In this paper, we compute the partial structure factors of Na_{1-x}Rb_x binary alloys (where x=0, 0.1, 0.2, ..., 1) employing the solution of Percus-Yevick (PY) equation for a multi-component hard-sphere model given by Hoshino [11] and the electrical resistivity of Na_{1-x}Rb_x binary alloy is computed using the method given by Faber-Ziman [8]. In the computation of electrical resistivity, we employ Ashcroft empty-core pseudo-potential [12] and the dielectric screening function due to Hartree [13-14]. The results obtained are compared with experimental results available in literature.

THEORY Resistivity

The electrical resistivity of a liquid metal binary alloy is given by Faber and Ziman [8] as

$$\rho = \frac{3\pi m^2 \Omega_0}{4Ze^2 \hbar^3 k_f^6} \int_0^{2k_f} \{c_1 S_{11}(q) V_1(q)^2 + c_2 S_{22}(q) V_2(q)^2 + 2\sqrt{c_1 c_2} S_{12}(q) V_1(q) V_2(q)\} q^3 dq. \quad (1)$$

Here Z is the valence of the liquid alloy and $Z = c_1 Z_1 + c_2 Z_2$, where c_1 and c_2 are the concentration of elements, $\Omega_0 = c_1 \Omega_1 + c_2 \Omega_2$ is the atomic volume of the alloy system, $V(q)$ is the form factor, $S(q)$ is the structure factor and k_f is the Fermi wave vector define by $k_f = \left(\frac{3\pi^2 Z}{\Omega_0}\right)$.

For the computation of electrical resistivity, we have considered Ashcroft's empty core potential [12] given by

$$V(r) = \begin{cases} 0, & r \leq R_c \\ -\frac{ze^2}{r}, & r > R_c \end{cases}, \quad (2)$$

where R_c is the core radius. The values of R_c for the constituent elements Na and Rb is taken from the values given in [12]. The form factor with dielectric screening effect is given by

[†] Cite as: R.R. Koireng, P.C. Agarwal, and A. Gokhroo, East. Eur. J. Phys. 1, 66 (2022), <https://doi.org/10.26565/2312-4334-2022-1-09>
© R.R. Koireng, P.C. Agarwal, A. Gokhroo, 2022

$$w(q) = \frac{w_b(q)}{\varepsilon(q)} = -\frac{4\pi Ze^2}{q^2 \varepsilon(q) \Omega_0} \cos qr_c \quad (3)$$

where $w(0) = -\frac{2}{3}E_f$.

Following Hartree's theory of dielectric screening, the dielectric screening function $\varepsilon(q)$ is given as [13]

$$\varepsilon(q) = 1 + \frac{4\pi e^2}{q^2} D(E_f) \left[\frac{1}{2} + \frac{4k_f^2 - q^2}{8qk_f} \ln \left| \frac{2k_f + q}{2k_f - q} \right| \right], \quad (4)$$

where $D(E_f) = 3n/2E_f$ represents the density of states at the Fermi energy E_f , n is the number density.

Structure factor

Computation of partial structure factors is a crucial step in calculating the electrical resistivity of an alloy. The partial structure factor, following the definition of Ashcroft-Langreth [11, 12] is given by the following expression

$$S_{ij}(q) = \delta_{ij} + \sqrt{c_i c_j} (a_{ij}(q) - 1), \quad (5)$$

where, δ_{ij} is the Kronecker delta function, c_i and c_j are the concentration of components, and

$$a_{ij}(q) = 1 + n \int d\mathbf{r} (g_{ij}(r) - 1) \exp(i\mathbf{k} \cdot \mathbf{r}).$$

Where n is the number density of the mixture and $g_{ij}(r)$ is the pair distribution function. For the detailed derivation and the analytical expressions of partial structure factors see Hoshino [11].

The total structure factor $S(q)$ of the alloy can be expressed by the weighted average of partial structure factors from equation (5) as

$$S(q) = \frac{c_1 b_1^2 S_{11}(q) + 2\sqrt{c_1 c_2} b_1 b_2 S_{12}(q) + c_2 b_2^2 S_{22}(q)}{c_1 b_1^2 + c_2 b_2^2}, \quad (6)$$

where the weights b_1 and b_2 are the neutron scattering lengths of the component elements of the alloy [15] and c_1 and c_2 are the concentrations of the component elements of the alloy.

CALCULATIONS

For computing the structure factor of the binary alloys, we need to fix the hard-sphere diameters (σ_i), packing fraction (η_i), and the concentration of components of elements. The hard sphere diameters (σ_i) have been determined using the relation,

$$\sigma_i = \left(\frac{6\eta_i \Omega_i}{\pi} \right)^{1/3} \quad (7)$$

where the value of η_i (packing fraction of i th species) is adjusted at temperature 373K according to the following relationship [16].

$$\eta_i = A_i \exp(-B_i T). \quad (8)$$

The atomic volume Ω_i of the i th species is calculated using the experimental values of densities at the desired temperature using the formula [17]

$$b_i = b_o - (T - T_{mi}) \frac{db}{dT} \quad (9)$$

Where T_{mi} is the melting temperature and b_o is the density at melting point of the i th species. Here, the densities are adjusted to the temperature 373 K.

Accordingly, the calculated value of Ω_i , σ_i and the other input parameters at the desired temperature are listed in Table 1.

Table 1. Input parameters use in calculating the structure factor and electrical resistivity of $\text{Na}_{1-x}\text{Rb}_x$ binary alloy

Element	T (K)	Valence (Z)	Ω_0 (a.u.)	σ (a.u.)	R_c (a.u.)
Na	373	1	278.240	6.265	1.663 [12]
Rb	373	1	659.220	8.279	2.722 [12]

RESULTS AND DISCUSSIONS

The representative partial structure factors and total structure factor as per the Ashcroft-Langreth [12] and Hoshino [11] for $\text{Na}_{50}\text{Rb}_{50}$ binary alloy is shown in Figure 1(a) and Figure 1(b) respectively. Using the partial structure factors for different compositions, the electrical resistivity of $\text{Na}_{1-x}\text{Rb}_x$ binary alloy system is computed. The electrical resistivity of $\text{Na}_{1-x}\text{Rb}_x$ binary alloy calculated at 373K using the Faber-Ziman formula [8] given in equation 1 are shown in Figure 2 along with the available experimental data reported by Hennepf et al. [17]. As seen in Figure 2, the result of the resistivity for $\text{Na}_{1-x}\text{Rb}_x$ binary alloys reported in this paper are very close to the data reported in literature.

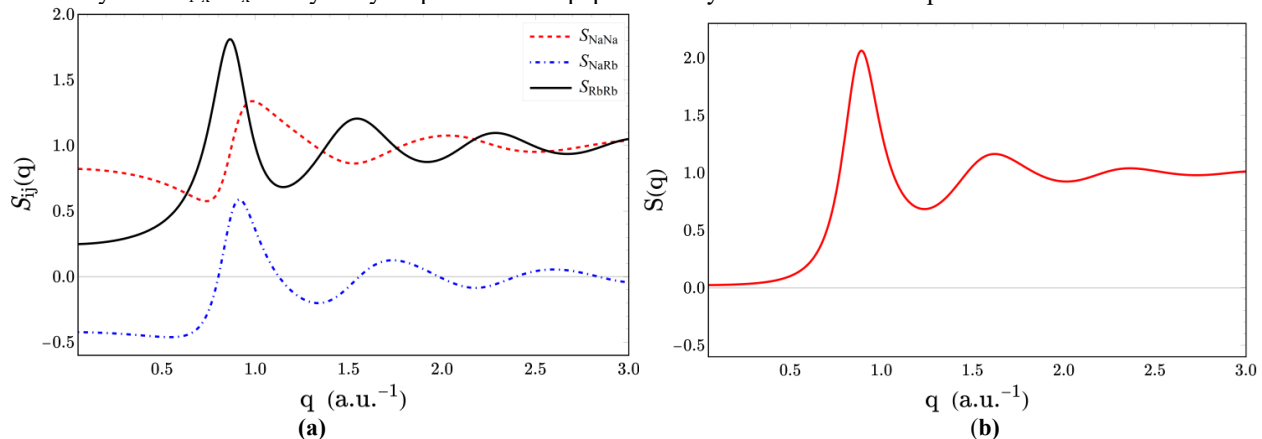


Figure 1. Representative partial structure factors $S_{ij}(q)$ and total structure factor $S(q)$ for $\text{Na}_{50}\text{Rb}_{50}$ binary alloy. (a) Partial structure factor of $\text{Na}_{50}\text{Rb}_{50}$, dashed, dot-dashed and solid lines represent Na-Na, Na-Rb and Rb-Rb respectively. (b) Total structure factor of $\text{Na}_{50}\text{Rb}_{50}$ binary alloy.

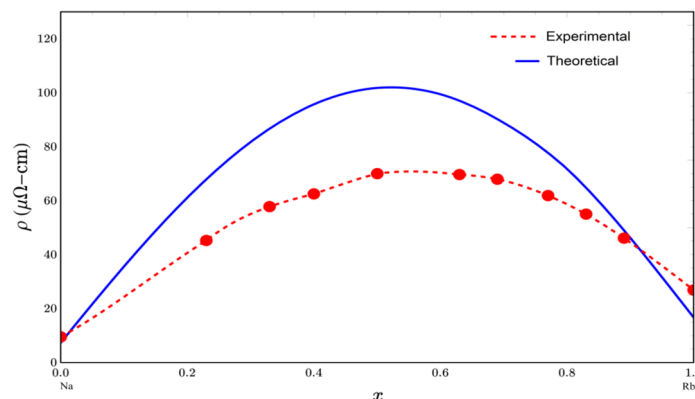


Figure 2. Resistivity of $\text{Na}_{1-x}\text{Rb}_x$ with concentration at 373K along with the experimental value [17].

We have used Ashcroft empty core pseudo-potential and Hartree dielectric screening function for computing resistivity of $\text{Na}_{1-x}\text{Rb}_x$ binary alloys. The results reported in this paper show better agreement with experimental data compared to previous theoretical study on resistivity of $\text{Na}_{1-x}\text{Rb}_x$ binary alloys as reported by Islam et.al [9] employing BS pseudo-potential along with Ichimaru-Utsumi (IU) and Vashishta-Singhwi (VS) dielectric field corrections.

CONCLUSIONS

We have computed the partial structure factors and total structure factor of $\text{Na}_{1-x}\text{Rb}_x$ binary alloys following the method prescribed by Ashcroft-Langreth [12]. The partial structures obtained for $\text{Na}_{1-x}\text{Rb}_x$ binary alloys were used for calculating electrical resistivity of $\text{Na}_{1-x}\text{Rb}_x$ binary alloys using Faber-Ziman formula [8]. In calculating the resistivity, we have employed Ashcroft empty core pseudo-potential along with Hartree dielectric screening function. The results obtained show good agreement with the experimental data available in literature. The use of Ashcroft empty core pseudo-potential along with Hartree dielectric screening for computing resistivity of $\text{Na}_{1-x}\text{Rb}_x$ binary alloys by Faber-Ziman formula shows good results. We are also working on the computation of the electrical resistivity of other alkali metal binary alloys using this approach.

ORCID IDs

R.R. Koireng, <https://orcid.org/0000-0003-3112-1078>; P.C. Agarwal, <https://orcid.org/0000-0002-1166-2611>
 Alpna Gokhroo, <https://orcid.org/0000-0002-5871-0983>

REFERENCES

- [1] S. Sharmin, G.M. Bhuiyan, M.A. Khaleque, R.I.M.A. Rashid, and S.M. Mujibur Rahman, Phys. Stat. Sol. B, **232**, 243 (2002), [https://doi.org/10.1002/1521-3951\(200208\)232:2<243::AID-PSSB243>3.0.CO;2-W](https://doi.org/10.1002/1521-3951(200208)232:2<243::AID-PSSB243>3.0.CO;2-W)

- [2] R. C. Malan, and A. M. Vora, AIP Conf. Proc. **1953**, 140014 (2018), <https://doi.org/10.1063/1.5033189>
- [3] Y. Ding, X. Guo, and G. Yu, Acs Cent. Sci. **6**(8), 1355 (2020), <https://doi.org/10.1021/acscentsci.0c00749>
- [4] L. Qin, W. Yang, W. Lv, L. Liu, Y. Lei, W. Yu, F. Kang, J.K. Kim, D. Zhai, and Q.H. Yang, Chem. Commun. **54**(58), 8032 (2018), <https://doi.org/10.1039/C8CC03545H>
- [5] Z.Kh. Kalazhokov, Z.V. Baragunova, Kh.Kh. Kalazhokov, V.A. Kvashin, N.S. Reutskaya, and M.A. Khokonov, High Temp. **57**, 343 (2019), <https://doi.org/10.1134/S0018151X19030076>
- [6] A.C. LaForge, M. Shcherbinin, F. Stienkemeier, R. Richter, R. Moshhammer, T. Pfeifer, and M. Mudrich, Nat. Phys. **15**, 247 (2019), <https://doi.org/10.1038/s41567-018-0376-5>
- [7] H. Zhou, S. Bag, and V. Thangadurai, ACS Energy Lett. **3**(9), 2181 (2018), <https://doi.org/10.1021/acseenergylett.8b00948>
- [8] T.E. Faber, and J.M. Ziman, Philos. Mag. **11**, 153(1965), <https://doi.org/10.1080/14786436508211931>
- [9] M. A. Mohaiminul Islam, R.C. Gosh, and G.M. Bhuiyan, J. Mol. Liq. **290**, 111224 (2019), <https://doi.org/10.1016/j.molliq.2019.111224>
- [10] J.L. Bretonnet, G.M. Bhuiyan, and M. Silbert, J. Phys.: Condens. Matter. **4**, 5359(1992), <https://doi.org/10.1088/0953-8984/4/24/005>
- [11] K. Hoshino, J. Phys. F: Met. Phys. **13**, 1981(1983). <https://doi.org/10.1088/0305-4608/13/10/010>
- [12] N.W. Ashcroft, and D.C. Langreth, Phys. Rev. **159**, 500 (1967), <https://doi.org/10.1103/PhysRev.159.500>
- [13] R.R. Koireng, P.C. Agarwal, and A. Gokhroo, J. Sci. Res. **13**(1), 21 (2021), <https://doi.org/10.3329/jsr.v13i1.47327>
- [14] R.R. Koireng, P.C. Agarwal, and A. Gokhroo, East Eur. J. Phys. **4**, 84 (2020), <https://doi.org/10.26565/2312-4334-2020-4-11>
- [15] V.F. Sears, Neutron News, **3**, 26 (1992), <https://doi.org/10.1080/10448639208218770>
- [16] Y. Waseda, Prog. Mater. Sci. **26**, 1 (1981), [https://doi.org/10.1016/0079-6425\(81\)90003-7](https://doi.org/10.1016/0079-6425(81)90003-7)
- [17] J. Hennessee, W. Van der Lugt, and G.W. Wright, Physica. **52**, 279 (1971), [https://doi.org/10.1016/0031-8914\(71\)90200-X](https://doi.org/10.1016/0031-8914(71)90200-X)

РОЗРАХУНОК СТРУКТУРИ ТА ЕЛЕКТРИЧНОГО ОПОРУ РІДКИХ СПЛАВІВ Na-Rb

Р.Р. Койренг^{a,b}, П.К. Агарваль^c, Альпана Гохроо^a

^aСамрат Прітвірай Чаухан Дердавний Колледж, Аймер-305001, Раджастхан, Індія

^bНаціональний інститут освіти (NCERT), Нью-Делі-110016, Індія

^cРегіональний Інститут Освіти (NCERT), Бхубанешвар-751022, Одіша, Індія

Структура та питомий електричний опір бінарних сплавів Na1-xRbx (де x = 0, 0,1, 0,2,...,1) розраховані за допомогою рівняння Перкуса-Євіка (PY), моделі твердої сфери та формули Фабера-Зімана відповідно. Часткові структурні коефіцієнти та загальний структурний коефіцієнт розраховані за допомогою моделі твердої сфери для Na1-xRbx. При розрахунку питомого опору за формулою Фабера-Зімана ми використали псевдопотенціал Ешкрофта з порожнім сердечником і діелектричне екранування Хартрі. Розраховані значення питомого опору порівнюються з результатами експерименту та іншими теоретичними значеннями, наведеними в літературі. Встановлено, що питомий електричний опір, розрахований за формулою Фабера-Зімана для бінарного сплаву Na1-xRbx, добре узгоджується з експериментальними значеннями.

Ключові слова: структурний фактор, питомий електричний опір, псевдопотенціал, діелектричний екран, рідкий метал.

ENHANCED THIRD GENERATION SEMICONDUCTOR MATERIAL-BASED SOLAR CELL EFFICIENCY BY PIEZO-PHOTOTRONIC EFFECT[†]

 Michael Gyan^{a,d*}, Joseph Parbby^{b,c},  Francis E. Botchey^c

^aSchool of Physics, University of Electronic Science and Technology of China, Chengdu 610054, China

^bSchool of Material Science, University of Electronic Science and Technology of China, Chengdu 610054, China

^cKoforidua, Technical University, Ghana, ^dUniversity of Education, Winneba, Ghana

*Corresponding Author: mgyan173@gmail.com; phone: +8613228202349

Received January 20, 2022; accepted March 16, 2022

By applying the outward uniform strain on the non-centrosymmetric piezoelectric semiconductor, the polarization charges on the material surface are induced. Polarization charges are often generated within the crystals provided that the applied strain is non-uniform. The strain applied has an effect on electronic transport and can be utilized to modulate the properties of the material. The effect of multiway coupling between piezoelectricity, semiconductor transport properties, and photoexcitation results in piezo-phototronic effects. Recent studies have shown the piezoelectric and semiconductor properties of third-generation semiconductors have been used in photodetectors, LEDs, and nanogenerators. The third-generation piezoelectric semiconductor can be used in high-performance photovoltaic cells. A third-generation piezo-phototronic solar cell material is theoretically explored in this manuscript on the basis of a GaN metal-semiconductor interaction. This study aims to determine the effects of piezoelectric polarization on the electrical performance characteristics of this solar cell material. Performance parameters such as Power Conversion Efficiency, Fill Factors, I-V Characteristics, Open Circuit Voltage, and Maximum Output Power have been evaluated. The piezophototronic effect can enhance the open-circuit current voltage by 5.5 percent with an externally applied strain by 0.9 percent. The study will open a new window for the next generation of high-performance piezo-phototronic effects.

Keywords: Polarization charges; Piezophototronic effect; Solar cell; third-generation semiconductor; piezoelectric effect.

PACS: 42.79.Ek; 42.70.Nq

Piezo-phototronics was initially proposed in 2010 [1-3]. The field of piezotronics has developed the study of the coupling between the semiconductor and piezoelectric characteristics for materials that concurrently exhibit semiconductor, photoexcitation, and piezoelectric characteristics. Also, the well-known field of optoelectronics studies the pairing of semiconductor properties with photo-excitation properties [4,5]. The field of piezo-photonics was determined by the analysis of the linkage between piezoelectric characteristics and the characteristics of photo-excitation. The field of piezoelectric optoelectronics, which was the basis for the development of the new piezophototronics, was further developed by working on the coupling of semiconductors, photo-excitation, and piezoelectric properties [6,7]. The central feature of the piezophototronic effect is the use of piezoelectric potential to control the generation, separation, transport, and recombination processes of carriers at interfaces or junctions [1,9]. High-efficiency optoelectronic devices, including solar cells, LEDs, and photodetectors, can be achieved by piezophototronic effects [6,10-12].

By Comparing first-generation semiconductors, (for example, silicon, germanium) with the second-generation semiconductors, (for example, gallium arsenide, indium antimonide), the third-generation semiconductor materials such as silicon carbide (SiC), zinc oxide (ZnO), gallium nitride (GaN) and cadmium sulfide (CdS) as a rule have wider bandgap, higher thermal conductivity, greater electron saturation rate and better radiation resistance properties, and in this way attract a lot of considerations in high temperature and high-frequency applications in recent years [1,13,14]. The greater part of the third-generation semiconductors is wurtzite structures, which have piezoelectric effects because of their absence of symmetry in certain directions [2,14,15]. These characteristics fill in as a decent scaffold for transferring mechanical stress signals between the adaptable semiconductor electronic device and the surrounding environment or the host (e.g., the human body) [16,17].

Third generation semiconductor materials, such as GaN and SiC, distinguished by a wide bandgap, have attracted considerable interest in emerging consumer electronics, 5G telecommunication technologies, automated vehicles, optoelectronics, and defense technology applications owing to their superior material properties, including high voltage resistance, high switching frequency, High-temperature tolerance and high radiation resistance [16]. The wide bandgap nature and the good piezoelectric properties of these materials indicate that piezotronic and piezophototronic couplings may be important, providing excellent platforms for the analysis of the fundamental coupling between the piezoelectricity and a variety of interesting processes such as high-frequency transmission, high-field activity, and two-dimensional (2D) electron gas in associated system structures [17]. Currently, ZnO has undergone extensive research as a candidate material for piezophototronic-based solar cells, but little is known about piezoelectric GaN and AlN. This paper could be used to fill this knowledge gap.

[†] Cite as: M. Gyan, J. Parbby, and F.E. Botchey, East. Eur. J. Phys. 1, 70 (2022), <https://doi.org/10.26565/2312-4334-2022-1-10>
© M. Gyan, J. Parbby, F.E. Botchey, 2022

In this manuscript, we present the performance of third-generation semiconductor solar cells using a piezophototronic effect. The study model is shown below in Figure 1. A third-generation semiconductor, such as GaN, is sandwiched between two metal electrodes on the substrate as seen in Figure 1(a). One part of the metal-semiconductor-metal unit is the solar cell and the other is the electrode (ohmic contact) so it has an opposite output voltage. Polarization charges are added to the interface of the solar cell through the application of external strain as seen in Figures 1(b) and (c). The piezoelectric field raises or decreases the height of the Schottky barrier [20-22] as seen below.

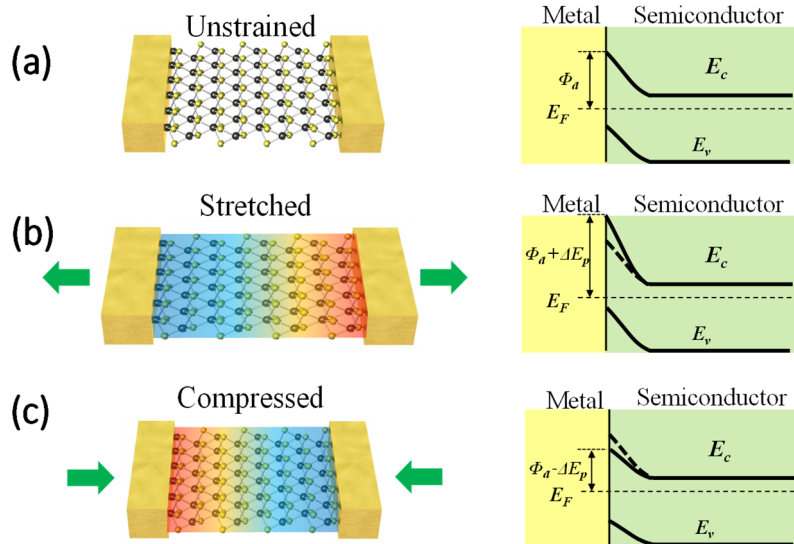


Figure 1. Schematic structure and energy band configuration of third-generation PSC semiconductor material (GaN). (a) Without strain; (b) with tensile strain; (c) with compressive strain;

MODULATION OF PIEZOPHOTOTRONICS SOLAR CELL

The theoretical models are optimized for p-n solar junction cells, and identical mathematical analyzes can be obtained for metal-semiconductor solar cells [20]. Polarization in semiconductor can be taken into account by expressing it as [21]

$$D = \epsilon_o \epsilon_r E + P \tag{1}$$

Where D is electric displacement, ϵ_o and ϵ_r are vaccum and relative permittivities respectively E is electric field and P is the total polarization.

Hook’s law can be use to describe the association between the polarization and a small form of mechanical strain and this is expressed by [22,23,24]

$$P = e_{ijk} S_{jk} \tag{2}$$

Where S is mechanical strain, e_{ijk} is the piezoelectric tensor (third order tensor). For a semiconductor grown along c-axis with the strain component S_{33} , the polarization P is expressed by

$$P = -e_{33} S_{33} = q \rho_{piezo} W_{piezo} \tag{3}$$

The poisson equation describes the electrostatic behavior of charges within semiconductor materials

$$\nabla^2 V = -\rho / \epsilon \tag{4}$$

Where V is the potential, ϵ is the permittivity of the material and P is the charge density.

Shockley's theory is now employed to calculate the I-V features of the piezoelectric dependent p-n junction, and evaluate the ideal p-n junction dependent on the aforementioned hypotheses: (1) the piezoelectric semiconductor has not degenerated in such a manner that the Boltzmann approximation can be implemented. (2) The piezoelectric p-n junction has an unstable depletion layer. (3) There is no generation and recombination present in the depletion layer, and the hole and electron currents are stable in the p-n junction. (4) The concentration of the dominant carrier is significantly greater than that of the minority injected. The total current density of the p-n solar cell is given by [22]:

$$J = J_o \left[\exp\left(\frac{qV}{KT}\right) - 1 \right] - J_{sc} \tag{5}$$

Here J_o is the saturation current, J_{sc} denotes the short-circuit current density, k stands for the Boltzmann constant, T represents the temperature, q is the elementary charge and V is the applied voltage. The saturation current can be achieved by [22]:

$$J_o = \frac{qD_p p_{no}}{L_p} + \frac{qD_n n_{po}}{L_n} \quad (6)$$

where L_n and L_p are the diffusion lengths of holes and electrons, respectively; n_{po} and p_{no} are the electron concentration inside the p-type semiconductor and the hole concentration inside the n-type semiconductor at thermal equilibrium, respectively. Thus, the intrinsic carrier density n_i can be calculated as

$$n_i = N_c \exp\left[-\frac{E_c - E_i}{KT}\right] \quad (7)$$

Here E_i is an underlying the intrinsic Fermi level, N_c is the effective density of states in the conduction band, and E_c is the bottom edge of the conduction band. Without a piezo potential at the interface of the p-n junction, the relationship between the saturated current density (J_{co}) and Fermi Level (E_{Fo}) can be articulated as

$$J_{co} = \frac{qD_p n_i}{L_p} \exp\left(\frac{E_i - E_{Fo}}{KT}\right) \quad (8)$$

The Fermi Level with piezo-potential at the interface of a p-n junction is determined by

$$E_F = E_{Fo} - \frac{q^2 \rho_{piezo} W_{piezo}^2}{2\epsilon_s} \quad (9)$$

By adding equation 3, 4, and 5 the I–V characteristics of the Piezophototronic solar cell based on a third-generation semiconductor can be derived as [25]

$$J = J_o \exp\left[\frac{q^2 \rho_{piezo} W_{piezo}^2}{2\epsilon_s KT}\right] \left[\exp\left(\frac{qV}{KT}\right) - 1\right] - J_{sc} \quad (10)$$

From Eqn. 6, the current transport through the p-n junction is a function of the piezoelectric charges, whose sign depends on the direction of the strain. Thus, both the magnitude and sign of the external strain (tensile or compressive) can be used to effectively adjust or control the transport current.

The open-circuit voltage (V_{oc}) can be evaluated by

$$V_{oc} = \frac{KT}{q} \left[\ln\left(\frac{J_{sc}}{J_{co}}\right) + \frac{q^2 \rho_{piezo} W_{piezo}^2}{2\epsilon_s KT} \right] \quad (11)$$

The piezo-phototronic modulation ratio of the PSC can be described in terms of the open-circuit voltage and other output performance obtained from the PSC [26]:

$$\gamma = \frac{\frac{q^2 \rho_{piezo} W_{piezo}^2}{2\epsilon_s KT}}{\ln\left(\frac{J_{sc}}{J_{co}}\right)} \quad (12)$$

In addition, the output power is estimated as

$$P(V) = VJ(V) \approx V \left\{ J_o \exp\left(\frac{q^2 \rho_{piezo} W_{piezo}^2}{2\epsilon_s KT}\right) \left[\exp\left(\frac{qV}{KT}\right) - 1\right] - J_{sc} \right\} \quad (13)$$

The maximum voltage satisfies the following equation [27]:

$$V_m + \frac{KT}{q} \ln\left(\frac{qV_m}{KT} + 1\right) = \frac{KT}{q} \left[\ln\left(\frac{J_{sc}}{J_{co}}\right) + \frac{q^2 \rho_{piezo} W_{piezo}^2}{2\epsilon_s KT} \right] \quad (14)$$

Consequently, V_m varies with the piezoelectric charges which are induced by the applied strain ϵ . The maximum current density can be obtained as:

$$J_m = J_o \exp\left[\frac{q^2 \rho_{piezo} W_{piezo}^2}{2\epsilon_s KT}\right] \left[\exp\left(\frac{qV_m}{KT}\right) - 1\right] - J_{sc} \tag{15}$$

The output maximum power P_m can be estimated as

$$P_m = V_m J_m \tag{16}$$

The fill factor can be derived from the method described in reference [28],

$$FF = \frac{J_m V_m}{J_{sc} V_{oc}} \approx \frac{P_m}{J_{sc} V_{oc}} \tag{17}$$

The power conversion efficiency (PCE) is defined in [19,28]:

$$PCE = \frac{J_{sc} V_{oc} FF}{P_{in}} \tag{18}$$

RESULT AND DISCUSSION

Typical constants are utilized in computations of the performance parameters such as the V_{oc} , P_m , PCE, and FF. The temperature was assigned at 300K, W_{piezo} is thought to be 0.543 nm [29], the relative dielectric constant of GaN is 8.9 [30], and ϵ_{33} of the GaN is estimated to be 0.73 C/m²[31].

The relative current density J/J_{pn0} versus voltage (J/J_{pn0} -V curve) of the GaN PSC with the external strain varying in the range of -0.9% to 0.9% When the short circuit current J_{sc} is taking to be 4.4 mA/cm²[32] is plotted in Figure 2(a).

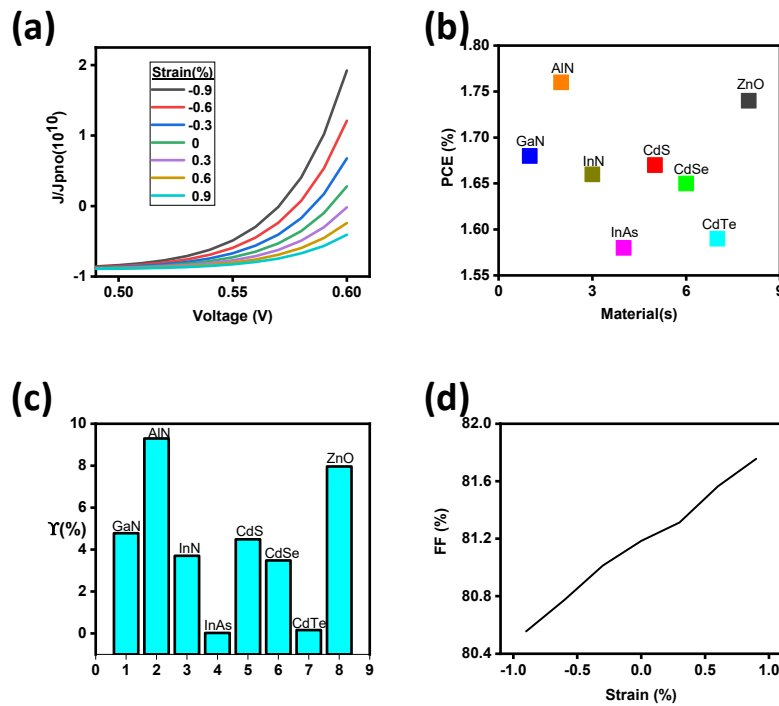


Figure 2. (a). Relative current density-voltage (J/J_{pn0} -V) curve with Strain (ϵ) increasing in the range of [-0.9% 0.9%]. (b) Comparative analysis of PCE for piezoelectric solar cell based on different types of materials with an external strain of 0.9%. (c) modulation ratio (γ) of the various types of piezoelectric solar cells material under an applied strain of 1% and (d) FF of GaN PSC with the applied strain varying in the region [-0.9% 0.9%].

Figure 2(b) shows the PCE of piezoelectric solar cells based on different types of materials at an external strain of 0.9%, indicating that the J increases with the strain and peaks at V_m . By employing equation (17) and equation (18), the Fill Factor (FF) and power conversion efficiency (PCE) parameter which aid in explaining the characteristics and performance of PSC is illustrated in Figure 2(c) and (d). The FF is linearly dependent on the externally applied strain between the regions -0.9% to 0.9% with a step of 0.3%. The improvement in FF can be credited to the increased V_{oc} when it is under strain. The PCE and modulation ratio (γ) considered in Figure 2 (b) and (c) is determined by utilizing similar parameters as in GaN such as J_{sc} , J_{pn0} , etc, at an applied strain of 0.9% and 1% respectively. The different parameters utilized are the piezoelectric constant and the relative dielectric constant. The piezoelectric constant and relative dielectric constant are given in Table 1. The PCE and modulation ratio (γ) of AlN is observed to increase more distinctly than GaN

and ZnO within the strain region of 0.9 and 1% respectively. This can be attributed to the large piezoelectric constant and small relative dielectric constant of AlN material. By considering the impact of material properties, the ratio of piezoelectric constant to that of relative dielectric constant plays an essential part in the performance of PSC[33,34]. Among the third-generation semiconductor materials, the AlN has a noteworthy modulation ratio of 9.3% follows by ZnO (7.96%) and GaN (4.78%). The modulation ratio of AlN happens to be almost twice greater than GaN. The superior performance of AlN, ZnO, and GaN is due to the large piezoelectric constant, this demonstrates that a good performing material is the one with a large piezoelectric constant and small relative dielectric constant.

Figure 3(a) and (b) show the graph of maximum power (Pm) and open-circuit voltage (Voc) against applied external strain. By utilizing Equation (11) and Equation (16), the Voc and Pm are linearly identifying with the strain(s). By introducing the piezo-phototronic effect, the performance parameters of the GaN PSC improve due to enhancement in Vm and Pm. The modulation ratio for GaN PSC as against W_{piezo} as a function of strain is illustrated in Figure 3(c). As the width of the piezo-charge opens up the modulation ratio also increases. Furthermore, the modulation ratio is linearly dependent on both the external applied strain and W_{piezo} . The semiconductor material and metal contact can influence W_{piezo} [35,36]. The piezoelectric constant and their dielectric constant of different third-generation semiconductor materials are plotted in Figure 3(d).

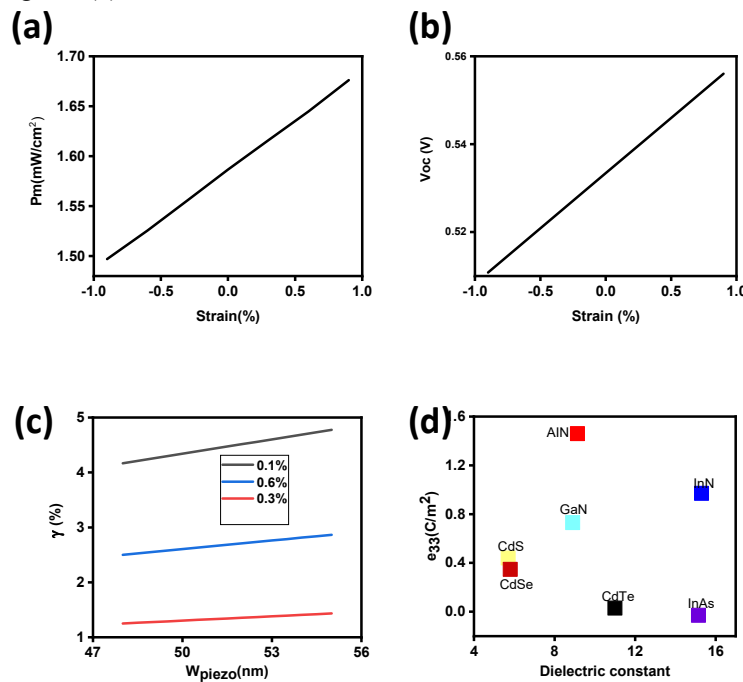


Figure 3. (a) Pm and (b) Voc versus the external strain applied. (c) Modulation ratio γ of the GaN PSC with W_{piezo} under the strain (ϵ) of 0.3% 0.6% and 1%. (d) The piezoelectric constant of various third-generation semiconductor materials as opposed to their various dielectric constant.

Table 1. shows the piezoelectric constant and relative dielectric constant.

Material(s)	Piezoelectric constant e_{33} (C/m ²)	Relative dielectric constant
GaN	0.73[31]	8.9[30]
AlN	1.46[37]	9.14[38]
InN	15.3[37]	0.97[30]
InAs	15.15[37]	-0.03[39]
ZnO	1.22[40]	8.92[40]
CdS	5.7[41]	0.44[42]
CdSe	5.8[41]	0.347[43]
CdTe	11[37]	0.03[44,45]

SUMMARY

In conclusion, we investigated the properties of a strained photovoltaic Schottky contact metal/semiconductor PV solar cell and examined the piezo-phototronic effect produced in the junction when the PV cell was strained. The piezoelectric effects in this structure are thought to be caused by external applied mechanical stress. Key performance parameters portraying the device including Voc, Pm, P, and FF have been mathematically determined. It is indicated that the PSC shows an enhanced performance under externally applied strains, especially for the modulation ratio. Additionally, GaN, ZnO, and AlN show a more prominent potential for high-efficiency PSCs. This gives physical insights into the PSCs and can serve as guidance on the design of third-generation piezo-phototronic energy harvesting devices.

Conflict of interest. The authors declare that they have no conflict of interest.

Funding. This research did not receive any specific grant from funding agencies in the public, commercial, or not-for-profit sectors.

ORCID IDs

Michael Gyan, <https://orcid.org/0000-0001-6337-2205>; Francis E. Botchey, <https://orcid.org/0000-0001-8327-4469>

REFERENCES

- [1] Z.L. Wang, Piezopotential gated nanowire devices: Piezotronics and piezo-phototronics, *Nano Today*, **5**(6), 540, 2010, <https://doi.org/10.1016/j.nantod.2010.10.008>
- [2] Z.L. Wang, W. Wu, and C. Falconi, Piezotronics and piezo-phototronics with third-generation semiconductors, *MRS Bulletin*, **43**, 922 (2018). <https://doi.org/10.1557/mrs.2018.263>
- [3] Y. Zhang, Y. Leng, M. Willatzen, and B. Huang, Theory of piezotronics and piezo-phototronics, *MRS Bull.*, **43**, 928 (2018). <https://doi.org/10.1557/mrs.2018.297>
- [4] X. Wen, W. Wu, C. Pan, Y. Hu, Q. Yang, and Z.L. Wang, Development and progress in piezotronics, *Nano Energy*, **14**, 276 (2014). <https://doi.org/10.1016/j.nanoen.2014.10.037>
- [5] Z.L. Wang, The new field of nanopiezotronics, *Mater. Today*, **10**(5), 20 (2007), [https://doi.org/10.1016/S1369-7021\(07\)70076-7](https://doi.org/10.1016/S1369-7021(07)70076-7)
- [6] J. Hao, and C.N. Xu, Piezophotonics: From fundamentals and materials to applications, *MRS Bull.*, **43**, 965 (2018). <https://doi.org/10.1557/mrs.2018.296>
- [7] M.C. Wong, L. Chen, G. Bai, L. B. Huang, and J. Hao, Temporal and Remote Tuning of Piezophotonic-Effect-Induced Luminescence and Color Gamut via Modulating Magnetic Field, *Adv. Mater.* **29**(43), 1701945 (2017). <https://doi.org/10.1002/adma.201701945>
- [8] Z.L. Wang, Progress in piezotronics and piezo-phototronics, *Advanced Materials*. **24**(34), 4632 (2012). <https://doi.org/10.1002/adma.201104365>
- [9] W. Wu and Z. L. Wang, Piezotronics and piezo-phototronics for adaptive electronics and optoelectronics, *Nat. Rev. Mater.* **1**(7), 16031 (2016). <https://doi.org/10.1038/natrevmats.2016.31>
- [10] R. Bao, Y. Hu, Q. Yang, and C. Pan, Piezo-phototronic effect on optoelectronic nanodevices, *MRS Bull.*, **43**, 952 (2018). <https://doi.org/10.1557/mrs.2018.295>
- [11] Z.L. Wang, Nanopiezotronics, *Adv. Mater.* **19**(6), 889 (2007). <https://doi.org/10.1002/adma.200602918>
- [12] C. Pan, J. Zhai, and Z.L. Wang, Piezotronics and Piezo-phototronics of Third Generation Semiconductor Nanowires, *Chemical Reviews*. **119**(15), 9303 (2019). <https://doi.org/10.1021/acs.chemrev.8b00599>
- [13] W. Wu, and Z.L. Wang, Piezotronics and piezo-phototronics for adaptive electronics and optoelectronics, *Nature Reviews Materials*. **1**, 16031 (2016). <https://doi.org/10.1038/natrevmats.2016.31>
- [14] Z.L. Wang, J. Zhai, and L. Zhu, Piezotronic and piezo-phototronic devices based on the third generation semiconductors, *Chinese Sci. Bull.* **65**(25), 2664 (2020). <https://doi.org/10.1360/tb-2019-0713>
- [15] W. Sha, J. Zhang, S. Tan, X. Luo, and W. Hu, III-nitride piezotronic/piezo-phototronic materials and devices, *Journal of Physics D: Applied Physics*. **52**, 213003 (2019). <https://doi.org/10.1088/1361-6463/ab04d6>
- [16] J. Millan, P. Godignon, X. Perpina, A. Perez-Tomas, and J. Rebollo, A survey of wide bandgap power semiconductor devices, *IEEE Trans. Power Electron.* **29**(5), 2155 (2014). <https://doi.org/10.1109/TPEL.2013.2268900>
- [17] X. Wang et al., Piezotronic Effect Modulated Heterojunction Electron Gas in AlGaN/AlN/GaN Heterostructure Microwire, *Adv. Mater.* **28**(33), 7234 (2016). <https://doi.org/10.1002/adma.201601721>
- [18] J. Fu, H. Zong, X. Hu, and H. Zhang, Study on ultra-high sensitivity piezoelectric effect of GaN micro/nano columns, *Nano Conver.* **6**, 33 (2019). <https://doi.org/10.1186/s40580-019-0203-4>
- [19] G. Michael et al., High-performance piezo-phototronic multijunction solar cells based on single-type two-dimensional materials, *Nano Energy*, vol. 76, Oct. (2020). <https://doi.org/10.1016/j.nanoen.2020.105091>
- [20] Z. Dongqi, Z. Zhao, R. Huang, J. Nie, L. Li, and Y. Zhang, High-performance piezo-phototronic solar cell based on two-dimensional materials, *Nano Energy*, **32**, 448 (2017). <https://doi.org/10.1016/j.nanoen.2017.01.005>
- [21] J. Sirohi and I. Chopra, Fundamental Understanding of Piezoelectric Strain Sensors, *J. Intell. Mater. Syst. Struct.* **11**(4), 246 (2000). <https://doi.org/10.1106/8BFB-GC8P-XQ47-YCQ0>
- [22] S.M. Sze, and K.K. Ng, *Physics of Semiconductor Devices*. 2006.
- [23] P. Paufler, *Fundamentals of Piezoelectricity*, *Zeitschrift für Krist.* (1992). <https://doi.org/10.1524/zkri.1992.199.1-2.158>
- [24] G.A. Maugin, and A.C. Eringen, Continuum Mechanics of Electromagnetic Solids, *J. Appl. Mech.* **56**(4), 986 (1989). <https://doi.org/10.1115/1.3176205>
- [25] Y. Zhang, Y. Liu, and Z.L. Wang, Fundamental theory of piezotronics, *Adv. Mater.* **23**(27), 3004 (2011). <https://doi.org/10.1002/adma.201100906>
- [26] K. Gu, D. Zheng, L. Li, and Y. Zhang, High-efficiency and stable piezo-phototronic organic perovskite solar cell, *RSC Adv.* **8**(16), 8694 (2018). <https://doi.org/10.1039/C8RA00520F>
- [27] Y. Wang, D. Zheng, L. Li, and Y. Zhang, Enhanced Efficiency of Flexible GaN/Perovskite Solar Cells Based on the Piezo-Phototronic Effect, *ACS Appl. Energy Mater.* **1**(7), 3063 (2018). <https://doi.org/10.1021/acsaelm.8b00713>
- [28] G. Michael, G. Hu, D. Zheng, and Y. Zhang, Piezo-phototronic solar cell based on 2D monochalcogenides materials, *J. Phys. D: Appl. Phys.* **52**(20), 204001 (2019). <https://doi.org/10.1088/1361-6463/ab0ac4>
- [29] W. Liu, A. Zhang, Y. Zhang, and Z. L. Wang, Density functional studies on wurtzite piezotronic transistors: Influence of different semiconductors and metals on piezoelectric charge distribution and Schottky barrier, *Nanotechnology*, **27**, 205204 (2016). <https://doi.org/10.1088/0957-4484/27/20/205204>
- [30] F. Schäffler, in *Properties of advanced semiconductor materials : GaN, AlN, InN, BN, SiC, SiGe*, edited by M.E. Levinshtein, S.L. Rumyantsev, and M.S. Shur, (John Wiley Sons Inc, New York, 2001), pp. 149-188.
- [31] S.P. Wan, J.B. Xia, and K. Chang, Effects of piezoelectricity and spontaneous polarization on electronic and optical properties of wurtzite III-V nitride quantum wells, *J. Appl. Phys.* **90**, 6210 (2001). <https://doi.org/10.1063/1.1413714>

- [32] C.-T. Huang, J. Song, W.-F. Lee, Y. Ding, Z. Gao, Y. Hao, L.-J. Chen, and Z.L. Wang, GaN nanowire arrays for high-output nanogenerators, *J. Am. Chem. Soc.* **132**(13), 4766 (2010). <https://doi.org/10.1021/ja909863a>
- [33] G. Hua, W. Guo, R. Yu, X. Yang, R. Zhou, C. Pan, and Z.L. Wang, Enhanced performances of flexible ZnO/perovskite solar cells by piezo-phototronic effect, *Nano Energy*, **23**, 27 (2016). <https://doi.org/10.1016/j.nanoen.2016.02.057>
- [34] J. Sun et al., Piezo-phototronic Effect Enhanced Efficient Flexible Perovskite Solar Cells, *ACS Nano*, **13**(4), 4507 (2019). <https://doi.org/10.1021/acs.nano.9b00125>
- [35] W. Liu, A. Zhang, Y. Zhang, and Z.L. Wang, First principle simulations of piezotronic transistors, *Nano Energy*, **14**, 355 (2015). <https://doi.org/10.1016/j.nanoen.2014.10.014>
- [36] N. Suvansinpan, F. Hussain, G. Zhang, C.H. Chiu, Y. Cai, and Y.W. Zhang, Substitutionally doped phosphorene: Electronic properties and gas sensing, *Nanotechnology*, **27**, 065708 (2016). <https://doi.org/10.1088/0957-4484/27/6/065708>
- [37] F. Bernardini, V. Fiorentini, and D. Vanderbilt, Spontaneous polarization and piezoelectric constants of III-V nitrides, *Phys. Rev. B - Condens. Matter Mater. Phys.* **56**, R10024(R) (1997). <https://doi.org/10.1103/PhysRevB.56.R10024>
- [38] A.T. Collins, E.C. Lightowers, and P.J. Dean, Lattice vibration spectra of aluminum nitride, *Phys. Rev.* **158**, 833 (1967). <https://doi.org/10.1103/PhysRev.158.833>
- [39] Y. Zhang, J. Nie, and L. Li, Piezotronic effect on the luminescence of quantum dots for micro/nano-newton force measurement, *Nano Res.* **11**, 1977 (2018). <https://doi.org/10.1007/s12274-017-1814-x>
- [40] Y. Zhang, Y. Yang, and Z. Wang, Piezo-phototronics effect on nano/microwire solar cells, *Energy Environ. Sci.* **5**, 6850 (2012). <https://doi.org/10.1039/C2EE00057A>
- [41] D. Berlincourt, H. Jaffe, and L.R. Shiozawa, Electroelastic properties of the sulfides, selenides, and tellurides of zinc and cadmium, *Phys. Rev.* **129**, 1009 (1963). <https://doi.org/10.1103/PhysRev.129.1009>
- [42] P.E. Lippens and M. Lannoo, Calculation of the band gap for small CdS and ZnS crystallites, *Phys. Rev. B*, **39**, 10935 (1989). <https://doi.org/10.1103/PhysRevB.39.10935>
- [43] T. Wakaoka et al., Confined synthesis of CdSe quantum dots in the pores of metal-organic frameworks, *J. Mater. Chem. C*, **2**, 7173 (2014). <https://doi.org/10.1039/c4tc01136h>
- [44] I. Strzalkowski, S. Joshi, and C.R. Crowell, Dielectric constant and its temperature dependence for GaAs, CdTe, and ZnSe, *Appl. Phys. Lett.* **28**, 350 (1976). <https://doi.org/10.1063/1.88755>
- [45] G.A. Samara, Temperature and pressure dependences of the dielectric constants of semiconductors, *Phys. Rev. B*, **27**, 3494 (1983). <https://doi.org/10.1103/PhysRevB.27.3494>

**ПІДВИЩЕННЯ ЕФЕКТИВНОСТІ СОНЯЧНИХ ЕЛЕМЕНТІВ ТРЕТЬОГО ПОКОЛІННЯ
НА ОСНОВІ П'ЄЗО – ФОТОТРОННОГО ЕФЕКТУ
Майкл Джан^a, Джозеф Парбі^{b,c}, Френсіс Е. Ботчей^c**

^a*Школа фізики, Університет електронних наук і технологій Китаю, Ченду 610054, Китай*

^b*Школа матеріалознавства, Університет електронних наук і технологій Китаю, Ченду 610054, Китай*

^c*Кофоріду, Технічний університет, Гана*

Прикладаючи зовнішню рівномірну деформацію на нецентросиметричний п'єзоелектричний напівпровідник, індуються поляризаційні заряди на поверхні матеріалу. Поляризаційні заряди часто генеруються всередині кристалів за умови, що прикладена деформація нерівномірна. Застосована деформація впливає на електронний транспорт і може бути використана для модуляції властивостей матеріалу. Ефект багатостороннього зв'язку між п'єзоелектрикою, властивостями перенесення напівпровідників і фотозбудженням призводить до п'єзо-фототронних ефектів. Останні дослідження показали, що п'єзоелектричні та напівпровідникові властивості напівпровідників третього покоління використовуються у фотодетекторах, світлодіодах та наногенераторах. П'єзоелектричний напівпровідник третього покоління можна використовувати у високоефективних фотоелементах. У цій роботі теоретично досліджується матеріал п'єзофототронного сонячного елемента третього покоління на основі взаємодії металу та напівпровідника GaN. Це дослідження спрямоване на визначення впливу п'єзоелектричної поляризації на електричні характеристики цього матеріалу сонячних елементів. Були оцінені такі експлуатаційні параметри, як ефективність перетворення потужності, коефіцієнт заповнення, I-V характеристики, напруга розімкнутого ланцюга та максимальна вихідна потужність. П'єзофототронний ефект може підвищити напругу струму разомкнутого ланцюга на 5,5 відсотка при зовнішній деформації на 0,9 відсотка. Дослідження відкриє нове вікно для наступного покоління високоефективних п'єзо-фототронних ефектів.

Ключові слова: поляризаційні заряди; п'єзофототронний ефект; сонячна панель; напівпровідник третього покоління; п'єзоелектричний ефект

INTERACTIONS OF NOVEL PHOSPHONIUM DYE WITH LIPID BILAYERS: A MOLECULAR DYNAMICS STUDY[†]

 Olga Zhytniakivska*

*Department of Medical Physics and Biomedical Nanotechnologies, V.N. Karazin Kharkiv National University
4 Svobody Sq., Kharkiv, 61022, Ukraine*

*Corresponding Author: olga.zhytniakivska@karazin.ua

Received February 1, 2022; revised February 11, 2022; accepted February 14, 2022

In the present work the 100-ns molecular dynamics simulations (MD) were performed in the CHARMM36m force field using the GROMACS package to estimate the bilayer location and mechanisms of the interaction between the novel phosphonium dye TDV and the model lipid membranes composed of the phosphatidylcholine (PC) and its mixtures with cholesterol (Chol) or/and anionic phospholipid cardiolipin (CL). Varying the dye initial position relative to the membrane midplane, the dye relative orientation and the charge state of the TDV molecule it was found that the one charge form of TDV, which was initially translated to a distance of 20 Å from the membrane midplane along the bilayer normal, readily penetrates deeper into the membrane interior and remains within the lipid bilayer during the entire simulation time. It was revealed that the probe partitioning into the model membranes was accompanied by the reorientation of TDV molecule from perpendicular to nearly parallel to the membrane surface. The analysis of the MD simulation results showed that the lipid bilayer partitioning and location of the one charge form of TDV depend on the membrane composition. The dye binds more rapidly to the neat PC bilayer than to CL- and Chol-containing model membranes. It was found that in the neat PC and CL-containing membranes the one charge TDV resides at the level of carbonyl groups of lipids (the distances ~ 1.1 nm, 1.2 nm and 1.3 nm from the bilayer center for the PC, CL10 and CL20 lipid membranes, respectively), whereas in the Chol-containing membranes the probe is located at the level of glycerol moiety (~ 1.5 nm and 1.6 nm for the Chol30 and CL10/Chol30 lipid membranes, respectively). It was demonstrated that the dye partitioning into the lipid bilayer does not affect the membrane structural properties.

Keywords: Phosphonium dye, lipid bilayer, molecular dynamics simulation.

PACS: 87.14.C++c, 87.16.Dg

In recent years, molecular dynamics simulation has emerged as a powerful computation tool for investigating a wide variety of biological systems [1-27]. Specifically, MD simulations have been used i) to characterize the structure of the lipid membranes [1-4], proteins [5-8] or nucleic acids [9-12]; ii) to study the physicochemical properties of the isolated virus proteins or capsids [13-16]; iii) to elucidate the nature of the energy transport in the light-harvesting complexes [17,18]; iv) to ascertain the binding mode of a therapeutic agent to a given biological target in the drug design strategies [19-22]; v) to identify antiviral inhibitors [23-25], to name only a few. Likewise, MD simulation appeared to be especially useful in examining the structural, physicochemical and thermodynamic properties of the ligand-macromolecule systems [26-30]. In particular, MD simulation has provided a unique framework for the atomic-level characterization of interactions between ligands and membranes [30-39]. A good deal of studies indicate that MD simulations can be used to achieve a fundamental understanding of the mechanisms underlying the interaction of proteins [31,32], peptides [33, 34] and drugs [35, 36] with lipid membranes. Notably, MD approaches appeared to be highly efficient in exploring the behavior of fluorescent membrane probes, that is of great importance for their biomedical application and synthesis of new fluorescent reporter molecules with improved properties [37-46]. To exemplify, the molecular dynamics simulation was used to develop a molecular design strategy of AIE-based fluorescent probes for selective targeting of mitochondrial membrane [37]; to characterize the partitioning and membrane disposition of the diphenylhexatriene probes [38], to characterize the solvation behavior of phthalocyanines [39], to explore the dynamical behavior of the DiI carbocyanine derivative in a lipid bilayer [40], to estimate the membrane location of ESIP fluorophores [41], coumarin derivatives [42], benzanthrone dye [43] and membrane polarity probes Prodan and Laurdan [44,45], to investigate the interactions of methylene blue with oxidized and non-oxidized lipid bilayers [46], to name only a few.

The aim of the present study was to explore the interaction of the novel phosphonium dye TDV (Fig. 1) with the model lipid membranes of different composition using the molecular dynamics simulation. To this end, the 100 ns MD simulations were carried out for TDV with the neat phosphatidylcholine bilayer (PC) and bilayers from PC mixtures with: i) anionic lipid cardiolipin (CL) with the PC:CL molar ratio 9:1 and 4:1 (denoted here as CL10 and CL20, respectively); ii) sterol cholesterol (Chol) with the PC:Chol ratio 7:3 (Chol30); iii) both CL and Chol lipids with the PC:CL:Chol ratio 6:1:3 (CL10/Chol30). To obtain the optimal conditions for the TDV-membrane simulations and an atomistically detailed picture of the TDV binding to the lipid bilayers, the MD calculations were performed at varying initial positions of the dye and its orientation relative to the bilayer normal. Moreover, to estimate the role of electrostatic interactions in the TDV membrane partitioning, two dye forms were considered for the simulation. The

[†] Cite as: O. Zhytniakivska, East. Eur. J. Phys. 1, 77 (2022), <https://doi.org/10.26565/2312-4334-2022-1-11>
© O. Zhytniakivska, 2022

first form of the TDV molecule possessed two positive charges (on the P atom of the phosphonium group and the N atom of the pyridine ring), while in the second one the charge on the P atom of the phosphonium group was neutralized by the iodine ion (one charge dye form).

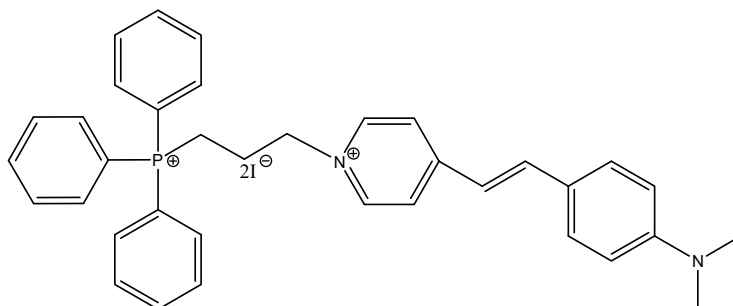


Figure 1. The structural formula of TDV

EXPERIMENTAL SECTION

System description

The input files of TDV-membrane systems for MD calculations were prepared using the web-based graphical interface CHARMM-GUI [47]. The .pdb-file of TDV was generated in OpenBabelGUI 2.4.1, using the structure drawn in MarvinSketch (mrv format). Two different dye structures were created for MD simulations, with total charges +2 and +1, respectively. In both cases the atomic charges of TDV were corrected using the RESP ESP charge Derive Server. The topology of TDV was generated using the CHARMM-GUI Ligand Reader and Modeler [48]. The obtained files were further used to generate the dye-lipid systems using the Membrane Builder option [49]. MD simulations were carried out for TDV with five different membrane systems with a nearly identical number of lipids. The first one was composed of TDV and 94 1-palmitoyl-2-oleoyl-*sn*-glycero-3-phosphatidylcholine (POPC) molecules in each monolayer. Hereafter, the neat POPC bilayer is referred to as PC. Two systems were represented by TDV and bilayers from POPC mixtures with anionic lipid cardiolipin (LOCCL2 lipid component in the CHARMM-GUI lipid bank) with the POPC:LOCCL2 ratios 9:1 and 4:2, referred to here as CL10 and CL20, respectively. The fourth type of the lipid bilayer (Chol30) was composed from TDV, 77 POPC and 33 cholesterol molecules in each monolayer (POPC:Chol ratio 7:3). The last type of lipid bilayers was composed from PC mixture with both CL and Chol lipids with the POPC:LOCCL2:Chol ratio 6:1:3 (CL10/Chol30). The initial distance of the TDV translation from the membrane midplane along the bilayer normal was varied from 0 to 30 Å. To obtain a neutral total charge of the system a necessary number of counterions was added.

Molecular dynamics simulation and data analysis

Molecular dynamics simulations and analysis of the trajectories were carried out using the GROMACS software (version 5.1) with the CHARMM36m force field in the NPT ensemble with the time step for MD simulations 2 fs. Calculations were performed at a temperature of 310 K. The Particle Mesh Ewald method was utilized for correct treatment of the long-range electrostatic interactions [50]. The bond lengths were constrained using the LINCS algorithm [51]. The pressure and temperature controls were performed using the Berendsen thermostat [52]. MD simulations were performed with minimization of 50000 steps and equilibration of 12500000 steps. The whole time interval for MD calculations was 100 ns. The GROMACS command `gmx density` was used to calculate the mass density distribution for various components of the lipid bilayer and density distribution of TDV across a lipid bilayer. The analyses of the membrane thickness, membrane area and area per lipid were conducted using the FATS LIM package [53]. The molecular graphics and visualization of the simulation evolution over time were performed using the Visual Molecular Dynamics VMD software.

RESULTS AND DISCUSSION

TDV, a phosphonium-based water-soluble fluorescent dye, has been reported to have a marked ability to biomolecular interactions. Specifically, it was demonstrated that TDV can be effectively used for optical detection of disease-related protein aggregates [54,55] and for elucidating the mechanisms of DNA interactions with amyloid fibrils [56]. Moreover, it was shown previously that TDV is highly suitable for membrane studies since it possesses a pronounced lipid-associating ability and high sensitivity to physicochemical properties of the model lipid bilayers [57]. In the present study the molecular dynamics simulation was used to explore the interaction between TDV and the model lipid membranes with the main emphasis on determining the depth of the probe location in a lipid bilayer. Besides, it was assumed previously that membrane electrostatics plays an important role in the membrane association of TDV [57]. Therefore, it was also interesting to assess the role of TDV charge in the dye membrane partitioning.

At the first step of study, the MD calculations were performed for the TDV molecule bearing two positive charges (on the P atom of the phosphonium group and on the N atom of the pyridine ring). Specifically, the TDV molecule was

initially translated to a distance of 30 Å from the membrane midplane along the bilayer normal. The phosphonium group of the TDV molecule was directed from the membrane center. In this case the TDV molecule did not show affinity to the PC bilayer during the entire simulation time (Fig.2 B). Probably, the formation of the hydration shell around the water-soluble dye hinders its penetration in the lipid bilayer. Similar behavior was observed for the phthalocyanine dye in the POPC bilayers [39]. The simulation was performed also for the mixed bilayers containing negatively charged cardiolipin and sterol cholesterol, but in both these cases the TDV-lipid binding did not occur (data not shown). Therefore, the MD calculations were carried out at varying the dye initial position from the membrane midplane along the bilayer normal. Moreover, initial location of the dye in the region of lipid headgroups at a distance 20 Å from the membrane center or at the bilayer midplane (Fig. 2 C) didn't change the final result, since to the end of the 100 ns simulation the TDV molecule left the membrane interior (Fig. 2 B,D). The MD simulations were also performed for the systems where the phosphonium group of the TDV molecule was oriented toward the membrane center, but the no TDV-membrane binding was found (data not shown). These MD data are in controversy with the experimental studies [57] providing evidence for strong partitioning of TDV into lipid bilayers of different composition. The most probable reason for the observed inconsistencies between the experimental data and modeling is the charge distribution over the dye molecule, rendering the penetration into membrane interior energetically unfavorable. Another possible reason is the short simulation period.

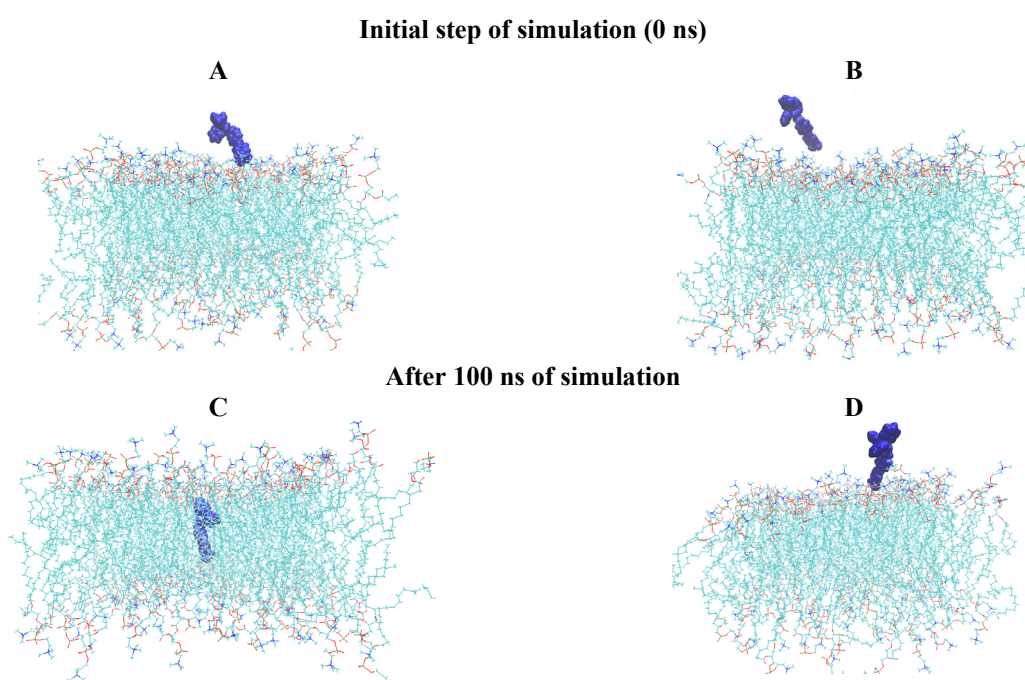


Figure 2. Snapshots of TDV in the PC lipid bilayer at the initial step (**A, C**) and after 100 ns (**B, D**) of simulation. The TDV molecule was translated perpendicular to the lipid bilayer to a distance of 30 Å (panel A) from the membrane midplane along the bilayer normal. Panel C represents transmembrane location of the TDV (0 Å). The TDV molecule is depicted in blue using the VDW drawing method. The lipid tails are represented as sticks in cyan, the phosphorus and nitrogen atoms of the lipid headgroups are shown by orange and blue, respectively. For clarity, water molecules and ions are not shown

The numerous studies indicate that the charge of fluorescent dye exerts significant influence on the probe affinity to the lipid membranes and its bilayer location [37, 40, 46]. Specifically, it was shown previously that the cationic and neutral forms of methylene blue display different affinities to the oxidized and non-oxidized lipid bilayers [46]. Specifically, the comparison of the results of molecular dynamics modelling of methylene blue interaction with the control and peroxidized DOPC lipid bilayers for the cationic dye form, neutral MB (reduced dye form) and neutral MB in the form of the undissociated salt indicates the stronger dye-lipid interaction of the cationic MB with the peroxidized lipids [46]. Moreover, the cationic MB exerts significant impact on the membrane area and the later diffusion of the peroxidized lipid bilayer [46]. The charge on the dye headgroups was shown to play a significant role in the bilayer translocation of the AIEgen fluorescent dyes [37]. Moreover, the MD simulation of the uncharged and charged carbocyanine dyes revealed the effect of headgroup charge on the dye orientation and bilayer location [40]. Therefore, at the next step of study it was interesting to ascertain how the charge on phosphonium head of the TDV molecule affects the dye- membrane partitioning. To this end, the 100 ns MD simulations were carried out for the TDV cationic form (the charge on the P atom of the phosphonium group was neutralized by the iodine ion) with the neat phosphatidylcholine bilayer and PC mixtures with cholesterol or/and anionic phospholipid cardiolipin. Fig. 3 illustrates the disposition of the one charge form of TDV with respect to lipid/water interface at different simulation times for the PC, CL10 and CL20 lipid bilayers.

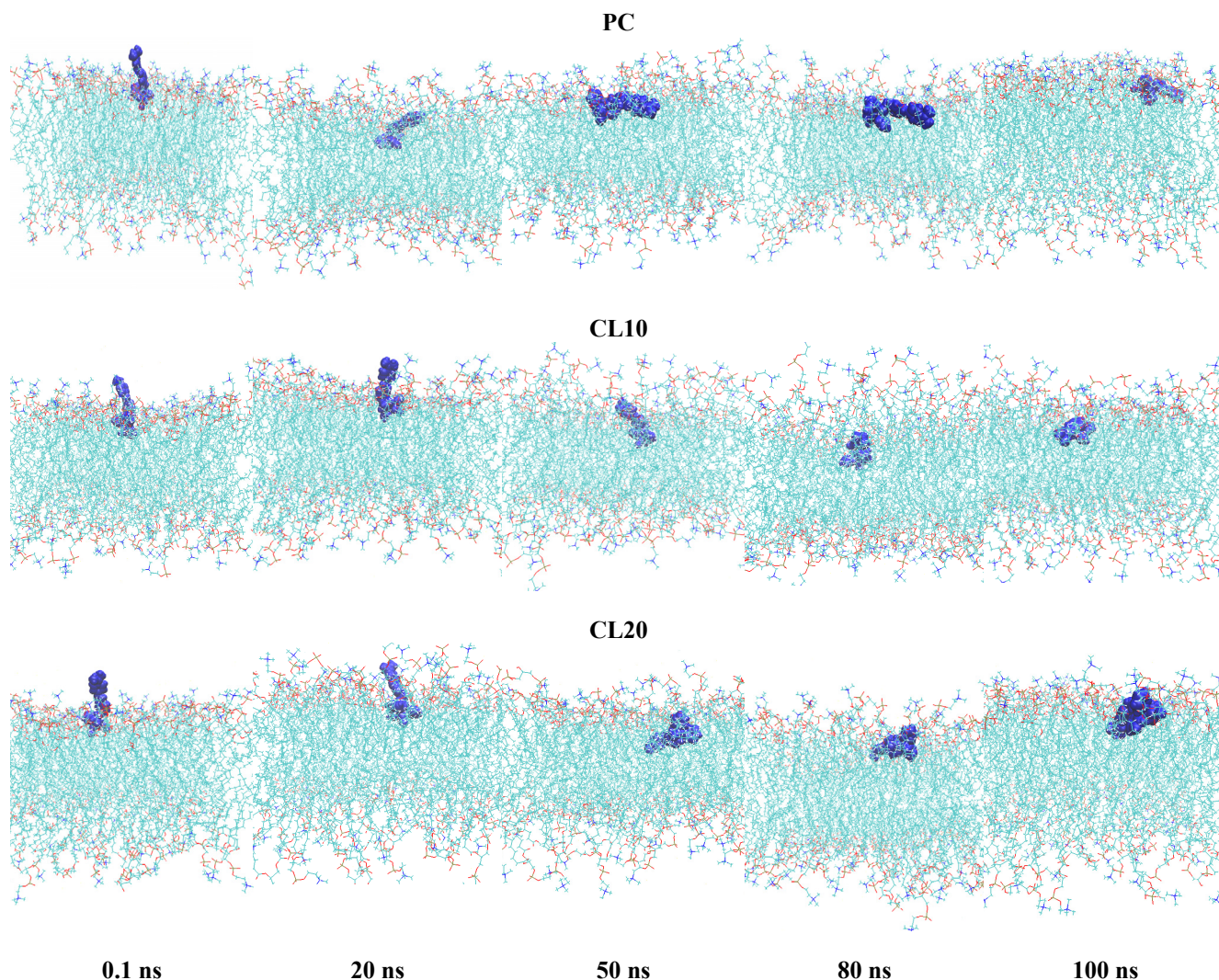


Figure 3. The snapshots of the partitioning of the one charge TDV into PC, CL10 and CL20 bilayers at different simulation time points. The TDV molecule is depicted in blue using the VDW drawing method. The lipid tails are represented as sticks in cyan, the phosphorus and nitrogen atoms of the lipid headgroups are shown by orange and blue, respectively. For clarity, water molecules and ions are not shown.

As can be seen from a simple visual inspection of simulation snapshots, the dye molecule which was initially translated to a distance of 20 Å from the membrane midplane along the bilayer normal moved deeper to the membrane interior and remained within the lipid bilayer for the rest of simulation time. The cationic form of TDV appeared to be sensitive to the changes in physicochemical properties of the lipid bilayers. More specifically, MD simulation demonstrated that the probe binds more rapidly to the neat PC bilayers than to CL-containing model membranes, penetrating deeper into bilayer interior after ~ 20 ns of simulation. Meanwhile, after 20 ns of MD calculation, the phosphonium group of the one charge TDV is positioned in the hydrophobic tail region, while the positively charged pyridine ring is localized at the level of the carbonyl groups of the polar/nonpolar interface. The partitioning of the one charge TDV into CL-containing membranes was accompanied only by a slight probe reorientation during the first 20 ns of simulations. Thereafter, the dye orientation changed from the perpendicular to the parallel (PC, CL10) or nearly parallel (CL20) to the membrane surface. The above effect was followed by the deeper penetration of the one charge TDV to the CL-containing lipid membranes, while in the neat PC bilayer the dye molecule became less buried due to the phosphonium group relocation to the same level as the rest of the molecule.

Fig.4 shows the snapshots of the partitioning of the one charge TDV into the Chol30 and CL10/Chol30 bilayers. During the first 20 ns of the simulations the reorientation of the probe was observed coupled with a slight penetration of the dye molecule to the membrane interior. Likewise, during the following period of time the position of the dye phosphonium head remained virtually unchanged while the positively charged tail tended to reside in the proximity to glycerol moiety of the lipid bilayers. Interestingly, the analysis of the positions occupied by the one charge TDV over the MD trajectory in the case of neat PC, CL or Chol containing membranes indicates that this probe prefers the orientation parallel to the membrane surface. Moreover, in the presence of cholesterol TDV tends to occupy more polar membrane binding sites. Fig.5 shows the time evolution of the separation between the dye center of mass and the bilayer center.

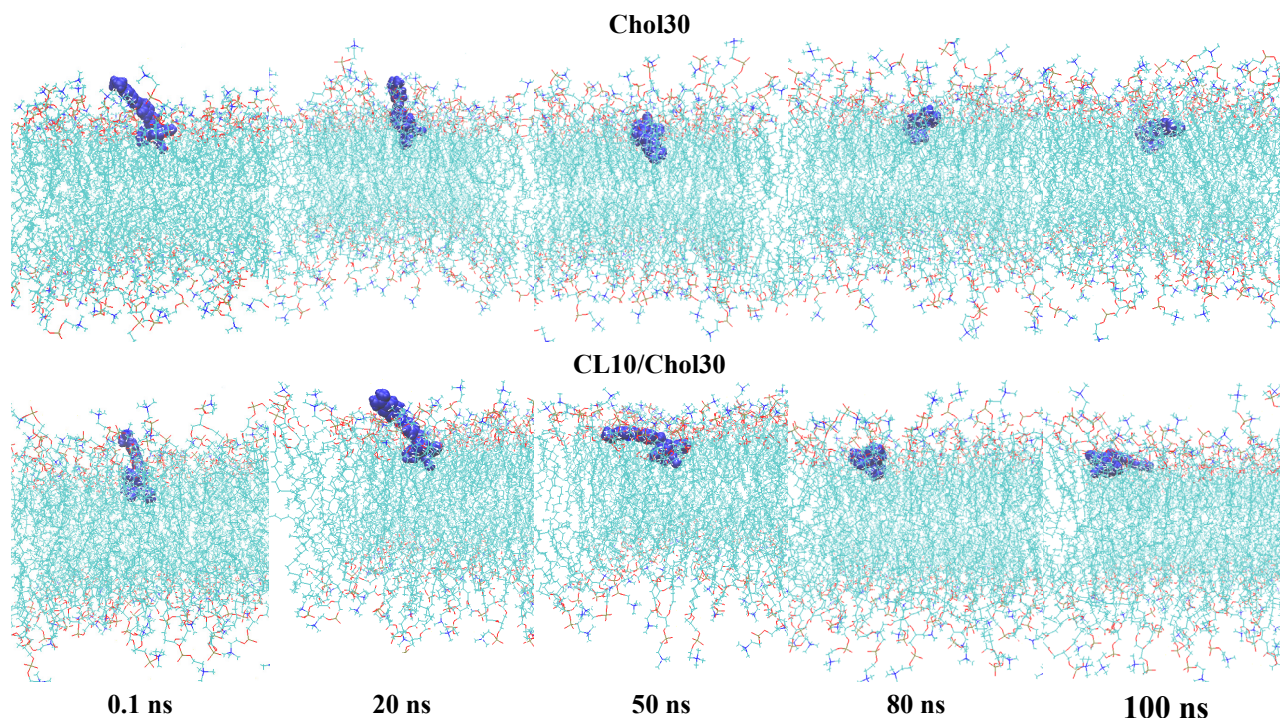


Figure 4. The snapshots of the partitioning of the one charge TDV into Chol30 and CL10/Chol30 bilayers at different simulation time points. The TDV molecule is depicted in blue using the VDW drawing method. The lipid tails are represented as sticks in cyan, the phosphorus and nitrogen atoms of the lipid headgroups are shown by orange and blue, respectively. For clarity, water molecules and ions are not shown.

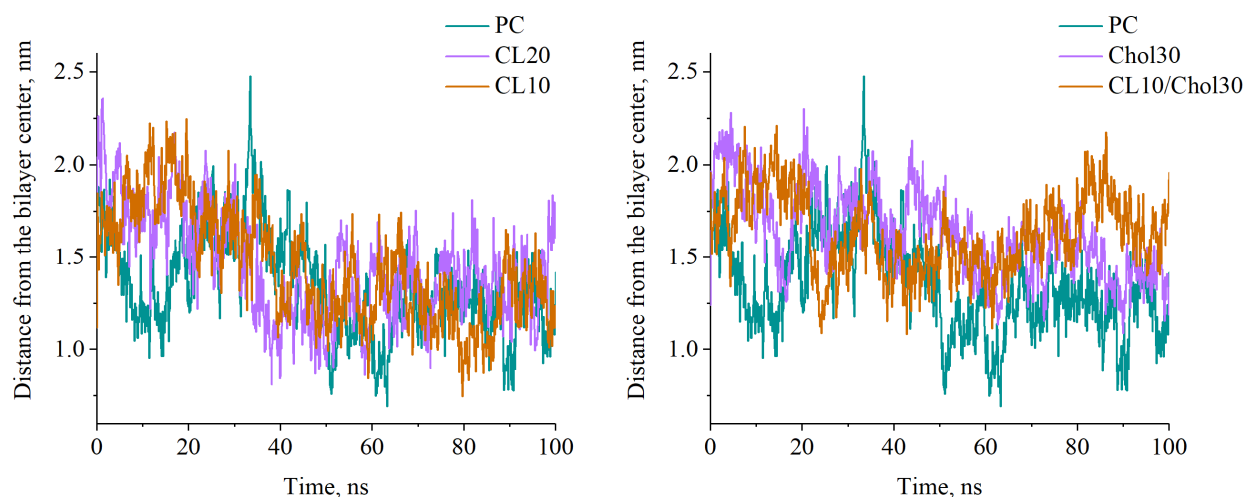


Figure 5. Time evolution of the TDV distance from the bilayer center

In order to determine the precise TDV location, the mass density distribution profiles of the dye, water and the molecular groups of lipids were plotted with respect to the bilayer normal (Fig. 6). As can be seen, the peak of the one charge TDV mass distribution in the PC (Fig. 6A), CL10 (Fig. 6B) and CL20 (Fig. 6C) bilayers is observed at the distances ~ 1.1 nm, 1.2 nm and 1.3 nm from the bilayer center. According to the partial density profile of the lipid membrane proposed by Marrink and Berendsen [58], a lipid bilayer can be divided into four regions: 1) the region of the hydrophobic lipid tails ($0-8$ Å from the membrane center); 2) the interfacial region between the upper carbons of hydrophobic tails and hydrophilic headgroups ($8-16$ Å from the membrane center); 3) the interfacial area containing negatively charged phosphate groups, positively charged choline groups and ($16-25$ Å) from the membrane center); 4) the region of the bulk water (>25 Å).

Therefore, in the PC and CL-containing membranes TDV resides in the region of carbonyl groups. In the Chol30 (Fig. 6D) and CL10/Chol20 (Fig. 6E) lipid membranes the peak of the dye distribution is observed at 1.5 nm and 1.6 nm, respectively, assuming the probe location at the level of glycerol moiety.

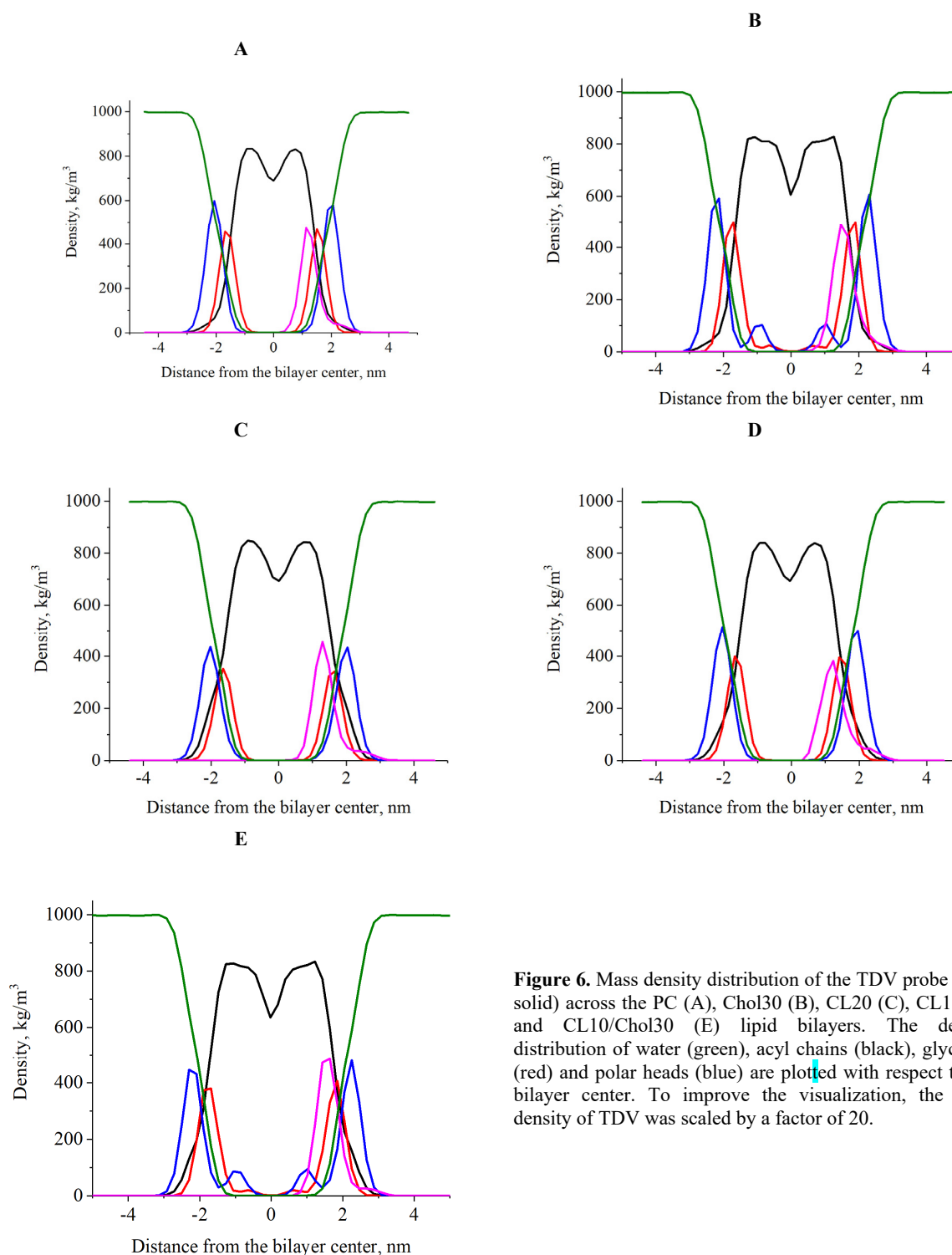


Figure 6. Mass density distribution of the TDV probe (pink solid) across the PC (A), Chol30 (B), CL20 (C), CL10 (D) and CL10/Chol30 (E) lipid bilayers. The density distribution of water (green), acyl chains (black), glycerols (red) and polar heads (blue) are plotted with respect to the bilayer center. To improve the visualization, the mass density of TDV was scaled by a factor of 20.

Table 1. Average properties of lipid bilayers in the presence of the one charge TDV

System	Control bilayers		In the presence of the dye	
	Membrane thickness (nm)	Area per lipid head group (nm ²)	Membrane thickness (nm)	Area per lipid head group (nm ²)
PC	3.886±0.06	0.656±0.012	3.895±0.058	0.652±0.012
CL10	4.438±0.056	0.695±0.012	4.448±0.072	0.689±0.014
CL20	3.951±0.066	0.971±0.022	3.946±0.065	0.967±0.022
Chol30	3.960±0.059	0.785±0.013	3.903±0.056	0.792±0.013
CL10/Chol30	4.370±0.062	0.938±0.027	4.345±0.057	0.929±0.022

To investigate the influence of the TDV one charge form on the structural properties of lipid bilayers, the average area per lipid head group and the membrane thickness were calculated for the dye-free PC, CL10, CL20, Chol30 and CL10/Chol30 bilayers and for the systems with one charge TDV. As seen in Table 1, the TDV does not significantly perturb the lipid bilayer structure.

CONCLUSIONS

To summarize, in the present study a 100 ns molecular dynamics simulation was performed to explore the interaction of the novel phosphonium dye TDV with the model lipid membranes composed of phosphatidylcholine and its mixtures with cholesterol or/and anionic phospholipid cardiolipin with the main emphasis on the determination of the probe bilayer location. It was found that the one charge form of TDV, which was initially translated to a distance of 20 Å from the membrane midplane along the bilayer normal, readily incorporates deeper into the membrane interior and remains within the lipid bilayer during the entire simulation time. The probe partitioning into the model membranes was accompanied by the TDV molecule reorientation from perpendicular to nearly parallel to the membrane surface. It was shown that the charge on the phosphonium group of the TDV molecule plays a significant role in the dye membrane partitioning.

ACKNOWLEDGEMENTS

This work was supported by the Ministry of Education and Science of Ukraine (the Young Scientist projects № 0120U101064 “Novel nanomaterials based on the lyophilic self-assembled systems: theoretical prediction, experimental investigation and biomedical applications” and the project No. 0119U002525 “Development of novel ultrasonic and fluorescence techniques for medical micro- and macrodiagnostics”). The author is grateful to Prof. Galyna Gorbenko and Dr. Uliana Tarabara, V.N. Karazin Kharkiv National University, for useful comments and discussions.

ORCID IDs

 Olga Zhytniakivska, <https://orcid.org/0000-0002-2068-5823>

REFERENCES

- [1] R.M. Venable, A. Kramer, R.W. Pastor, *Chem. Rev.* **119**, 5954-5997 (2019). <https://doi.org/10.1021/acs.chemrev.8b00486>.
- [2] M.L. Berkowitz, *Biochim. Biophys. Acta.* **1788**, 86-96 (2009). <https://doi.org/10.1016/j.bbamem.2008.09.009>
- [3] M. Pasenkiewicz-Gierula, T. Rog, K. Kitamura, A. Kusumi, *Biophys. J.* **78**, 1376-1389 (2000), [https://doi.org/10.1016/S0006-3495\(01\)75867-5](https://doi.org/10.1016/S0006-3495(01)75867-5).
- [4] T. Rog, M. Pasenkiewicz-Gierula, *FEBS Letters*, **502**, 68-71 (2000). [https://doi.org/10.1016/S0014-5793\(01\)02668-0](https://doi.org/10.1016/S0014-5793(01)02668-0).
- [5] L. Heo, M. Feig, *PNAS*, **115**, 13276-13281 (2018). <https://doi.org/10.1073/pnas.1811364115>.
- [6] B. Urbanc, M. Betnel, L. Cruz, G. Bitan, D.B. Teplow, *J. Am. Chem. Soc.*, **132**, 4266-4280 (2010). <https://doi.org/10.1021/ja9096303>.
- [7] Z. Qin, M. J. Buehler, *Phys. Rev. Lett.* **104**, 198304 (2010). <https://doi.org/10.1103/PhysRevLett.104.198304>.
- [8] L. Tran, T. Ha-Duong, *Peptides*, **69**, 86-91 (2015). <https://doi.org/10.1016/j.peptides.2015.04.009>.
- [9] A. D. MacKerell, N. K. Banavali, *J. Comp. Chem.* **21**, 105-120 (2000). [https://doi.org/10.1002/\(SICI\)1096-987X\(20000130\)21:1<105::AID-JCC3>3.0.CO;2-P](https://doi.org/10.1002/(SICI)1096-987X(20000130)21:1<105::AID-JCC3>3.0.CO;2-P).
- [10] K.E. Furse, S. A. Corcelli, *J. Phys. Chem. Lett.* **1**, 1813-1820 (2010). <https://doi.org/10.1021/jz100485e>.
- [11] A. Noy, A. Perez, F. Lankas, F.J. Luque, M. Orozco. *J. Mol. Biol.* **343**, 627-638 (2004). <https://doi.org/10.1016/j.jmb.2004.07.048>.
- [12] I.-C. Yeh, G. Hummer. *Biophys. J.* **86**, 681-689 (2004). [https://doi.org/10.1016/S0006-3495\(04\)74147-8](https://doi.org/10.1016/S0006-3495(04)74147-8).
- [13] H. Ode, M. Nakashima, S. Kitamura, W. Sugiura, H. Sato, *Front. Microbiol.* **3**, 00258 (2012). <https://doi.org/10.3389/fmicb.2012.00258>.
- [14] J.R. Perilla, J.A. Hadden, B.C. Goh, C.G. Mayne, K. Schulten, *J. Phys. Chem. Lett.* **7**, 1836-1844 (2016). <https://doi.org/10.1021/acs.jpcclett.6b00517>.
- [15] D. Suarez, N. Diaz, *J. Chem. Inf. Model.* **60**, 5815-5831 (2020). <https://doi.org/10.1021/acs.jcim.0c00575>.
- [16] C. M. Quinn, M. Wang, M. P. Fritz, B. Runge, J. Ahn, C. Xu, J.R. Perilla, A. Grohenborn, T. Polenova, *PNAS*, **115**, 11519-11524 (2018). <https://doi.org/10.1073/pnas.1800796115>.
- [17] A. Damjanović, I. Kosztin, U. Kleinekathöfer, K. Schulten. *Phys. Rev. E.* **65**, 031919 (2002). <https://doi.org/10.1103/PhysRevE.65.031919>.
- [18] D. Chandler, J. Strumpfer, M. Sener, S. Scheuring, K. Schulten, *Biophys. J.* **106**, 2503-2510 (2014). <https://doi.org/10.1016/j.bpj.2014.04.030>.
- [19] L. Liang, J.-W. Shen, Q. Wang, *Colloids Surf. B* **153**, 168-173 (2017). <https://doi.org/10.1016/j.colsurf.2017.02.021>.
- [20] H. Zhao, A. Caflisch, *Eur. J. Med. Chem.* **91** 4-14 (2015). <https://doi.org/10.1016/j.ejmech.2014.08.004>.
- [21] P.-C. Do, E.H. Lee, L. Le, *J. Chem. Inf. Model.* **58** 1473-1482 (2018). <https://doi.org/10.1021/acs.jcim.8b00261>.
- [22] M. Hernandez-Rodriguez, M. C. Rosales-Hernandez, J. E. Mendieta-Wejebe, M. Martinez-Archundia, J. Correa Basurto, *Curr. Med. Chem.* **23** 3909-3924 (2016).
- [23] J. Wang, C. Ma, G. Fiorin, V. Carnevale, T. Wang, F. Hu, R. Lamb, et al. *J. Am. Chem. Soc.* **133**, 12834-12841 (2011). <https://doi.org/10.1021/ja204969m>.
- [24] J. Fantini, H. Chahinian, N. Yahi, *Int. J. Antimicrob. Agents* **56**, 106020 (2020). <https://doi.org/10.1016/j.ijantimicag.2020.106020>.
- [25] M. Métfiot, K. Maddali, B. Johnson, S. Hare, S. Smith et al. *ACS Chem. Biol.* **8**, 209-217 (2012). <https://doi.org/10.1021/cb300471n>.
- [26] Z. Dolenc, C. Ostenbrink, J. Koller, W. van Gusteren, *Nucleic Acids Res.* **33**, 725-733 (2005). <https://doi.org/10.1093/nar/gki195>.
- [27] T.A. de Oliveira, L.R. Medaglia, E.H. Bechelane Maia, et al. *Pharmaceuticals* **15**, 132 (2022). <https://doi.org/10.3390/ph15020132>.
- [28] A. Hospital, J.R. Goni, M. Orozco, J. L. Gelpi, *Adv. Appl. Bioinform. Chem.* **8**, 37-47 (2015). <https://doi.org/10.2147/AABC.S70333>.

- [29] N. Ahalawat, R.K. Murarka, J. Biomol. Struct. Dyn. **33**, 1-13 (2015). <https://doi.org/10.1080/07391102.2014.996609>.
- [30] Y. Fu, J. Zhao, Z. Chen, Comput. Math. Methods Med. **2018**, 3502514 (2018). <https://doi.org/10.1155/2018/3502514>.
- [31] K. Goossens, H. De Winter, J. Chem. Inf. Model. **58**, 2193-2202 (2018). <https://doi.org/10.1021/acs.jcim.8b00639>.
- [32] J. Loschwitz, O. Olubiyini, J.S. Hub, B. Strodel, H.S. Poojari, PMBTS, **170**, 273-403 (2020). <https://doi.org/10.1016/bs.pmbts.2020.01.001>.
- [33] Yi. Wang, D.E. Schalamadinger, J.D. Kim, J.A. McCammon, Biochim. Biophys. Acta, **1818**, 1402-1409 (2012). <https://doi.org/10.1016/j.bbame.2012.02.017>.
- [34] H. Jang, B. Ma, T. Woolf, R. Nussinov, Biophys. J., **91**, 2848-2859 (2006). <https://doi.org/10.1529/biophysj.106.084046>.
- [35] T.J. Yacoub, A.S. Reddy, I. Szleifer, Biophys. J. **101**, 378-385 (2011). <https://doi.org/10.1016/j.bpj.2011.06.015>.
- [36] A. Kabedev, S. Hossain, M. Hubert, P. Larson, C. Bergstrom, J. Pharm. Sci. **110**, 176-185 (2021). <https://doi.org/10.1016/j.xphs.2020.10.061>.
- [37] X. Zheng, D. Wang, W. Xu, S. Cao, Q. Peng, B. Zhong Tang, Mater. Horiz. **6**, 2016-2023 (2019). <https://doi.org/10.1039/C9MH00906J>.
- [38] A.M.T.M. do Canto, J.R. Robalo, P.D. Santos, et al., Biochim. Biophys. Acta, **1858**, 2647-2661 (2016), <https://doi.org/10.1016/j.bbame.2016.07.013>.
- [39] P. S. Orekhov, E. G. Kholina, M. E. Bozdoganyan, A. M. Nesterenko, I.B. Kovalenko, M. G. Strahovskaya, J. Phys. Chem. B **122**, 3711-3722 (2018). <https://doi.org/10.1021/acs.jpcc.7b11707>.
- [40] R.P. Gullapalli, M. Demirel, P.J. Butler, Phys Chem Chem. Phys. **10**, 3548-3560 (2008). <https://doi.org/10.1039/b716979e>.
- [41] Y.O. Posokhov, A. Kyrychenko, Biophys. Chem. **235**, 9-18 (2018). <https://doi.org/10.1016/j.bpc.2018.01.005>.
- [42] O. Garcia-Beltran, N. Mena, O. Yanez, J. Caballero, V. Vargas, M. Tunes, et al., Eur. J. Med. Chem. **67**, 60-63 (2013), <https://doi.org/10.1016/j.ejmech.2013.06.022>.
- [43] O. Zhytniakivska, East European Journal of Physics, **3**, 134-140 (2020). <https://doi.org/10.26565/2312-4334-2020-3-17>.
- [44] M.W. Baig, M. Pederzoli, P. Jurkiewicz, L. Cwiklik, J. Pittner, Molecules, **23**, 1707 (2018). <https://doi.org/10.3390/molecules23071707>.
- [45] J. Barucha-Kraszewska, S. Kraszewski, P. Jurkiewicz, C. Ramseyer, M. Hof, Biochim. Biophys. Acta, **1798**, 1724-1734 (2010). <https://doi.org/10.1016/j.bbame.2010.05.020>.
- [46] N. I. Ercan, P. Stroeve, J.W. Tringe, R. Faller, Langmuir **34**, 4314-4323 (2018). <https://doi.org/10.1021/acs.langmuir.8b00372>.
- [47] S. Jo, T. Kim, V. G. Iyer, W. Im, J. Comp. Chem. **29**, 1859-1865 (2008). <https://doi.org/10.1002/jcc.20945>.
- [48] S. Kim, J. Lee, S. Jo, C.L. Brooks, H.S. Lee, W. Im, J. Comp. Chem. **38**, 1879-1886 (2017). <https://doi.org/10.1002/jcc.24829>.
- [49] J. Lee, D.S. Patel, J. Stähle, S.-J. Park, N.R. Kern, S. Kim, et al., J. Chem. Theory Comp. **15**, 775-786 (2017), <https://doi.org/10.1021/acs.jctc.8b01066>.
- [50] T. Darden, D. York, L. Pedersen, J. Chem. Phys. **98**, 10089-10092 (1993). <https://doi.org/10.1063/1.464397>.
- [51] B. Hess, H. Bekker, H.J.C. Berendsen, J.G.E.M. Fraaije, J. Comp. Chem. **18**, 1463-1472 (1997). [https://doi.org/10.1002/\(SICI\)1096-987X\(199709\)18:12<1463::AID-JCC4>3.0.CO;2-H](https://doi.org/10.1002/(SICI)1096-987X(199709)18:12<1463::AID-JCC4>3.0.CO;2-H).
- [52] H. Berendsen, J. Postma, W. van Gunsteren, A. DiNola, J. Haak, J. Chem. Phys. **81**, 3684-3690 (1984). <https://doi.org/10.1063/1.448118>.
- [53] S. Buchoux, FATSliM/fatslim: FATSliM v 0.2.1 (2016). <http://doi.org/10.5281/zenodo.158942>.
- [54] G. Gorbenko, V. Trusova, T. Deligeorgiev, N. Gadjev, C. Mizuguchi, H. Saito, J. Mol. Liq. **294** 111675 (2019). <https://doi.org/10.1016/j.molliq.2019.111675>.
- [55] G. Gorbenko, O. Zhytniakivska, K.Vus, U. Tarabara, V. Trusova, Phys. Chem. Chem. Phys. **23**, 14746-14754 (2021). <https://doi.org/10.1039/D1CP01359A>.
- [56] O. Zhytniakivska, U. Tarabara, K.Vus, V. Trusova G. Gorbenko, East. Eur. J. Phys. **2**, 19-26 (2019). <https://doi.org/10.26565/2312-4334-2019-2-03>.
- [57] O. Zhytniakivska, East European Journal of Physics, **4**, 107-113 (2021). <https://doi.org/10.26565/2312-4334-2021-4-12>
- [58] S.J. Marrink, H.J.C. Berendsen, J. Phys. Chem. **98**, 4155-4168 (1994). <https://doi.org/10.1021/j100066a040>.

ВЗАЄМОДІЯ НОВОГО ФОСФОНІЄВОГО ЗОНДУ З ЛІПІДНИМИ МЕМБРАНАМИ: МОЛЕКУЛЯРНО-ДИНАМІЧНЕ ДОСЛІДЖЕННЯ





О. Житняківська

Кафедра медичної фізики та біомедичних нанотехнологій, Харківський національний університет імені В.Н. Каразіна
м. Свободи 4, Харків, 61022, Україна

У даній роботі з використанням 100-нс молекулярно-динамічного моделювання (MD) у силовому полі CHARMM36m пакету GROMACS досліджено локалізацію в ліпідному бішарі та механізми взаємодії між новим фосфонієвим барвником TDV та модельними ліпідними мембранами, що склалися із фосфатидилхоліну. (ФС) та його сумішей з холестерином (Хол) та/або аніонним фосфоліпідом кардіоліпіном (КЛ). При варіюванні початкового положення та орієнтації барвника було виявлено, що однозарядна форма TDV, яка спочатку була розташована на відстані 20 Å від центру бішару, проникає глибше у внутрішню частину мембрани і залишається всередині ліпідного бішару протягом усього часу моделювання. Виявлено, що вбудовування зонду в модельні мембрани супроводжується переорієнтацією молекули TDV з перпендикулярної на паралельну до поверхні мембрани. Результати молекулярно-динамічного дослідження свідчать про те, що розподіл в ліпідну фазу та локалізація однозарядної форми TDV в ліпідному бішарі в значній мірі залежать від складу мембрани. Барвник швидше зв'язується з ФХ-бішаром, у порівнянні з модельними мембранами, що містять КЛ та Хол. Продемонстровано, що у ФХ бішарі та мембранах, що містять КЛ, однозарядна форма TDV локалізується на рівні карбонільних груп ліпідів (на відстані ~ 1.1 нм, 1.2 нм і 1.3 нм від центру бішару для ФХ, КЛ10 і КЛ20 ліпідних мембран, відповідно), тоді як у бішарах, що містили Хол, зонд розташовується на рівні гліцеринів (~ 1,5 нм та 1,6 нм для Хол30 та КЛ10/Хол30 ліпідних мембран, відповідно). Виявлено, що взаємодія барвника з ліпідним бішаром не впливає на структурні властивості мембрани.

Ключові слова: фосфонієвий барвник, ліпідний бішар, молекулярно-динамічне моделювання.

USING A SCANNER TO MEASURE ABSORBED DOSES WITH RADIOCHROMIC FILM DOSIMETERS[†]

 Volodymyr Morgunov^{*,a},  Serhii Lytovchenko^a,  Volodymyr Chyshkala^a,
 Natalia Didenko^b, Valentyn Vynnyk^a

^aV. N. Karazin Kharkiv National University, 4 Svobody Sq., Kharkiv, 61022, Ukraine;

^bKharkiv National Automobile and Highway University, 25 Yaroslava Mudrogo str., Kharkiv, 61002, Ukraine

*Corresponding Author: v.morgunov@karazin.ua

Received January 26, 2022; revised February 1, 2022; accepted February 21, 2022

The article provides a sequence of steps for using RISØ calorimeters for calibration and subsequent use of B3 radiochromic film dosimeters (GEX corporation) and a scanner for measuring absorbed doses. Calibration was carried out with the help of electron beam accelerator in the range of absorbed doses of 3 – 40 kGy (measurement range of RISØ calorimeters).

In the course of the work, the following was carried out:

- calibration of B3 radiochromic dosimetry films using RISØ calorimeters;
- plotting a calibration curve for B3 radiochromic dosimetric films;
- calculation of approximation functions;
- development of a technique for using a flatbed scanner to measure absorbed doses;
- estimation of the measurement uncertainties of absorbed doses.

Accelerator operation parameters: scanning frequency of the accelerated electron beam – 5 Hz, pulse frequency – 120 Hz, electron energy – 5 MeV, electron beam current – 60 μ A. The measurement error of the absorbed dose is 5.8 %.

Keywords: absorbed dose, calorimeter, radiochromic dosimetry films, scanner, uncertainty.

PACS: 06.20.-f; 29.40.Vj; 29.40.Wk

INTRODUCTION

Measurement of absorbed doses is an important and indispensable task in radiation processing operations. The absorbed dose is the main criterion for assessing the degree of radiation processing of materials. There are several ways to measure the absorbed dose, which can be roughly divided into two categories: physical and chemical. But one of the most widespread methods of measuring doses in recent years has become a method using radiochromic films. The reason for this popularity is the simplicity and convenience of measurements. The measurement of absorbed doses by radiochromic films is based on the change in the color of the films depending on the absorbed dose. Spectrophotometers are used to measure the color change. In works [1, 2] examples of using office scanners for measuring absorbed doses by B3 film dosimeters are given.

This article provides a sequence of actions for the possibility of using B3 film dosimeters to measure absorbed doses at an electron accelerator in accordance with the relevant standards given above.

INITIAL EVALUATION OF CALORIMETER PERFORMANCE

In the course of this work, we used dosimeters No 1856, 1935, 1936 manufactured by RISØ. Doses were originally measured for a conveyor speed $v_d = 0.6$ mm/sec. The results of measurements of the absorbed dose are shown in Table 1.

Based on the initial dose measurements given in Table 1, it was decided not to use calorimeter No. 1856 for calibrating film dosimeters, since the readings of this dosimeter differ from the others by almost 2 %, while the difference between dosimeters No. 1935 and No. 1936 is less than 1 %.

THE PROCEDURE FOR MEASURING THE ABSORBED DOSE WITH CALORIMETERS

In accordance with § 8.1.5 of ISO/ASTM 51631: 2013(E) Practice for use of calorimetric dosimetry systems for electron beam dose measurements and dosimetry system calibrations, after the calorimeters passed through the irradiation zone, the time elapsed since the end of the dosimeter and the resistance was recorded [3]. The measurement data are shown in Table 2

The data from Table 2 are presented in Fig. 1. To determine the resistance at the end of the irradiation,

[†]**Cite as:** V. Morgunov, S. Lytovchenko, V. Chyshkala, N. Didenko, V. Vynnyk East. Eur. J. Phys. 1, 85 (2022), <https://doi.org/10.26565/2312-4334-2022-1-12>.

Table 1: Initial measurement of absorbed doses with calorimeters.

Dosimeter no.	Resistance before irradiation, Ohm	Temperature before irradiation, °C	Resistance after irradiation, Ohm	Temperature after irradiation, °C	Absorbed dose, kGy
1935	2185	22.68	796	50.63	38.11
1936	2218	22.33	789	50.63	38.54
1856	2127	23.40	779	51.31	37.42

Table 2: Dependence of the calorimeter resistance R on the time t that has passed since the end of the irradiation.

Time t , min	Resistance R , Ohm	
	Dosimeter No	
	1935	1936
1	792	799
2	795	802
3	798	805
4	803	809
5	809	815
6	816	821
7	824	828
8	833	836
9	842	844
10	851	853
12	872	871
15	905	900
18	940	932
20	965	954

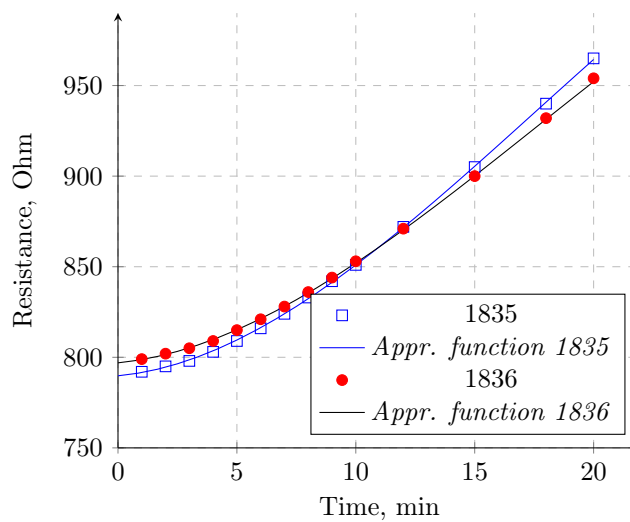


Figure 1: The dependence of the resistance of the calorimeters on the time elapsed since the end of the irradiation.

it is necessary to extrapolate the approximating functions shown in Fig. 1. To determine the type of the approximating function, we used the ROOT statistical package (<https://root.cern/>). For dosimeter No. 1835, the following approximating function was obtained:

$$R(t) = -0.011464 \cdot t^3 + 0.605339 \cdot t^2 + 1.208758 \cdot t + 789.785827 \quad (1)$$

For dosimeter No. 1836, the following approximating function was obtained:

$$R(t) = -0.009683 \cdot t^3 + 0.520607 \cdot t^2 + 1.292768 \cdot t + 796.933373 \quad (2)$$

Based on Table 2 and formulas (1, 2), we compose Table 3 of the change in resistance ΔR with time t .

Table 3: Dependence of the change in the resistance of the calorimeters ΔR on the time t that has passed since the end of the irradiation.

Time, min	ΔR , Ohm	
	No of dosimeter	
	1935	1936
1	2	2
2	5	5
3	8	8
4	13	12
5	19	18
6	26	24
7	34	31
8	43	39
9	52	47
10	61	56
12	82	74
15	115	103
18	150	135
20	175	157

Thus, to determine the resistance of the calorimeter at the time of the end of its irradiation, it is necessary to measure the time elapsed from the end of the irradiation to the start of the resistance measurement. From Table 3, proceeding from the time from the end of irradiation to the beginning of measurement, the correction ΔR is determined, which is subtracted from the measured resistance of the calorimeter. And, thus, the value of the resistance of the calorimeter at the moment of the end of the irradiation is obtained.

MEASUREMENT OF ABSORBED DOSES FOR DIFFERENT CONVEYOR SPEEDS AND PREPARATION OF CALIBRATION RADIOCHROMIC FILM DOSIMETERS

The calorimeters were placed in aluminum containers at a distance of 6 cm from the edge of the container on foam stands (about 1 cm high) to avoid heating the calorimeter from the container. The container was positioned at a distance of 20 cm from the edge of the conveyor. A phantom was first placed on the container, then a calorimeter. Radiochromic film dosimeters were located in phantoms, between two polystyrene plates, marked with the letter "A" in Fig. 2.

The results of measuring the absorbed doses for different conveyor speeds are shown in Table 4.

Four film dosimeters were used for each value of the absorbed dose. Each dosimeter was scanned with a resolution of 1200 dpi, and using the written Python code, the green channel was highlighted (in the form of values of gray) and the gray value was determined using the GIMP graphical editor. For each conveyor speed, the absorbed dose was averaged and these gray values entered in Table 5.

GETTING THE CALIBRATION FUNCTION

To obtain a calibration curve, it is necessary to convert the dose-signal data into a smooth function. For this, you can use statistical software packages. In this work, we used the ROOT data handling package (CERN, <https://root.cern/>). In accordance with the recommendations given in NPL Report CIRM 29 [4], the selection of the calibration function is performed starting with a polynomial of the 1st degree. For this, the function is searched for in the polynomial form $Dose = f(signal)$. To select the degree of the polynomial function, "percentage residuals" are calculated using the formula:

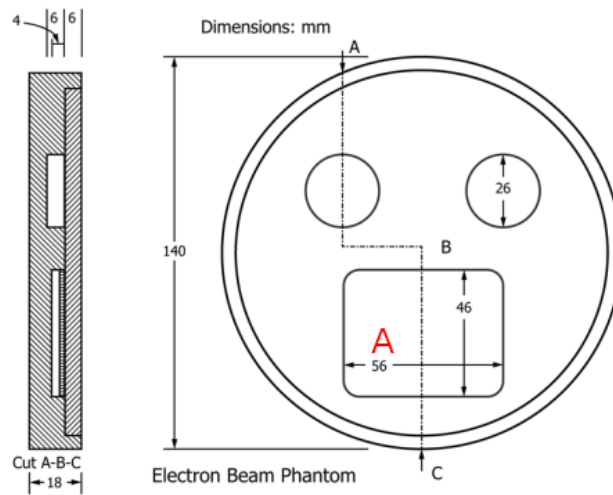


Figure 2: Phantom for irradiation of routine dosimeters. The letter "A" denotes the location of the film dosimeters.

$$\frac{D_{calculated} - D_{delivered}}{D_{delivered}} \cdot 100 \tag{3}$$

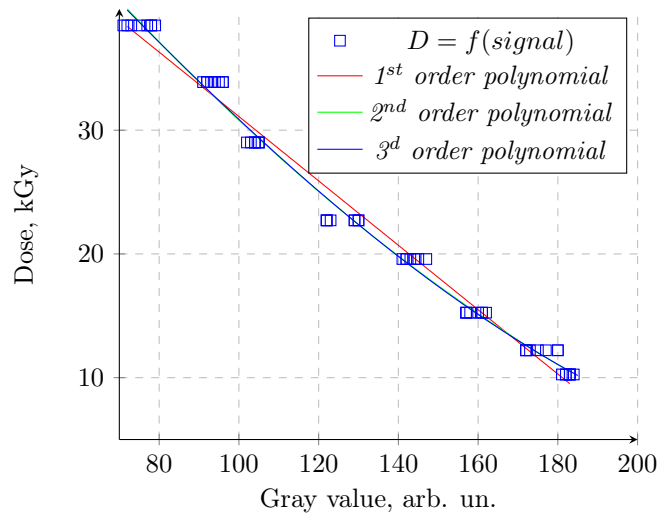


Figure 3: Dose versus gray value and approximation curves.

It can be seen from Fig. 3 that the 1st order polynomial approximates the points on the graph less well. Therefore, the calibration (approximating) function will be sought in the form of polynomials of the 2nd or 3rd orders. Figures 4 and 5 show the percentage deviations depending on the dose. The largest deviation was for the 2nd degree polynomial (9.53 %). For the 3rd degree polynomial, the maximum deviation was 9.37 %.

Therefore, a third-degree polynomial was chosen for the calibration function in the dose range of 10 – 40 kGy:

$$Dose = 1.55466 \cdot 10^{-6} \cdot x^3 + 8.14774 \cdot 10^{-5} \cdot x^2 - 0.364245 \cdot x + 64.92610, \tag{4}$$

where, *Dose* is the absorbed dose, kGy; *x* is the gray value, arbitrary units.

Carrying out similar calculations, for a dose range of 3 – 10 kGy, we obtain the following calibration function:

$$Dose = 7.55213 \cdot 10^{-6} \cdot x^3 - 0.00189324 \cdot x^2 - 0.332016 \cdot x + 87.5538, \tag{5}$$

Fig. 6 shows the dependence of the dose on the gray value and the approximation curves of the 3rd order polynomial. The dose range is 3 – 10 kGy.

Table 4: Absorbed dose values for different conveyor speeds.

No of dosemeter	Conveyor speed, mm/s	Resistance before irradiation, Ohm	Resistance after irradiation, Ohm	Time after irradiation, min	Real resistance after irradiation, Ohm	Absorbed dose, kGy
10 – 40 kGy						
1935	0.6	2130	777	1,0	775	38,40
1936		2183	790	1,0	788	38,54
1935	0.7	2180	863	1,0	861	34,18
1936		2173	880	1,0	878	33,60
1935	0.8	2219	982	1,0	980	29,25
1936		2201	995	1,0	993	28,77
1935	1.0	2162	1130	1,0	1128	22,78
1936		2170	1145	1,0	1143	22,61
1935	1.2	2166	1230	1,0	1228	19,54
1936		2161	1231	1,0	1229	19,64
1935	1.5	2158	1374	1,5	1371	15,31
1936		2161	1385	1,0	1383	15,19
1935	1.9	2254	1548	1,0	1546	12,35
1936		2230	1551	1,0	1549	12,07
1935	2.3	2183	1598	1,0	1596	10,24
1936		2175	1596	1,0	1594	10,27
3 – 10 kGy						
1935	2.4	2123	1590	1,0	1588	9,56
1936		2098	1581	1,0	1579	9,46
1935	3.0	2071	1643	1,0	1641	7,63
1936		2080	1653	1,0	1651	7,63
1935	3.6	2064	1695	1,0	1693	6,45
1936		2045	1692	1,0	1690	6,28
1935	5.0	2088	1808	1,5	1805	4,66
1936		2077	1799	1,0	1797	4,68
1935	7.0	2077	1868	1,0	1866	3,39
1936		2073	1869	1,0	1867	3,34

UNCERTAINTY ESTIMATION

To estimate uncertainty, all possible sources of uncertainty must first be identified and then quantified.

When measurements are associated with statistical effects such as random variation between individual dosimeters, errors are referred to as "Type A" errors. The other component of the error, such as the effect of

Table 5: Gray values for different absorbed doses.

Dose, kGy	Gray values							
	Film dosimeter No							
	I	II	III	IV	V	VI	VII	VIII
	10 – 40 kGy							
38,47	77	78	79	78	75	71	73	72
33.89	94	96	96	95	91	92	93	92
29.01	102	105	105	104	104	103	105	104
22.71	122	123	122	122	129	130	129	130
19.59	144	147	145	144	142	141	142	143
15.25	158	157	157	157	161	161	162	160
12.21	172	173	172	172	175	180	177	180
10.26	184	183	182	183	183	181	182	183
	3 – 10 kGy							
9.51	185	183	184	186	185	185	185	185
7.63	192	192	191	192	187	188	188	187
6.37	202	202	202	202	197	196	196	195
4.67	205	204	205	204	209	208	207	208
3.37	215	214	213	215	222	221	221	221

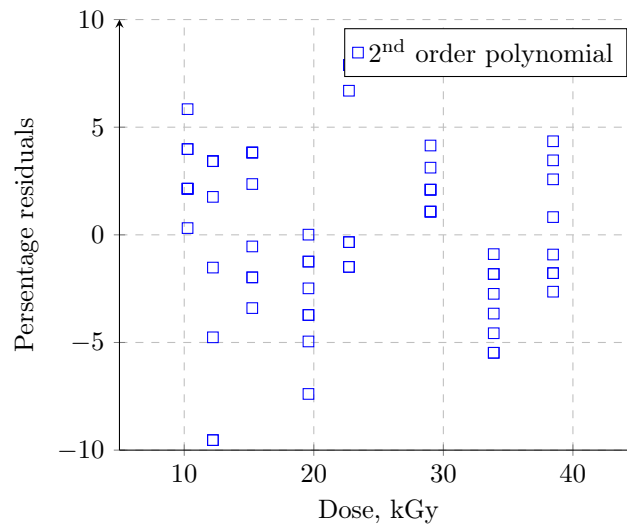


Figure 4: Percentage residual as a function of dose for the 2nd order approximation polynomial. Dose range 10 – 40 kGy.

the dose rate on the response of the dosimeter, for example, cannot be measured directly. This error is "Type B".

Let us consider the types of uncertainties in measuring the absorbed dose.

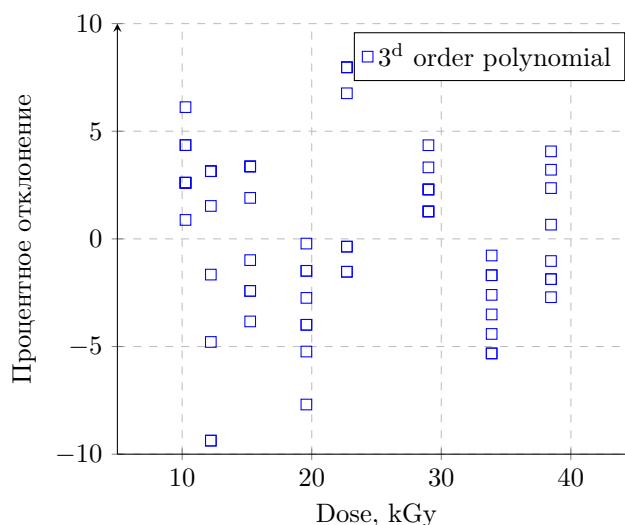


Figure 5: Percentage residual as a function of dose for the 3^d order approximation polynomial. Dose range 10 – 40 kGy.

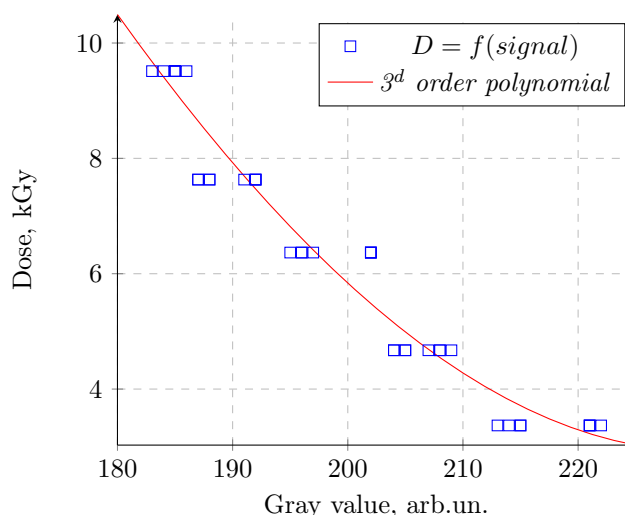


Figure 6: Dose versus gray value and approximation curves of the 3rd order polynomial. Dose range 3 – 10 kGy.

Uncertainty in determining the calibration function Instrument uncertainty

The resistance of the calorimeters was measured with a METEX M32700 multimeter with a measurement error of 0.8 %.

Uncertainty in the manufacturing of calibrated dosimeters

The inconsistency in the placement of calibrated dosimeters inside the phantom can introduce an error in the absorbed dose. This applies especially to electron accelerators. Since the phantom was installed using a tape measure twice (one time it was when - the phantom was installed relative to the container, and the second time - when the container was installed relative to the conveyor), then double half of the roulette division unit - 1 mm is taken as the permissible error. The dosimeters in the phantom were located in the middle; we assume the error in this case is 5 mm. In accordance with the electron beam homogeneity test, the variability of the absorbed dose in the center of the beam within 1 cm is about 1.5 %.

Uncertainty when fitting the calibration function

As recommended in NPL Report CIRM 29 [4], the error in fitting the calibration function was defined as the root-mean-square percentage deviation. In this case, the percentage deviation was averaged for each dose value. Applying the above method, we obtain an error in fitting the calibration function equal to 2.5 %.

Uncertainties associated with the variability of the irradiation process

During irradiation, the beam energy, beam current, etc. can change. The instructions for the accelerator indicate that the uniformity of the dose along the scan length is $\pm 5\%$.

Resultant uncertainty

The summary table, taking into account all uncertainties, is as follows:

Table 6: The summary table of uncertainties.

Type of the uncertainty	Uncertainty, %
Instrument uncertainty	0,8
Uncertainty in the manufacture of calibrated dosimeters	1,5
Uncertainty when fitting the calibration function	2,5
Uncertainties associated with the variability of the irradiation process	5,0

To calculate the combined uncertainty, we use the following formula (NPL Report CIRM 29 [4]):

$$u_c = \sqrt{u_1^2 + u_2^2 \dots u_i^2}.$$

Substituting the uncertainties values from Table 6, we obtain the following value of the combined uncertainty:

$$u_c = 5,8\%.$$

1 Sequence of actions when measuring the absorbed dose using a scanner

1. After irradiation, scan the dosimeter with a resolution of 1200 dpi.
2. Open the resulting file in GIMP. Press the right mouse button on the image. Then: Colors \rightarrow Component \rightarrow Decompose (fig. 7).
3. Uncheck "Decompose to layers" (fig. ??)
4. Close all images, except for the image received from the green channel.
5. Instead of pp. 2-4, you can use the developed Python program "convertToGRayScale.py", which extracts a green channel from the image into a grayscale image. The format for using this program: from the command line, call ***python3 convertToGRayScale.py "filename.jpg"***. The result of the program will be a file with a grayscale image named "filename grayScale.jpg". Open the resulting file in the graphics editor GIMP and continue with 6.
6. Select the "Color picker tool". Enable checkboxes in the "Pick Target" menu in the "Pick only" and "Use info window" items (Fig. 9).
7. Left-click on the image and read the "V" readings in the "Pixel" section in the information window (Fig. 10). This is the gray value.
8. Substitute the obtained value into the formula (4) or (5) depending on the size of the measured dose.

*For this program to work correctly, the *opencv-python* (<https://pypi.org/project/opencv-python/>) should be installed.

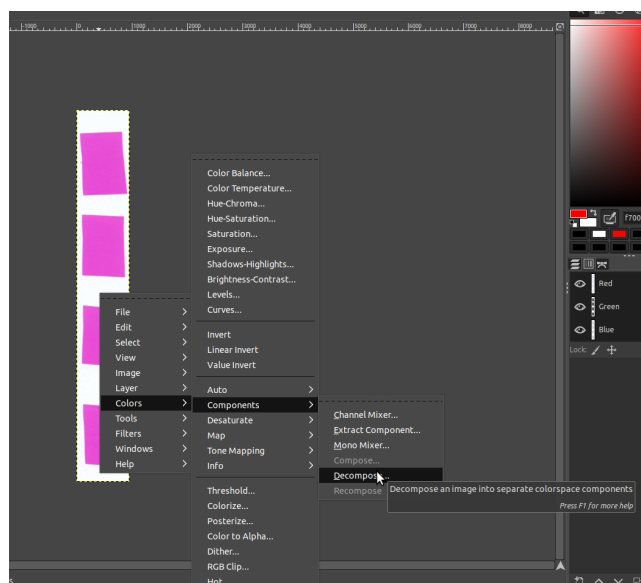


Figure 7: Color-coded image.

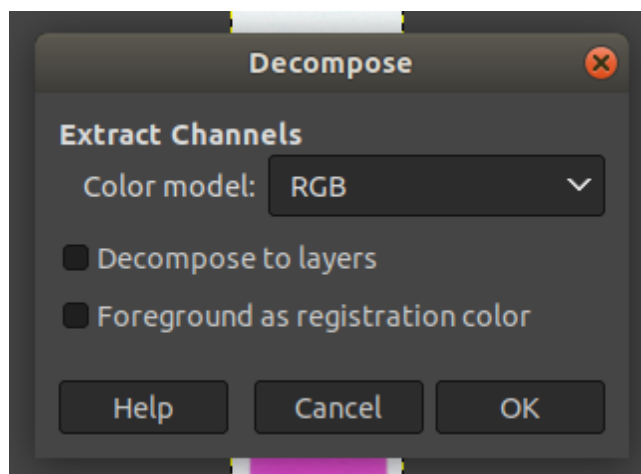


Figure 8: Decompose to layers.

CONCLUSION

Calibrated radiochromic dosimeters were received for the following doses: 38.47; 33.89; 29.01; 22.71; 19.59; 15.25; 12.21; 10.26; 9.51; 7.63; 6.37; 4.67; 3.37 kGy and a technique was developed for using the scanner to measure absorbed doses in the range of 3 – 10 kGy. For each dose, 4 film dosimeters were prepared. To calculate the absorbed dose by calorimeters, macros were developed for LibreOffice Calc and Microsoft Excel spreadsheets. All dosimeters were scanned and a green channel was highlighted using the developed program (the result was obtained in the form of an image in shades of gray). Using the graphical editor GIMP (<https://www.gimp.org/>), a gray value was determined for each dosimeter. In accordance with the recommendations given in NPL Report CIRM 29 [4], the measurement range of the RISØ calorimeter was divided into two areas: 10 – 40 kGy and 3 – 10 kGy. For each area, the dose dependences on the gray value were plotted and the approximation curves were obtained in the form of a third-order polynomial:


$$3 - 10 \text{ kGy} - \quad \text{Dose} = 7.55213 \cdot 10^{-6} \cdot x^3 - 0.00189324 \cdot x^2 - 0.332016 \cdot x + 87.5538,$$

$$10 - 40 \text{ kGy} - \quad \text{Dose} = 1.55466 \cdot 10^{-6} \cdot x^3 + 8.14774 \cdot 10^{-5} \cdot x^2 - 0.364245 \cdot x + 64.9261.$$

The uncertainty of the absorbed dose measurement is 5.8 %.

ORCID IDs

 Volodymyr Morgunov <https://orcid.org/0000-0002-8681-1941>,

 Serhii Lytovchenko <https://orcid.org/0000-0002-3292-5468>,

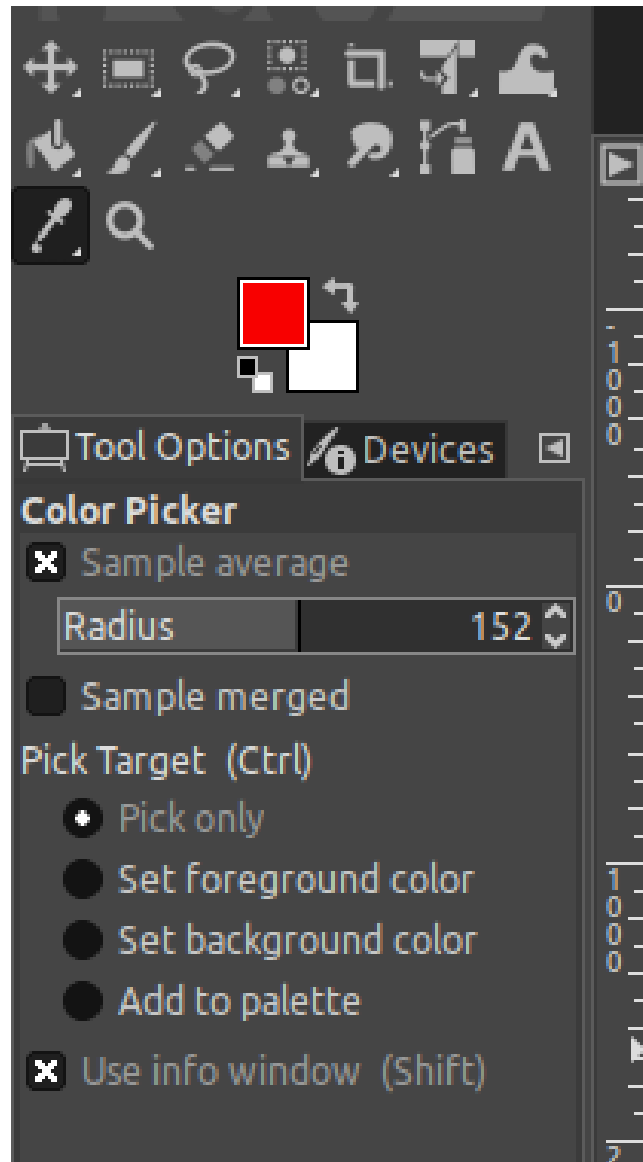


Figure 9: "Color Picker" settings menu.

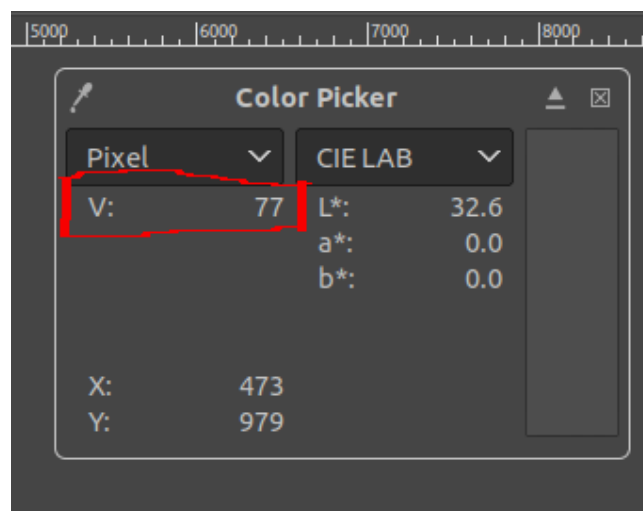


Figure 10: Gray value.

 Volodymyr Chyshkala <https://orcid.org/0000-0002-8634-4212>,
 Nataly Didenko <https://orcid.org/0000-0003-3318-438X>.

REFERENCES

- [1] A. Miller, P. Hargittai, and A. Kovacs, Radiation Physics and Chemistry **57**, 679–685 (2000), [https://doi.org/10.1016/S0969-806X\(99\)00507-1](https://doi.org/10.1016/S0969-806X(99)00507-1).
- [2] S. Devic, J. Seuntjens, E. Sham, E. B. Podgorsak, C. R. Schmidlein, A. S. Kirov, and C. G. Soares, Medical physics **32**, 2245–2253 (2005), <https://doi.org/10.1118/1.1929253>.
- [3] International Organization for Standardization, *ISO/ASTM 51631:2020 Practice for use of calorimetric dosimetry systems for dose measurements and dosimetry system calibration in electron beams*, Standard (International Organization for Standardization, Geneva, CH, Feb. 2020).
- [4] P. Sharpe and A. Miller, National Physical Laboratory. NPL Rep. CIRM **29** (2009).

ВИКОРИСТАННЯ СКАНЕРА ДЛЯ ВИМІРЮВАННЯ ПОГЛИНЕНИХ ДОЗ РАДІОХРОМНИМИ ПЛІВКОВИМИ ДОЗИМЕТРАМИ

В. В. Моргунов^а, С. В. Літовченко^а, В. О. Чішкала^а, Н. В. Діденко^б, В. О. Винник^а

^а Харківський національний університет імені В. Н. Каразіна, Пл. Свободи, 4, Харків, 61022, Україна;

^б Харківський національний автомобільно-дорожній університет, вул. Ярослава Мудрого, 25, Харків, 61002, Україна

У статті наведено послідовність етапів використання калориметрів RISØ для калібрування та подальшого використання радіохромних плівкових дозиметрів ВЗ (корпорація GEX) та сканера для вимірювання поглинених доз. Калібрування проводилося за допомогою електронного пучка в діапазоні поглинених доз 3 – 40 кГр (діапазон вимірювань RISØ калориметрів).

В ході роботи було проведено наступне:

- калібрування радіохромних дозиметричних плівок ВЗ за допомогою RISØ калориметрів;
- побудова калібрувальної кривої для радіохромних дозиметричних плівок ВЗ;
- розрахунок апроксимаційних функцій;
- розробка методики використання планшетного сканера для вимірювання поглинених доз;
- оцінка невизначеності вимірювання поглинених доз.

Параметри роботи прискорювача: частота сканування пучка прискорених електронів – 5 Гц, частота імпульсів – 120 Гц, енергія електронів – 5 МеВ, струм електронного променя – 60 μ А. Похибка вимірювання поглиненої дози становить 5,8 %.

Ключові слова: поглинена доза, калориметр, радіохромні дозиметричні плівки, сканер, невизначеність.

FLUORESCENCE STUDY OF THE INTERACTIONS BETWEEN INSULIN AMYLOID FIBRILS AND PROTEINS[†]

 **Uliana Tarabara***,  **Olga Zhytniakivska**,  **Kateryna Vus**,
 **Valeriya Trusova**,  **Galyna Gorbenko**

*Department of Medical Physics and Biomedical Nanotechnologies, V.N. Karazin Kharkiv National University
4 Svobody Sq., Kharkiv, 61022, Ukraine*

**Corresponding Author: uliana.tarabara@karazin.ua*

Received January 15, 2022, revised January 22, 2022; accepted January 23, 2022

Self-assembly of proteins and peptides into amyloid fibrils is the subject of intense research due to association of this process with multiple human disorders. Despite considerable progress in understanding the nature of amyloid cytotoxicity, the role of cellular components, in particular proteins, in the cytotoxic action of amyloid aggregates is still poorly investigated. The present study was focused on exploring the fibril-protein interactions between the insulin amyloid fibrils and several proteins differing in their structure and physicochemical properties. To this end, the fluorescence spectral properties of the amyloid-sensitive fluorescent phosphonium dye TDV have been measured in the insulin fibrils (InsF) and their mixtures with serum albumin (SA) in its native solution state, lysozyme (Lz) and insulin (Ins) partially unfolded at low pH. It was found that the binding of TDV to the insulin amyloid fibrils is followed by considerable increase of the fluorescence intensity. In the system (InsF + TDV) the TDV fluorescence spectra were decomposed into three spectral components centered at ~ 572 nm, 608 nm and 649 nm. The addition of SA, Lz or Ins to the mixture (InsF + TDV) resulted in the changes of the fluorescence intensity, the maximum position and relative contributions ($f_{i,3}$) of the first and third spectral components into the overall spectra. The Förster resonance energy transfer between the TDV as a donor and a squaraine dye SQ1 as an acceptor was used to gain further insights into the interaction between the insulin amyloid fibrils and proteins. It was found that the presence of SA do not change the FRET efficiency compared with control system (InsF + chromophores), while the addition of Lz and Ins resulted in the FRET efficiency decrease. The changes in the TDV fluorescence response in the protein-fibril systems were attributed to the probe redistribution between the binding sites located at InsF, the non-fibrillized Ins, SA or Lz and protein-protein interface

Keywords: phosphonium probe, insulin amyloid fibrils, fibril-protein complexation.

PACS: 87.14.C++c, 87.16.Dg

A conformational space of protein molecules includes a variety of structures differing in their free energy, among which are unfolded, partially folded and native structural states, oligomers, amorphous aggregates and amyloid fibrils [1-4]. Of these, most attention has been paid in the last decade to the amyloid fibril state of a polypeptide chain [1-4]. A distinctive feature of this state is the presence of cross- β core in which intermolecular β -sheets propagate along the main fibril axis [5], resulting in a characteristic X-ray diffraction picture with reflections corresponding to separation of β -sheet strands (~0.5 nm) and spacing between β -sheet layers (1 nm), respectively [6]. Amyloid fibrils are currently a subject of keen interest, mostly in biomedical and nanotechnological aspects [7,8]. Multiple lines of evidence indicate that fibrillar protein aggregates and their precursors are involved in the development of more than forty human disorders, such as neurological diseases, systemic amyloidosis, type II diabetes, etc. [9,10]. The amyloid assemblies have been found both in intracellular and extracellular space and their cytotoxicity is primarily associated with the impairment of cell membranes [11,12]. The structurally flexible early oligomeric intermediates with extensive hydrophobic areas have been shown to cause membrane disintegration [13,14], formation of non-specific ionic channels [15], uptake of membrane lipids [16,17], etc. Furthermore, it has been demonstrated that not only protein oligomers, but an ensemble of cross- β -sheet-rich protein aggregates including mature fibrils display a high cytotoxic potential. Specifically, mature lysozyme fibrils have been reported to produce hemolysis of erythrocytes [14], mitochondrial failure and increase of plasma membrane permeability [18]. However, it seems likely that membranes are not the only target for cytotoxic action of amyloid aggregates and other cellular components, such as proteins can be affected by amyloids under in vivo conditions. In view of this, the aim of the present study was to explore the interactions between the insulin amyloid fibrils and several proteins differing in their structure and physicochemical properties, viz. serum albumin (SA) in its native solution state, lysozyme (Lz) and insulin (Ins) partially unfolded at low pH. The amyloid-sensitive fluorescent phosphonium dye TDV was employed to monitor the fibril-protein complexation.

EXPERIMENTAL SECTION

Materials

Bovine insulin (Ins), bovine serum albumin (BSA), egg yolk lysozyme (Lz), Tris and thioflavin T (ThT) were purchased from Sigma. The phosphonium dye TDV and squaraine dye SQ1 were kindly provided by Prof. Todor

[†] **Cite as:** U. Tarabara, O. Zhytniakivska, K. Vus, V. Trusova, and G. Gorbenko, East. Eur. J. Phys. 1, 96 (2022), <https://doi.org/10.26565/2312-4334-2022-1-13>

© U. Tarabara, O. Zhytniakivska, K. Vus, V. Trusova, G. Gorbenko, 2022

Deligeorgiev (Faculty of Chemistry, University of Sofia, Bulgaria). All other reagents were of analytical grade and used without the further purification. The structural formulas of the employed fluorescent dyes are shown in Fig. 1.

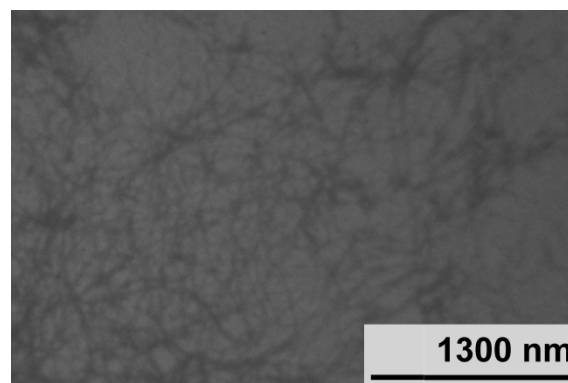
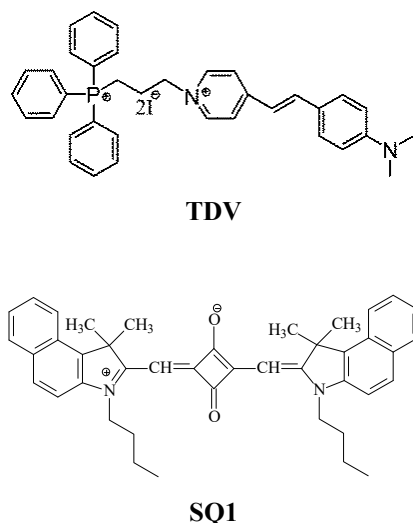


Figure 1. Chemical structures of the employed fluorophores.

Figure 2. Transmission electron microscopy photograph of insulin amyloid fibrils.

Preparation of working solutions

The insulin solution (10 mg/ml) was prepared by dissolving the protein in 10 mM glycine buffer (pH 2.0). To prepare the amyloid fibrils, this solution was subjected to constant agitation on the orbital shaker at 37 °C. The stock solutions of ThT and TDV were prepared in 10 mM Tris-HCl buffer (pH 7.4), while SQ1 was dissolved in dimethyl sulfoxide. The concentrations of the protein and dyes were determined spectrophotometrically using the extinction coefficients $\varepsilon_{277} = 6.1 \cdot 10^3 \text{ M}^{-1}\text{cm}^{-1}$ (Tyr residues of insulin, [19]), $\varepsilon_{412} = 3.6 \cdot 10^4 \text{ M}^{-1}\text{cm}^{-1}$ (ThT, [20]), $\varepsilon_{676} = 2.3 \cdot 10^5 \text{ M}^{-1}\text{cm}^{-1}$ (SQ1, [21]), $\varepsilon_{480} = 2.05 \cdot 10^4 \text{ M}^{-1}\text{cm}^{-1}$ (TDV). The amyloid nature of the protein aggregates was confirmed by ThT assay and the transmission electron microscopy (Fig. 2). To monitor the kinetics of ThT fluorescence, the aliquots of insulin solution (10 μl) were withdrawn every 24 hours and added to ThT solution in Tris-HCl buffer (3.72 μM), with subsequent recording of the dye fluorescence spectra.

TEM measurements

The samples for the transmission electron microscopy assay were prepared as follows: a 10 μl drop of the insulin solution (378 μM) in Tris-HCl buffer (pH 7.4) was applied to a carbon-coated grid and blotted after 1 min. A 10 μl drop of 1.5% (w/v) phosphotungstic acid solution was placed on the grid, blotted after 30 s, and then washed 3 times by deionized water, air dried and viewed at 75 kV by a Selmi EM-125 electron microscope (Selmi, Ukraine).

Fluorescence measurements

The fluorescence measurements were carried out in 10 mM Tris-HCl buffer (pH 7.4) with a Perkin-Elmer FL-6500 spectrofluorometer (Perkin Elmer, UK). The steady-state fluorescence spectra of TDV were recorded at 25 °C within the range of 490–750 nm at the excitation wavelength of 470 nm using 10 mm path length quartz cuvettes. The excitation and emission slit widths were set at 10 nm.

Deconvolution of fluorescence spectra and FRET data analysis

The deconvolution of the total fluorescence spectra of TDV into separate peaks was performed with the Origin software (version 9.4) using the log-normal asymmetric function [22]:

$$I = I_{\max} \exp \left[-\frac{\ln 2}{\ln^2(\rho)} \ln^2 \left(\frac{a - \nu}{a - \nu_c} \right) \right] \quad (1)$$

where ν is the wavenumber, I is the fluorescence intensity on the wavenumber scale $I(\nu) = \lambda^2 I(\lambda)$ [23]; $I_{\max} = I(\nu_c)$ is the fluorescence intensity maximum (the peak amplitude), ν_c is the peak center; $\rho = (\nu_c - \nu_{\min}) / (\nu_{\max} - \nu_c)$ is the asymmetry of the band, ν_{\max} and ν_{\min} are the maximum and minimum wavenumber values at the half-amplitude; $a = \nu_c + (\nu_{\max} - \nu_{\min}) \cdot \rho / (\rho^2 - 1)$ is the limiting wavenumber, after reaching which the peak intensity becomes equal to zero.

The FRET efficiencies were determined from the decrease of the TDV fluorescence in the presence of SQ1 [23]:

$$E = 1 - \frac{I_{DA}k}{I_D} \tag{2}$$

where I_D , I_{DA} are the donor fluorescence intensities in the absence and presence of the acceptor, respectively; $k = 10^{(A_a^{ex} + A_a^{em})/2}$ is the inner filter effect correction factor; A_a^{ex} and A_a^{em} are the acceptor absorbance at the donor excitation and emission wavelengths, respectively. The Förster radii were calculated for each donor-acceptor pair using the Mathcad 15.0 software (PTC) as [23]:

$$R_0 = 979(\kappa^2 n_r^{-4} Q_D J)^{1/6}, \quad J = \int_0^\infty F_D(\lambda) \varepsilon_A(\lambda) \lambda^4 d\lambda / \int_0^\infty F_D(\lambda) d\lambda \tag{3}$$

where J is the overlap integral derived from numerical integration; $F_D(\lambda)$ is the donor fluorescence intensity; $\varepsilon_A(\lambda)$ is the acceptor molar absorbance at the wavelength λ ; n_r is the refractive index of the medium; Q_D is the donor quantum yield; κ^2 is the orientation factor, depending on the relative spatial orientation of the donor and acceptor transition dipoles. The quantum yield of the donor required for the calculation of the Förster radius, was estimated as:

$$Q_D = \frac{Q_{st} (1 - 10^{-A_{st}}) S_D n_D^2}{(1 - 10^{-A_D}) S_{st} n_{st}^2} \tag{4}$$

where subscripts D and st refer to the donor dye and standard, respectively; A_D , A_{st} are the optical densities at the excitation wavelength; S_D , S_{st} are the integrated areas of fluorescence spectra; n_D , n_{st} are the refractive indexes of the dye solutions.

The standard used for TDV was Rhodamine 6G in water ($Q_{st} = 0.93$). In the fibril-bound state the quantum yield of TDV was found to be 0.11. To obtain the quantitative estimates for the average donor-acceptor separation, the results of FRET measurements were treated in terms of the classical expression for the distance dependence of FRET efficiency:

$$E = \frac{R_0^6}{R_0^6 + R^6}; \quad R = R_0 (1/E - 1)^{1/6} \tag{5}$$

RESULTS AND DISCUSSION

As illustrated in Fig. 3A, the binding of TDV to the insulin amyloid fibrils (InsF) is followed by considerable increase of the fluorescence intensity (more than 30-fold at the emission maximum 610 nm), arising presumably from the reduced polarity and mobility of the dye molecular environment. Using the previously determined quantitative parameters of the TDV-InsF complexation (the association constant - $28.6^{±5.4} \mu\text{M}^{-1}$, the binding stoichiometry - $0.07^{±0.013}$ [24]), the fraction of the fibril-bound under the employed experimental conditions dye was estimated to be ~ 26% (0.23 μM at InsF and TDV total concentrations 3.5 μM and 0.9 μM , respectively). Furthermore, it appeared that the TDV fluorescence spectra can be decomposed into three spectral components centered for the system (InsF + TDV) at ~ 572 nm, 608 nm and 649 nm (Table 1).

Table 1. Spectral characteristics of TDV in the presence of insulin fibrils and proteins

System	Band	A_{\max}^*	λ_c , nm	FWHM, nm	f , %	R^2
TDV in free state	I	768.9	578.2	78.5	27	0.998
	II	1740.2	622	68.4	45	
	III	286.1	655.8	169.7	28	
TDV+InsF	I	19885.9	572	53.6	17.9	0.998
	II	80601.0	608.8	50	51.5	
	III	37796.3	649.2	57.25	30.6	
(TDV+InsF)+BSA	I	30803.0	578.9	63.4	34.8	0.998
	II	51435.6	613.8	58.8	51.6	
	III	9602.0	670	69.9	13.6	
(TDV+InsF)+Lz	I	28105.8	579.9	74.9	64.5	0.997
	II	15283.5	608.9	49.5	23.9	
	III	4380.0	647.6	62.9	11.6	
(TDV+InsF)+Ins	I	99120.9	587.1	83.5	71.4	0.998
	II	53455.5	605.7	43.6	20.5	
	III	11579.5	648.8	61.8	8.1	

*the maximum fluorescence intensity is given after baseline subtraction

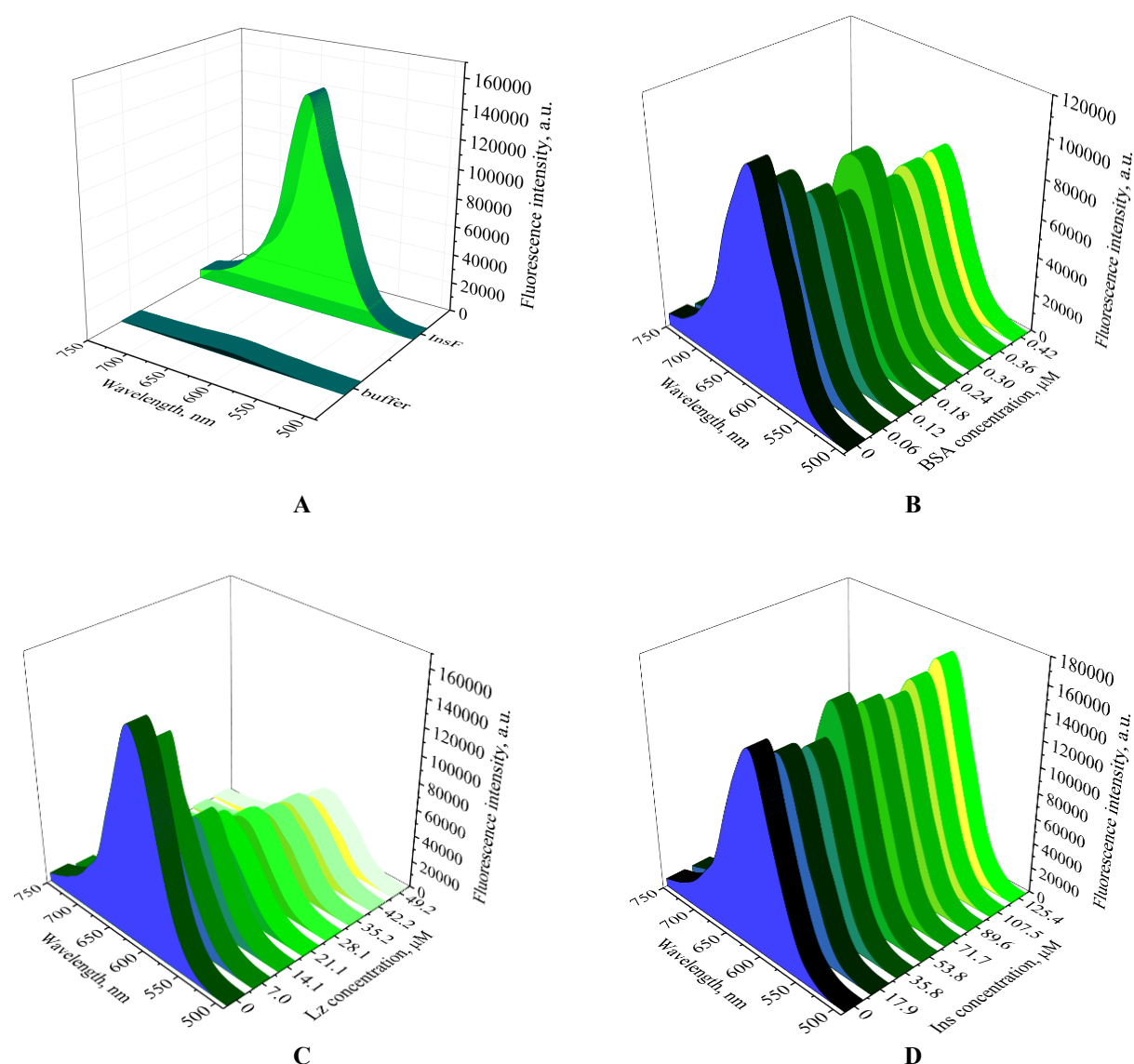


Figure 3. TDV fluorescence spectra in buffer and in the presence of insulin fibrils (A). The fluorescence spectra of TDV in the fibril-bound state at the increasing concentration of serum albumin (B), lysozyme (C) and insulin (D). InsF concentration was 3.5 μM , dye concentration was 0.9 μM .

Three bands in the dye fluorescence spectra in the system (InsF + TDV) most probably result from the existence of the different modes of TDV binding to the insulin fibrils. In our previous studies we demonstrated that the solvent-exposed groove Gln15_Glu17 provides the most energetically favorable binding sites for TDV due to electrostatic interactions between a negatively charged side chain of glutamic acid and TDV molecule which bears two positive charges localized on phosphorus and nitrogen atoms [24]. Moreover, it was shown that TDV only partially inserts into Gln15_Glu17 groove, adopting a non-planar conformation. However, due to the preference of TDV and classical amyloid marker ThT to the same binding sites [24], we cannot rule out the possibility of TDV accumulation in the clustered areas of fibril network (the cavities formed between the intertwined insulin fibrils) as was previously demonstrated for ThT [25].

Next, the amyloid-sensitive fluorescent phosphonium dye TDV was employed to monitor the interactions between the insulin amyloid fibrils and proteins such as serum albumin, lysozyme or insulin in the non-fibrillized form (Fig 3, Fig 4). The addition of BSA to the mixture (InsF + TDV) resulted in the decrease of fluorescence intensity coupled with the changes in the maximum position and relative contributions ($f_{1,3}$) of the first and third spectral components into the overall spectra (Fig. 3B, Fig. 4A). As seen in Table 1, BSA gives rise to f_1 increase (from 18% to 35%) and f_3 decrease (from 31% to 14%), along with the red shift of the position of band I, band II and band III for 6.9 nm, 5 nm and 20.8 nm, respectively, compared with the system (TDV+InsF). These effects were accompanied by the broadening of all

bands relative to the TDV spectral components in InsF. Only limited information is available up to now about interaction between albumins and mature amyloid fibrils. In particular, albumin has been reported to inhibit the amyloid- β fibrillization through affecting the conformational ensemble of A β by nonspecific interactions only at the initial stage of the A β aggregation [26]. Likewise, Siposova et al. have demonstrated that albumin-modified magnetic fluids are able to destroy the insulin amyloid fibrils in vitro [27]. To ascertain whether the observed spectral changes are the result of direct TDV-BSA interaction or due to the TDV sensitivity to the BSA-induced changes in the insulin amyloid fibrils, we measured the fluorescence spectra of TDV in the presence of BSA (without InsF). It appeared that TDV-BSA complexation leads to the fluorescence intensity increase only up to 2.3 times (data not shown) with 15-nm hypsochromic shift.

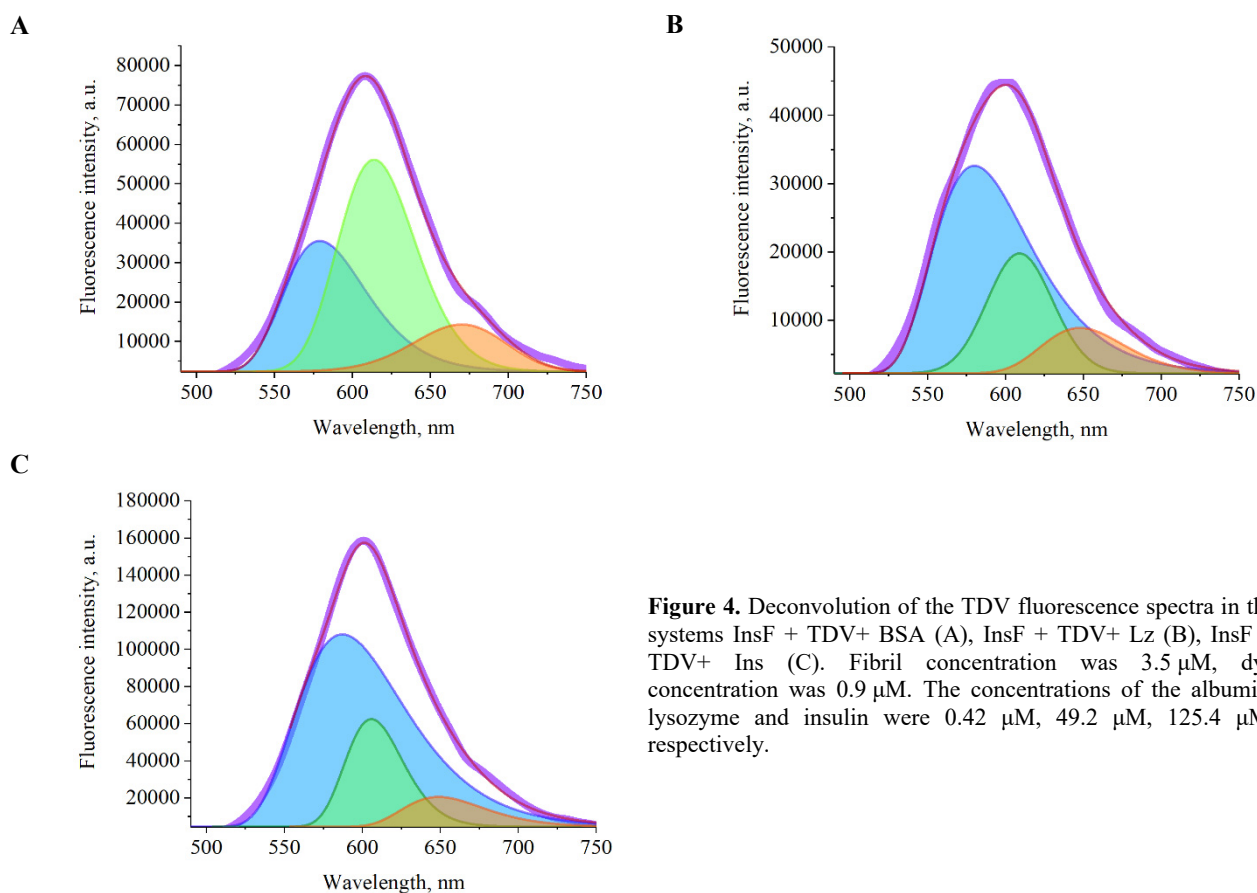


Figure 4. Deconvolution of the TDV fluorescence spectra in the systems InsF + TDV+ BSA (A), InsF + TDV+ Lz (B), InsF + TDV+ Ins (C). Fibril concentration was 3.5 μ M, dye concentration was 0.9 μ M. The concentrations of the albumin, lysozyme and insulin were 0.42 μ M, 49.2 μ M, 125.4 μ M, respectively.

Therefore, the aforementioned spectral changes most likely reflect the redistribution of TDV molecules between the binding sites located at InsF, BSA and protein-protein interface. Given that at pH 7.4 BSA bears a negative charge [28], the redistribution of the positively charged TDV in the presence of BSA is most probably driven by the electrostatic attraction between BSA and TDV. Numerous studies indicate that the principal ligand-binding sites are located in hydrophobic cavities in bovine serum albumin subdomains, referred to as site I and site II according to terminology proposed by Sudlow et al [29]. Moreover, the positively charged dyes (cyanines, squaraines, etc.) generally exhibit a higher specificity to the binding site II of albumins [30,31], so it can be hypothesized that the same mode of binding is realized in our system.

Interestingly, while comparing the fluorescence spectra of TDV+InsF in the presence of the positively charged lysozyme and negatively charged albumin, it becomes evident that the spectral changes induced by Lz are more drastic than those observed for BSA (Fig. 3C, Fig. 4B). More specifically, the addition of lysozyme to the TDV+InsF system resulted in 1.4-fold enhancement of the fluorescence intensity of band I along with a marked drop in the amplitude of the band II (5.3 times) and band III (8.6 times). This effect was accompanied with ~ 8 nm bathochromic shift of the position of band I coupled with the broadening of bands I and III (Table 1). Moreover, the addition of Lz to the mixture (InsF + TDV) produced the changes in the relative contributions ($f_{i,3}$) of the first and third spectral components into the overall spectra, more significant in comparison with those observed in the presence of BSA (Fig. 3B, Fig. 4A). As seen in Table 1, Lz gives rise to f_1 increase (from 18% to 65%) and f_3 decrease (from 31% to 12%).

More pronounced fluorescence decrease and the changes of spectral profile in the presence of the positively charged Lz (Fig. 5B, Fig. 6B), is indicative of essential contribution of electrostatic interactions to stabilization of the protein-fibril and dye-protein complexes. Notably, in the absence of insulin fibrils Lz insignificantly influenced the TDV spectral response, giving rise to only 1.2-fold enhancement of the dye fluorescence. One of the most probable

reason for the drastic decrease of TDV fluorescence after lysozyme addition to the TDV+InsF mixture seems to lie in the competition between the positively charged probe and lysozyme for the binding sites on the insulin amyloid fibrils. It is well known that electrostatic interactions play a crucial role in the complexation of lysozyme with lipid membranes [32, 33], nanoparticles [34] and drugs [35]. Therefore, it is highly probable that electrostatic interactions of the positively charged lysozyme with the solvent-exposed negatively charged amino acid residues of InsF partially block TDV binding sites on the insulin fibrils, thereby causing the TDV fluorescence decrease.

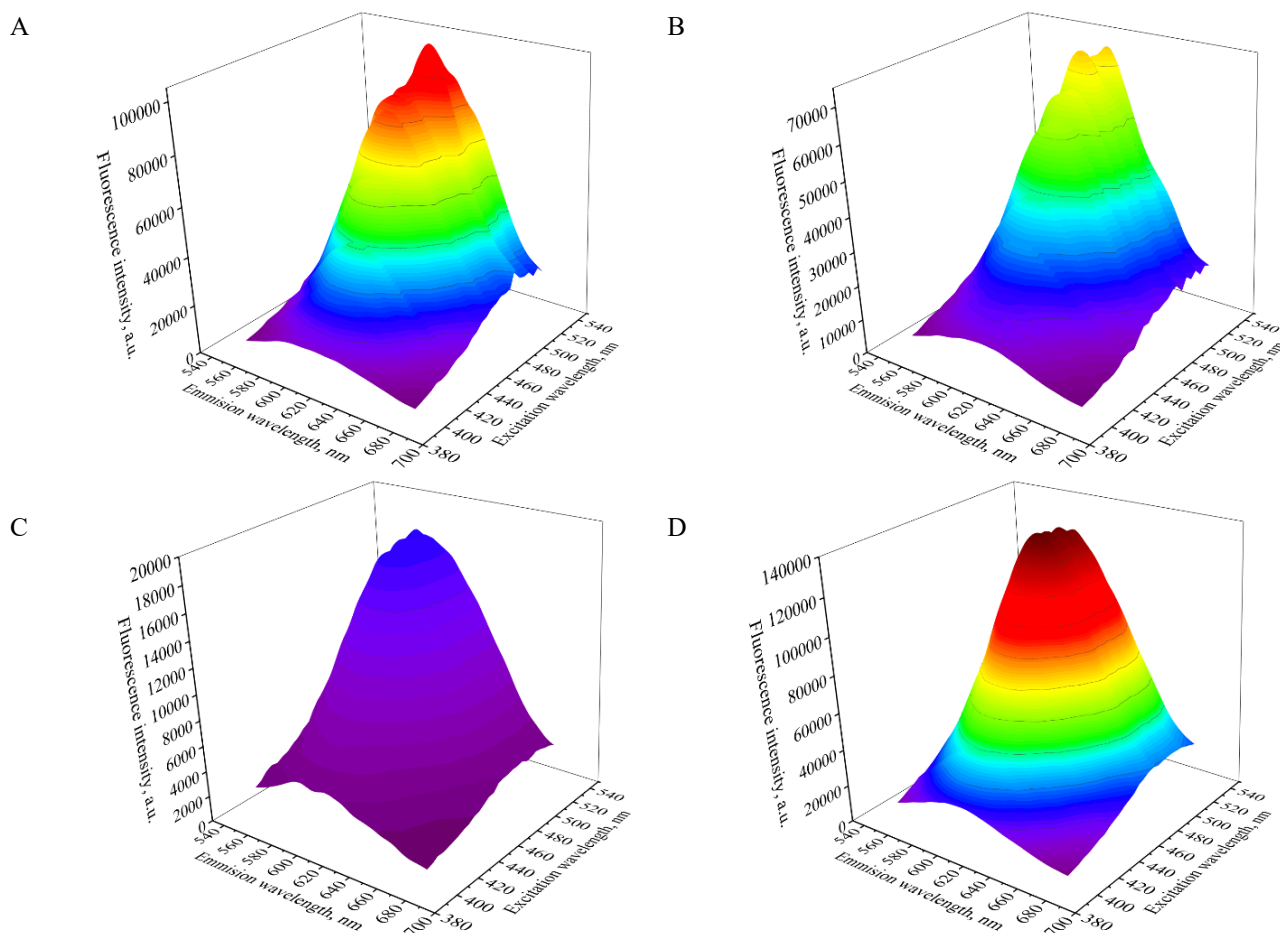


Figure 5. 3D fluorescence spectra of the systems TDV+InsF (A) and after BSA (B), Lz (C) and Ins (D) addition. The emission and excitation wavelengths were varied within the ranges 580–680 nm and 400–530 nm, respectively. The excitation and emission slit widths were set at 10 nm. The false color scale ranging from 1050 a.u. (violet) to 136500 a.u. (red) was used for fluorescence intensity.

The addition of partially unfolded insulin to the system (TDV+InsF) resulted in a slight fluorescence intensity increase coupled with the alterations in the maximum position and relative contributions ($f_{1,3}$) of the first and third spectral components into the overall spectra (Fig. 3D, Fig. 4C). More specifically, the addition of partially unfolded insulin to the system (TDV+InsF) the following spectral changes were observed:

- 1) increase of the band I intensity (5 times), coupled with a slight attenuation of the band II (1.5 times) and band III (3.3 times);
- 2) rise of the relative contribution of the first spectral component f_1 (from 18% to 71%) and decrease in that of the third component f_3 (from 31% to 8%);
- 3) broadening of all spectral bands.

The above spectral changes most likely reflect the redistribution of TDV molecules between the binding sites located at InsF, the partially unfolded insulin and protein-protein interface. The comparison of the spectral responses of TDV in the presence of negatively charged proteins serum albumin and insulin shows that the spectral changes induced by Ins are more drastic. One of the most probable reason for the above effect is a strong affinity of TDV for the insulin partially unfolded at low pH. We observed that the TDV binding to Ins leads to the 17-fold fluorescence increase along with a 21-nm hypsochromic shift of the emission maximum (data not shown). It seems that the electrostatic interactions TDV and Ins/BSA play the predominant role in the TDV-protein complexation and strong hydrophobicity of the BSA binding sites hampers the dye association with this protein. This finding is also

confirmed by the distinct 3D fluorescence patterns of TDV in the examined systems. As seen in Fig. 5, in the presence of the partially unfolded Ins TDV displays a more-intensive 3D pattern than that in the TDV+InsF system. Likewise, the addition of BSA and Lz led to the decrease in the intensity of 3D fluorescence spectra, being more pronounced for lysozyme.

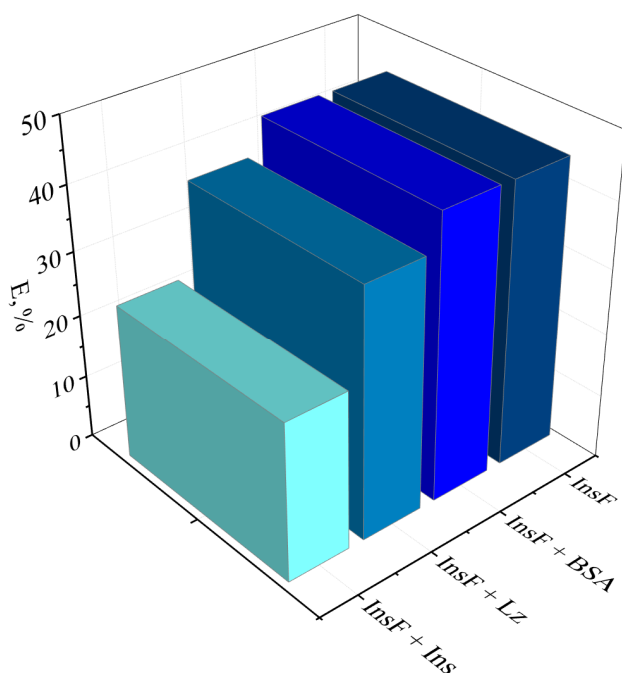


Figure 6. Efficiencies of energy transfer for the donor-acceptor pair TDV-SQ1 in different systems.

At the next step of the study the Förster resonance energy transfer between TDV as a donor and a squaraine dye SQ1 as an acceptor was used to study the interaction between the insulin amyloid fibrils and serum albumin, lysozyme and insulin. Our previous findings indicate that insulin amyloid fibrils can serve as a scaffold for TDV and SQ1, so the energy can be transferred between these fluorophores by a distance-dependent Förster mechanism [24]. The addition of SQ1 to the TDV+InsF system in the absence and presence of the non-fibrillized proteins led to significant quenching of the TDV fluorescence with the magnitude of this effect being dependent on the protein. Using the previously determined FRET parameters for the donor-acceptor pair TDV-SQ1, *viz.* the Förster radius (4.75 nm) and overlap integral ($6.68 \times 10^{15} \text{ M}^{-1} \text{ cm}^{-1} \text{ nm}^4$) [24], the efficiencies of energy transfer in different systems were estimated from the decrease of TDV fluorescence (at 600 nm) in the presence of SQ1 (Fig. 6). It appeared that BSA does not affect the FRET efficiency compared with control system (InsF + chromophores), while the addition of Lz and Ins resulted in the decrease of this parameter (by 5.3 % and 19.5 %, respectively). The average interchromophore distances for the donor-acceptor pair TDV-SQ1 were estimated to fall in the range from 4.9 nm (for InsF and InsF+BSA systems) to 5.7 nm (for InsF+Ins system).

Presented in Fig.7 are 3D fluorescence spectra of the donor-acceptor pair TDV-SQ1 recorded in the presence of InsF, (InsF + BSA), (InsF + Lz) and (InsF + Ins) at the emission and excitation wavelengths covering the range 550-750 nm and 400-452 nm, respectively. More specifically, in the presence of the insulin fibrils the 3D pattern is highly-intensive with the two well-defined and comparable by the intensity maxima centered at ~ 620 nm and ~ 680 nm, corresponding to emission of fibril-bound TDV and SQ1, respectively. The addition of albumin or lysozyme to the system (InsF + chromophores) gives rise to the decrease of the fluorescence signal for both TDV and SQ1 dyes. Notably, the system (InsF + chromophores + Ins) displays highly emissive 3D pattern where the TDV fluorescence signal is significantly greater than that of SQ1. Obviously, the redistribution of TDV and SQ1 driven by their strong affinity to the partially unfolded at low pH insulin resulted in the decreased amount of the acceptor SQ1 in the proximity to the donor (required for the effective FRET) leading to the decrease of the energy transfer rate in the system InsF + Ins.

CONCLUSIONS

In summary, the present study demonstrated that the amyloid-sensitive fluorescent phosphonium dye TDV can be employed for the characterization of the interactions between the insulin amyloid fibrils and several proteins differing in their structure and physicochemical properties. Based on the comprehensive analysis of the spectral characteristics of TDV in the amyloid fibrils and in the presence of serum albumin (in its native solution state), lysozyme or insulin (partially unfolded at low pH) we observed the changes of the fluorescence intensity, the maximum position and relative contributions of the first and third spectral components into the overall spectra after the protein addition to the mixture (InsF + TDV). These effects presumably reflect the redistribution of TDV

molecules between the binding sites located at InsF, the non-fibrillized Ins, BSA or Lz and protein-protein interface.

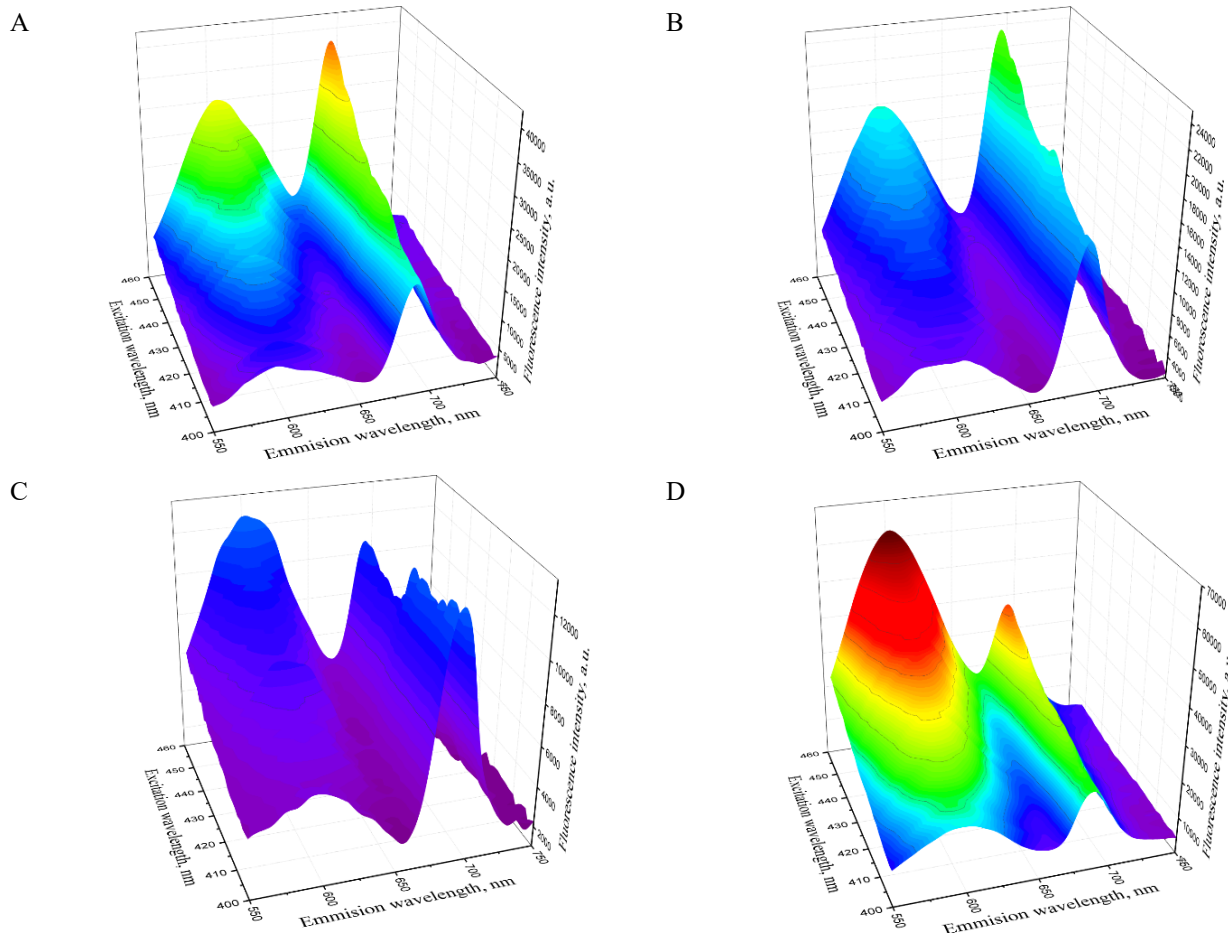


Figure 7. 3D fluorescence spectra of the donor-acceptor pair TDV-SQ1 recorded in the presence of InsF (A), InsF + BSA (B), InsF + Lz (C) and InsF + Ins (D). The emission and excitation wavelengths were varied within the ranges 550-750 nm and 400-452 nm, respectively. The excitation and emission slit widths were set at 10 nm. The false color scale ranging from 800 a.u. (violet) to 65800 a.u. (red) was used for fluorescence intensity. SQ1 concentration was 0.35 μ M.

ACKNOWLEDGEMENTS

This work was supported by the Ministry of Education and Science of Ukraine (the Young Scientist projects № 0120U101064 “Novel nanomaterials based on the lyophilic self-assembled systems: theoretical prediction, experimental investigation and biomedical applications” and the project № 0119U002525 “Development of novel ultrasonic and fluorescence techniques for medical micro- and macrodiagnostics”).

ORCID IDs

- Uliana Tarabara**, <https://orcid.org/0000-0002-7677-0779>;
 Olga Zhytniakivska, <https://orcid.org/0000-0002-2068-5823>
Kateryna Vus, <https://orcid.org/0000-0003-4738-4016>;
 Valeriya Trusova, <https://orcid.org/0000-0002-7087-071X>
Galyna Gorbenko, <https://orcid.org/0000-0002-0954-5053>

REFERENCES

- [1] R. Gallardo, N.A Ranson, S.E Radford, *Curr. Opin. Struct. Biol.* **60**, 7-16 (2020). <https://doi.org/10.1016/j.sbi.2019.09.001>.
- [2] V. Martorana, S. Raccosta, D. Giacomazza, L. A. Ditta, R. Noto, P. L. S. Biagio, M. Manno, *Biophys. Chem.* **253**, 106231 (2019). <https://doi.org/10.1016/j.bpc.2019.106231>.
- [3] C.M. Dobson, *Cold Spring Harb. Perspect. Biol.* **9**, a023648 (2017). <https://doi.org/10.1101/cshperspect.a023648>.
- [4] P. C. Ke, R. Zhou, L. C. Serpell, R. Riek, T. P. J. Knowles, H. A. Lashuel, E. Gazit, I. W. Hamley, T. P. Davis, M. Fändrich, D. E. Otzen, M. R. Chapman, C. M. Dobson, D. S. Eisenberg, R. Mezzenga, *Chem. Soc. Rev.* **49**, 5473-5509 (2020). <https://doi.org/10.1039/C9CS00199A>.
- [5] O.S. Makin, L.C. Serpell, *FEBS J.* **272**, 5950-5961 (2005). <https://doi.org/10.1111/j.1742-4658.2005.05025.x>.
- [6] R. Nelson, D. Eisenberg, *Curr. Opin. Struct. Biol.* **16**, 260-265 (2006). <https://doi.org/10.1016/j.sbi.2006.03.007>.
- [7] Z. Wang, S. Kang, S. Cao, M. Krecker, V. Tsukruk, S. Singamaneni, *MRS Bulletin* **45**, 1017-1026 (2020). <https://doi.org/10.1557/mrs.2020.302>.
- [8] T.P.J. Knowles, R. Mezzenga, *Adv. Mater.* **28**, 6546-6561 (2016). <https://doi.org/10.1002/adma.201505961>.
- [9] M. Stefani, *Biochim. Biophys. Acta*, **1739**, 5-25 (2004). <https://doi.org/10.1016/j.bbadis.2004.08.004>.

- [10] F. Chiti, C. M. Dobson, *Annu. Rev. Biochem.*, **75**, 333-366 (2006). <https://doi.org/10.1146/annurev.biochem.75.101304.123901>.
- [11] M. Bucciantini, S. Rigacci and M. Stefani, *J. Phys. Chem. Lett.*, **5**, 517-527 (2014). <https://doi.org/10.1021/jz4024354>.
- [12] S. M. Butterfield and H. A. Lashuel, *Angew. Chem., Int. Ed.*, **49**, 5628-5654. <https://doi.org/10.1002/anie.200906670>.
- [13] A. A. Meratan, A. Ghasemi and M. Nemat-Gorgani, *J. Mol. Biol.*, **409**, 826-838 (2011). <https://doi.org/10.1016/j.jmb.2011.04.045>.
- [14] B. Huang, J. He, J. Ren, X. Y. Yan and C. M. Zeng, *Biochemistry*, **48**, 5794-5800 (2009). <https://doi.org/10.1021/bi900219c>.
- [15] B. Caughey, P. T. Lansbury, *Annu. Rev. Neurosci.*, **6**, 267-298 (2003). <https://doi.org/10.1146/annurev.neuro.26.010302.081142>.
- [16] E. Sparr, M. F. M. Engel, D. V. Sakharov, M. Sprong, J. Jacobs, B. de Kruijf, J. W. M. Hoppener, J. A. Killian, *FEBS Lett.*, **577**, 117-120 (2004). <https://doi.org/10.1016/j.febslet.2004.09.075>.
- [17] M. F. Engel, L. Khemtémourian, C. C. Kleijer, H. J. Meeldijk, J. Jacobs, A. J. Verkleij, B. de Kruijf, J. A. Killian and J. W. Hoppener, *Proc. Natl. Acad. Sci. U. S. A.*, **105**, 6033-6038 (2008). <https://doi.org/10.1073/pnas.0708354105>.
- [18] A. L. Gharibyan, V. Zamotin, K. Yanamandra, O. S. Moskaleva, B. A. Margulis, I. A. Kostanyan and L. A. Morozova-Roche, *J. Mol. Biol.*, **365**, 1337-1349 (2007). <https://doi.org/10.1016/j.jmb.2006.10.101>.
- [19] J.F. Brandts, L.J. Kaplan, *Biochemistry* **12**, 2011-2024 (1973). <https://doi.org/10.1021/bi00734a027>.
- [20] M. Groenning, *J. Chem. Biol.* **3**, 1-18 (2010). <https://doi.org/10.1007/s12154-009-0027-5>.
- [21] V.M. Ioffe, G.P. Gorbenko, T. Deligeorgiev, N. Gadjev, A. Vasilev, *Biophys. Chem.* **128**, 75-86 (2007). <https://doi.org/10.1016/j.bpc.2007.03.007>.
- [22] M. Bacalum, B. Zorila, M. Radu, *Anal. Biochem.* **440**, 123-129 (2013). <https://doi.org/10.1016/j.ab.2013.05.031>.
- [23] J.R. Lakowicz, *Principles of fluorescence spectroscopy*, 3rd ed., (Springer, New York, 2006).
- [24] G. Gorbenko, O. Zhytniakivska, K. Vus, U. Tarabara, V. Trusova, *Phys. Chem. Chem. Phys.* **23**, 14746-14754 (2021). <https://doi.org/10.1039/D1CP01359A>.
- [25] I. M. Kuznetsova, A.I. Sulatskaya, V. N. Uversky, K. K. Turoverov, *Mol. Neurobiol.* **45**, 488-498 (2012). <https://doi.org/10.1007/s12035-012-8272-y>.
- [26] H. Xie, C. Guo, *Front. Mol. Biosci.* **7**, 629520 (2021). <https://doi.org/10.3389/fmolb.2020.629520>.
- [27] K. Siposova, M. Kubovcikova, Z. Bednarikova, M. Koneracka, V. Zavisova, A. Antosova, P. Kopcansky, Z. Daxnerova, Z. Kazova, *Nanotechnology*, **23**, 055101 (2012). <https://doi.org/10.1088/0957-4484/23/5/055101>.
- [28] U. Bohme, U. Scheder, *Chem. Phys. Lett.*, **434**, 342-345 (2007). <https://doi.org/10.1016/j.cplett.2006.12.068>.
- [29] G. Sudlow, D. J. Birkett, D.N. Wade, *Mol. Pharmacol.*, **12**, 1052-1061 (1976).
- [30] A. Samanta, S. Jana, D. Ray, N. Guchhait, *Spectrochim. Acta. A*, **121**, 23-34 (2014). <https://doi.org/10.1016/j.saa.2013.10.049>.
- [31] V. S. Jisha, K. T. Arun, M. Hariharan, D. Ramaiah, *J. Phys. Chem. B*, **114**, 5912-5919 (2010). <https://doi.org/10.1021/jp100369x>.
- [32] G. Gorbenko, V. Ioffe, P. Kinnunen, *Biophys J.*, **93**, 140-153 (2007). <https://doi.org/10.1529/biophysj.106.102749>.
- [33] G. Gorbenko, V. Ioffe, J. Molotkovsky, P. Kinnunen, *Biochim. Biophys. Acta*, **1778**, 1213-1221 (2008). <https://doi.org/10.1016/j.bbame.2007.09.027>.
- [34] G. Ghosh, L. Panicker, K.C. Barick, *118*, 1-6 (2014). <https://doi.org/10.1016/j.colsurfb.2014.03.026>.
- [35] L. Li, W. Xu, H. Liang, L. He, S. Liu, Y. Li, B. Li, Y. Chen, *126*, 459-466 (2015). <https://doi.org/10.1016/j.colsurfb.2014.12.051>.





ФЛУОРЕСЦЕНТНЕ ДОСЛІДЖЕННЯ ВЗАЄМОДІЇ МІЖ АМІЛОЇДНИМИ ФІБРИЛАМИ ІНСУЛІНУ ТА БІЛКАМИ У. Тарабара, О. Житняківська, К. Вус, В. Трусова, Г. Горбенко

*Кафедра медичної фізики та біомедичних нанотехнологій, Харківський національний університет імені В.Н. Каразіна
м. Свободи 4, Харків, 61022, Україна*

Самоорганізація білків та пептидів в амілоїдні фібрили є предметом інтенсивних досліджень, оскільки встановлено зв'язок цього процесу з численними захворюваннями людини. Незважаючи на значний прогрес у розумінні цитотоксичності амілоїдів, роль клітинних компонентів, зокрема білків, у цитотоксичній дії амілоїдних агрегатів досі повністю не з'ясована. Дана робота спрямована на вивчення взаємодії між амілоїдними фібрилами інсуліну та деякими білками, які відрізняються за своєю структурою та фізико-хімічними властивостями. З цієї метою, було досліджено флуоресцентні спектральні властивості амілоїд-чутливого фосфонієвого барвника TDV у фібрилах інсуліну (InsF) та їх сумішах із нативним сироватковим альбуміном (SA), лізоцимом (Lz) та інсуліном (Ins), частково розгорнутими при низькому рН. Виявилось, що зв'язування TDV з амілоїдними фібрилами інсуліну супроводжується значним зростанням інтенсивності флуоресценції. У системі (InsF + TDV) спектри флуоресценції зонду можна розкласти на три спектральні компоненти з максимумами на довжинах хвиль ~ 572 нм, 608 нм і 649 нм. Додавання SA, Lz або Ins до суміші (InsF + TDV) призводило до зміни інтенсивності флуоресценції, положення максимуму флуоресценції та відносного внеску першої та третьої спектральних компонентів у загальний спектр. Для отримання додаткової інформації щодо взаємодії між амілоїдними фібрилами інсуліну та білками досліджено Фьорстерівський резонансний перенос енергії між TDV у якості донора, і скварайнового барвника SQ1 як акцептора. Встановлено, що SA не змінює ефективність переносу енергії порівняно з контрольною системою (InsF + хромофори), тоді як додавання Lz та Ins призвело до зниження ефективності. Зміни флуоресцентного відгуку TDV у системах білок-фібрили можна пояснити перерозподілом молекул зонду між сайтами зв'язування, розташованими на InsF, нефібрилізованих Ins, SA або Lz та інтерфейсі білок-білок.

Ключові слова: фосфонієвий зонд, амілоїдні фібрили інсуліну, комплекс фібрила-білок.

INVESTIGATION OF INTERACTION MECHANISMS OF HIGH ENERGY ELECTRONS AND GAMMA QUANTUM WITH AQUEOUS SOLUTION OF METHYL ORANGE DYE[†]

 Vitaliy V. Tsyats'ko^{a,*},  Sergey P. Gokov^a,
 Yuri G. Kazarinov^{a,b},  Tetiana V. Malykhina^{a,b}
^aNational Science Center "Kharkiv Institute of Physics and Technology"
 1, Akademichna str., 61108, Kharkiv, Ukraine
^bKharkiv V.N. Karazin National University
 4, Svobody sq., 61022, Kharkiv, Ukraine
 *Corresponding Author: stek@kipt.kharkov.ua

Received February 2, 2022; revised February 16, 2022; accepted March 3, 2022

The level of development of modern nuclear technologies forms a request for the development of new branches of science. At the same time, chemical dosimetry methods are also being improved [1, 2]. The essence of such methods consists in the quantitative determination of the radiation-chemical damages to the molecules of a substance when it is exposed to ionizing radiation [3, 4]. Liquid and solid solutions of organic dyes have intense bands optical absorption and fluorescence in the visible region of the spectrum, which makes it possible to use them in dosimetry systems [5, 6]. The use of organic dyes makes it possible to determine the absorbed dose in the range from 10^{-6} to 10^4 M Rad [7, 8]. In this work, we studied the processes of interaction of gamma-ray and high-energy electron fluxes with an aqueous solution of the organic dye methyl orange ($C_{14}H_{14}N_3O_3SNa$) [9, 10]. The calculations and experiment were carried out on a resonant electron accelerator with energies up to 30 MeV. The electron beam energy was 15 MeV. A tungsten converter was used to generate gamma quanta. The thickness of the converter varied from 0 to 6 mm. We have developed a computer program in C++ to simulate the irradiation process. This program uses the Geant4 class library based on the Monte Carlo method and runs in multi-threaded mode. For calculations, the model "PhysicsList emstandard_opt3" was chosen as the most suitable one. The value of radiation damage per one incident electron and produced gamma-quantum is determined in the work. The simulation results are compared with experimental data. Based on the results obtained, conclusions were drawn about the main mechanisms leading to the decomposition of organic dye molecules, and methods for optimizing the experiment for further research were proposed.

Keywords: organic dye, electron, gamma quantum, dosimetry

PACS: 61.72.Cc, 61.80.Hg, 78.20.Ci, 87.80.+s, 87.90.+y, 07.05.Tp, 78.70.-g

Soon after the discovery of X-ray radiation, the need arose for scientific research on the processes of interaction of ionizing radiation with complex organic objects. The result of such research can be the solution of many problems in various areas of science, as well as many applied problems.

The current level of development of nuclear energy and nuclear technologies is such that there is a need for new approaches to the organization of radiation protection. There is also a need for modern, more compact, easy-to-handle and competitive dosimetry systems and methods. The development of industrial capacities and space exploration generates a need for new materials with modified molecular structures that have both resistant properties to radiation and increased strength characteristics. The results obtained in the course of studies of the mechanisms of interaction of ionizing radiation with molecules of organic matter can be completely extrapolated to a living organism. A living organism is a complex organic system with a number of different properties. These properties can be attributed to both biological and chemical, and physical [11]. Thus, the interest of medical science in such research becomes obvious. For medicine in general and for radiation therapy in particular, organic dyes can be a good research material [12]. This is not a complete list of problems that can be solved by the research that we are conducting in the framework of this work.

In this work, research was carried out with the aim of developing a methodology for using the degradation of organic dye molecules that have been exposed to ionizing radiation as a tool for determining the absorbed dose.

COMPUTER SIMULATION OF EXPERIMENTAL CONDITIONS

Real experiments are planned to study the radiation damage processes of a methyl orange organic dye solution under the influence of an electron beam. The energy of the incident electrons is 15 MeV in an experiment. Before carrying out a series of experiments, it is necessary to carry out computer simulation in order to preliminary estimate the experimental conditions and expected results. Changes to the planned conditions of the experiment are possible based on the preliminary calculations results, as well as geometric parameters clarifications. These parameters include thickness and quantity of tungsten converter layers, distance to the target, etc. Therefore, the estimation of some important parameters required computer simulation. A computer program has been developed in the C++ object-oriented programming language to solve this task. Nuclear-physical processes that occur during the passage of radiation through matter are described in this work using the Geant4 class library [13]. The Geant4 library is a modern toolkit that

[†] **Cite as:** V.V. Tsyats'ko, S.P. Gokov, Y.G. Kazarinov, and T.V. Malykhina, East. Eur. J. Phys. 1, 105 (2022), <https://doi.org/10.26565/2312-4334-2022-1-14>
 © V.V. Tsyats'ko, S.P. Gokov, Y.G. Kazarinov, T.V. Malykhina, 2022

is essential for solving practical problems to describe linear electron accelerators models. In particular, one can solve the tasks of developing and improving the parameters of bremsstrahlung converters using Geant4 toolkit.

The program we have developed contains several main modules. There are modules for describing the geometry of an experiment, a module for describing the primary particles source, a module for determining models of physical processes, etc. In addition, the program contains some functions required to select the appropriate level of the results detail.

The Geant4 toolkit is based on the Monte Carlo method. Therefore, it is necessary to simulate a large number of primary particles passing through the experimental setup to obtain results with a minimum statistical error in calculations. The quantity of primary electrons $N_e=10^7$ for performing virtual nuclear physics experiments. The statistical error of calculation by the Monte Carlo method is less than 1% in this case. The use of a large number of primary particles usually leads to a calculation time increasing. The calculations were carried out in a multithreaded mode in order to reduce the total computation time. These calculations were performed using the OpenMPI library [14], which is free and open source software.

The module for describing physical processes in the developed program is based on the "emstandard_opt3" model, which is most suitable [15, 16] in the considered energy range (up to 15 MeV) for all primary and secondary particles. The threshold energies E_{cut} were chosen to be equivalent to a range of 100 μm in the substance. The user does not directly define the energy threshold because there is a special method of threshold calculations [15] used in Geant4 for different materials. The user defines a unique cut in range [13], whose value is transformed into a kinetic energy threshold per each material at initialization time of user's program.

The schematic diagram of the experimental setup is shown in Figure 1. Elements of this scheme were used to describe the model geometric parameters used in the developed program.

The distance between the accelerator outlet window (Figure 1) and the bremsstrahlung converter is 50 mm. The accelerator outlet window contains titanium foil. The thickness of the foil is 0.05 mm. The real converter is made of tungsten. Transverse dimensions of the converter are 50 mm \times 50 mm. The target transverse dimensions are 10 mm \times 10 mm. The thickness of the converter was varied from 1 to 8 mm in this series of computational experiments. These calculations are necessary to determine the thickness of the converter that produces the maximum amount of gamma quanta that reach the target boundaries.

The simulated energy spectra of bremsstrahlung gamma quanta emitted from the tungsten converter and reached the target are shown in Figure 2 for different values of the converter thickness. The results are normalized to 1 incident electron.

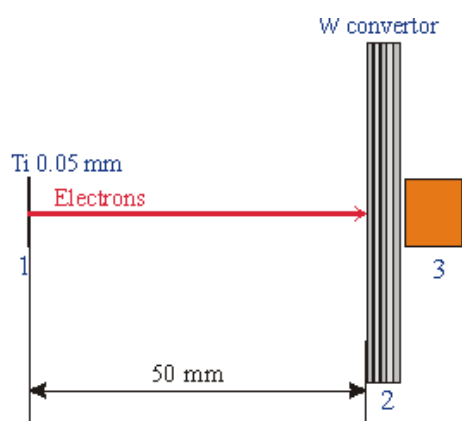


Figure 1. Simplified diagram of the experimental setup: 1 – accelerator outlet window; 2 – bremsstrahlung converter; 3 – the target

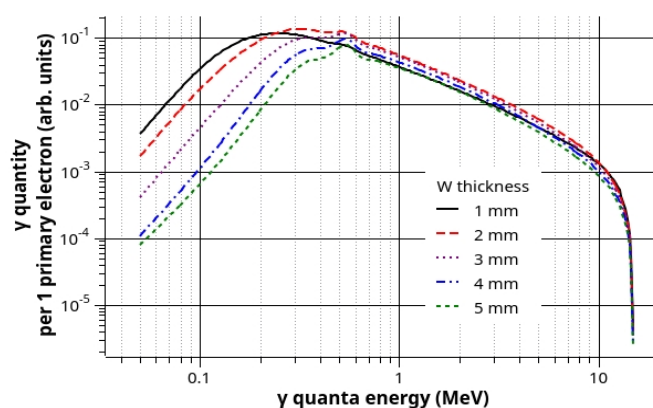


Figure 2. Bremsstrahlung gamma quanta energy spectra for different thickness values of the tungsten converter

As a result of the calculation data analysis, it turned out that the maximum yield of bremsstrahlung gamma quanta is at a tungsten plate thickness of 2 mm. The amount of bremsstrahlung gamma quanta in front of the target slightly decreases at a plate thickness of 3 mm.

The presented materials belong to a series of our works on the study of the behavior of organic substances under the action of ionizing radiation. We carried out measurements with a solution of the organic dye methylene blue ($\text{C}_{16}\text{H}_{18}\text{N}_3\text{SCl}$) in a previous publication [17]. The results are shown in Figure 3 and Figure 4 for various converter thickness values. The result of determining the most probable values of the energy absorbed in the target with methyl orange dye solution is shown in Figure 5. The target dimensions are 10 mm \times 10 mm \times 10 mm. The most probable value of the energy absorbed in the solution is 1.65 MeV for incident electrons with an initial energy of 15 MeV.

Therefore, it is expedient for us to study the processes of the organic dye destruction for several thickness values of the bremsstrahlung converter. We chose 2 mm, 4 mm, and 6 mm. The flow of particles hitting the target contains

mainly gamma quanta at 4 mm converter thickness. The flow of particles crossing the target boundaries contains a negligibly small number of electrons at a converter thickness of 6 mm due to the complete stoppage of primary electrons in the converter material. The flow of particles hitting the target contains gamma quanta, as well as electrons, at 2 mm converter thickness. These values chosen by us are sufficient for studying the dynamics of the processes that occur in the substance of the methyl orange dye under the influence of ionizing radiation.

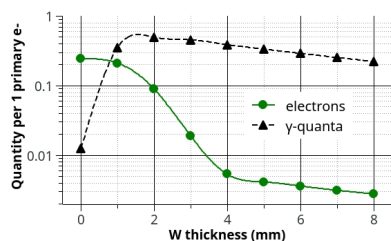


Figure 3. The bremsstrahlung gamma quanta flux in comparison with the electrons flux [17] in front of the target

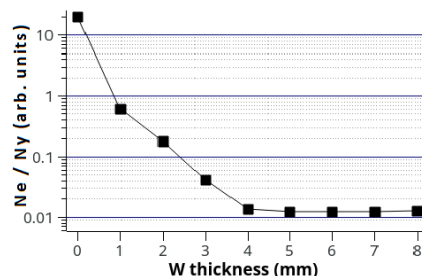


Figure 4. Coefficient of the ratio of electrons and gamma quanta fluxes [17] in front of the target

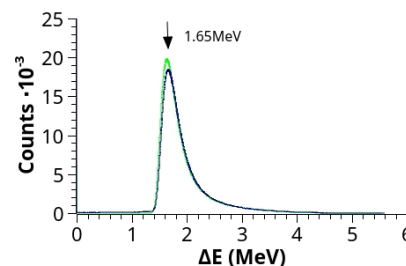


Figure 5. The most probable value of the energy absorbed in the solution for 15 MeV incident electrons

DESCRIPTION OF THE EXPERIMENT

The experimental part of the work was carried out on the LINAC LUE-300 NSC KIPT [12, 17]. The target was an aqueous solution of methyl orange dye with a volume of 1 cm³. It was located in the path of the electron beam in a rigidly fixed glass tube. Target positioning accuracy was ensured by using a fixed stand. This made it possible to set the test tube in a constant position when changing solutions relative to the axis of the accelerator. Conventionally, the experiment can be divided into two parts: irradiation of the target with an electron beam and irradiation of the target with a beam of gamma rays. To generate gamma quanta, a converter was used, which consisted of a set of tungsten plates 50 × 50 × 2 mm in size. The converter was located in front of the target in the direction of the beam. The total thickness of the converter was changed during the experiment in increments of 2 mm (0, 2, 4, and 6 mm).

A tungsten converter, when irradiated with an electron beam, is also a source of neutrons. However, the contribution of neutrons to the change in the color of the dye solution does not exceed ten percent [12]. Since the destruction of methyl orange molecules under the action of a neutron flux on it is insignificant, this contribution was not taken into account in the work.

The experiment was carried out with an electron beam energy of 15 MeV. The current density in this case was 1 μA/cm².

The equipment on which the experiments were carried out is shown in Figure 6.

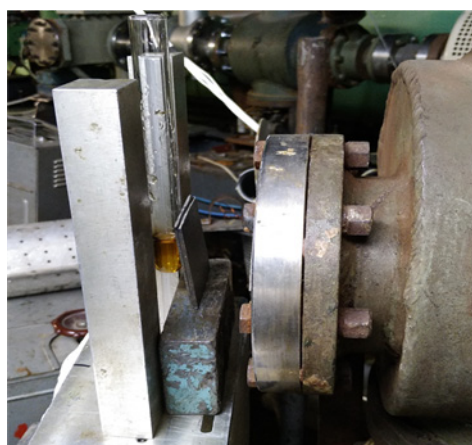


Figure 6. Experimental setup

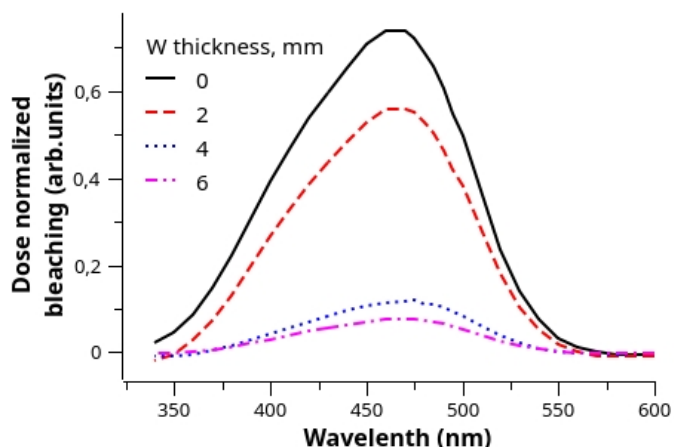


Figure 7. Degradation of methyl orange under the influence of ionizing radiation (normalized to 1 second)

During this experiment, considerable attention was paid to the concentration of the dye solution. To obtain the minimum error in determining the change in the optical density of the solution under the action of irradiation, the initial concentration of the dye in the solution was chosen so that the optical absorption at the maximum of its absorption band (460 nm) was close to unity.

Figure 7 shows the differential absorption spectra (before and after irradiation) normalized per unit time (dose) of irradiation. The spectra were measured on a single-beam spectrophotometer SF-46, in the range from 300 to 600 nm, since the main optical absorption peak of an aqueous solution of methyl orange is in this region. As can be seen from

the graph, when exposed to ionizing radiation for one second on an aqueous solution of methyl orange, a significant destruction of the dye molecules occurs. A decrease in the degree of degradation of dye molecules is observed with an increase in the thickness of the tungsten converter. The black solid line in Figure 7 shows the degree of dye destruction when exposed to an electron beam, that is, at zero tungsten thickness.

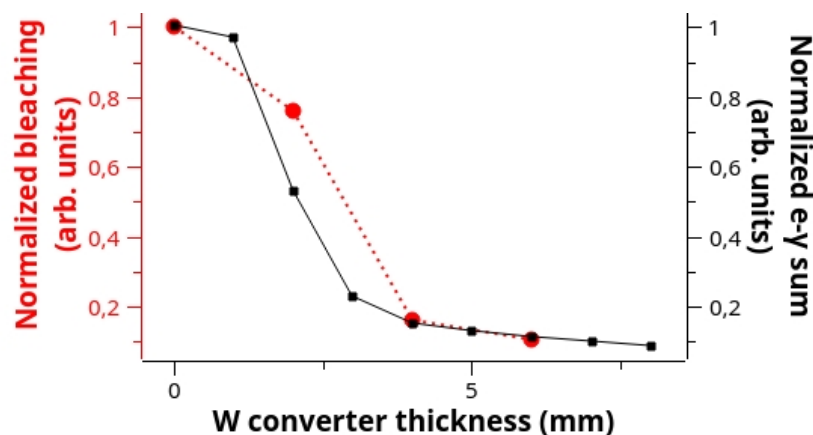


Figure 8. Normalized radiation destruction of the methyl orange solution – left curve, the normalized sum of the number of electrons and gamma quanta that affected the methyl orange solution – right curve

When the radiation length of an electron in tungsten is 3.5 mm, the maximum thickness of the converter used does not exceed two radiation lengths. From here, it follows that the average energy of electrons in front of the target is about 2 MeV or more, which exceeds the average value of the electron energy loss in the solution equal to 1.65 MeV. In this case, the influence of the thickness of the converter on the loss of color of the solution when exposed to electrons can be reduced only to a change in the number of electrons. The dependence of the spectrum of gamma rays on the thickness of tungsten is more pronounced in the energy range up to 0.5 MeV (see Figure 2). In this range, the photoelectric effect, that is, ionization prevails in the interaction cross section. On the other hand, the fraction of gamma quanta with an energy of more than 0.5 MeV does not change significantly, but the Compton effect becomes the dominant interaction channel, and this ensures the destruction of the dye when using converters with a thickness of 4 and 6 mm, when the number of electrons, compared with the initial flow, decreases by 40 times or more, and the level of loss of color by the solution is only 6-8 times.

CONCLUSIONS

In this work, a research was carried out of the processes that occur when an aqueous solution of an organic dye methyl orange ($C_{14}H_{14}N_3O_3SNa$) is exposed to flows gamma quanta and electron. The gamma-ray flux was generated by a relativistic electron beam with an energy of 15 MeV, using a tungsten bremsstrahlung converter of various thicknesses.

In this work, we compared the results of computer simulation of the processes that occur during the passage of an electron beam through a tungsten converter of different thicknesses (0, 2, 4, 6 mm) with the data on the degradation of the dye solution, which were obtained during the experimental. This made it possible to separate the effects of the interaction of electrons from the effects of the interaction of gamma quanta on the dye solution.

We also carried out an approximation of the experimental dependence of the efficiency of the loss of color of the methyl orange solution on the thickness of the tungsten converter. As a result, it was found that the effect of relativistic electrons on the dye leads to the destruction of its molecules 12 times more efficiently than the effect of bremsstrahlung gamma-ray fluxes.

Since the difference in the effectiveness of the effect of these types of ionizing radiation on the methyl orange dye solution is so significant (1/12), we can state the following: when determining the absorbed dose of electron irradiation with an error of less than 10%, the accompanying gamma background can be neglected, provided that the quantitative ratio of electrons and gamma quanta is one.

Based on the studies we have done in this work, it can be argued that an aqueous solution of the organic dye methyl orange is the most optimal object for measuring the absorbed dose of a substance.

ORCID IDs

✉ Vitaliy V. Tsyats'ko, <https://orcid.org/0000-0002-7347-0500>; ✉ Sergey P. Gokov, <https://orcid.org/0000-0002-3656-3804>
✉ Yuri G. Kazarinov, <https://orcid.org/0000-0001-5143-8545>; ✉ Tetiana V. Malykhina, <https://orcid.org/0000-0003-0035-2367>

REFERENCES

- [1] V.F. Plyusnin. *Радиационная химия. Учебное пособие [Radiation chemistry. Tutorial]*, (Novosibirsk, Izd. NGU, 2010), pp. 198. (in Russian)

Using the dependences of the number of electrons and gamma quanta that interacted with the dye solution (the dependences are shown in Figure 3), an analysis was made of the efficiency of dye destruction depending on the thickness of the tungsten converter. This analysis was performed by comparing the change in optical absorption at the wavelength maximum (460 nm) (left dependence in Figure 8) and the normalized sum of the number of electrons and gamma quanta (right dependence in Figure 8). During the analysis, it was found that at a ratio of electrons and gamma quanta equal to 1/12, the maximum coincidence of the dependences was obtained.

- [2] J.-V. Kratz. *Nuclear and Radiochemistry: Fundamentals and Applications (2 Volume Set) 4th Edition*. (Wiley-VCH, 2022). pp. 973. ISBN 978-3-527-34905-0
- [3] M. Spothem-Maurizot, M. Mostafavi, T. Douki, and J. Belloni, (ed.) *Radiation Chemistry: From Basics to Applications in Material and Life Sciences EDP Sciences*, 2008. pp. 324. ISBN 978-2-7598-0024-7
- [4] А.К. Рикаев. *Современная радиационная химия. Основные положения. Экспериментальная техника и методы [Modern radiation chemistry. Basic provisions. Experimental technique and methods]*, (Nauka, Moscow, 1985), pp. 375. (in Russian)
- [5] P.V. Kuchinskiy, and V.I. Popechits, *Vestnik Belorusskogo gosudarstvennogo universiteta*. Ser. 1, Fizika. Matematika. Informatika, **2**, 5 (2011). (in Russian)
- [6] S. Voros, A. Mathias, and B. Boillat, *Physics in medicine and biology*, **57**(5), 1413 (2012).
- [7] V.K. Goncharov, K.V. Kozadayev, V.I. Popechits, and M.V. Puzyrev, *Vestnik Belorusskogo gosudarstvennogo universiteta*. Ser. 1, Fizika. Matematika. Informatika, **1**, 3 (2010). (in Russian)
- [8] A.L. Khusnulina, D.Yu. Kolokolov, and M.I. Kaykanov. *Issledovaniye primeneniya dozimetra Frikke pri izmerenii pogloshchennoy dozy poluchennoy s pomoshch'yu impul'snogo elektronnoy puchka [Elektronnyy resurs]// Sbornik nauchnykh trudov II Vserossiyskoy nauchno-issledovatel'skoy konferentsii molodykh uchennykh, aspirantov i studentov s mezhdunarodnym uchastiyem «Vysokiye tekhnologii v sovremennoy nauke i tekhnike»*, Tomsk. – 2013. – T. 1. – P. 81-85. <http://www.lib.tpu.ru/fulltext/c/2013/C17/V1/020.pdf> (in Russian)
- [9] Sabnis R.W. *Handbook of Acid-Base Indicators* CRC Press, 2007. — 416 p. — ISBN 9780849382185 Basha M. *Analytical Techniques in Biochemistry* Springer, 2020. — 132 p. — (Springer Protocols Handbooks). — ISBN 978-1-0716-0133-4.
- [10] Meesat R., Houde D. *Femtosecond laser pulse filamentation characterized by polymer gel dosimetry and Fricke dosimetry // The 6th International Conference on 3D Radiation Dosimetry*. – IOP Publishing, 2010. – P. 1088-1092
- [11] Basha M. *Analytical Techniques in Biochemistry* Springer, 2020. — 132 p. — (Springer Protocols Handbooks). — ISBN 978-1-0716-0133-4
- [12] S. P. Gokov, Y. G. Kazarinov, S. A. Kalenik, V. Y. Kasilov, T. V. Malykhina, Y. V. Rudychev, V. V. Tsiats'ko, *East. Eur. J. Phys.* **4**, 130 (2021), <https://doi.org/10.26565/2312-4334-2021-4-16>
- [13] J. Allison et.al. Recent developments in GEANT4. *Nuclear Instruments and Methods in Physics Research, Section A*, **835**, 185 (2016). <https://doi.org/10.1016/j.nima.2016.06.125>
- [14] *A High Performance Message Passing Library*, 2021, URL: <https://www.open-mpi.org>
- [15] Geant4 Collaboration, *Book For Application Developers*, 2020, <http://cern.ch/geant4-userdoc/UsersGuides/ForApplicationDeveloper/BackupVersions/V10.6c/fo/BookForApplicationDevelopers.pdf>
- [16] Geant4 Collaboration, *Physics Reference Manual*, 2020, <http://cern.ch/geant4-userdoc/UsersGuides/PhysicsReferenceManual/BackupVersions/V10.6c/fo/PhysicsReferenceManual.pdf>
- [17] S.P. Gokov, Yu.G. Kazarinov, S.A. Kalenik, V.Y. Kasilov, V.V. Kantemirov, O.O. Mazilov, T.V. Malykhina, V.V. Tsiats'ko, and E.V. Tsiats'ko, *PAST*, **6**(136), 42 (2021), <https://doi.org/10.46813/2021-136-42>

ДОСЛІДЖЕННЯ МЕХАНІЗМІВ ВЗАЄМОДІЇ ВИСОКОЕНЕРГЕТИЧНИХ ЕЛЕКТРОНІВ І ГАММА-КВАНТІВ З ВОДНИМ РОЗЧИНОМ БАРВНИКА МЕТИЛОВОГО ОРАНЖОВОГО

В.В. Цяцько^a, С.П. Гоков^a, Ю.Г. Казарінов^{a,b}, Т.В. Малихіна^{a,b}

^aНаціональний науковий центр Харківський фізико-технічний інститут
вул. Академічна, 1, 61108, Харків, Україна

^bХарківський національний університет імені В.Н. Каразіна
майдан Свободи, 4, 61022, Харків, Україна

Рівень розвитку сучасних ядерних технологій формує запит у розвиток нових галузей науки. Натомість удосконалюються і хімічні методи дозиметрії [1, 2]. Суть таких методів полягає у кількісному визначенні радіаційно-хімічних ушкоджень молекул речовини при впливі на нього іонізуючого випромінювання [3, 4]. Рідкі та тверді розчини органічних барвників мають інтенсивні смуги поглинання та флуоресценції у видимій частині спектру, внаслідок чого можуть використовуватись у системах дозиметрії [5, 6]. Використання органічних барвників дозволяє визначати поглинену дозу в діапазоні від 10^{-6} до 10^4 Мрд [7, 8,]. У цій роботі досліджувалися процеси взаємодії потоків гамма-квантів та високоенергетичних електронів з водним розчином органічного барвника метилового оранжевий ($C_{14}H_{14}N_3O_3SNa$) [9, 10]. Розрахунки та експеримент було проведено на резонансному прискорювачі електронів з енергією до 30 МеВ. Енергія електронного пучка становила 15 МеВ. Для генерації гамма-квантів використали вольфрамовий конвертер. Товщина конвертера змінювалась від 0 до 6 мм. Для моделювання процесу опромінення нами була розроблена комп'ютерна програма мовою C++. Ця програма використовує бібліотеки класів Geant4, які базуються на методі Монте-Карло, і функціонує в багатопотоковому режимі. Для розрахунків була обрана модель “emstandard_opt3” складового модулю PhysicsList програми, як найбільш прийнятна у діапазоні енергій до 15 МеВ для процесів, що розглядаються. У роботі було визначено відносну кількість радіаційних пошкоджень, що припадають на один первинний електрон, та створений гамма-квант. Проведено порівняння результатів моделювання з експериментальними даними. На основі отриманих результатів зроблено висновки щодо основних механізмів, які призводять до розвалу молекул органічного барвника, а також запропоновано способи оптимізації експерименту для подальших досліджень.

Ключові слова: органічний барвник, електрон, гамма-квант, дозиметрія

POSITIVELY CHARGED MACROPARTICLES IN LOW-TEMPERATURE PLASMA[†]

 Aleksander A. Bizyukov^a,  Aleksandr D. Chibisov^b,  Dmitry V. Chibisov^{a,*},
 Oksana A. Zhernovnykova^b,  Tamara I. Deynichenko^b, Nikolai N. Yunakov^a

^aV.N. Karazin Kharkiv National University, Svobody Sq., 4, 61002, Kharkiv, Ukraine

^bH.S. Skovoroda Kharkiv National Pedagogical University
 Alchevskyyh St., 29, 61002, Kharkiv, Ukraine

*Corresponding Author: dmitriychibisov@karazin.ua

Received December 14, 2021; revised January 18, 2022; accepted March 12, 2022

The evolution of a positively charged metallic macroparticle placed into the low-temperature plasma is considered. The influence of the value of the initial macroparticle charge on the dynamics of the electrical potential and temperature of the macroparticle, as well as the possibility of evaporation of a macroparticle due to its interaction with plasma particles are studied. The system of equations of the energy balance and the current balance based on the OML theory, that takes into account the changing of macroparticle potential and its temperature over the time is solved numerically. The solution of the system of equations shows the evolution of the macroparticle potential and temperature within the time interval from the moment when the macroparticle is placed in the plasma until the moment the macroparticle has charged to the floating potential. The positive charge of the macroparticle excludes the thermionic emission and secondary electron emission from the macroparticle surface, as well as the mechanisms of cooling of the macroparticle associated with these emission processes. Analytical expressions that determine the macroparticle potential, the electron current on the macroparticle, as well as the power transferred by plasma electrons in the case when the energy of attraction of electrons to the macroparticle strongly exceeds the energy of thermionic electrons, the energy of secondary electrons and the energy of plasma ions are obtained. A simplified system of equations of the energy balance and the current balance for a positively charged macroparticle is solved; the solution of the simplified equations matches with the solution of the general equations in the region of positive values of the macroparticle potential. Calculations show that during the charging of the macroparticle, its temperature increases up to the boiling point of the macroparticle substance. An equation that determines the conditions under which evaporation of macroparticles is possible has been obtained and solved numerically. The possibility of evaporation of macroparticles of a given size (critical value of the radius) due to initial charging to high positive values of potential is shown. The dependencies of the critical value of the radius on the initial value of the potential for tungsten and copper macroparticles that can be evaporated in a low-temperature plasma are obtained. These solutions bound the region of the parameters where evaporation of a macroparticle is possible and where it is not. The critical values of the potential for copper and tungsten particles with sizes of 0.1 and 1 μm are calculated. The dependence of the radius of a macroparticle on time during the process of vaporization is obtained.

Keywords: macroparticles, dusty particles, dusty plasma, floating potential, vaporization

PACS: 52.40.Hf

The investigations of plasma with charged dust particles (dusty plasma) are aimed at various technological and scientific applications [1-5]. Charging of the dust particles or macroparticles (MPs) negatively is performed by the electron beam. It was experimentally and theoretically shown that the charge of micron-sized particles can reach 10^6 electrons [1]. In this case, the particle charge is limited by the effects of thermionic and field emission of electrons. The high negative potential of the particle leads to intensive flow of plasma ions on it and, as a result, to the heating and vaporization of this particle. In paper [3], the processes of charging and vaporization of macroparticles in a low-temperature plasma in the steady state approximation have been studied; it was considered the effect of plasma-beam system parameters on the floating potential and temperature. The transient processes were neglected; it has been shown that interaction of the MPs with low-temperature plasma leads to partial or complete vaporization of MPs. This effect can be used to eliminate microdroplets generated in a vacuum-arc discharge, which is used to thin film coatings. In paper [4] the interaction of MP with a high energy electron beam has been studied. It was shown that intense charging by an electron beam may cause develop of Rayleigh instability that lead to disruption of the MPs into smaller ones and their further decay is possible.

Thus, the behavior in plasma of MPs charged with a high negative potential for their heating and evaporation is well studied. At the same time, the behavior of a positively charged particle in plasma is of interest, which is due to the absence of thermionic emission, as well as the field emission of electrons from the particle.

To introduce a particle with a large positive charge into the plasma, one can use the method developed in the works [6,7]. In those works, positively charged particles of micron and submicron sizes are used to reproduce the flow of micrometeorites in laboratory conditions. These particles are accelerated by high voltages of up to 2 MV. The speed and charge of such particles reach values of 80 km/s and values 10^7 of proton charges, respectively [6,7].

In this work, transient processes of charge and heating of positively charged particles in low-density plasma are studied. The possibility of evaporation of such particles, caused by the flow of energetic electrons from the plasma, is also discussed.

[†] Cite as: A.A. Bizyukov, A.D. Chibisov, D.V. Chibisova, O.A. Zhernovnykova, T.I. Deynichenko, and N.N. Yunakov, East. Eur. J. Phys. 1, 110 (2022), <https://doi.org/10.26565/2312-4334-2022-1-15>
 © A.A. Bizyukov, A.D. Chibisov, D.V. Chibisov, O. A. Zhernovnykova, T.I. Deynichenko, N.N. Yunakov, 2022

MODEL DESCRIPTION

MP placed into the plasma interacts with the plasma in different ways. In such system the following charging processes are take place: absorption of plasma ions and electrons, secondary electron emission, thermionic emission. The process of MP charging by flows of electrons and ions is also accompanied by heating of the MP. The processes of charging and heating of the MP act on each other through the process of thermionic emission from the MP surface.

In general, the floating potential and the temperature of the MP are described by the set of equations [4]:

$$\begin{cases} I_i^{pl} + I_e^{pl} - I_e^s - I_e^{th} = dQ_{mp}/dt; \\ P_e^{pl} + P_i^{pl} - P_s - P_r - P_{th} - P_{vap} = mc dT/dt. \end{cases} \quad (1)$$

The first equation of (1) describes the changing of the MP charge and includes the following charging processes: I_i^{pl} and I_e^{pl} are the ion and electron currents from the plasma onto the MP surface, I_e^s is the secondary electron emission current from the MP surface, I_e^{th} is the thermionic emission current from the MP surface.

Absorption of plasma particles is described by the OML theory and has the form

$$I_\alpha^{pl}(\varphi_a) = e \langle n_0 v_\alpha \sigma_\alpha^{OML} \rangle = e \cdot \Gamma_\alpha,$$

where $\alpha = i, e$ denote the particle species.

$$\Gamma_\alpha = \sqrt{8\pi} a^2 n_0 v_{T\alpha} \left(1 + \frac{|e\varphi_a|}{kT_\alpha} \right),$$

is the current of particles α in a case of attractive MP potential and

$$\Gamma_\alpha = \sqrt{8\pi} a^2 n_0 v_{T\alpha} \exp\left(-\frac{|e\varphi_a|}{kT_\alpha}\right)$$

in a case of repulsive MP potential, n_0 is the plasma number density, $v_{T\alpha}$ is the thermal velocity of particles α , a is the initial MP radius, φ_a is the MP potential. Secondary electron emission is described by the relation:

$$I_e^s = \delta I_e,$$

where

$$\delta = \delta_{\max} \frac{|e\varphi_a|}{E_m} \exp\left(2\left(1 - \sqrt{\frac{|e\varphi_a|}{E_m}}\right)\right)$$

is the secondary electron emission yield: E_m is the electron energy which corresponds to the maximum of secondary emission yield δ_{\max} . Thermionic emission current is described by the Richardson's law

$$I_e^{th} = 4\pi a^2 A T_a^2 \exp\left(\frac{e\Phi - \Delta W}{k_B T_a}\right),$$

where, $A = \frac{4\pi m_e k_B^2 e}{h^3}$, h is the Planck constant, k_B is the Stefan–Boltzmann constant, $e\Phi$ is the work function, T_a is

the temperature of the MP. $\Delta W = \sqrt{e^3 \varphi_a / a}$ is the decreasing of the electron work function (Schottky effect).

The second equation of (1) describes the changing of MP temperature caused by energy flows the following processes: $P_{i(e)}^{pl}$ is the energy flow of plasma particles to the MP; P_r is the energy radiated from the MP surface, P_{vap} is the cooling due to vaporization of MP substance, P_{th} is the energy flow from the MP surface is transferred by the electrons of thermionic current, P_s is the energy flow due to the secondary electron emission. The values of the respective energy flows are determined by the following relations: $P_e^{pl} = \Gamma_e \cdot (2kT_e + e\Phi)$, $P_i^{pl} = \Gamma_i \cdot (2kT_i + e\varphi + I + e\Phi)$, $P_r = \sigma T^4$, $P_{th} = \Gamma_e^{th} \cdot (2k_B T_a)$, $P_s = \Gamma_s \cdot (\langle \varepsilon_s \rangle + e\Phi)$, $P_{vap} = \Gamma_a \cdot (2k_B T_a + p)$, where I is the ionization energy, $\Gamma_a = n' \sqrt{\frac{k_B T_a}{2\pi m_a}} \exp\left(-\frac{p}{k_B T_a}\right)$ is the atom flow of vaporized MP substance, n' is the concentration

of atoms in metal, p is the energy of vaporization an atom, $\Gamma_e^{th} = I_e^{th} / e$, $\Gamma_s = I_s^{e-e} / e$, $\langle \varepsilon_s \rangle$ is the averaged energy of the secondary electrons.

SPECIFIC OF CHARGING AND VAPORIZATION OF POSITIVELY CHARGED MP

We consider the case of positively charged MP placed into the plasma. We suppose plasma number density n_0 is 10^9 cm^{-3} electron T_e and ion T_i temperatures are 10eV and 0.03eV respectively. Calculations was performed for the residual gas pressure 10^{-4} torr , under this conditions the boiling point of the copper is close to the melting point and approximately equal 1350K [8]. The processes of charging and heating of the positively charged MP occurs the different way than the negatively charged MP. We suppose that the magnitude of MP charge is high enough such that $|e\varphi_a| \gg e\Phi$, $|e\varphi_a| \gg \varepsilon_s$, $|e\varphi_a| \gg T_e > T_i$, that is thermionic electrons and secondary electrons are captured by the electric field of the MP, the plasma ions are scattered on the positive potential of the MP. Therefore the ion current on the MP surface and the processes of thermionic emission and the secondary emission from the MP surface can be neglected as well as the energy flows related with these processes. Therefore charging of the MP is entirely as a result of absorption of plasma electrons. Thus, the set of equation (1) in the case of positively charged MP can be simplified:

$$\begin{cases} I_e^{pl} = dQ_{mp}/dt; \\ P_e^{pl} - P_r - P_{vap} = mc \cdot dT/dt. \end{cases} \quad (2)$$

Figure 1a represents the positive part of the MP potential which is solution of the first equation of the sets of equations (1) and (2). From the Figure 1a it can be seen, that typical time of full (except the time interval where $\varphi \leq -T_e / e$) charging τ_{ch} of MP depending on its size is $10^{-6} \div 10^{-4} \text{ s}$.

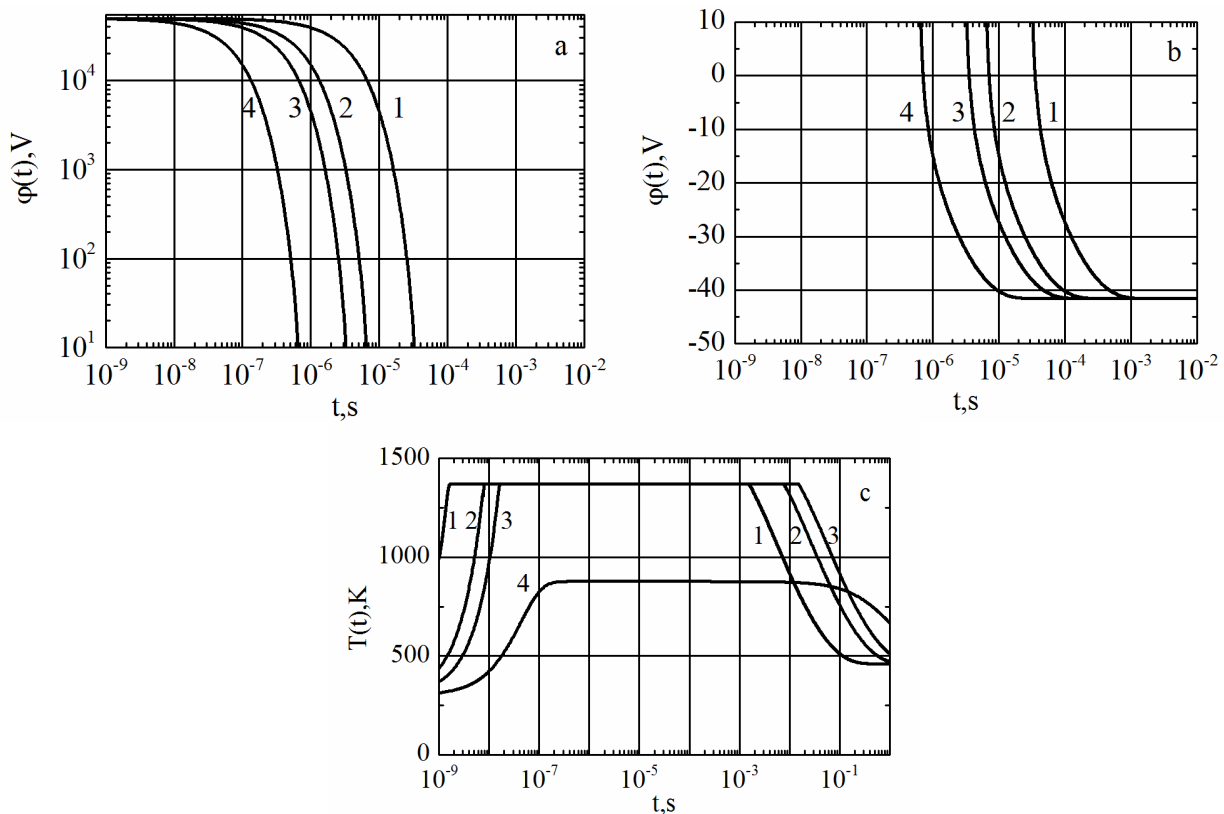


Figure 1. The dependence of the MP potential on the time (a) $\varphi \gg -T_e / e$, (b) $\varphi < -T_e / e$ and related temperature (c), the MP substance is copper initial value of MP potential is $\varphi_0 = 50\text{kV}$, initial MP temperature is $T_0 = 300\text{K}$: 1 – $a = 0.1\mu\text{m}$, 2 – $a = 0.5\mu\text{m}$, 3 – $a = 1\mu\text{m}$, 4 – $a = 5\mu\text{m}$.

Figure 1b shows the part of the solution where the MP potential is lower than 10V including negative values of the MP potential as well as steady state values (floating potential), which is obtained by solving of the set of equation (1). This result is consistent with previous work [4]. Further we will consider the case $\varphi \gg -T_e / e$ that is described well by the set of equation (2).

The Figure 1c shows the numerical solution of the second equation of the sets of equations (1) and (2) that represents the changing of the MP temperature on the time. The MP temperature grows until reaches the boiling point T_b for the MPs sized $0.1 \div 1 \mu\text{m}$ it takes $4 \cdot 10^{-9} \div 4 \cdot 10^{-8} \text{ s}$, then temperature stays constant for some time interval during which the vaporization of the MP occurs. During simulation the dependence the heat capacity on the temperature as well as the process of melting was neglected.

In order to evaluate the parameters MP and plasma when the vaporization of the MP is possible we obtain analytical relations for the basic parameters such as electric potential of the MP, electron and power flows on the MP surface. From the first equation of (2) we obtain MP potential as a function of time:

$$\varphi(t) = \varphi_0 e^{-\beta at}, \quad (3)$$

where $\beta = 4\pi e^2 n_0 v_{Te} T_e^{-1}$. Obtained function (3) described MP potential shown in Figure 1a. Electron flow and power associated with this flow on the MP surface in approximation OML theory under condition $\varphi \gg -T_e / e$ have the form

$$I(t) = \beta a^2 \varphi = \beta a^2 \varphi_0 e^{-\beta at}, \quad (4)$$

$$P_e^{pl}(t) = \beta a^2 \varphi_0^2 e^{-2\beta at}. \quad (5)$$

The time interval τ_b when vaporization of the MP is possible can be found from the condition of equality energy flows on the MP surface $P_e^{pl}(\tau_b) - P_r(\tau_b) = 0$:

$$\tau_b \approx \frac{1}{2\beta a} \ln \frac{\beta \varphi_0^2}{4\pi\sigma T_b^4}. \quad (6)$$

The process of cooling related with vaporization of the MP substance excluded from the equality (6), since the energy losses related with the vaporization lead to mass changing and it will be further taken into account.

The energy transferred to the MP in the time interval τ_b cause the MP vaporization and can be evaluated as:

$$\varepsilon = \int_0^{\tau_b} (P_e^{pl}(t) - P_r(T_b)) dt = \frac{\varphi_0^2 a}{2} - \frac{2\pi\sigma T_b^4}{\beta} a \left(1 + \ln \frac{\beta \varphi_0^2}{4\pi\sigma T_b^4} \right). \quad (7)$$

The energy required to complete vaporization of the MP of radius a is $\varepsilon_{vap} = m_a H = \frac{4}{3} \pi a^3 \rho H$, where H is the heat of vaporization, ρ is the density of MP substance. Substituting this value into (7) gives the condition of vaporization of MPs of radius a in the case of positively charged MP:

$$\frac{\varphi_0^2}{2} - \frac{2\pi\sigma T_b^4}{\beta} \left(1 + \ln \frac{\beta \varphi_0^2}{4\pi\sigma T_b^4} \right) = \frac{4}{3} \pi a^2 \rho H. \quad (8)$$

This equation gives the relation between specific parameters of MP substance such as density and heat of vaporization, the critical initial value of the MP potential and the critical MP radius that can be vaporized. Critical means that the obtained parameters separate two regions of the parameters where MPs can be vaporized and where is not. The numerical solution of the equation (8) is shown in the Figure 2.

Figure 2 shows the critical curves for copper (1) and tungsten (2), the region of the parameters that lies under the curve corresponds to conditions the vaporization of the MP is possible.

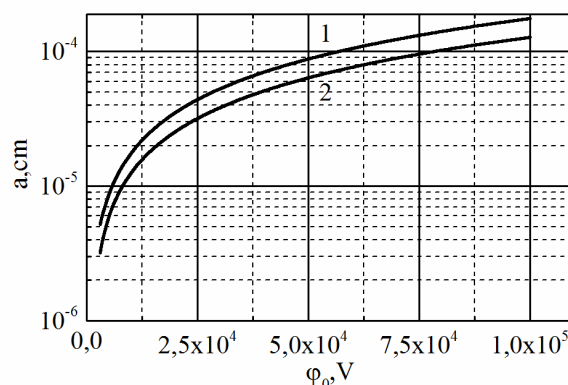


Figure 2. The dependence of the critical MP radius on the critical initial value of the MP potential which can be vaporized: 1 - copper, 2 - tungsten.

The closer to the curve parameters are the longer the process vaporization is, and vice versa the far the parameters from the curve the faster the process vaporization is. In the table 1 some critical values of initial MP potential and MP radius is shown.

Table 1. Some critical values of initial MP potential and MP radius

	0.1 μm	0.5 μm	1 μm
Cu	6kV	28.5kV	57kV
W	8.5kV	39.5kV	78.5kV

When the vaporization of the MP is possible the changing of the MP radius r is described by the equation:

$$\beta\phi_0^2 e^{-2\beta r t} - 4\pi\sigma T_b^4 = 4\pi\rho H \frac{dr}{dt} \tag{9}$$

Numerical solution of the equation (9) for the copper MP is shown in the Figure 3.

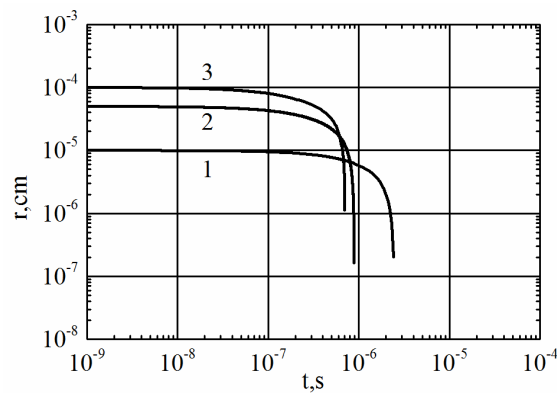


Figure 3. The dependence of the radius on the time at different initial radii a and initial potential ϕ_0 of the copper MP, initial MP temperature is $T_0 = 300K$: 1. $a = 0.1\mu m, \phi_0 = 10kV$, 2. $a = 0.5\mu m, \phi_0 = 40kV$ 3. $a = 1\mu m, \phi_0 = 70kV$.

To simulation of vaporization process the initial parameters of the MP was taken close to the curve 1. From the Figure 3 it can be seen that at given parameters the time of vaporization of the MP with the radius $0.1 \div 1\mu m$ is $0.7\mu s - 2\mu s$. This result correlate with the simulation MP potential and MP temperature (see Figure 1a and Figure 1c) in this time interval the MP temperature is at boil point and MP potential still high enough ($\phi_0 \sim 5 \cdot 10^3 \div 4 \cdot 10^4 kV$). Thus we can conclude that the placing preliminarily positively charged MP to high enough potential can lead to it partially or complete MP vaporization.

CONCLUSIONS

For the preliminarily positively charged metallic macroparticle placed into the low-temperature plasma the set of equations energy and current balance has been solved numerically. The transient values of the MP potential as well as relative temperature have been obtained.






The particle is charged by the flow of electrons from the plasma. It is shown that the time of full (up to values of $\varphi = -T_e / e$) charging τ_{ch} of MP depending on its size is $6 \cdot 10^{-7} \div 3 \cdot 10^{-5} s$.

The electron current from the plasma heats up the particle. In the case of $\varphi \ll -T_e / e$ analytical relations for the MP potential, electron flow and power associated with this flow have been obtained. It was found that the MP heating time up to the boiling point for the MPs sized $0.1 \div 1\mu m$ is $4 \cdot 10^{-9} \div 4 \cdot 10^{-8} s$.

The equation for the initial value of the MP potential and its critical radius at which the particle can be vaporized has been derived and solved numerically. The critical values of radius and potential for copper and tungsten particles, which determine the region of the parameters where MPs can be vaporized, have been obtained. It is found that the initial potentials of the particles of radius $a = 1\mu m$ for the copper and tungsten MP that evaporated are equal $57kV$ and $78.5kV$ respectively.

The equation describing the change in the MP radius during evaporation is derived and solved numerically. It is shown that for given initial potential of MP the time of vaporization of MP with the radius $0.1 \div 1\mu m$ is $0.7\mu s - 2\mu s$. Thus the possibility of partially or complete vaporization in plasma of the preliminarily positively charged metallic MP has been shown.

ORCID IDs

-  Aleksander A. Bizyukov, <https://orcid.org/0000-0003-0192-5219>;  Aleksandr D. Chibisov, <https://orcid.org/0000-0001-9670-3912>
 Dmitry V. Chibisov, <https://orcid.org/0000-0002-6154-9772>;  Oksana A. Zhernovnykova, <https://orcid.org/0000-0002-5383-4493>
 Tamara I. Deynichenko, <https://orcid.org/0000-0003-4117-1503>

REFERENCES

- [1] A. V. Filippov, A. F. Pal', A. N. Starostin, A. V. Gavrikov, V. E. Fortov, O. F. Petrov, and M. N. Vasil'ev Physics of Plasmas, **16**, 093702 (2009), <https://doi.org/10.1063/1.3227646>
- [2] Yu.S. Akishev, V.B. Karal'nik, A.V. Petryakov, A.N. Starostin, N.I. Trushkin, and A.V. Filippov, Plasma Phys. Rep. **42**, 14 (2016), <http://dx.doi.org/10.1134/S1063780X16010013>
- [3] A.A. Bizyukov, K.N. Sereda, and A.D. Chibisov, Problems of atomic science and technology. Series: Plasma physics, **1**(17), 107 (2011), https://vant.kipt.kharkov.ua/ARTICLE/VANT_2011_1/article_2011_1_107.pdf
- [4] A.A. Bizyukov, A.D. Chibisov, E.V. Romashchenko, and Yu.E. Kolyada. Problems of atomic science and technology. Series: Plasma physics, **1**(23), 163 (2017), https://vant.kipt.kharkov.ua/ARTICLE/VANT_2017_1/article_2017_1_163.pdf
- [5] S.I. Kopnin, T.I. Morozova, and S.I. Popel. IEEE Transactions on Plasma Science, **46**(4), 701 (2018) <https://doi.org/10.1109/TPS.2017.2748378>
- [6] A. Mocker, S. Bugiel, S. Auer, et al. Rev. Sci. Instrum. **82**, 095111 (2011). <https://doi.org/10.1063/1.3637461>
- [7] J.D. Kerby, R.T. Daly, and D.E. Austin, Earth Planets Space, **65**, 157 (2013). <http://dx.doi.org/10.5047/eps.2012.08.005>
- [8] T. Iida, and R.I.L. Guthrie, *The Physical Properties of Liquid Metals*, (Oxford, 1988), pp. 86-87, <https://www.amazon.com/Physical-Properties-Liquid-Metals/dp/0198563310>

ПОЗИТИВНО ЗАРЯДЖЕНІ МАКРОЧАСТКИ В НИЗЬКОТЕМПЕРАТУРНІЙ ПЛАЗМІ

Олександр А. Бізюков^а, Олександр Д. Чібісов^б, Дмитро В. Чібісов^а,
Оксана А. Жерновникова^б, Тамара І. Дейніченко^б, Микола М. Юнаков^а

^аХарківський національний університет імені В.Н. Каразіна
61022, Україна, м. Харків, пл. Свободи, 4

^бХарківський національний педагогічний університет імені Г. С. Сковороди,
61002, Україна, м. Харків, бул. Алчевських, 29

Розглянуто еволюцію позитивно зарядженої металевої макрочастинки, яка поміщена в низькотемпературну плазму. Досліджено вплив значення початкового заряду макрочастинки на динаміку електричного потенціалу та температуру макрочастинки, а також можливість випаровування макрочастинки внаслідок її взаємодії з частинками плазми. Чисельно розв'язана система рівнянь балансу енергії та балансу струмів, яка заснована на OML теорії та враховує зміну потенціалу макрочастинки та її температури з плином часу. Розв'язок системи рівнянь показує еволюцію потенціалу та температури макрочастинки протягом інтервалу часу з моменту розміщення макрочастинки у плазмі до моменту, коли макрочастинка зарядилася до плаваючого потенціалу. Позитивний заряд макрочастинки виключає появу термоелектронної емісії та вторинної електронної емісії з поверхні макрочастинки, а також механізми охолодження макрочастинки які пов'язані з цими процесами. Отримано аналітичні вирази, що описують потенціал макрочастинки, електронний струм на макрочастинку, а також потужність, що передається електронами плазми у випадку, коли енергія притягання електронів до макрочастинки значно перевищує енергію термоелектронів, енергію вторинних електронів та енергію іонів плазми. Розв'язано спрощена система рівнянь балансу енергії та балансу струмів для позитивно зарядженої мікрочастинки, розв'язки спрощених рівнянь збігаються з розв'язками загальних рівнянь в області позитивних значень потенціалу макрочастинки. Розрахунки показують, що під час заряджання макрочастинки її температура зростає аж до температури кипіння речовини макрочастинки. Отримано та чисельно розв'язане рівняння, яке визначає умови, за яких можливе випаровування макрочастинки. Показано можливість випаровування макрочастинки заданого розміру (критичне значення радіуса) внаслідок початкової зарядки до високих позитивних значень потенціалу. Отримано залежності критичного значення радіуса від початкового значення потенціалу для макрочастинки вольфраму та міді, які можна випарувати в низькотемпературній плазмі. Отримані розв'язки обмежують область параметрів, де випаровування макрочастинки можливе, а де ні. Розраховано критичні значення потенціалу для частинок міді та вольфраму з розмірами 0,1 і 1 мкм. Отримано залежність радіуса макрочастинки від часу в процесі випаровування.

Ключові слова: макрочастинки, пилові частинки, пилова плазма, плаваючий потенціал, випаровування.

RESOLUTION OF THE ULTRASOUND DOPPLER SYSTEM USING COHERENT PLANE-WAVE COMPOUNDING TECHNIQUE[†]

 Iryna V. Sheina*,  Eugen A. Barannik

*Department of Medical Physics and Biomedical Nanotechnologies, V.N. Karazin Kharkiv National University
4, Svobody Sq., 61022, Kharkiv, Ukraine*

**Corresponding Author: i.sheina@karazin.ua*

Received June 10, 2021; revised February 10, 2022; accepted March 14, 2022

In this work, in the process of plane-wave ultrasound probing from different angles the attainable spatial resolution was estimated on the basis of the previously developed theory of the Doppler response formation. In the theoretical calculations coherent compounding of the Doppler response signals was conducted over the period of changing the steering angles of probing. For this case an analytical expression for the ultrasound system sensitivity function over the field, which corresponds to the point spread function, is obtained. In the case of a rectangular weighting window for the response signals, the resolution is determined by the well-known sinc-function. The magnitude of the lateral resolution is inversely proportional to the range of the steering angles. It is shown that the theoretically estimated magnitude of the Doppler system lateral resolution, when using the technique of coherent plane-wave compounding, is in good agreement with the experimental data presented in literature.

Keywords: ultrasound imaging, Doppler spectra, synthetic aperture technique, coherent plane-wave compounding, continuum model of scattering, sensitivity function, point spread function, response formation.

PACS: 43.28.Py, 43.35.Yb, 43.60.-c, 87.63.D-, 87.63.dk

At present, along with the conventional techniques of ultrasound probing, some techniques, which use plane waves with different propagation directions [1-3] or wave fronts with a different spatial configuration, are rapidly developing [4, 5]. The essence of the technique is in the coherent compounding of the set of recorded ultrasound response signals for each point in space. The described principle of ultrasound probing is implemented, in particular, with the methods of synthetic aperture [4], coherent plane-wave compounding (CPWC) [3], as well as with their varieties and specific techniques [6-13].

The synthetic aperture data acquisition technologies allow achieving the best focusing at any point in the region of interest and obtain a sufficient amount of data for accurate resolution of flows velocity. The described advantages of the technique, in comparison with the conventional ultrasound one, are significant and make it possible to build full field-of-view tissue displacement and Doppler images at high frame rates and high resolution for various medical applications, including Dopplerography [8-11, 14-16], elastography [2, 3, 12, 13], and so on. However, application of these techniques requires massive computational demands, what entails an increase in the cost of medical equipment [17, 18]. Therefore, the task to develop new technique modifications, which can be easily integrated into the existing ultrasound systems and utilize the delay-and-sum hardware to reduce the computational costs and improve the image quality, remains highly relevant [6, 7]. It is also necessary to optimize the parameters that affect (characterize) the quality of images, obtained using the synthetic aperture technology [3, 11, 13, 15, 19-24].

The development of ultrasound Doppler techniques, with using the technology of coherent compounding of ultrasound response signals, made it possible to improve spectral estimations in comparison with those obtained, when using the conventional Doppler techniques [8]. A number of experimental works are devoted to the estimation of the velocity vector [9, 14, 22, 25], visualization of low-velocity blood flows [8, 10] and of small vessels [26], simultaneous visualization of blood flow and the vessel wall motion in the arteries [27], as well as the implementation of three-dimensional imaging for all the Doppler techniques (3-D ultrafast power Doppler, pulsed Doppler, color Doppler imaging) [11]. The effect of the influence of the ultrasound scatterers motion on the Doppler signal correlation function was theoretically investigated in [28], and in [23, 29] a motion correction scheme, which allowed to improve the accuracy of the velocity estimation, as well as to improve the signal-to-noise ratio, was developed. A number of experimental works are devoted to the development of new techniques within the frame of the plane-wave compounding technique, which allow improving the image quality in terms of lateral resolution, contrast ratio, and contrast-to-noise ratio both for two-dimensional B-mode (brightness mode) images [30-34] and for Doppler techniques [35-37].

Despite the existence of numerous theoretical and experimental works, devoted to the coherent compounding for Doppler applications, the studies of the best achievable spatial resolution of an ultrasound system are ongoing up to now, with using the Doppler method for determining the rate of motion. A general theory of the Doppler response formation was developed in [38, 39], which in [40] was generalized for the case of application of the technology of the emitted ultrasound beam dynamic focusing by the synthesized aperture method. In the present work, the spatial

[†] Cite as: I.V. Sheina, and E.A. Barannik, East. Eur. J. Phys. 1, 116 (2022), <https://doi.org/10.26565/2312-4334-2022-1-16>
©I.V. Sheina, E.A. Barannik, 2022

resolution for the plane-wave coherent compounding was estimated on the basis of the previously developed theory of the Doppler response formation.

THEORETICAL MODEL

The present theoretical model of ultrasound scattering by biological tissues and fluids is based on the fact that these objects interact with the ultrasound field like an isotropic continuous medium [41, 42]. Within the framework of the continuum model, the ultrasound is scattered by the density inhomogeneities $\rho(\vec{r}, t)$ and by the medium bulk compressibility $\beta(\vec{r}, t)$, and the power spectrum of the Doppler response signal can be represented as in [39, 40, 43]

$$S(\omega) = k^4 \int d\tau e^{i\omega\tau} \iint_R e^{2i\vec{k}(\vec{r}_1 - \vec{r}_0)} \overline{G_p'^*(\vec{r}_0, t_0) G_p'(\vec{r}_1, t_1)} C(\vec{r}_1 - \vec{r}_0, \tau) d\vec{r}_0 d\vec{r}_1, \quad (1)$$

$$C(\vec{r}_1 - \vec{r}_0, \tau) = \left\langle \left(\tilde{\beta}(\vec{r}_0, t_0) - \tilde{\rho}(\vec{r}_0, t_0) \right) \left(\tilde{\beta}(\vec{r}_1, t_1) - \tilde{\rho}(\vec{r}_1, t_1) \right) \right\rangle,$$

where \vec{k} and $k = 2\pi/\lambda$ are the wave vector and wave number of the ultrasound transducer field in the plane-wave approximation, λ is the wavelength, $\langle \dots \rangle$ is the mean value over the statistical ensemble, $\tau = t_1 - t_0$, $\tilde{\rho}(\vec{r}, t) = \rho^{-1}(\vec{r}, t) [\rho(\vec{r}, t) - \rho_0]$ and $\tilde{\beta}(\vec{r}, t) = \beta_0^{-1} [\beta(\vec{r}, t) - \beta_0]$ are the dimensionless fluctuations of the medium density and its volume compressibility relative to their space-time mean values ρ_0 and β_0 , and the space-time characteristics of the density and compressibility fluctuations are described by the correlation function $C(\vec{r}_1 - \vec{r}_0, \tau)$. The complex function of the distribution of the ultrasound system sensitivity $G_p'(\vec{r}, t)$ over the field depends on the shape of the probing pulses, as well as on the amplitude and phase characteristics of the incident and reflected wave beams. When considering a synthesized aperture regardless of the method applied for determining the Doppler shift frequency and the spectra, described in [40, 43], in the known sensitivity function [41] its time dependence must be taken into account:

$$G_p'(\vec{r}, t) = G_t'(\vec{r}, t) G_r'(\vec{r}, t) b \left(T_1 - \frac{2x'(\vec{r})}{c(t)} \right), \quad (2)$$

where $b(t)$ is the envelope of the probing pulse, T_1 is the sampling time that determines the probing depth, $G_t'(\vec{r}, t)$ and $G_r'(\vec{r}, t)$ are the amplitude of incident waves and the function of the transducer sensitivity to the scattered waves, respectively, $x'(\vec{r})$ is the distance along the axis of transducer from its emitting surface to the origin of the coordinate system x, y, z in the region of interest, $c(t)$ is the propagation velocity of wave front along the axis $x'(\vec{r})$. The time dependence of the magnitude $c(t)$ arises due to the change in the direction of propagation of the emitted plane waves at different probings, as well as to different directions of the wave reception. As a result, in addition to averaging over the statistical ensemble, an averaging over the initial instant of time t_0 is necessary, which is indicated in expression (1) by the top line.

Two different feasible strategies for collection of information in the process of an ultrasound Doppler signal formation are described in [40], which utilize the dynamic change in the angles of radiation and the wave beam reception. For each case, general expressions were obtained for the Doppler signal power spectrum, whose width, according to the well-known Nyquist limit and the Rao-Cramer relation [41, 44], allows assessing the measurement accuracy of the Doppler spectrum average frequency. It was noted in [43], that the formation of the Doppler response directly from a sequence of response signals for the sequence of different directions could lead to broadening of the Doppler signal spectrum. In the physical sense, such a broadening has the same nature as that in the case of uniformly accelerated motion of ultrasound scatterers [45].

To the coherent compounding of discrete complex Doppler response signals at different directions of probing, their summation corresponds, in which the Doppler response is formed from such total values. In the first approximation, the summation can be replaced by integration over the period T of changing the directions of probing. In the case of coherent compounding, the Doppler spectrum width does not depend on the frequency-response characteristics of the sensitivity function [40]:

$$S(\omega_k) = \frac{k^4}{(2\pi)^3} T^2 \int d\vec{q} C(\vec{q}, \omega_k) \left| G(\vec{q} + 2\vec{k}, 0) \right|^2, \quad (3)$$

where $G(\vec{q} + 2\vec{k}, \omega_i)$ is the Fourier-transform of the sensitivity function $G'_p(\vec{r}, t)$, $C(\vec{q}, \omega_k)$ are the spectral components of the correlation function, ω_k are the Doppler shift frequencies of the scattered wave, and \vec{q} is the scattering wave vector. This circumstance indicates the principal feasibility to combine the optimal parameters of the Doppler estimation of the blood flow velocity with a high spatial resolution.

RESULTS

Expression (3) establishes only a general relationship between the power spectrum of the ultrasound Doppler response signal with the scatterers' motion spectral characteristics and the sensitivity function of the system. In general case, the resolution of the ultrasound diagnostic system is determined by its point spread function (PSF). To demonstrate the advantages of the synthetic aperture technology over conventional methods in terms of improving the spatial resolution, let us analyze the function of sensitivity $|G'_p(\vec{r}, \omega_i = 0)|$. In the case, when the plane-wave coherent compounding is considered, it is just this quantity that represents the PSF of the ultrasound diagnostic system. Therefore, the resolution at the given level can be estimated from the corresponding width of the sensitivity function $|G'_p(\vec{r}, \omega_i = 0)|$.

In the case of probing a biological medium by plane waves at different angles, the quantities $G'_i(\vec{r}, t)$ and $G'_r(\vec{r}, t)$ are time dependent due to the wave vector $\vec{k}(t)$, which changes with the change in the direction of probing in time (see Fig. 1, left). The propagation velocity of the plane-wave inclined front with the wave vector $\vec{k}(t)$ along the direction x' is equal to $c(t) = c_0 / \cos \Phi(t)$, where c_0 is the equilibrium rate of ultrasound waves in the medium, $\Phi(t)$ is the angle between the direction of the wave vector $\vec{k}(t)$ and the axis x' . In accordance with this fact, the probing depth for the given sampling time is equal to $l_0 = c_0 T_1 / 2 \cos \Phi$.

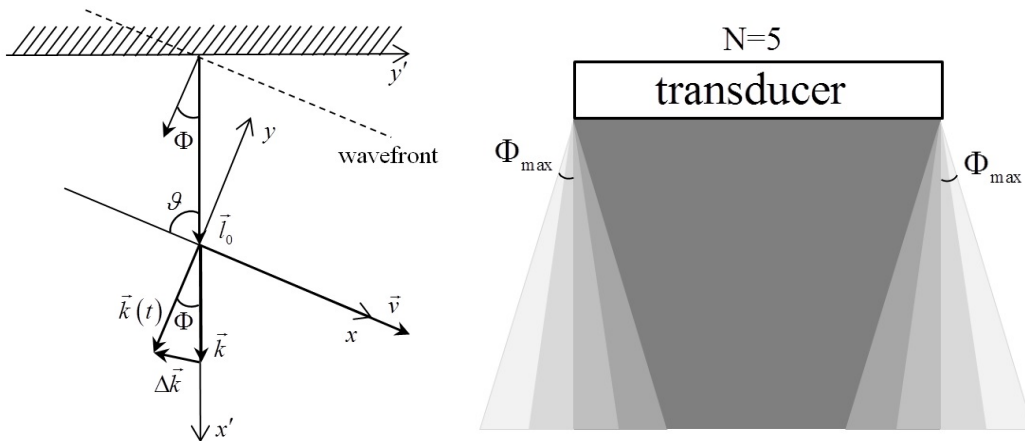


Figure 1. Relative position of the coordinate systems linked to the transducer and the region of interest, when probing with plane-wave fronts at different angles (left). Example of CPWC: five plane waves are transmitted and compounded. The least transparent region is the region with the highest resolution (right).

In the case of plane-wave fronts, the sensitivity function has the form:

$$G'_p(\vec{r}, t) = G_0 e^{2i\{\vec{k}(t) - \vec{k}\} \vec{r}} b \left(T_1 - \frac{2x' \cos \Phi(t)}{c_0} \right), \tag{4}$$

where G_0 is a constant dimensional coefficient, $\vec{k}(t)$ is the direction wave vector, corresponding to time t , and its Fourier component can be described by the expression

$$G'_p(\vec{r}, \omega_j) = \frac{G_0}{T} \int_{-T/2}^{T/2} e^{2i\{\vec{k}(t) - \vec{k}\} \vec{r}} b \left(T_1 - \frac{2x' \cos \Phi(t)}{c_0} \right) e^{i\omega_j t} dt, \tag{5}$$

As a rule, in CPWC the angle $\Phi(t)$ at all steering angles can be considered small, then from Fig. 1 (left) it is obvious that the first term in the exponent of the integrand can be represented as

$$2\{\vec{k}(t) - \vec{k}\} \vec{r} \approx 2\Delta k \vec{e}_y \cdot \vec{r} = 2\Delta k \vec{e}_y \cdot (\vec{r}' - \vec{l}_0) = 2\Delta k y' = 4k \sin \frac{\Phi(t)}{2} y'.$$

Then, substituting the last expression in (5), we obtain

$$G'_p(\vec{r}, \omega_j) = \frac{G_0}{T} \int_{-T/2}^{T/2} e^{4ik \sin \frac{\Phi(t)}{2} y' + i\omega_j t} b \left(T_1 - \frac{2x' \cos \Phi(t)}{c_0} \right) dt. \tag{6}$$

Generally, in CPWC all the transmit angles are distributed symmetrically about 0° and equally spaces, as Fig. 1 (right) shows. As a result, the expression for the frequency component of the sensitivity function is reduced to the integral, which can be easily taken analytically. Then, when integrating (6), one can introduce the angular velocity of rotation of the wave vector $\vec{k}(t)$ in accordance with the law $\Phi(t) = \Omega t$. In addition, with the smallness of the angle Φ taken into account, one can use the expansion of the sine and cosine in the linear approximation in Φ .

$$G'_p(\vec{r}, \omega_j) \cong \frac{G_0}{T} \int_{-T/2}^{T/2} e^{4ik \frac{\Omega t}{2} y' + i\omega_j t} b \left(T_1 - \frac{2x'}{c_0} \right) dt = G_0 \frac{\sin(2k\Omega y' + \omega_j) \frac{T}{2}}{(2k\Omega y' + \omega_j) \frac{T}{2}} b \left(T_1 - \frac{2x'}{c_0} \right). \tag{7}$$

In the general case of a dynamically changing radiation field, the Doppler signal is a sequence of discrete values of the response signals for the sequence of different angles, and the dependence on frequency ω_j of the sensitivity function is described by expressions (5)-(7). This value has its maximum at the frequency component, which depends on the value of the transverse coordinate y' : $\omega_j = -2k\Omega y'$. In the considered case of coherent plane-wave compounding, the sensitivity function takes the form:

$$G'_p(\vec{r}, \omega_j = 0) \cong G_0 \frac{\sin k\Omega T y'}{k\Omega T y'} b \left(T_1 - \frac{2x'}{c_0} \right). \tag{8}$$

We note right away, that in accordance with these expressions, the resolution in the transverse direction does not depend on the probing depth and is determined by the so-called sinc-function $\text{sinc}(x) = \sin x / x$. Such a form is associated with the choice of the rectangular weighting function for the response signals at different steering angles. The use of other known weighting windows, when integrating in (6), allows suppressing the side lobes of the sensitivity function with some broadening of the main lobe.

Nevertheless, when using expression (8), it is easy to estimate the attainable resolution. In particular, the first zero of the sensitivity function appears at such a value of the transverse coordinate, which satisfies the equality $k\Omega T y'_0 = \pi$.

Here we obtain the width of the sensitivity function

$$d = 2y'_0 = 2 \frac{\lambda}{2\Omega T} = \frac{\lambda}{2\Phi_{\max}}, \tag{9}$$

where $2\Phi_{\max}$ is the entire range of the steering angles, i.e. the angle between the extreme directions of the wave vector.

In a number of experimental works [30, 35], the full width at half maximum (FWHM, -6 dB beam width), which characterizes the main lobe of the directivity diagram, is used to estimate the resolution for the point targets both in the longitudinal and transverse directions. The numerical estimate for the sensitivity function width at the level of 6 dB gives the value

$$d_{6dB} = 2y'_{6dB} \approx \frac{0.3\lambda}{\Phi_{\max}}, \tag{10}$$

Where y'_{6dB} is the root of the equation $\sin y'_{6dB} = \frac{1}{2} y'_{6dB}$ along the interval $0 \leq y'_{6dB} \leq \pi$.

DISCUSSION

Generally, the CPWC uses a sequence of N of several consecutive emissions of broad wave beams at different angles Φ (see Fig. 1 (right)). As it follows from expressions (9)-(10), the Doppler system lateral resolution depends only on the maximum angle Φ_{\max} , but not on the number N of the probing angles. For this reason, an increase in the frame rate at the same resolution can be obtained by decreasing the number of probing angles (without changing the value of the maximum probing angle).

However, the number of insonifications of the medium significantly affect the image contrast and the signal-to-noise ratio [3, 35]. It is the expression (3) that shows the response signal power to be proportional to the value T^2 , which actually represents the square of the value N of the number of probing wavefronts over time T . Therefore, a

decrease in the value N , while maintaining the value of the maximum angle leads to a decrease in the contrast [35], and the signal-to-noise ratio increases with an increase of N , as long as, when summing the random noise, its power increases by N times, what results in the signal-to-noise ratio to be proportional to N , which corresponds to [3].

If assuming $\Delta\alpha = \pi/12$, then from (9) and (10) we obtain $d = 2\lambda$ and $d_{\text{6dB}} \approx 1.2\lambda$, respectively, which correspond to the values, which are usual for the lateral resolution in the focal region of the standard system. Thus, in [35] the central frequency was equal to 8MHz , which corresponded to the wavelength $\lambda = 0.1925\text{mm}$, $\Delta\alpha = 12^\circ = \pi/15$, and the resolution was in the range from 0.33mm (at the probing depth of 1cm) to 0.50mm (at the probing depth of 2.8cm). The resolution values, calculated according to expressions (9) and (10), are equal to $d \approx 0.46\text{mm}$ and $d_{\text{6dB}} \approx 0.28\text{mm}$, respectively.

Strictly speaking, when using the synthetic aperture technique, the width of the measuring volume is determined not only by the functions $G'_i(\vec{r}, t)$ and $G'_r(\vec{r}, t)$, but also, to a small extent, by the probing pulse duration. This effect can be taken into account, if in the expression for the Fourier component of the sensitivity function (6), the expansion is carried out up to the quadratic ones by Φ terms in the argument of the pulse envelop, what will result in additional weak time dependence.

The estimates of the Doppler system lateral resolution show that, in contrast to the traditional Doppler methods, the attainable lateral resolution, when the technique of the coherent plane-wave compounding in the entire range of the probing depth is applied, is not worse than that in the focal region at the traditional ultrasonic focusing. Such methods as ultrafast power Doppler imaging (Coherent Flow Power Doppler – CFPD) [10] make it possible to evaluate low-velocity blood flows in small vessels ($<1\text{mm}$). Color Doppler mapping in small vessels is extremely important, for example, in clinical cases of the development of abnormal growth of vessels structures, such as angiogenesis in cancer [46], or those caused by inflammation processes [47]. The varieties of Doppler techniques allow suppressing incoherent noises and artifacts, associated with the biological structures motion, thereby significantly improving the quality of the resulting image, what is confirmed by clinical investigations [48, 49].

From the point of view of spectral estimates, when using the technology of coherent plane-wave compounding, it is necessary to determine properly the total Doppler power spectrum. To obtain the corresponding analytical expression, the integral in expression (3) should be calculated using the expression for the sensitivity function (8), which was obtained in the present work. The solution to this problem is beyond the scope of this work and is of interest for further studies of the CPWC method.

CONCLUSIONS

Improving the quality of biological object images, obtained by ultrasound Doppler studies, is an urgent task. The problem of low- flow imaging in small vessels is especially acute, when using traditional imaging techniques, where the feasibility of clutter filtering is a major challenge, since only a small number of temporary samples are available for processing.

The appearance of the new technique for the coherent plane-wave compounding has provided a better quality of B-images and the possibility of continuous collection of information for the Doppler modes, as compared to the traditional techniques. The technique allows to build the full field-of-view tissue displacement and Doppler images at high frame rates and high resolution, while continuous data collection provides new opportunities for clutter filtering and imaging the low-velocity flows. In accordance with the CPWC technology, a high-resolution image is formed by coherent compounding of ultrasound response signals, obtained from a set of probing pulses from different steering angles.

In this work, an estimation of the achievable spatial resolution was carried out with using the CPWC technology based on the previously developed theory of the Doppler response formation with a dynamic change in the direction of ultrasound waves. An analytical expression has been obtained for the ultrasound system field sensitivity, which in the case of a rectangular weighting window for the response signals is determined by the sinc-function, well known from the theory of focusing. The magnitude of the lateral resolution, which is inversely proportional to the range of the steering angles, does not depend on the total number of the steering angles and the probing depth. It is shown that the theoretically estimated magnitude of the Doppler system lateral resolution, when using the coherent plane-wave compounding, is no worse than that in the focal region with the traditional focusing of ultrasound, and is in good agreement with the experimental data presented in literature.

ORCID IDs

 Iryna V. Sheina, <https://orcid.org/0000-0002-0293-4849>;  Evgen A. Barannik, <https://orcid.org/0000-0002-3962-9960>

REFERENCES

- [1] J.Y. Lu, IEEE Trans. Ultrason., Ferroelec., Freq. Contr. **44**(4), 839 (1997), <https://doi.org/10.1109/58.655200>
- [2] M. Tanter, J. Bercoff, L. Sandrin, and M. Fink, IEEE Trans. Ultrason. Ferroelectr.Freq. Contr.**49**(10), 1363 (2002), <https://doi.org/10.1109/TUFFC.2002.1041078>
- [3] G. Montaldo, M. Tanter, J. Bercoff, N. Benech, and M. Fink, IEEE Trans. Ultrason.Ferroelectr.Freq.Contr. **56**(3), 489 (2009), <https://doi.org/10.1109/TUFFC.2009.1067>

- [4] J.A. Jensen, S.I. Nikolov, K.L. Gammelmarkand, and M.H. Pedersen, *Ultrasonics*, **44**(1), e5 (2006), <https://doi.org/10.1016/j.ultras.2006.07.017>
- [5] J.-l. Gennisson et al., *IEEE Trans. Ultrason. Ferroelec. Freq. Contr.* **62**(6), 1059 (2015), <https://doi.org/10.1109/TUFFC.2014.006936>
- [6] M. A. Lediju, G. E. Trahey, B. C. Byram and J. J. Dahl, *IEEE Trans. Ultrason. Ferroelec. Freq. Contr.* **58**(7), 1377 (2011), <http://doi.org/10.1109/TUFFC.2011.1957>
- [7] Y.L. Li, J.J. Dahl, *J. Acoust. Soc. Am.* **141**(3), 1582 (2017), <https://doi.org/10.1121/1.4976960>
- [8] J. Bercoff, G. Montaldo, T. Loupas, D. Savery, F. Meziere, M. Fink, and M. Tanter, *IEEE Trans. Ultrason. Ferroelec. Freq. Contr.* **58**(1), 134 (2011), <https://doi.org/10.1109/TUFFC.2011.1780>
- [9] J. A. Jensen and N. Oddershede, *IEEE Trans. Med. Imag.* **25**(12), 1637-1644(2006), <https://doi.org/10.1109/TMI.2006.883087>
- [10] Y.L. Li, J.J. Dahl, *IEEE Trans. Ultrason. Ferroelec. Freq. Contr.* **62**(6), 1022 (2015), <https://doi.org/10.1109/TUFFC.2014.006793>
- [11] J. Provost, C. Papadacci, C. Demene, J. Gennisson, M. Tanter and M. Pernot, *IEEE Trans. Ultrason. Ferroelec. Freq. Contr.* **62**(8), 1467 (2015), <https://doi.org/10.1109/TUFFC.2015.007032>
- [12] J. Bercoff, M. Tanter, and M. Fink, *IEEE Trans. Ultrason. Ferroelec. Freq. Contr.* **51**(4), 396 (2004), <https://doi.org/10.1109/TUFFC.2004.1295425>
- [13] C. Papadacci, M. Pernot, M. Couade, M. Fink and M. Tanter, *IEEE Trans. Ultrason. Ferroelec. Freq. Contr.* **61**(2), 288 (2014), <http://doi.org/10.1109/TUFFC.2014.6722614>
- [14] J. Udesen, F. Gran, K. L. Hansen, J. A. Jensen, C. Thomsen and M. B. Nielsen, *IEEE Trans. Ultrason. Ferroelec. Freq. Contr.*, **55**(8), 1729 (2008), <https://doi.org/10.1109/TUFFC.2008.858>
- [15] J. Jensen, M. B. Stuart, and J. A. Jensen, *IEEE Trans. Ultrason. Ferroelec. Freq. Contr.* **63**(11), 1922 (2016), <https://doi.org/10.1109/TUFFC.2016.2591980>
- [16] B. Osmanski, M. Pernot, G. Montaldo, A. Bel, E. Messas and M. Tanter, *IEEE Trans. Med. Imag.*, **31**(8), 1661 (2012), <http://doi.org/10.1109/TMI.2012.2203316>
- [17] M. Tanter and M. Fink, *IEEE Trans. Ultrason. Ferroelectr. Freq. Control.* **61**(1), 102 (2014), <https://doi.org/10.1109/TUFFC.2014.6689779>
- [18] S. I. Nikolov, B. G. Tomov and J. A. Jensen, *2006 Fortieth Asilomar Conference on Signals, Systems and Computers*, 2006, pp. 1548-1552, <https://doi.org/10.1109/ACSSC.2006.355018>
- [19] R. Moshavegh, J. Jensen, C. A. Villagómez-Hoyos, M. B. Stuart, M. C. Hemmsen and J. A. Jensen, in *Proceedings of SPIE Medical Imaging* (San Diego, California, United States, 2016) pp. 97900Z-97900Z-9, <https://doi.org/10.1117/12.2216506>
- [20] J. Kortbek, J. A. Jensen and K. L. Gammelmark, *Ultrasonics*, **53**(1), 1 (2013), <https://doi.org/10.1016/j.ultras.2012.06.006>
- [21] J. Cheng and J.Y. Lu, *IEEE Trans. Ultrason. Ferroelec. Freq. Contr.* **53**(5), 880 (2006), <https://doi.org/10.1109/TUFFC.2006.1632680>
- [22] N. Oddershede and J. A. Jensen, *IEEE Trans. Ultrason. Ferroelec. Freq. Contr.* **54**(9), 1811 (2007), <https://doi.org/10.1109/TUFFC.2007.465>
- [23] B. Denarie et al., *IEEE Trans. Med. Imaging* **32**(7), 1265 (2013), <https://doi.org/10.1109/TMI.2013.2255310>
- [24] Y. Tasinkevych, I. Trots, A. Nowicki, P.A. Lewin, *Ultrasonics* **52**(2), 333 (2012), <https://doi.org/10.1016/j.ultras.2011.09.003>
- [25] S. Ricci, L. Bassi and P. Tortoli, *IEEE Trans. Ultrason. Ferroelec. Freq. Contr.* **61**(2), 314 (2014), <https://doi.org/10.1109/TUFFC.2014.6722616>
- [26] Y. L. Li, D. Hyun, L. Abou-Elkacem, J. K. Willmann, J.J. Dahl, *IEEE Trans. Ultrason. Ferroelec. Freq. Contr.* **63**(11), 1878 (2016), <https://doi.org/10.1109/TUFFC.2016.2616112>
- [27] I. K. Ekroll, A. Swillens, P. Segers, T. Dahl, H. Torp and L. Lovstakken, *IEEE Trans. Ultrason. Ferroelec. Freq. Contr.* **60**(4), 727 (2013) <https://doi.org/10.1109/TUFFC.2013.2621>
- [28] D. Hyun, J.J. Dahl, *J. Acoust. Soc. Am.* **147**(3), 1323 (2020), <https://doi.org/10.1121/10.0000809>
- [29] I.K. Ekroll, M.M. Voormolen, O.K.-V. Standal, J.M. Rau and L. Lovstakken, *IEEE Trans. Ultrason. Ferroelec. Freq. Contr.* **62**(9), 1634 (2015), <https://doi.org/10.1109/TUFFC.2015.007010>
- [30] Y. Wang, C. Zheng, H. Peng and C. Zhang, *IEEE Access* **6**, 36927 (2018), <https://doi.org/10.1109/ACCESS.2018.2852641>
- [31] S. Salles, F. Varray, Y. Bénane and O. Basset, *2016 IEEE International Ultrasonics Symposium (IUS)*, 2016, pp. 1-4, <https://doi.org/10.1109/ULTSYM.2016.7728751>
- [32] C. Zheng, Q. Zha, L. Zhang and H. Peng, *IEEE Access* **6**, 495 (2018), <https://doi.org/10.1109/ACCESS.2017.2768387>
- [33] Y.M. Benane et al., *2017 IEEE International Ultrasonics Symposium (IUS)*, 2017, pp. 1-4, <https://doi.org/10.1109/ULTSYM.2017.8091880>
- [34] X. Yan, Y. Qi, Y. Wang, Y. Wang, *Sensors* **21**, 394 (2021), <https://doi.org/10.3390/s21020394>
- [35] C. Golfetto, I. K. Ekroll, H. Torp, L. Lovstakken and J. Avdal, *IEEE Trans. Ultrason. Ferroelec. Freq. Contr.* **68**(4), 1105 (2021), <https://doi.org/10.1109/TUFFC.2020.3033719>
- [36] S. Salles, H. Liebgott, O. Basset, C. Cachard, D. Vray and R. Lavarello, *IEEE Trans. Ultrason. Ferroelec. Freq. Contr.* **61**(11), 1824 (2014), <https://doi.org/10.1109/TUFFC.2014.006543>
- [37] C.-C. Shen, Y.-C. Chu, *Sensors* **21**, 4856 (2021), <https://doi.org/10.3390/s21144856>
- [38] E.A. Barannik, *Ultrasonics* **39**(2), 311 (2001), [https://doi.org/10.1016/S0041-624X\(01\)00059-2](https://doi.org/10.1016/S0041-624X(01)00059-2)
- [39] I.V. Skresanova and E.A. Barannik, *Ultrasonics* **52**(5), 676 (2012), <https://doi.org/10.1016/j.ultras.2012.01.014>
- [40] I.V. Sheina, O.B. Kiselov and E.A. Barannik, *East Eur. J. Phys.* **4**, 5 (2020), <https://doi.org/10.26565/2312-4334-2020-4-01>
- [41] P. J. Fish, in: *Physical Principles of Medical Ultrasonics*, edited by C.R. Hill (EllisHorwood, Chichester, 1986), pp. 338-376.
- [42] R.J. Dickinson, D.K. Nassiri, in: *Physical principles of medical ultrasonics*, edited by C. R. Hill, J. C. Bamber, G. R. terHaar (John Wiley & Sons, West Sussex, 2004), pp. 191-222.
- [43] E.A. Barannik and O.S. Matchenko, *East Eur. J. Phys.* **3**(2) 61 (2016), <https://doi.org/10.26565/2312-4334-2016-2-08>. (in Russian)

- [44] W. Gilson and S. Orphanoudakis, in: *Proceedings of the Annual International Conference of the IEEE Engineering in Medicine and Biology Society* (IEEE, New Orleans, 1988), pp. 473-474, <https://doi.org/10.1109/IEMBS.1988.94615>
- [45] O.S. Matchenko and E.A. Barannik, *Acoust. Phys.* **63**(5), 596 (2017), <https://doi.org/10.1134/S106377101705008>
- [46] R.S. Apte, D.S. Chen, N. Ferrara, *Cell*, **176**(6), 1248-1264 (2019), <https://doi.org/10.1016/j.cell.2019.01.021>
- [47] J. Gallo, M. Raska, E. Kriegova, S. B. Goodman, *Journal of Orthop. Translat.*, **10**, 52 (2017), <https://doi.org/10.1016/j.jot.2017.05.007>
- [48] M. Jakovljevic, B.C. Yoon, L. Abou-Elkacem, D. Hyun, Y. Li, E. Rubesova, J.J. Dahl, *IEEE Trans. Ultrason. Ferroelectr. Freq. Control.* **68**(1), 92 (2021), <https://doi.org/10.1109/TUFFC.2020.3010341>
- [49] Y.L. Li, D. Hyun, I. Durot, J.K. Willmann and J.J. Dahl, *2018 IEEE International Ultrasonics Symposium (IUS)*, 2018, pp. 1-9, <https://doi.org/10.1109/ULTSYM.2018.8579726>

РОЗДІЛЬНА ЗДАТНІСТЬ УЛЬТРАЗВУКОВОЇ ДОПЛЕРІВСЬКОЇ СИСТЕМИ ПРИ ВИКОРИСТАННІ ТЕХНОЛОГІЇ КОГЕРЕНТНОГО КОМПАУНДІНГУ ПЛОСКИХ ХВИЛЬ

І.В. Шеїна, Є.О. Баранник

Кафедра медичної фізики та біомедичних нанотехнологій, Харківський національний університет імені В.Н. Каразіна М. Свободи 4, Харків, 61022, Україна

В роботі на підставі розвиненої раніше теорії формування доплерівського відгуку проведені оцінки досяжної просторової роздільної здатності при ультразвуковому зондуванні плоскими хвилями з різних ракурсів. В теоретичних розрахунках когерентний компаундінг сигналів доплерівського відгуку проводився за періодом зміни ракурсів зондування. У цьому випадку здобуто аналітичний вираз для функції чутливості ультразвукової системи за полем, яка відповідає функції відгуку точкового джерела. У випадку прямокутного зважувального вікна для сигналів відгуку роздільна здатність визначається добре відомою sinc-функцією. Величина поперечної роздільної здатності обернено пропорційна діапазону ракурсних кутів. Показано, що теоретично оцінена величина поперечної роздільної здатності доплерівської системи при використанні технології когерентного компаундінгу плоских хвиль добре відповідає представленим в літературі експериментальним даним.

Ключові слова: ультразвукова візуалізація, доплерівський спектр, технологія синтезованої апертури, когерентний компаундінг плоских хвиль, континуальна модель розсіяння, функція чутливості, функція відгуку точкового джерела, формування відгуку

INSTRUCTIONS FOR PREPARING MANUSCRIPT IN THE EAST EUROPEAN JOURNAL OF PHYSICS

Nikita F. Author^{a,*}, Peter V. Co-Author(s)^{b,†}

^aAffiliation of first author

^bAffiliation of second author (if different from the first Author)

*Corresponding Author: corresponding_authors@mail.com, ^aORCID ID

[†]E-mail: co_authors@mail.com, ^bORCID ID

Received May 25, 2021; revised June 25, 2021 accepted July 5, 2021

Each paper must begin with an abstract. The abstract should be typed in the same manner as the body text (see below). Please note that these Instructions are typed just like the manuscripts should be. The abstract must have at least **1800 phonetic symbols**, supplying general information about the achievements, and objectives of the paper, experimental technique, methods applied, significant results and conclusions. Page layout: the text should be printed on the paper A4 format, at least **5 pages**, with margins of: **Top - 3, Bottom, Left and Right - 2 cm**. The abstract, keywords should be presented in **English** (only for foreign authors), and **Ukrainian**.

Keywords: there, must, be, 5-10 keywords

PACS: specify PACS code(s) here

This is **Introduction** section. This paper contains instructions for preparing the manuscripts. The text should be prepared in “**doc**” or “**docx**” format.

INSTRUCTIONS

The text should be typed as follows:

- **title:** Times New Roman, 12 pt, ALL CAPS, bold, 1 spacing, centred;
- **authors:** name, initials and family names; Times New Roman, 12 pt, bold, 1 spacing, centred;
- **affiliation(s):** Times New Roman, 9 pt, italic, 1 spacing, centred;
- **abstract:** Times New Roman, 9 pt, 1 spacing, justified;
- **body text:** Times New Roman, 10 pt, 1 spacing, justified; paragraphs in sections should be indented right (tabulated) for 0.75 cm;
- **section titles:** Times New Roman, 10 pt, bold, 1 spacing, centred, without numbering, one line should be left, blank above section title;
- **subsection titles:** Times New Roman, 10 pt, bold, 1 spacing, centred, without numbering in accordance to the section (see below), one line should be left blank above subsection title;
- **figure captions:** width of the figure should be 85 or 170 mm, Figures should be numbered (**Figure 1.**) and titled below Figures using sentence format, Times New Roman, 9 pt, 1 spacing, centred (if one line) or justified (if more than one line); one line should be left blank below figure captions;
- **table captions:** width of the table should be 85 or 170 mm, tables should be numbered (**Table 1.**) and titled above tables using sentence format, Times New Roman, 10 pt, 1 spacing, justified, Tables should be formatted with a single-line box around the outside border and single ruling lines between rows and columns; one line should be left blank below tables;
- **equations:** place equations centred, numbered in Arabic: (1), flush right, equations should be specially prepared in **MathType** or “**Microsoft Equation**”, Times New Roman, 10 pt, one line should be left blank below and above equation.

Additional instructions

Numerated figures and tables should be embedded in your text and placed after they are cited. Only sharp photographs and drawings are acceptable. Letters in the figures should be 3 mm high. The figures should be presented in one of the following graphic formats: jpg, gif, pcx, bmp, tif.

REFERENCES

Cite references in AIP style (<https://guides.lib.monash.edu/citing-referencing/aip>). Numbering in the order of referring in the text, e.g. [1], [2-5], etc. References should be listed in numerical order of citation in the text at the end of the paper (justified), Times New Roman, 9 pt, 1 spacing.

Journal Articles

- [1] T. Mikolajick, C. Dehm, W. Hartner, I. Kasko, M.J. Kastner, N. Nagel, M. Moert, and C. Mazure, *Microelectron. Reliab.* **41**, 947 (2001), [https://doi.org/10.1016/S0026-2714\(01\)00049-X](https://doi.org/10.1016/S0026-2714(01)00049-X).
- [2] S. Bushkova, B.K. Ostafiyshuk, and O.V. Copaiev, *Physics and Chemistry of Solid State.* **15**(1), 182 (2014), <http://page.if.ua/uploads/pcss/vol15/!1501-27.pdf>. (in Ukrainian)
- [3] M. Yoshimura, E. Nakai, K. Tomioka, and T. Fukui, *Appl. Phys. Lett.* **103**, 243111 (2013), <http://dx.doi.org/10.7567/APEX.6.052301>.

E-print Resources with Collaboration Research or Preprint

- [4] M. Aaboud et al. (ATLAS Collaboration), *Eur. Phys. J. C*, **77**, 531 (2017), <http://dx.doi.org/10.1140/epjc/s10052-017-5061-9>
- [5] Sjöstrand et al., *Comput. Phys. Commun.* **191**, 159 (2015), <https://doi.org/10.1016/j.cpc.2015.01.024>.
- [6] Boudreau, C. Escobar, J. Mueller, K. Sapp, and J. Su, (2013), <http://arxiv.org/abs/1304.5639>.

Books

- [7] S. Inoue, and K.R. Spring, *Video Microscopy: The fundamentals*, 2nd ed. (Plenum, New York, 1997), pp. 19-24.
- [8] I. Gonsky, T.P. Maksymchuk, and M.I. Kalinsky, *Біохімія Людини [Biochemistry of Man]*, (Ukrmedknnya, Ternopil, 2002), pp. 16. (in Ukrainian)

Edited Books

- [9] Z.C. Feng, editor, *Handbook of Zinc Oxide and Related Materials: Devices and Nano Engineering*, vol. 2, (CRC Press/Taylor & Francis, Boca Raton, FL, 2012)

Book Chapters

- [10] P. Blaha, K. Schwarz, G.K.H. Madsen, D. Kvasnicka, and J. Luitz, in: *WIEN2K, An Augmented Plane Wave Plus Local Orbitals Program for Calculating Crystal Properties*, edited by K. Schwarz (Techn. Universität Wien, Austria, 2001).
- [11] M. Gonzalez-Leal, P. Krecmer, J. Prokop, and S.R. Elliot, in: *Photo-Induced Metastability in Amorphous Semiconductors*, edited by A.V. Kolobov (Wiley-VCH, Weinheim, 2003), pp. 338-340.
- [12] A. Kochelap, and S.I. Pekar, in: *Теорія Спонтанної у Стимульованій Хемілюмінесценції Газов [Theory of Spontaneous and Stimulated Gas Chemiluminescence]* (Naukova dumka, Kyiv, 1986), pp. 16-29. (in Russian)

Conference or Symposium Proceedings

- [13] C. Yaakov, and R. Huque, in: *Second International Telecommunications Energy Symposium Proceedings*, edited by E. Yow (IEEE, New York, 1996), pp. 17-27.
- [14] V. Nikolsky, A.K. Sandler, and M.S. Stetsenko, in: *Автоматика-2004: Матеріали 11 Міжнародної Конференції по Автоматичному Управлінню [Automation-2004: Materials of the 11th International Conference on Automated Management]* (NUHT, Kyiv, 2004), pp. 46-48. (in Ukrainian)

Patent

- [15] I.M. Vikulin, V.I. Irha, and M.I. Panfilov, Patent Ukraine No. 26020 (27 August 2007). (in Ukrainian)

Thesis / Dissertation

- [16] R.E. Teodorescu, Ph.D. dissertation, The George Washington University, 2009.

Special Notes

1. Use International System of Units (SI system). 2. It is undesirable to use acronyms in the titles. Please define the acronym on its first use in the paper. 3. Refer to isotopes as ¹⁴C, ³H, ⁶⁰Co, etc.

Наукове видання

СХІДНО-ЄВРОПЕЙСЬКИЙ ФІЗИЧНИЙ ЖУРНАЛ

Номер 1, 2022

EAST EUROPEAN JOURNAL OF PHYSICS

No 1, 2022

Збірник наукових праць
англійською та українською мовами

Коректор – Коваленко Т.О.
Технічний редактор – Гірник С.А.
Комп'ютерне верстання – Гірник С.А.

Підписано до друку 11.04.2022. Формат 60×84/8. Папір офсетний.

Друк цифровий.

Ум. друк. арк. 10,5. Обл.-вид. арк. 10,9

Тираж 50 пр. Зам. № 60/2021. Ціна договірна

Видавець і виготовлювач

Харківський національний університет імені В.Н. Каразіна

61022, Харків, майдан Свободи, 4

Свідоцтво суб'єкта видавничої справи ДК № 3367 від 13.01.09

Видавництво Харківський національний університет імені В.Н. Каразіна
тел. +380-057-705-24-32